Title
Interplanetary Field Enhancements: The Interaction between Solar Wind and Interplanetary Dusty Plasma Released by Interplanetary Collisions

Author
Lai, Hairong

Publication Date
2014

UNIVERSITY OF CALIFORNIA

Los Angeles

Interplanetary Field Enhancements:

The Interaction between Solar Wind and Interplanetary Dusty Plasma

Released by Interplanetary Collisions

A dissertation submitted in partial satisfaction of the requirements for the degree

Doctor of Philosophy in Geophysics and Space Physics

by

Hairong Lai

2014

ABSTRACT OF THE DISSERTATION

Interplanetary Field Enhancements: The Interaction between Solar Wind and Interplanetary Dusty Plasma Released by Interplanetary Collisions

by

Hairong Lai

Doctor of Philosophy in Geophysics and Space Physics

University of California, Los Angeles, 2014

Professor Christo T. Russell, Chair

Interplanetary field enhancements (IFEs) are unique large-scale structures in the solar wind. During IFEs, the magnetic-field strength is significantly enhanced with little perturbation in the solar-wind plasma. Early studies showed that IFEs move at nearly the solar-wind speed and some IFEs detected at $0.72AU$ by *Pioneer Venus Orbiter* (PVO) are associated with material co-

orbiting with asteroid Oljato. To explain the observed IFE features, we develop and test an IFE formation hypothesis: IFEs result from interactions between the solar wind and clouds of nanoscale charged dust particles released in interplanetary collisions.

This hypothesis predicts that the magnetic field drapes and the solar wind slows down in the upstream. Meanwhile the observed IFE occurrence rate should be comparable with the detectable interplanetary collision rate. Based on this hypothesis, we can use the IFE occurrence to determine the spatial distribution and temporal variation of interplanetary objects which produce IFEs.

To test the hypothesis, we perform a systematic survey of IFEs in the magnetic-field data from many spacecraft. Our datasets cover from 1970s to present and from inner than $0.3AU$ to outer than $5AU$. In total, more than 470 IFEs are identified and their occurrences show clustering features in both space and time. We use multi-spacecraft simultaneous observations to reconstruct the magnetic-field geometry and find that the magnetic field drapes in the upstream region. The results of a superposed epoch study show that the solar wind slows down in the upstream and there is a plasma depletion region near the IFE centers. In addition, the solar-wind slowdown and plasma depletion feature are more significant in larger IFEs. The mass contained in IFEs can be estimated by balancing the solar-wind pressure force exerted on the IFEs against the solar gravity. The solar-wind slowdown resultant from the estimated mass is consistent with the result in superposed epoch study.

The interplanetary collision rate is estimated based on the flux model of Ceplecha [1992] and collision model of Grün [*et al*., 1985]. A debris distribution model of Fujiwara [*et al*., 1977] is modified to estimate the mass carried by nanoscale dust particles. The integrated collision rate inside a detectable volume, which is a truncated cone starting from $0.2AU$, is used to compare with the observed IFE rate. At $1AU$, we find that in the same mass range, the two rates are comparable. Inside $1AU$, both rates increase slowly as the heliocentric distance increases.

We reanalyze the PVO observations and confirm the association between IFEs and co-orbiting material of asteroid 2201 Oljato. An analogous study is performed at $1AU$ and we find that material co-orbiting with asteroid 138175 produces many IFEs there. We then compare the earlier PVO observations with the present *Venus Express* (VEX) observation and find that the IFE production rate of the material co-orbiting with Oljato has decreased in the past three decades. A comparison between earlier IMP 8 observations and current observations shows a similar decrease in the rate of IFEs associated with asteroid 138175. Such a rate decrease can be explained by the gravitational scattering of co-orbiting material accompanying both asteroids, as they make occasional close passes of the Earth and Venus. Simulations show that due to the gravitational perturbations from the Earth and Venus, gaps can be formed in the otherwise continuous debris trails in periods of decades [Connors *et al*., 2014a].

The importance of this IFE study is discussed in this thesis. We now have a better understanding of a previous mysterious phenomenon, sufficient to use the IFE occurrence to identify small interplanetary objects. Material of tens of meters across co-orbiting with near-Earth objects is too small to detect by traditional survey methods, but still can cause great property and civilian damage once it enters the Earth's atmosphere. In addition, due to gravitational perturbations, the co-orbiting material can be spread along and across the orbits of their parent bodies, which otherwise might be considered to have been well determined and safe.

With our new small-object-identification technique, we can obtain the spatial distribution of the potentially hazardous material and develop a planetary defense stratagem.

The dissertation of Hairong Lai is approved.

Vassilis Angelopoulos

Robert J. Strangeway

Edward L. Wright

Christo T. Russell, Committee Chair

University of California, Los Angeles

2014

For my parents and Prof. Russell…

TABLE OF CONTENTS

Appendix

List of Figures

List of Tables

ACKNOWLEDGMENTS

Here I would like to express my sincerest gratitude and respect to a number of people without whom my work would not be possible.

Foremost I would like to offer my very great appreciation to my advisor, Prof. Christopher T. Russell, for guiding me through my graduate study with his wisdom, experience and patience. I am also strongly inspired by Prof. Russell’s enthusiasm for space physics and dedication to academia.

I would like to express my special thanks to my dissertation committee members, Prof. Christopher Russell, Prof. Vassilis Angelopoulos, Dr. Robert Strangeway, and Prof. Edward Wright, for their advice, guidance, and valuable time.

I gratefully acknowledge the faculty and researches who have taught me a lot both inside and outside the academic area: Prof. Christopher Russell, Prof. Margaret Kivelson, Prof. Robert McPherron, Prof. Ray Walker (also helped me in preparing the field examination), Prof. Vassilis Angelopoulos, Dr. Robert Strangewary, and others.

Special appreciation goes to my wonderful research group at UCLA, led by Prof. Christopher Russell. They are Dr. Robert Strangeway, Dr. Yingdong Jia, Dr. Yingjuan Ma, Dr. Lan Jian, Dr. Hanying Wei, Dr. Peter chi, and others. Without discussion with them, my work would be less rewarding.

I also would like to acknowledge the professors in the department of physics and astronomy and in the department of atmospheric and oceanic sciences. I benefit a lot from the lectures they gave.

A great deal of gratitude is due to Dr. Gian Luca Delzanno and Prof. Martin Connors for their collaboration with me. Their conversations and comments have been helpful to my work.

Furthermore, I would like to thank my officemates and other fellow graduate students in our department, with whom I have had a great time.

In addition, I gratefully acknowledge the always helpful staff in our department: Lauri Holbrook, Marjorie Sowmendran, Sharon Uy, Richard Satakane, Jim Nakatsuka, and many others.

Lots of gratitude also goes to my parents and my friends, who have been so supportive to me all the time.

This work could not be done without the solar-wind data measured at different heliocentric distances. I am truly respectful to people who have put so many efforts to make the missions successful and make these data available.

This work was supported by the THEMIS project, IGPP at Los Alamos National Laboratory and the National Aeronautics and Space Administration under research grand NNX12AQ98G.

VITA

June 2008	B.S., Geophysics and Space Physics
	University of Science and Technology of China
	Graduate with Guomoruo Scholarship
Sept. 2008-present	Graduate Student Researcher
	Department of Earth, Planetary, and Space Sciences
	University of California, Los Angeles
June 2010	M.S., Geophysics and Space Physics
	University of California, Los Angeles
Sept. 2013	Harold and Mayla Sullwold Scholarship
	Department of Earth, Planetary, and Space Sciences
	University of California, Los Angeles

Publications

Connors, M., C.T. Russell and **H.R. Lai** (2014), A temporary Earth co-orbital as a source of interplanetary dust, *Mon. Not. R. Astron. Soc.*, submitted

Lai, H.R., C.T. Russell, H.Y. Wei and T.L. Zhang (2014). The evolution of co-orbiting material in the orbit of 2201 Oljato from 1980 to 2012 as deduced from Pioneer Venus Orbiter and Venus Express magnetic records, *Meteoritics & Planetary Science*, 49: 28-35

Lai, H.R., H.Y. Wei and C.T. Russell (2013). Solar wind plasma profiles during interplanetary field enhancements (IFEs): Consistent with charged-dust pickup, *AIP Conf. Proc*. 1539: 402-405

Lai, H.R., H.Y. Wei, C.T. Russell, C.S. Arridge and M.K. Dougherty (2012). Reconnection at the magnetopause of Saturn: Perspective from FTE occurrence and magnetosphere size, *J.Geophys. Res.*, 117, A05222

Lai, H.R., C.T. Russell, L.K. Jian, X. Blanco-Cano, B.J. Anderson, J.G. Luhmann and A. Wennmacher (2012). The radial variation of interplanetary shocks in the inner heliosphere: Observations by Helios, MESSENGER, and STEREO, *Sol. Phys.*, 278: 421-433

Jia, Y.D., Y.J. Ma, C.T. Russell, **H.R. Lai**, G. Toth and T.I. Gombosi (2012). Perpendicular flow deviation in a magnetized counter-streaming plasma, *Icarus*, 218: 895-905

Peng, Z., **H. R. Lai** and Y.Q. Hu (2008). Transpolar potential and reconnection voltage of the Earth from global MHD simulations, *J. Geophys. Res.*, 114, A04203

Chapter 1

Introduction: Interactions and Intra-actions in the Heliosphere

In this thesis we examine a new interplanetary phenomenon which has not been studied in detail previously. It is believed to result from the interaction between the neutral matter and magnetized plasmas in the solar system. To provide some context for what is to follow, we present a brief overview of some well studied phenomena and processes in the heliosphere. While this new phenomenon does not fit easily into our current paradigms, the more familiar processes in the solar system do prepare us for this investigation.

1.1 The Sun

The Sun is the dominant body in the solar system. Its mass of $2 \times 10^{30} kg$ is comprised of mainly hydrogen (90%) and helium (10%) and it far outweighs the other bodies of the solar system. The Sun can be considered to be a point mass that determines the foci of the orbits of various objects in the solar system. It is the provider of the radiative energy that heats the solar-system objects and magnetizes the plasma that flows outward through the solar system.

1.1.1 Interior and Atmospheric Layers

Although the solar interior is hidden from view, theoretical models predict that energy is produced by nuclear fusion in the core, which extends from the center of the Sun to about 0.25 solar radii. From 0.25 to about 0.75 solar radii there is the radiative zone, where the material is so hot and dense that thermal radiation is the primary process of energy transfer from the core. The Sun's outmost interior layer is the convective zone, where thermal convection carries the majority of the heat to the solar surface. In the solar interior, the temperature decreases from about $1.5 \times 10^7 K$ in the inner core, to $8 \times 10^6 K$ at the inner boundary of radiative zone, to $5 \times 10^5 K$ at the inner boundary of convection zone and finally to about $6600K$ at the solar surface [Kivelson and Russell, 1995].

The Sun's lowest atmospheric layer is called the photosphere, which is about $500km$ thick. Since it connects directly to the convection zone, the granular pattern, outlining the convection cells, covers this layer uniformly. Above the photosphere lie the chromosphere and the corona. The temperature reaches its minimum ($\sim 4200K$) at the boundary between photosphere and chromosphere. It then slowly increases through the chromosphere and suddenly rises to about $2 \times 10^6 K$ at the inner boundary of corona.

1.1.2 Solar Magnetic Field and Solar Wind

The Sun is a magnetically active star. The solar magnetic field can be nearly dipolar at solar minimum and becomes more complex and reverses its direction at solar maximum. Usually it takes 11 years from solar minimum to maximum, and this period is called a solar cycle. The solar magnetic field is responsible for the Sun's activity, storing and releasing energy to the plasma. For example, a sunspot is a region on the photosphere where the magnetic field is so strong that the thermal convection is inhibited. Thus the sunspot region is cooler than the surrounding regions and appears visibly as a dark spot. Magnetic reconnection is a rapid way to transfer energy to the plasma, producing solar flares. Although the detailed processes have not been fully understood, there is no doubt that the magnetic field plays a key role in coronal heating.

Due to the huge amount of heat deposited in the solar corona, the pressure difference between the solar corona and interplanetary space drives a flow of solar plasma with a remnant of the solar magnetic field outward. This flow, called the solar wind, pervades interplanetary space and interacts with interplanetary objects of different natures. Momentum and energy are transferred from the solar wind to those objects during the interactions. More characteristics of the solar wind are reviewed in Section 1.4 and the details of the interactions between solar wind and interplanetary objects are discussed in Section 1.5.

1.2 Small Interplanetary Objects in the Solar System

Since the mass of the Sun accounts for 99.86% of the total mass of the solar system [Woolfson 2000], the Sun strongly controls the dynamics in the solar system via its gravitational attraction. Therefore all the eight planets and various small solar system objects orbit the Sun directly. Among those objects, most of the large ones are orbiting near the ecliptic plane. In this section, we focus on the small interplanetary objects and will briefly discuss the ones that can reach the inner solar system. Such objects are relatively better documented and depending on their orbits, can be potentially hazardous to Earth.

1.2.1 Comets

The orbits of comets are often highly eccentric, and the orbital periods are variable. Short-period (<200 years) comets are usually believed to originate in the Kuiper belt, while long-period (200~1000s years) comets are believed to originate in the Oort cloud.

Comets are often described as “dirty snowballs” or “icy dirtballs”, because their nuclei are composed of loose collections of ice, dust and small rocky particles. When the comets are near the Sun, comas and tails are formed by the sublimating and ionizing of the icy surfaces. Although the solid nuclei of comets are generally less than $60km$ across, the comas may be thousands or millions of kilometers across. Those comas and tails make the comets easy to identify when they pass close to the Sun.

Comets end their lives in many ways. Some comets come to resemble small asteroids after they have passed close to the Sun many times and have lost nearly all of their volatile ices and dust. These comets are referred to as extinct comets. Some comets have fragile nuclei and will break up. This can happen when the comets pass their perihelia and are unevenly heated. In this way, newly generated gases can break out of a weak spot on the surface of the comets’ nuclei and cause the nuclei to spin. When the spin is fast enough, the nuclei split apart. Some comets meet their end by falling into the Sun or colliding with other interplanetary bodies.

1.2.2 Asteroids

There are millions of asteroids in the solar system and a large majority of them orbit in the asteroid belt between the orbits of Mars and Jupiter. The size of the asteroids varies widely, from tens of meters across to almost $1000km$. Most of the asteroids are small and are irregularly shaped. But some of them are large enough to be considered as small planets.

It is believed that collisions in the asteroid main belt are the primary mechanism for the production and destruction of small asteroids [Bottke *et al.*, 1994]. Some asteroids, named as rubble piles, are formed when originally monolithic interplanetary objects are broken into pieces by impacts. Later this debris can accrete due to self-gravitation. Sometimes a trail of debris co-orbiting with the parent body can be formed after an impact. The orbits of these debris pieces are subject to the gravitational perturbations when they encounter large planetary objects. A recent simulation study shows that the spatial distribution of material co-orbiting with asteroid 138175 can be significantly changed by the gravitational perturbations in only decades [Connors *et al.*, 2014a]. This asteroid, occasionally making close passes of the Earth and Venus, is classified as a potentially hazardous asteroid (PHA). As Figure 1.1 shows, gaps can be formed in the otherwise continuous debris trail. Meanwhile the orbits of debris can be spread in the radial direction. Thus even though the parent body will not approach the Earth closely in hundreds of years, its co-orbiting material may acquire large impact probabilities due to those ever spreading orbits.

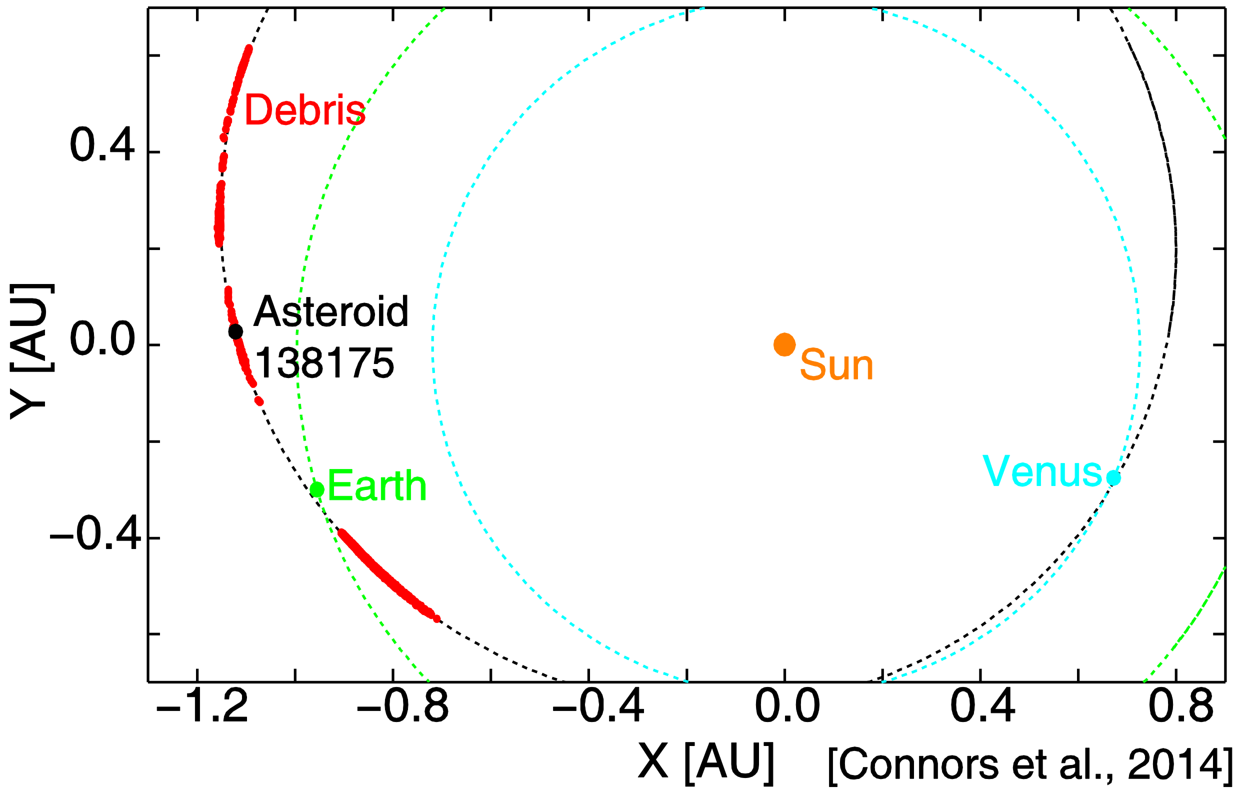

Figure 1.1 Debris distribution of asteroid 138175 in about 13 years. This asteroid can make close passes of the Earth and Venus occasionally. The debris in the trail, which was initially continuously distributed, is subject to the gravity perturbation from the Earth and Venus. In about 13 years, gaps are formed in the debris trail and some debris has also been spread in the radial direction. [Connors *et al.*, 2014a]

1.2.3 Meteoroids

Meteoroids are rocky or metallic bodies, ranging in size from small grains to one meter-wide objects. The meteoroids orbit the Sun in a variety of orbits and at various velocities. They are thought to be either fragments from comets or asteroids, or impact debris ejected from bodies such as Mars, the Moon and Vesta.

Meteoroids can become visible as meteors when they enter the Earth's atmosphere at night. Millions of meteors enter in the Earth's atmosphere daily. Most meteoroids that cause "shooting stars" have diameters of several to tens of centimeters. Since some meteoroids cluster in streams, when they enter the atmosphere of the Earth, meteor showers are observed.

1.2.4 Near-Earth Objects

The comets, asteroids or meteoroids with perihelia less than $1.3AU$ are generally called near-Earth objects (NEOs). Since some NEOs might impact the Earth, they have attracted increased interest. By January 2014, about 96% of the near-Earth asteroids (NEAs) of larger than $1000m$ in diameter have been discovered. However, the percentage of discovery decreases sharply when the diameters of the NEAs decrease. It is estimated that less than 1% of the NEAs with diameters smaller then $100m$ have been discovered [slide 22 in http://sservi.nasa.gov/wp-content/uploads/2014/02/NASA-NEO-Program-AGC-Seminar.pdf].

Among all the NEOs, the ones which have Earth-minimum-orbit-intersection distances of $0.05AU$ or less and diameters of $150m$ or larger are considered as potentially hazardous objects (PHOs). By early 2013, the orbits of over 1400 PHAs have been determined [http://www.jpl.nasa.gov/spaceimages/details.php?id=PIA17041].

Although PHOs are defined to be objects of $150m$ across or larger, this does not mean the resultant damage of smaller NEOs are negligible. Take the 2013 Chelyabinsk meteor as an example. It is estimated to have been only $17m$ across before it entered the Earth's atmosphere. But over 1500 people were injured by the broken glass when the shock wave arrived after it explored in the atmosphere. A greater number of casualties would be expected if this meteor hit a more populated area. In Table 1.1, we list the documented impacts since Tunguska event. Here we can see that even the catastrophic Tunguska asteroid might be at most 70m across.

Date	Location	NEO Diameter	Energy Released
1908-06-30	Tunguska	$45 \sim 70m$	$10MT$ TNT
1930-08-13	Brazil	N/A	$0.1 \sim 5MT$ TNT
1979-09-22	South Atlantic and the Indian Ocean	N/A	N/A
2002-06-06	Mediterranean Sea	$10m$	$26kT$ TNT
2008-10-07	Sudan	$4.1m$	$0.9 \sim 2.1kT$ TNT
2009-10-08	Indonesia	$10m$	$50kT$ TNT
2013-02-15	Chelyabinsk	$17m \sim 20m$	$440kT$ TNT

Table 1.1 Documented historical impacts on Earth since Tunguska event [http://en.wikipedia.org/wiki/Near_Earth_Objects]. As shown here, even the catastrophic Tunguska meteor is at most $70m$ in diameter. Thus although PHOs are defined to be at least $150m$ in diameter, smaller NEOs, that are more difficult to discover, can still cause great damage.

A recent study in the damage caused by vertical entry of small stony asteroids into the Earth's atmosphere shows that bodies with diameters of about $50m$ are most efficient in destruction [Shuvalov *et al*., 2013]. The simulation results of that paper are summarized in Figure 1.2. The black line indicates the radii of areas where the overpressure can destroy brick walls. As expected, the larger impactor can cause damage in a larger area. The red line shows the damage areas per year with the consideration of the impactor probability. It peaks when the impactor is around $50m$ in diameter. Thus such "small" sized NEOs should attract the most attention even though the much rarer large events could individually cause more damage. However, as we reviewed previously, they are hard to detect before entering the Earth's atmosphere with traditional methods.

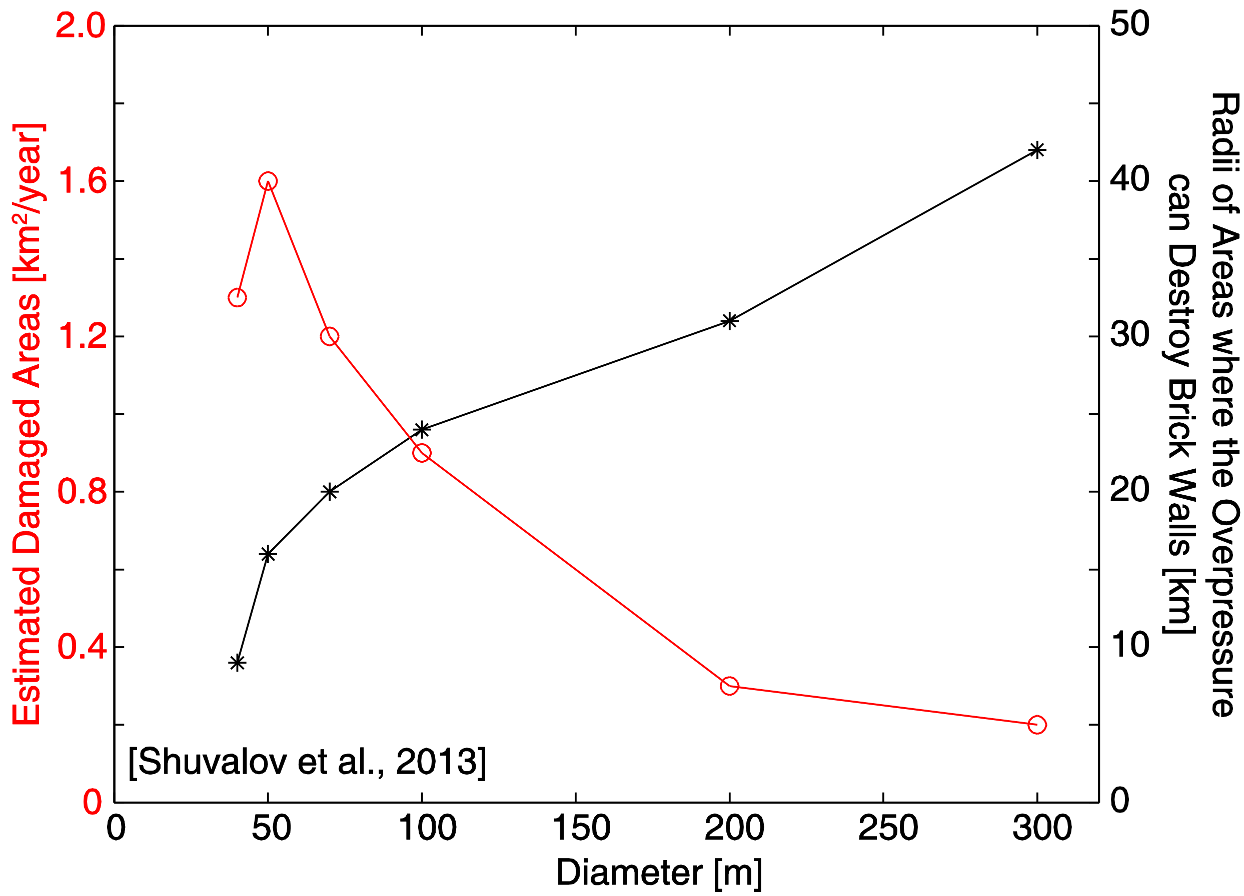

Figure 1.2 The damage of a vertical impact based on simulations [Shuvalov *et al.*, 2013]. The black line shows the radii of areas where the overpressure can destroy brick walls. The red line shows the estimated damage areas per year. As the red line indicates, when the impactor probability is considered, asteroids with diameter of $50m$ can cause the largest integrated damage.

1.3 Interplanetary Collisions

Collisions play important roles in producing and destroying small interplanetary objects. The debris released in those collisions can be widely dispersed around the orbits of their parent bodies. Meanwhile the orbits of debris are subject to change due to gravitational perturbations. Therefore even the “safe” NEOs might have potentially hazardous co-orbiting material which can cause civilian catastrophes. Thus we need to have a better understanding and a better way to identify those potential interplanetary colliders.

The interplanetary collision rate is determined by the number density of the interplanetary objects. Since generally the larger bodies are fewer, larger collisions are rarer. We can take the interplanetary objects impacting the Earth as an example: the impact interval for an object of about Cretaceous–Tertiary impactor size ($\sim 10km$ across), of about Tunguska impactor size and of Chelyabinsk impactor size is hundreds of millions of years, hundreds of years and tens of years, respectively [Harris *et al*., 2008]; while millions of pebble-sized meteors enter the Earth’s atmosphere every day.

The traditional optically method can only identify the very largest collisions. Therefore to better detect the interplanetary collisions, and thus to inventory small interplanetary objects, we need to determine other signatures associated with collisions. Since debris of different sizes can be released in interplanetary collisions and the solar wind can interact differently with obstacles of different natures, we look for perturbations in the solar wind which result from interplanetary collisions.

1.4 The Solar Wind

As we introduced in Section 1.1.2, solar wind is an outflow of magnetized solar plasma. The magnetic field carried into the interplanetary space is called the interplanetary magnetic field (IMF). Because the solar wind is an ideal collisionless plasma, the magnetic flux can be frozen into the fluid, which means that all particles initially on a flux tube will remain linked along that flux tube as they convect through space.

A fluid model considering the equilibrium state of the corona predicts that solar wind is a continuous supersonic flow; the rotation of the Sun, under the frozen-in condition, causes the IMF to take the shape of an Archimedes spiral, known as the Parker spiral. Both predictions have been confirmed by the observations. Based on the in situ measurements, we now know that the IMF strength, the solar-wind proton number density and proton temperature decrease monotonically as the radial distance increases; while bulk flow velocity is generally constant and due to the large mobility of the electrons, their temperature can be viewed as a constant. Near the orbit of the Earth, *i.e.*, $1AU$ from the Sun, the average solar-wind physical properties are listed in Table 1.2. We can see that solar wind is quasi-neutral and all the charged components are minor ones except protons and electrons. Solar-wind properties, especially the IMF, are modulated by the solar cycle: the IMF strength is larger during solar maximum and vice versa.

Solar-Wind Properties	Value
Proton Density	$6.6\ cm^{-3}$
Electron Density	$7.1cm^{-2}$
He^{2+} Density	$0.25cm^{-3}$
Flow Speed	$450km/s$

Proton Temperature	$120000K$
Electron Temperature	$140000K$
Magnetic-Field Magnitude	$7nT$

Table 1.2 Observed properties of the solar wind near $1AU$ [Kivelson and Russell 1995].

Before looking for signatures associated with interplanetary collisions in the solar wind, we need to understand how solar wind interacts with different kinds of obstacles and how the large-scale structures in the solar wind evolve.

1.5 Solar-wind Collisions

The solar wind meets many disparate obstacles on its way through interplanetary space and can interact with them via both electromagnetic and non-electromagnetic processes. Depending on the intrinsic properties, these obstacles can be divided into six categories: Moon-like obstacles, Venus-like obstacles, comets, Earth-like obstacles, clouds of plasmas and charged dust particles.

1.5.1 Moon-like Obstacles

A Moon-like obstacle has neither an intrinsic magnetic field nor a highly conducting ionosphere. In this situation, no bow shock will be formed upstream as there is no deflection of the flow. When the solar wind is incident on the Moon, the solar-wind plasma will be absorbed and the IMF will penetrate the very weakly conducting crust, with little perturbation in the upstream IMF orientation. The only significant feature of the interaction between solar wind and the obstacle is the plasma-absorption wake left behind the body. The geometry of this wake is determined by the upstream IMF orientation and the plasma thermal velocity. If the IMF is parallel to the flow and the plasma thermal velocity is small compare to the flow speed, the wake can persist to a large distance. Otherwise, the solar-wind plasma can refill the empty space within a short distance downstream of the obstacle.

1.5.2 Venus-like Obstacles

A Venus-like obstacle has a weak intrinsic magnetic field but a highly conducting ionosphere with sufficient thermal pressure to deflect the dynamic pressure of the solar-wind flow. Since the IMF is not steady, the ionosphere generates a canceling magnetic field via Lenz's Law that prevents the IMF from penetrating it until such a time as the field can diffuse into the ionosphere. A bow shock will be formed upstream since the supersonic solar wind needs such a shock to allow it to be deflected around the ionospheric obstacles.

The outer boundary of the obstacle is called the ionopause. There the ionospheric plasma pressure balances the post-shock solar-wind incident pressure. Being different from the gas-dynamic model, the post-shock solar-wind flow is not continuously compressed as it approaches the ionopause [Spreiter *et al*., 1966]. Instead, as predicted by magnetohydrodynamics (MHD) theory, there will be a plasma depletion region in the upstream of the ionopause [Zwan and Wolf, 1976]. The existence of such a plasma depletion region, called the magnetic barrier, is confirmed by observations [Zhang *et al*., 1991]. While the bow shock is associated with the fast-mode MHD wave, the magnetic barrier is associated with the slow-mode wave. The slow-mode wave effectively allows the thermal motion of the ions to remove plasma from the nose of the interaction along the magnetic field, developing a magnetic cushion in front of the obstacle. We will encounter an analogous magnetic cushion later in this thesis.

1.5.3 Comets

An extreme example of solar wind interacting with atmospheres of objects occurs in the case of comets. As we introduced in Section 1.2, when a comet is close to the Sun, it is heated and begins to outgas. Unlike the planetary atmosphere, the cometary sublimated neutral atmosphere is not bound by cometary gravity. Instead, it flows outward from the nuclei at several kilometers per seconds and is meanwhile ionized. The dynamic pressure of the out-flowing plasma creates a small field free region. At the boundary the outward pressure balances the post-shock solar-wind incident pressure. Before encountering this obstacle, which is called the contact surface, the solar wind is substantially slowed by the accumulation of the heavy ions of atmospheric origin through charge exchange. Meanwhile, the magnetic field is bent and compressed and the familiar cometary shape is produced.

The ionized gas follows the magnetic-field lines and forms the ion or type I tail. It always points directly away from the Sun. This direction is different from the orientation of the dust or type II tail, which is usually curved and follows the orbital trajectory. In fact, the observation of ion tails contributed significantly to the discovery of the continually flowing solar wind.

1.5.4 Earth-like Obstacles

An Earth-like obstacle has a large intrinsic magnetic field. This produces a region called the magnetosphere where the dynamics of the charged particles are controlled by the planetary magnetic field. The intrinsic magnetic field stops solar-wind flow from penetrating into magnetosphere. Similar to the Venus-like interactions, a bow shock is formed upstream.

The boundary that separates the post-shock plasma flow and the magnetosphere is called magnetopause. At the Earth, generally, the incident dynamic pressure is balanced by the magnetospheric magnetic pressure across the magnetopause. A plasma depletion layer is also observed in front of the magnetopause [Crooker *et al*., 1979], where the magnetic field is compressed and the plasma density drops. In both magnetic barrier and plasma depletion layer, the magnetic field accommodates the solar-wind dynamic pressure before the ionosphere or magnetosphere takes over the retarding pressure role.

1.5.5 Clouds of Plasmas

When the obstacle is a cloud of plasma, the dynamics has some similarities to the one in the interaction between solar wind and comets. The only difference is that there is continuous outgassing from the nuclei in the comets' situation while a cloud of plasma is generally a transient phenomenon.

A relatively well studied example of solar-wind-dust-plasma interaction is the AMPTE (Active Magnetospheric Particle Trace Explorers) artificial comet. On 27 December 1984, the first artificial comet was produced by the release of two-kilogram barium from two canisters carried by the IRM (Ion Release Module). These two canisters were ignited $600s$ after deployed from the IRM. At that time they were $1.75km$ apart with the IRM halfway in between. In about $28s$, the barium was photoionized. The two expanding plasma clouds then merged when they reached IRM. Based on the IRM observation, the IMF piled up to ten times its ambient strength in the upstream of the plasma cloud. During this experiment, there is a significant magnetic-field component anti-parallel to the direction of solar-wind-convection electric field [Lühr *et al*, 1986]. This is due to the different charge to mass ratio of the two plasma constituents (barium and the solar wind) and has been reproduced in multi-fluid MHD [Jia *et al*., 2012]. The plasma measurements revealed that the solar wind was decelerated and deflected antiparallel to the convection electric field [Rodgers *et al*., 1986]. Meanwhile the barium cloud moved in the electric field direction. After 4.6 minutes, the barium cloud began to move in the solar-wind direction [Valenzuela *et al*., 1986].

1.5.6 Single Charged Dust Particles

Single charged dust particles can be produced in interplanetary collisions between larger objects and can be released by Sun-grazing comets. They are charged in the solar wind due to the plasma collection and photoelectron emission. Inside $1AU$, the particles are positively charged and have surface potentials at about $4V$ in equilibrium state [Kimura and Mann, 1998].

These charged dust particles in the interplanetary space are subjected to many forces, *e.g.*, gravity, radiation pressure, and Lorentz force. Different forces dominate the dynamics of particles according to their sizes. For particles of micrometer scale or larger, the solar gravity outweighs the other forces and particles will fall toward the Sun if their initial velocity is zero. Particles of sizes comparable to or greater than the wave length of light (~$500nm$) can be strongly influenced by the radiation pressure. And nanoscale particles can be picked up by the solar wind via the Lorentz force.

Thus generally we only expect nanoscale sized particles to interact with solar wind strongly. Such fine dust particles moving at the solar-wind speed is suggested to explain the STEREO/WAVES observations [Meyer-Venet *et al*., 2009]. During 2007 and 2010, the wave instrument on STEREO detected frequent bursts which cannot be explained by the known solar-wind plasma emissions. A possible scenario is that nanoscale particles with solar-wind speed strike the spacecraft and produce expanding plasma clouds, which are detected by the electric antennas as electric field pulses.

1.6 Well-known Large-scale Structures in the Solar Wind

Now we know how the solar wind interacts with various obstacles in the solar system. To find the solar-wind perturbations associated with collisions, the next step is to examine the large-scale structures in the solar wind. We will review some well-known ones first.

1.6.1 Heliospheric Current Sheets

The heliospheric current sheets (HCSs) are the surface where the polarity of the IMF changes from pointing toward the Sun to away from the Sun. The shape of the HCS can be very complicated due to the variable IMF. As the definition indicates, when a spacecraft crosses the HCS, the radial and azimuthal field components are found to reverse directions and the magnetic-field strength decreases. Meanwhile the plasma density increases [Borrini *et al*., 1981].

1.6.2 Interplanetary Coronal Mass Ejections

Interplanetary coronal mass ejections (ICMEs), as their name indicates, are related to flare-associated eruptions in the corona. They contain strong and large flux ropes initially anchored in the solar corona. When a spacecraft passes the flux rope, it will detect that the magnetic-field strength increases and the magnetic-field direction changes smoothly through a large angle [Hirshberg and Colburn, 1969]. When the magnetic field inside the flux rope is closed, *i.e.*, connected to the Sun on both sides, the proton and election may show bidirectional signature. Since the magnetic field of a rope can be self-balancing, the behavior of the temperature of proton and electron may be quite different from that of the magnetic field [Neugebauer and Goldstein 1997]. If the expansion of the ICME front is faster than the fast-mode magnetosonic wave speed, the ICME will drive a shock in front of it. Between the shock and the flux rope, there is the sheath region, where the magnetic field and plasma are compressed and disturbed [McComos *et al*., 1988].

1.6.3 Stream Interaction Regions

The origin of stream interaction regions (SIRs) can be traced back to coronal holes where fast solar-wind streams are emitted. Due to the rotation of the Sun, these fast streams will catch up with and compress the relatively slow steams [Smith and Wolfe, 1976]. Since the magnetized plasma in the two streams cannot interpenetrate, a compression region is created at the interface, pushing forward and backward [Gosling and Pizzo, 1999]. In the compression region, the magnetic field and solar-wind velocity increase. In the slow stream, the density and pressure increase, while in the fast stream, the density and pressure decrease [Jian *et al*., 2006]. If the velocity gradient at the front and/or trailing edge of the compression region is larger than the fast-mode magnetosonic wave speed, one or two shocks can develop. The forward shock accelerates the slow stream while the reverse shock decelerates the fast stream.

1.7 Interplanetary Field Enhancements

All the IMF structures mentioned in Section 1.6 and many others have significant correlated plasma and magnetic signatures. However, there is a unique phenomenon in the solar wind named an interplanetary field enhancement (IFE), which has strongly perturbed IMF signatures with at most weak plasma signatures correlated.

1.7.1 Discovery

IFEs were first observed at Venus in the *Pioneer Venus Orbiter* (PVO) magnetic-field data [Russell *et al*. 1983a]. Figure 1.3 shows the first recognized IFE which was recorded on February 11, 1982. As the figure shows, the magnetic-field strength was observed to rise slowly to a cusp-shaped maximum, reaching 165% of the ambient field strength with a strong current sheet near the peak. The leading increase and the trailing decrease of the magnetic field lasted more than 12 hours, making this IFE one of the largest. The same IFE was observed by Venera 13 and 14, which were approaching Venus. The time delays between the observations taken by different spacecraft were consistent with the structure being carried outward at nearly the solar-wind speed [Russell *et al*, 1985].

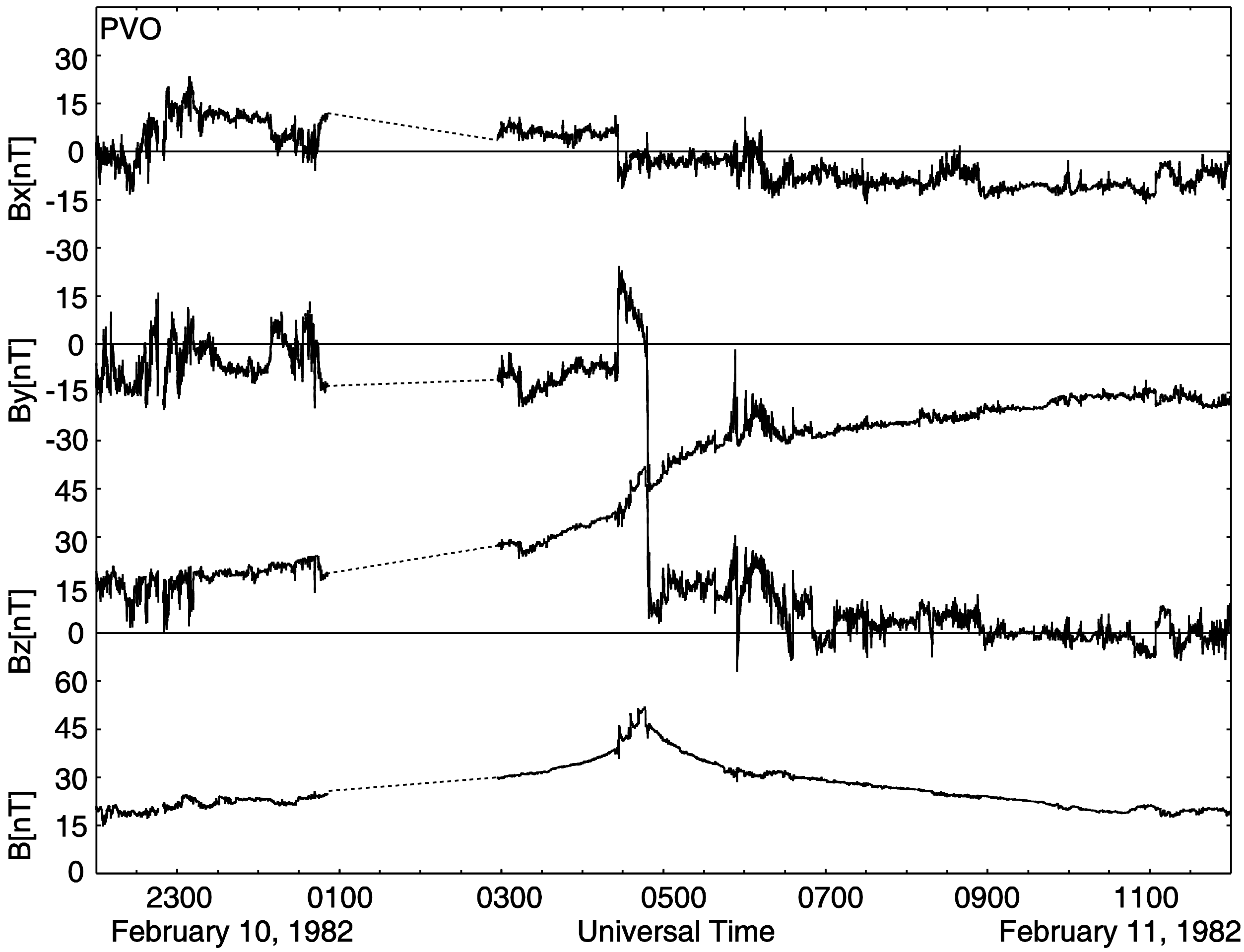

Figure 1.3 The first reported IFE observed by PVO on February 11, 1982. This IFE has a magnetic-field enhancement of 165% and a duration longer than 12 hours. The magnetic-field enhancement is cusp-shaped and there is a strong current sheet near the peak of the enhancement.

1.7.2 Early Statistical Studies

Since the discovery of the IFEs, statistical studies have been performed at $0.72AU$ with PVO observations [Russell *et al.* 1984a], at $1AU$ with ISEE (International Sun-Earth Explorer) 3 and IMP (Interplanetary Monitoring Platform) 8 observations [Arghavani *et al.*, 1985], and from $1AU$ to $5AU$ with *Ulysses* observations [Jones *et al*. 2003a]. At all distance the IFEs can last as short as several minutes and as long as many hours. The magnetic-field enhancement of the IFEs is also variable and central current sheets are observed in most of the IFEs [Russell *et al*., 1984a]. Jones *et al*. [2003a] also reported that some IFEs have magnetic-field depressions at the boundaries. Based on all the statistical results, no solar activity or solar-wind structures are found to be associated with IFEs [Russell *et al.*, 1985; Jones *et al*. 2003a].

With the available plasma data of *Ulysses*, Jones *et al*. [2003a] performed a superposed epoch analysis on the solar-wind proton number density, proton temperature and solar-wind velocity during IFEs. The authors concluded that the plasma parameters have some subtle changes. With all the parameters normalized to the ambient value, the average magnetic-field enhancement is about 50%, while the changes in the proton number density and thermal pressure are less than 10%.

1.7.3 IFEs Travel at Solar-wind Velocity

The velocity of IFEs themselves can be determined by four-, and over-determined by more, spacecraft simultaneous observations. The only reported IFE detected by four spacecraft was on December 24, by the ACE (Advanced Composition Explorer), *Wind*, STEREO (Solar TErrestrial RElations Observatory) A and STEREO B [Russell *et al*. 2010]. With the method developed by Russell *et al*. [1983b], the perturbation plane of this IFE was found to be traveling radially outward from the Sun at nearly the solar-wind speed. When IFEs were observed by two [Arghavani *et al.*, 1985] or three spacecraft [Russell *et al.*, 1985] simultaneously, the velocities can be estimated under the assumption that the perturbation plane is moving at the same direction as the solar-wind flow. Their velocities are also found to be close to the in situ solar-wind velocity.

1.7.4 Association between IFEs and Oljato at $\mathbf{0.72}\boldsymbol{AU}$

In the IFE statistical study at $0.72AU$ [Russell *et al*, 1984a], the authors found that IFEs tend to cluster near certain ecliptic longitudes, implying that IFEs are associated with small Venus-crossing bodies. Such an asteroid named Oljato, whose orbit lies upstream of the one of Venus at that longitudinal range with a small inclination, was suggested [Russell *et al*., 1984b]. When Oljato returned in 1986, IFEs with a higher-than-average rate were observed at the expected locations. In addition, the IFE rate peaks when the phase difference between Oljato and Venus is small [Russell 1987]. These studies further confirmed the association between Oljato and IFEs detected at $0.72AU$. Although IFEs occurred more often when Oljato was nearby, most of the IFEs are either trailing or leading the asteroid in longitude. Thus it is highly probable that it is the material co-orbiting with Oljato rather than Oljato itself that is responsible for these IFEs [Russell *et al*., 1984b].

The longitudinal distribution of IFEs detected by ISEE 3 and IMP 8 at $1AU$ was also studied [Arghavani *et al*., 1985]. The clustering of occurrence was not as significant as it was at $0.72AU$. Therefore no further survey for an associated asteroid was pursued.

1.7.5 Early Formation Hypothesis: Microscale Dust Trail

To understand the formation of IFEs, based on the IFE-Oljato association, Jones *et al*. [2003b] developed a dust trail model: micrometer charged particles form dust trails in the orbits of asteroids or comets; the IMF would be distorted by this dust trail and spacecraft would observe IFEs when they pass through this magnetic distortion region. As we reviewed in Section 1.5, microscale dust particles are too heavy to be accelerated to solar-wind speed and their dynamics are dominated by gravity. Therefore, under this dust trail hypothesis, the distorted IMF, after formation, would be nearly stationary in space anchored to the dust trail. Meanwhile, a bow shock would be formed in the upstream region and between the shock and the dust trail there would be a compression region. This is inconsistent with the fact that IFEs move at a velocity close to the solar-wind speed. And no associated shocks or compression regions have been observed in IFEs.

1.7.6 Current Formation Hypothesis: Nanoscale Dust Cloud

From early studies we know that the typical signature in an IFE is the magnetic-field enhancement with no significant associated plasma features. This is similar to the cases in magnetic cushion regions, where magnetic field piles up to transfer momentum from the solar wind to the obstacles. Meanwhile the plasma is guided by the magnetic field to flow around the obstacles. We suggest the same mechanism applies to the IFEs: momentum from the solar wind is transferred to some obstacle via the enhanced magnetic field. Because IFEs move at nearly the solar-wind speed, the obstacle must also move at the same speed. Considering the fact that only nanoscale charged dust can be accelerated to such a high speed and IFEs are large structures, we suggest the obstacles in IFEs are clouds of nanoscale charged dust particles. When the dust particles have been accelerated to nearly the solar-wind speed, momentum transfer is still needed to overcome the solar gravity exerted on the dust. Therefore our IFE formation mechanism is that IFEs result from interactions between solar wind and clouds of nanoscale charged dust.

The above IFE formation theory is different from the dust trail theory developed by Jones [*et al*., 2003b]. In our IFE formation theory, since the dust is of nanometer-scale, they can be accelerated and carried by the solar wind. No shocks will be formed in such a subsonic interaction. As the solar-wind plasma can be guided by the draped magnetic field and flow around the obstacle, similar to the case in a magnetic barrier and in a plasma depletion layer, no the plasma compression regions will be formed in the upstream of the dust clouds. All features are consistent with the observations.

1.7.7 Sources of IFEs: Collisions between Small Bodies in Interplanetary Space

If IFEs result from interactions between solar wind and clouds of charged dust, from where do those charged dust clouds come? From earlier studies, we know that generally the IFE occurrence is random and relatively rare. From multi-spacecraft observations we know that the region perturbed by IFEs can be millions of kilometers in both radial and cross-flow directions, requiring the dust cloud to be large. A good hint of dust source comes from the association between PVO observed IFEs and the passage of Oljato [Russell *et al*., 1984b; Russell 1987]. In that study, the authors suggested that the co-orbiting material of Oljato should be responsible for many IFEs. To produce dust clouds from co-orbiting material, a good candidate is a collision.

Although optically detectable collisions between large interplanetary objects may not occur for decades, collisions involving small objects are not that rare, as such objects are more numerous in space. An encounter with small impactors does not always result in weak impacts. When the colliding velocity is about $20\ km/s$, impactors can catastrophically destroy targets of 10^6 times heavier [Grün *et al.*, 1985]. In this situation, a meteoroid of tens of centimeters can destroy an asteroid of tens of meters disruptively.

Fine dust released in collisions can have initial non-zero charge due to the tribo-electric charging process [Lowell *et al*., 1986]. They can also become charged in the solar wind. In AMPTE observations, the barium ionization rate was about 2.4×10^{23} ions$/s$. Such a high ionization rate ensures that the dust interacts with the solar wind shortly after released.

1.7.8 Predictions and Applications of Our IFE Formation Hypothesis

Our IFE formation hypothesis is that IFEs are formed by the interaction between solar wind and clouds of charged fine dust which are released in interplanetary collisions. This hypothesis can explain most of the reported IFE features, such as its magnetic field and plasma signatures, its isolated and almost random occurrence, the association between IFEs and Oljato at $0.72AU$ and the nearly solar-wind speed feature. This hypothesis also predicts some IFE features which need to be tested. We expect the following:

(a) The magnetic field drapes in the upstream region. This is due to the momentum transfer between the solar wind and dust clouds. To detect such a feature, we need to reconstruct the magnetic-field geometry. This requires multi-spacecraft simultaneous observations.

(b) In the upstream, to conserve the momentum, the solar wind should slow down. And we expect that the slowdown is more significant when the dust cloud is more massive.

(c) The IFE occurrence rate should be consistent with the rate of collisions which can release appropriate amount of mass carried by nanoscale dust particles.

Once all the predicted features have been found, we can use the distribution of IFE occurrences to identify interplanetary objects. There is already a successful example in which Oljato co-orbiting material is found to be responsible for many IFEs detected at $0.72AU$. We expect to find other IFE sources. Near-Earth region is a good place to perform this survey. Not only because we have many spacecraft orbiting in this region and our knowledge of interplanetary objects is best near $1AU$, but also because NEOs near $1AU$ are potentially hazardous.

This application is extremely important. Because as we reviewed in Section 1.2.2, co-orbiting material of known asteroids can be in spread orbits either due to the initial impacts when it was created or due to the later gravity perturbations. Therefore even though the parent bodies are considered to be safe, the dispersed material can have a finite impact probability thus become hazardous to Earth. Such material with diameters of tens of meters can cause great civilian damage but it challenges the detectability of traditional optical survey techniques. Based on our hypothesis, the existence and spatial distribution of such small matter can be revealed once it collides with meteoroids which are numerous in space. Clouds of nanoscale charged dust released in the collisions can interact with the solar wind and produce IFEs which can be detected by magnetometers in space. Once the spatial distribution of the co-orbiting material is inferred from the IFE observations, radar observations can be followed up to trace these potentially hazardous objects. Such detections can enable a planetary defense system to be developed.

1.8 Summary

In this thesis, we will first test our hypothesis and then use IFE observations to identify potentially hazardous co-orbiting material with known asteroids. In the hypothesis testing part, we first briefly introduce the datasets and our IFE survey criteria in Chapter 2. We then show the IFEs' observations that can prove our first two predictions and teach us more about the collisions in Chapter 3. A quantitative comparison between the observed IFE rate and estimated detectable collision rate is discussed in Chapter 4. Chapter 5 is the application study: we first reanalyze the association between Oljato and IFEs observed at $0.72AU$ and then identify IFE associated interplanetary objects at $1AU$. The temporal variations of the co-orbiting material are also discussed in Chapter 5. Last but not least, we will summarize this study and describe a research plan for the future work in Chapter 6.

Chapter 2

Methods: Datasets and IFE Selection Criteria

To test our hypothesis, a lot of IFE samples should be studied. Therefore we need to perform a systematic survey of IFEs. From early statistical studies we know that IFEs are generally rare and random phenomena and can be detected at all heliocentric distances. Therefore our database must cover a large range of heliocentric distances. As we are also interested in the temporal variation of IFE occurrences, that database must also cover a long time. Since the durations and strengths of IFEs are variable, to select an unambiguous set of IFE events, we need to find the key observational parameters of IFEs and determine the selection criteria based on these parameters.

2.1 Datasets

In order to have a relatively complete database, we surveyed the available magnetic-field data from many spacecraft, whose observations cover from 1970s to present and from inner than $0.3AU$ to outer than $5AU$. Although IFEs can be identified with magnetic-field data only, solar-wind plasma data can improve our understanding of the IFE nature, so we will also check the plasma profiles during IFEs when those data are available. In this section, we will briefly introduce the spacecraft whose data have been used in our IFE survey.

2.1.1 Spacecraft near 1AU

IMP 8 (Figure 2.1) was launched on October 26, 1973 in a near-circular, $35R_E$ and 12-day orbit. The inclination of the orbit varied between $0°$ and about $55°$ with a period of several years. The $3Hz$ magnetic-field data are available from October 30, 1973 to Jun 10, 2000 (ftp://spdf.gsfc.nasa.gov/pub/data/imp/imp8/mag/320ms_ascii/). The solar-wind data are hourly averaged and will not be used in this study. Since IMP 8 spent a long time downstream of the terrestrial bow shock, its observation does not have a continuous coverage in the solar wind. However, as IMP 8 has high resolution magnetic-field data in the early days, which can be used to study the long-term variation of IFE properties, we survey IMP 8 data obtained during some intervals in which we are interested (Chapter 5).

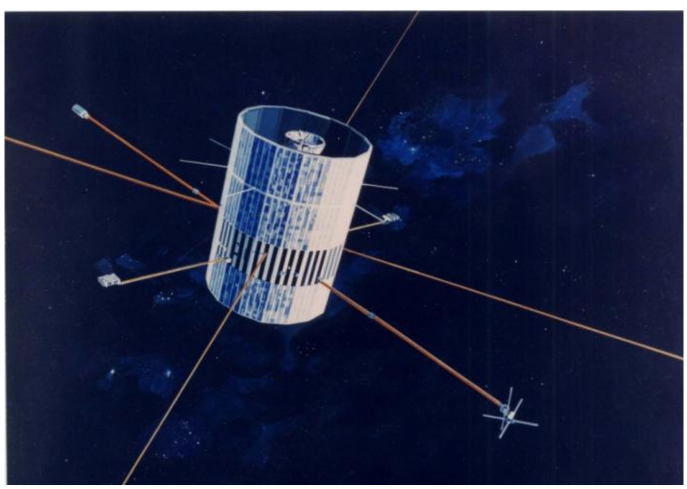

Figure 2.1 The IMP 8 spacecraft is the last satellite of the IMP series. It was a drum-shaped spacecraft, 135.6cm across and 157.4cm high.

Geotail (Figure 2.2) was launched on July 24, 1992. Its orbit extended from the near-Earth region ($8R_E$) to the distant tail ($200R_E$). The 64-second magnetic-field data are available from September 4, 1992 [Kokubun *et al*., 1992]. Since *Geotail* also spends a long time in the magnetotail, we only check its data to see if it has simultaneous observations when the other spacecraft near $1AU$ detect an IFE.

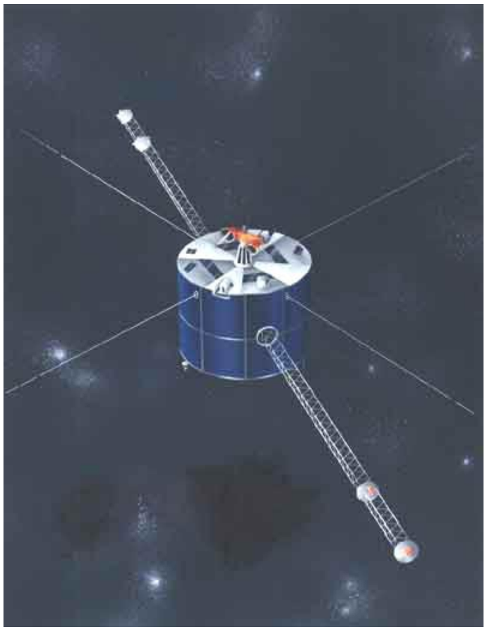

Figure 2.2. Geotail spacecraft.

Wind (Figure 2.3) was launched on November 1, 1994. Its orbit has been adjusted much since launched. Before 2004 it orbited the Earth and spent considerable time in the Earth's magnetotail. Later it began to orbit the Sun at the L-1 Lagrangian point. There are 3-second magnetic-field data available from Nov 16, 1994 [Lepping *et al*., 1995] and on average 99-sec plasma data are available from Nov 01, 1994 [Lin *et al*., 1995]. In our study, we only use the observations from *Wind* after 2004.

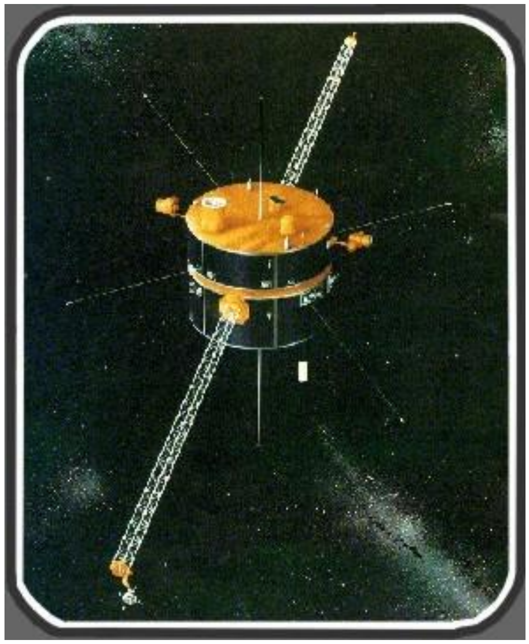

Figure 2.3 *Wind* spacecraft. It began to orbit around the Sun at the L-1 point after 2004.

ACE (Figure 2.4) was launched on August 25, 1997 and operates near the L-1 Lagrangian point. It provides $1Hz$ magnetic-field data (MAG) from January 1, 1998 [Smith *et al*. 1998] and 64-second plasma data (validated level 2 of SWEPAM), from January 1, 2000 [McComas *et al*., 1998]. Since ACE has the longest temporal coverage at $1AU$ and both high-resolution magnetic-field and plasma data are available, many of our IFE statistical studies performed in Chapter 3 are based on the ACE observations.

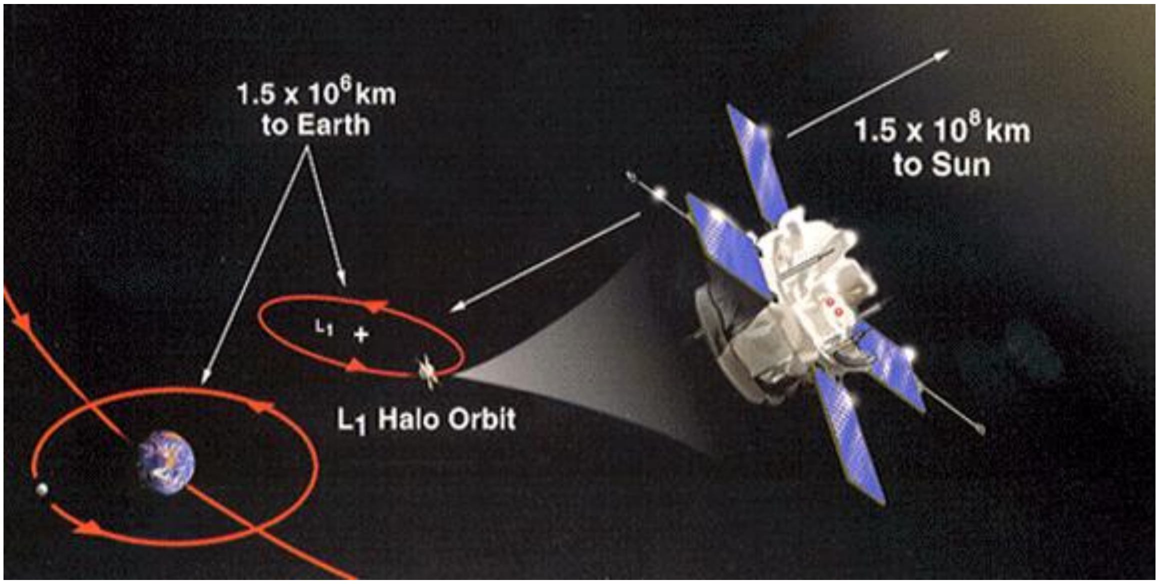

Figure 2.4 ACE spacecraft. The distances from the Earth to the L-1 point and from the L-1 point to the Sun are also indicated in this figure.

The STEREO mission (Figure 2.5) consist two nearly identical spacecraft. They were launched on 25 October 2006 and orbit around the Sun with one spacecraft (STEREO A) leading the Earth and the other (STEREO B) trailing the Earth. The $1Hz$ magnetic-field data are available from November 7, 2006 [Acuña *et al.*, 2008] and the 1-minute plasma data are available from February 15, 2007 on STEREO A and from March 1, 2007 on STEREO B [Galvin *et al.*, 2008]. Since STEREO A and STEREO B are not bound to the near Earth region, their observations provide the opportunities to study IFEs in a larger longitudinal range near $1AU$, which will be discussed in more detail in Chapter 5.

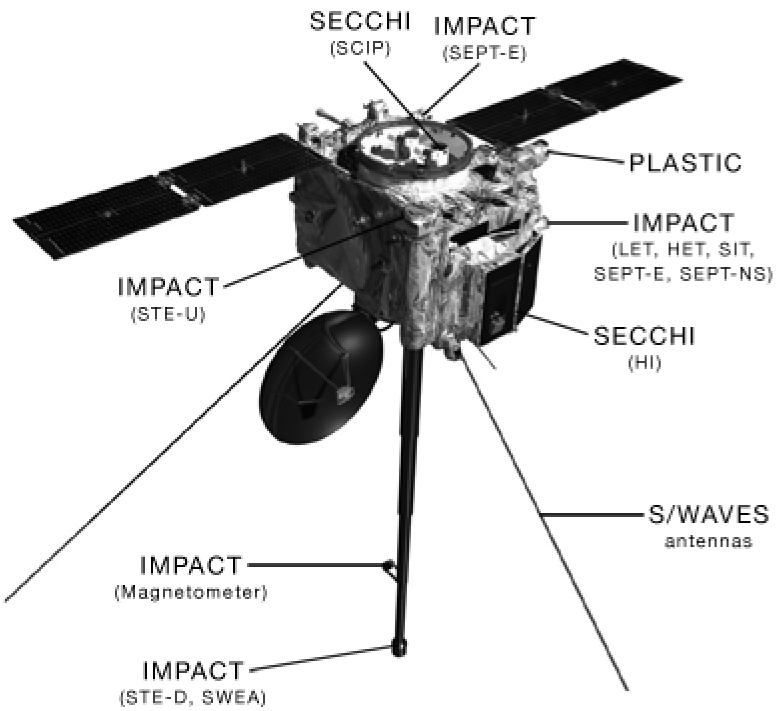

(a)

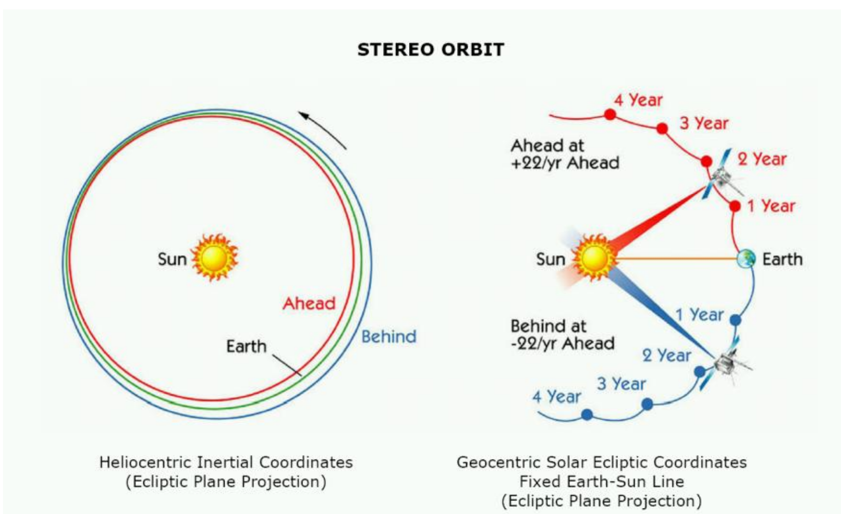

(b)

Figure 2.5. (a) One of STEREO spacecraft and (b) their trajectory. STEREO A is leading the Earth while STEREO B is trailing the Earth.

ARTEMIS (Acceleration, Reconnection, Turbulence and Electrodynamics of the Moon's Interaction with the Sun) mission (Figure 2.6) [Angelopoulos *et al*., 2011] contains two outermost spacecraft (P1 and P2) of NASA's MIDEX (Medium-Class Explorers) mission THEMIS (Time History of Events and Macroscale Interactions during Substorms). From October 2010, they started orbit around the Earth-Moon L-1 and L-2 Lagrangian points, respectively. The magnetic-field data are available from then on and its time resolution is generally three seconds. As ARTEMIS spend long times downstream of the bow shock, we only check their observations when the other spacecraft near $1AU$ detecte an IFE.

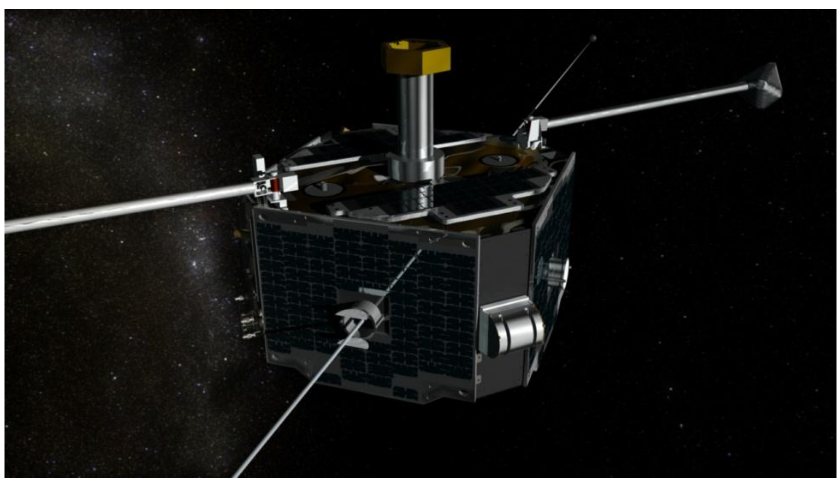

(a)

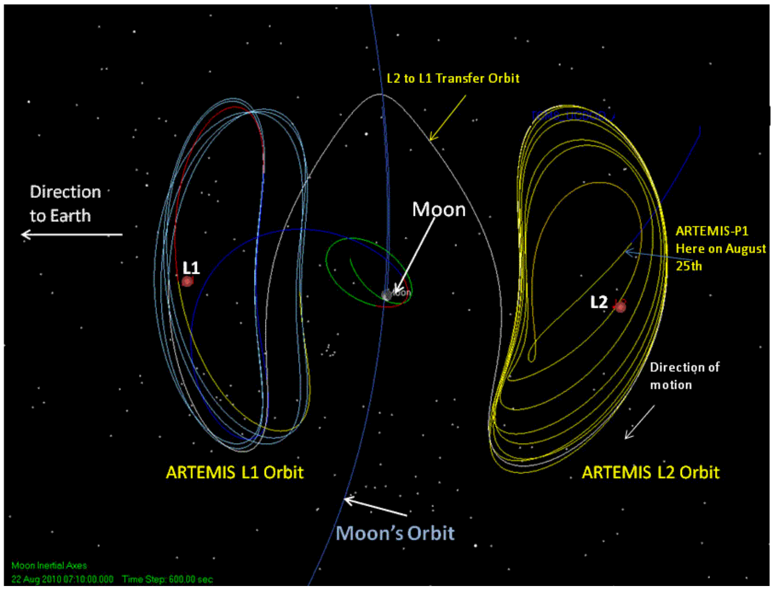

(b)

Figure 2.6 (a) One of ARTEMIS spacecraft and (b) their orbits.

As we see from the above descriptions, with many spacecraft observations available, IFEs detected at $1AU$ have a large chance to be observed by more than one spacecraft. Multi-spacecraft simultaneous study is very important in understanding the IFE traveling speed, temporal variation and geometry. That is why we include the observations of ARTEMIS and *Geotail* in our study, even though they spend long times inside the bow shock. We do not use their data to survey IFEs, and only check their observations when ACE, *Wind*, STEREO A or STEREO B detected an IFE.

2.1.2 Spacecraft near $0.72AU$

PVO (Figure 2.7) was launched on May 20, 1978 and orbited Venus in a 24-hour highly elliptic near polar orbit. The $2Hz$ magnetic-field data [Russell *et al*., 1980] are available from December 5, 1978 to October 14, 1988. The data have a large gap in interplanetary coverage each Venus year when the apogee passes through Venus' magnetotail and magnetosheath. Excluding all the data gaps, the total coverage of the data is 2320.2 days. The 10-minute solar-wind plasma data are available from December 6, 1978 to August 7, 1988. Similar to the magnetic-field data, there are many data gaps in the plasma data.

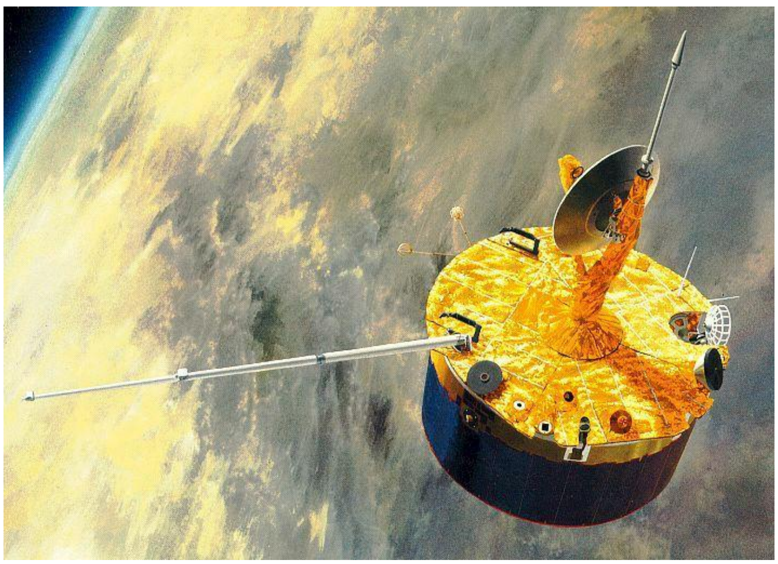

(a)

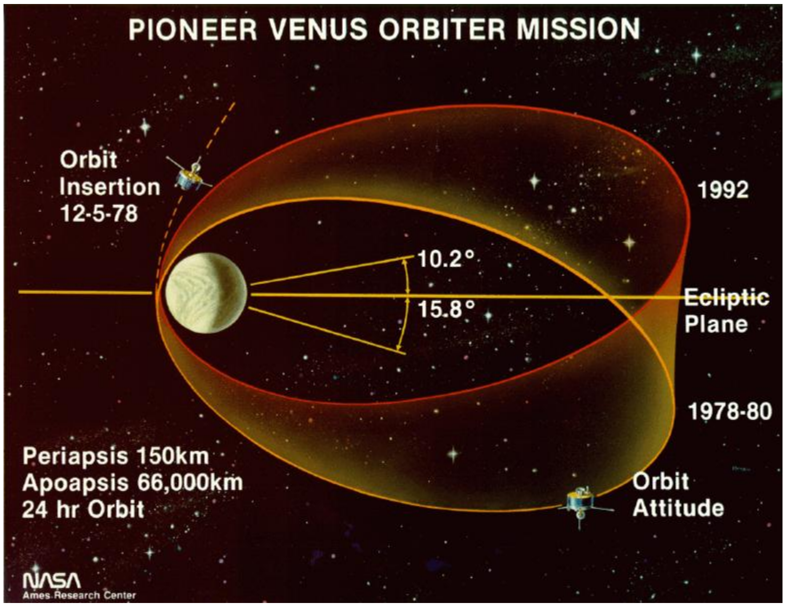

(b)

Figure 2.7 (a) PVO spacecraft and (b) its orbit.

VEX (Figure 2.8), launched on November 9, 2005, is also in a near-polar 24-hour orbit, with periapsis over the north pole rather than in the ecliptic plane but otherwise the orbits are similar. The 1Hz magnetic-field data are available from April 24, 2006 to May 31, 2012 [Zhang *et al.*, 2006].

(a)

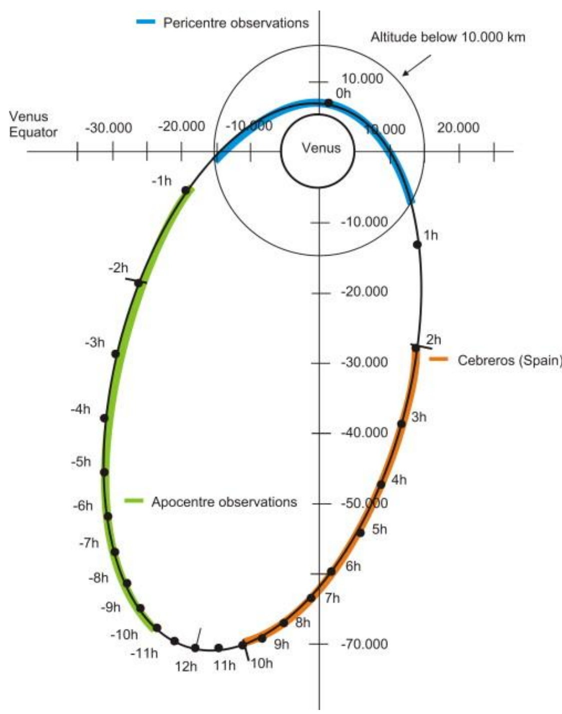

(b)

Figure 2.8 (a) VEX spacecraft and (b) its orbit.

By comparing the early PVO observations with the current VEX observations, we can find out the temporal variation of IFE occurrence, therefore the temporal variation of material co-orbiting with Oljato, at $0.72AU$.

2.1.3 Spacecraft Covering Large Range of Heliocentric Distance

Helios 1 and 2 (Figure 2.9) were launched on December 10, 1974 and January 15, 1976, respectively. Their observations covered the heliocentric-distance from 0.28 to $1.0\ AU$. The magnetic-field data are generally at $4Hz$ and have a highest resolution at $8Hz$ [Neubauer *et al*., 1977]. The solar-wind data have a best temporal resolution of 40.5 second [Rosenbauer *et al*., 1977] but most of the time the plasma data temporal resolution is low. In our study, we only use the magnetic-field data from 1974 to 1981 on *Helios* 1 and from 1976 to 1980 on *Helios* 2 to survey IFEs. There are large data gaps especially when the spacecraft passed behind the Sun as seen from the Earth, thus cutting off communication.

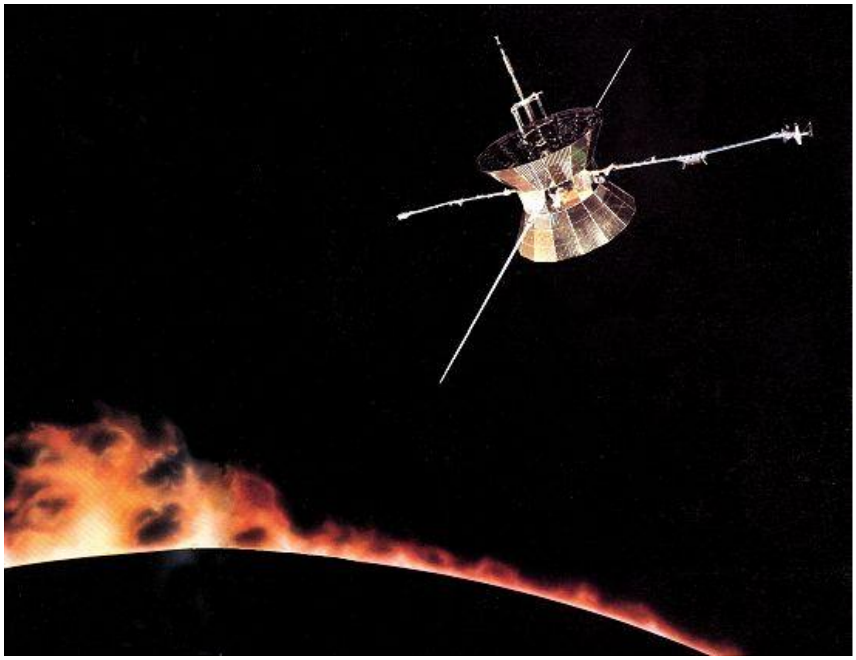

(a)

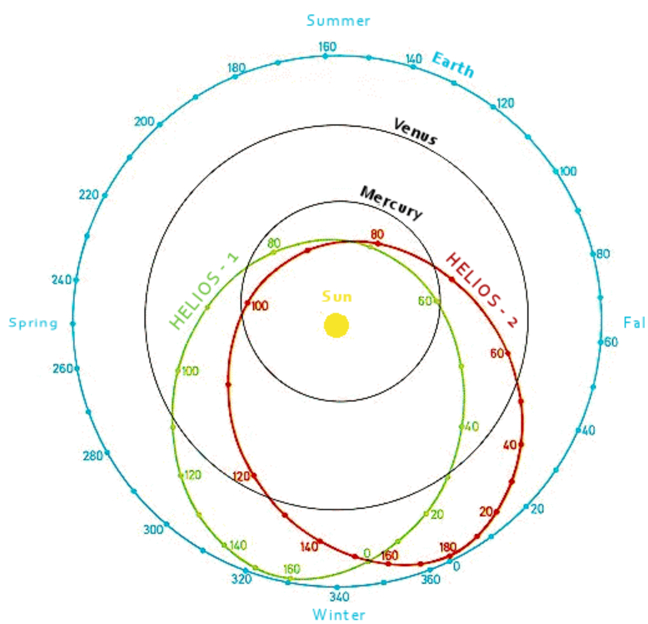

Figure 2.9 (a) *Helios* mission and (b) their orbits

MESSENGER (Figure 2.10) was launched on August 4, 2004, but its magnetometer boom was not deployed until 2005. Here the $1Hz$ magnetic-field data we use are from 2007 to 2010, covering a heliocentric distance from 0.3 to $0.7AU$ [Anderson *et al*., 2007]. The solar-wind plasma data from MESSENGER are not available. In our study, we only use the magnetic-field data during its cruise phase to survey IFEs.

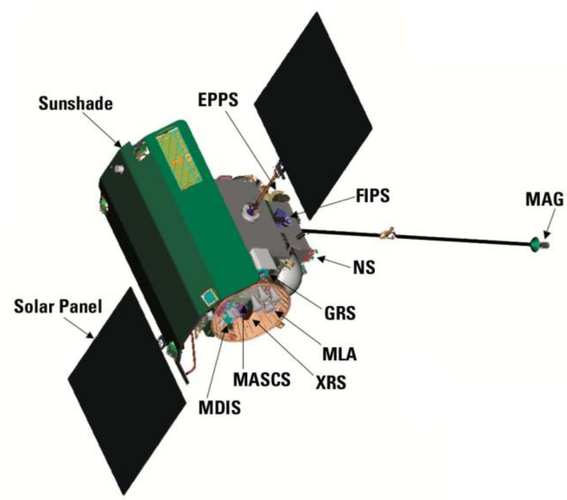

(a)

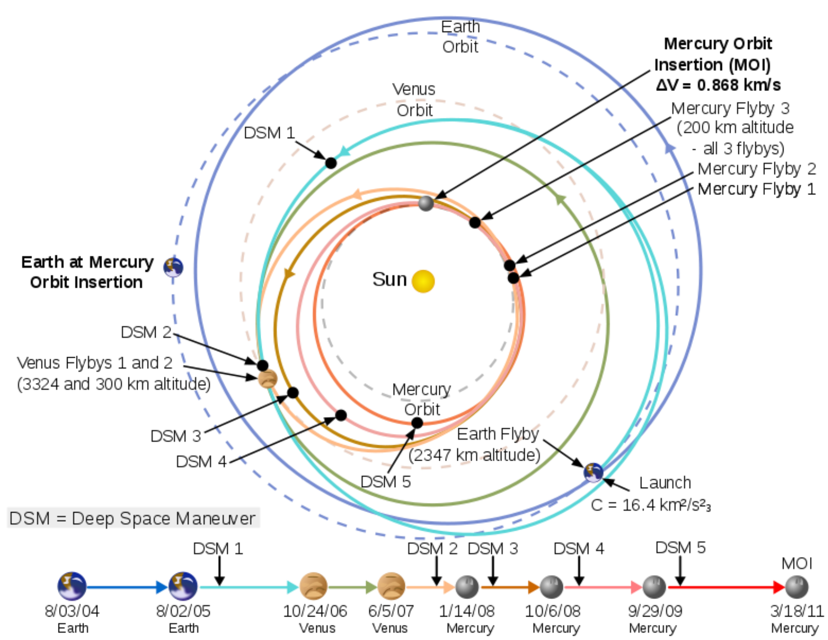

(b)

Figure 2.10 (a) MESSENGER spacecraft and (b) its orbit

Ulysses (Figure 2.11) was launched on October 6, 1990. Unlike the other spacecraft, which stay close to the ecliptic plane, *Ulysses* was designed to study the Sun at high latitude, thus its orbit is highly inclined, *i.e.*, 80.2°. Due to this high inclination, we need to carefully decouple the IFE radial and latitudinal variations in the statistical study. The $2Hz$ magnetic-field data [Balogh *et al*., 1992] and the 4-8-minute solar-wind data [Bame *et al*., 1992] we use are from Oct 25, 1990 to May 29, 2005.

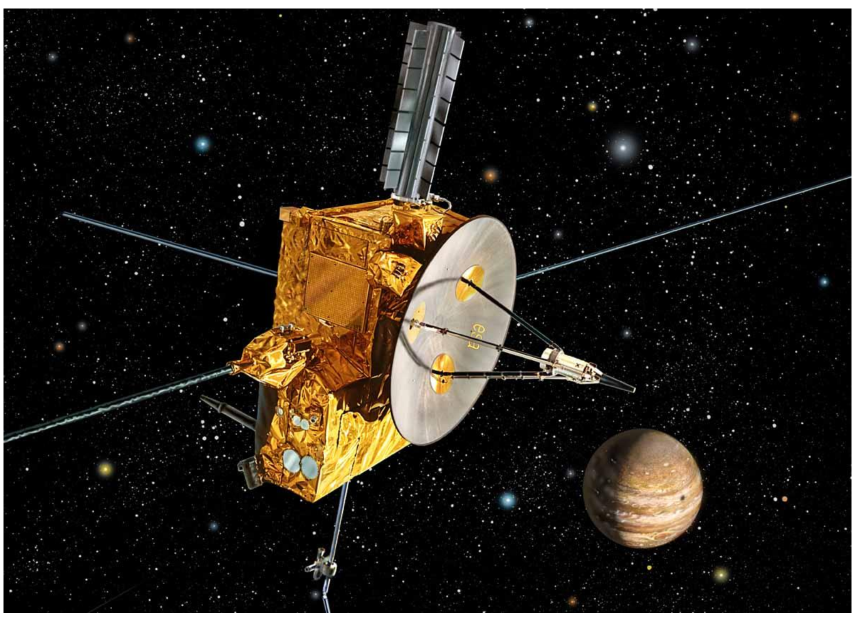

(a)

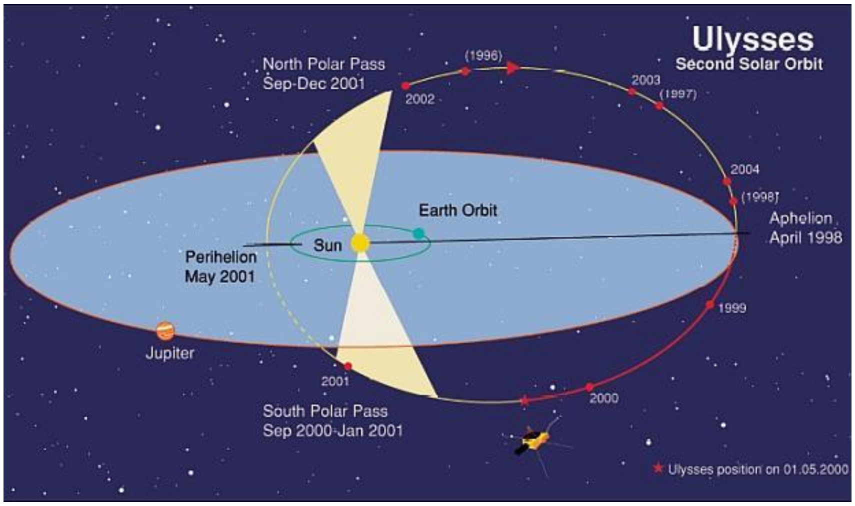

(b)

Figure 2.11 (a) *Ulysses* spacecraft and (b) its orbit

Observations taken by the same spacecraft but at different heliocentric distance are important in understanding the heliocentric radial variation of the IFE formations. Again, the *Ulysses* observations should be carefully analyzed since the latitude variation and the heliocentric radial variation are coupled.

2.2 IFE Quantifications: Scale and Strength

With the magnetic-field and plasma data available, we can define four scale-related parameters and two strength-related parameters. The scale-related ones are as following: (1) IFE duration, which is the interval when the magnetic field is stronger than the ambient one; (2) period of magnetic influence, which includes the magnetic depressions at the IFE boundaries; (3)

IFE radial scale $V_{SW} \cdot T_{IFE}$, while V_{SW} is the solar-wind speed and T_{IFE} is the duration of the IFE; (4) IFE cross-flow radius, which will be estimated in Section 3.3. The two strength-related parameters are: (1) the magnetic-field enhancement $\Delta B = \frac{B_{max}-B_{amb}}{B_{amb}}$, where B_{max} is the peak magnetic-field strength and B_{amb} is the ambient magnetic-field strength; (2) the pressure enhancement index $\Delta P = \frac{P_{max}-P_{amb}}{P_{amb}}$, where P_{max} is the peak total pressure (including magnetic and plasma thermal) and P_{amb} is the ambient total pressure.

Figure 2.12 illustrates the definitions of the above parameters except the cross-flow radius, which cannot be determined by single spacecraft observation and will be discussed in Chapter 3. This is an IFE detected by ACE on August 19, 2007. In Figure 2.12, from top to bottom, we show the magnetic-field components in Radial Tangential Normal (RTN) coordinate system, the strength of the magnetic field and the sum of the magnetic and plasma thermal pressure as the total pressure. In the RTN coordinate system, the spacecraft is at origin, R points away from the Sun, N is northward and T completes the right-handed coordinate system. The vertical lines in Figure 2.12 bracket the IFE duration of 34 minutes (from $1307UT$ to $1341UT$) and the shaded region indicates the period of magnetic influence of 81 minutes (from $1254UT$ to $1415UT$). With the in situ solar-wind velocity at $390km/s$, this IFE has a radial scale of $7.69 \times 10^5 km$. Also in this figure, the horizontal lines show the B_{max} of 8.87nT, B_{amb} of 6.35nT, P_{max} of $52.22pPa$ and P_{amb} of $37.45pPa$. Thus coincidently both the magnetic-field enhancement and the pressure enhancement index are 40%. Here we need to notice that the ambient solar-wind properties are defined in the upstream of the IFE structure, which is the part closer to the Sun and "later" in time series. This is more significantly illustrated in the definition of P_{amb} in Figure 2.12. Also we notice that the total pressure does not have significant depression regions even though the magnetic field does. That is why we use the total pressure rather than the magnetic pressure to define the pressure enhancement. This feature will be discussed later.

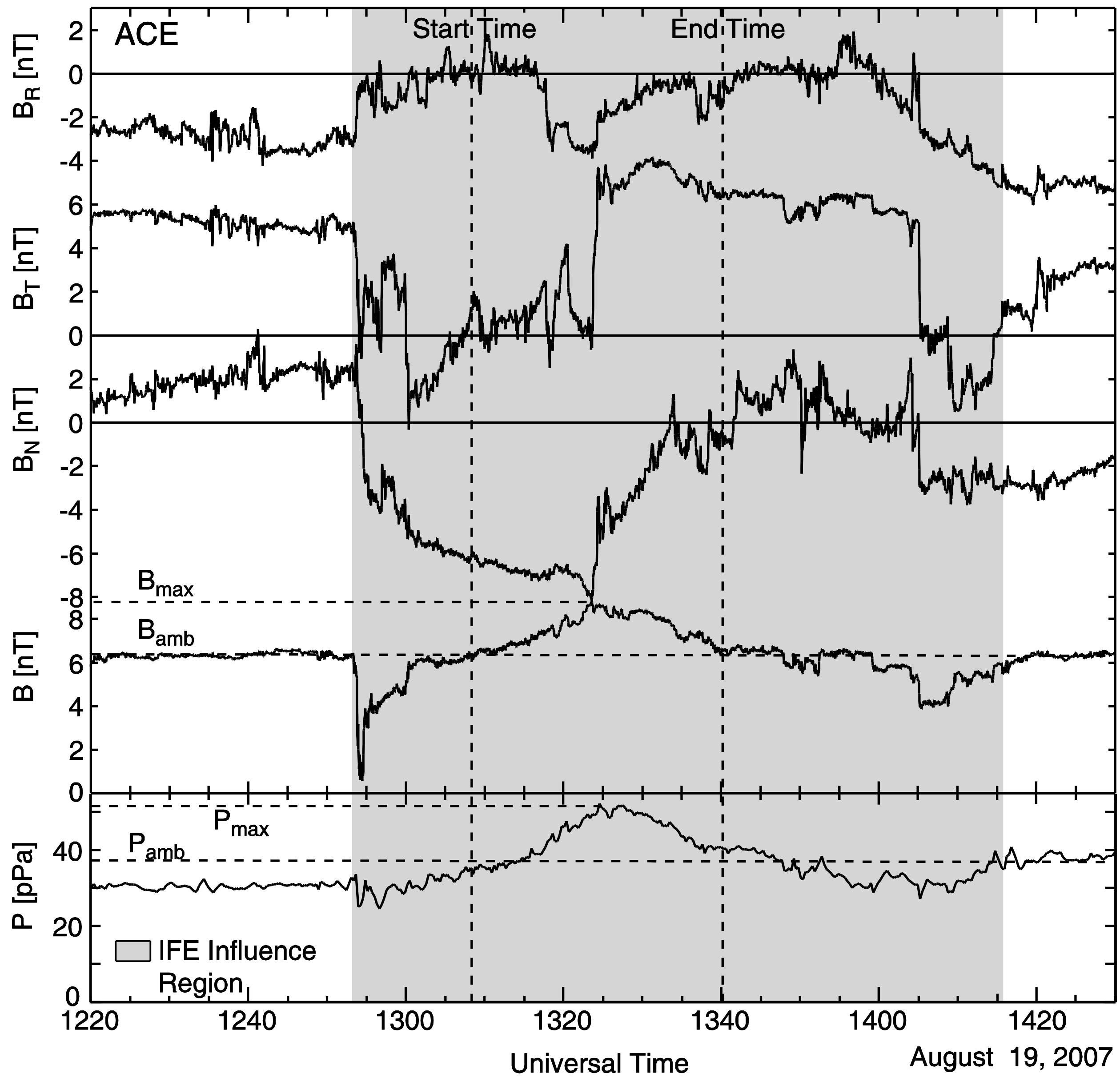

Figure 2.12 An IFE example illustrates the definitions of IFE parameters. This is an IFE detected by ACE on August 19, 2007. From top to bottom shows three components of the magnetic field, the strength of the magnetic field and the total pressure (the sum of magnetic and plasma thermal pressure) of the IFE. The shaded area indicates the IFE influence period. The vertical dashed lines bracket the IFE duration. The

four horizontal dashed lines from top to bottom indicate the maximum magnetic-field strength, the ambient magnetic-field strength, the maximum total pressure and the ambient total pressure.

2.3 IFE Selection Criteria

Since we use magnetic-field data to identify the IFEs, the selection criteria is based on the magnetic-field profile: (1) the maximum magnetic-field enhancement is at least 25%; (2) the period of magnetic influence is longer than 10 minutes; (3) at least one of the magnetic-field components does not rotate smoothly during the enhancement in field strength. The third criterion is to exclude flux ropes from the study. Since we set quantitative criteria in selecting the IFE dataset, it is expected that some small and weak IFEs are undercounted. This will be discussed in more details in the following chapters.

Chapter 3

IFE Properties

In this chapter, we will first give an overview of our IFE population. Case studies as well as statistical studies based on these recorded IFEs will be performed to test the first two predictions of our IFE formation hypothesis: magnetic-field draping and solar-wind slowdown in the upstream region. In order to compare the IFE rate with the collision rate in Chapter 4, we need to know the mass contained in the IFEs; while to find IFE associated interplanetary objects in Chapter 5, we need to determine the spatial distribution of IFE occurrence. All the information needed for the later studies will also be provided in this chapter.

3.1 Overview of the IFEs

3.1.1 Annual Rate

Table 3.1 lists the general properties of IFEs detected by different spacecraft, and Appendix I lists the date and key parameters of these IFEs. For the spacecraft staying at nearly constant heliocentric distances, we list the numbers of IFEs, spacecraft observation times and annual rates in Table 3.1(a). For spacecraft cruising at variable heliocentric distances, we count the IFE rate at different ranges of heliocentric distances and show the corresponding spacecraft observation time and IFE annual rates in Table 3.1(b). Since the magnetic-field data recorded by *Helios* 1 and

2 have many data gaps, to accumulate longer observation times, we combine their observation results in Table 3.1(b).

S/C	Number of IFEs	Observation Time [year]	Annual Rate [/year]
Wind	70	7.81	8.96
ACE	103	14	7.36
STEREO A	48	6.17	7.78
STEREO B	47	6.17	7.62
PVO	62	6.36	9.74
VEX	53	6.11	8.67

(a)

S/C	Range of Heliocentric Distance [AU]	Number of IFEs	Observation Time [year]	Annual Rate [/year]
	0.3~0.6	9	0.98	9.18
***Helios* 1 & 2**	0.6~0.9	3	1.25	2.4
	0.9~1	8	1.11	7.2
MESSENGER	0.3~0.5	11	1.63	6.75
	0.5~0.7	16	1.27	12.60

	1~2	15	1.72	8.72
	2~3	13	1.76	7.39
Ulysses	3~4	7	2.18	3.21
	4~5	18	3.36	5.36
	>5	12	4.57	2.63

(b)

Table 3.1 An overview of the IFEs population. (a) shows those detected by spacecraft located at constant heliocentric distances. (b) shows those detected by *Helios* 1 and 2, MESSENGER and *Ulysses*. Here we group the results by different ranges of heliocentric distances and show the corresponding annual rates.

From Table 3.1(a), we can see that the IFE annual rate is 7.84 on average near $1AU$ while it was 9.91 in the 1980s and is 8.67 presently at $0.72AU$. From Table 3.1(b), we can see that the IFE annual rate varies with the heliocentric distances, which will be discussed in more detail later.

During the survey, we find that IFEs can be detected at all heliocentric distances. Some IFE examples are shown in Figure 3.1. These IFEs are ordered by heliocentric distance from $0.31AU$ to $5.33AU$. And we choose the IFEs with durations of about 20 minutes and present them in 90-minute intervals. We can see that their strength is variable and detailed structures are different.

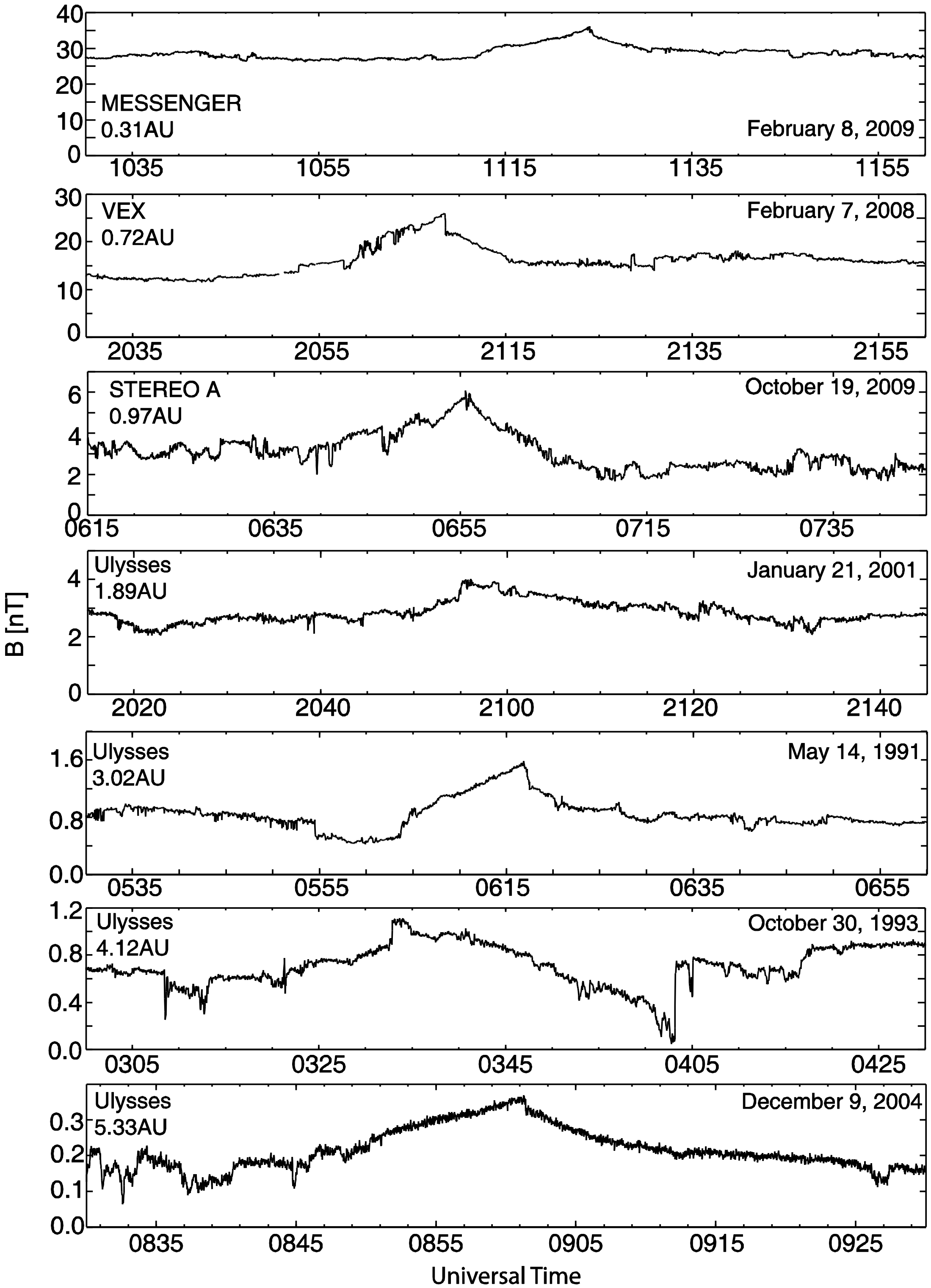

Figure 3.1 IFE examples detected by different spacecraft at different heliocentric distances. Their strength and durations are variable.

Since in Jones *et al*. [2003a], the authors listed all the IFEs (mentioned as “Jones’ list” in later discussion) detected by *Ulysses* from 1990 to 2001 based on their criteria, we can compare our IFE list with theirs. In the Jones’ list, the “weak, thorn-shaped enhancements” and “small-scale flux ropes” are excluded and all the recorded ‘IFEs’ have maximum magnetic-field enhancements of larger than 30%. In total, 39 IFEs were recorded in Jones’ list. During Jones’ period of observations, we in contrast recorded 56 IFEs. Figure 3.2(a) shows the comparison. We have not identified all the IFEs in Jones’ list, and the reasons are summarized in Figure 3.2(b). The difference between the two IFE lists is generally due to the differences in selection criteria and in definition of the ambient magnetic field. Figure 3.3 shows an example of perturbation which is counted as an IFE in Jones’ list but not included in our list. The lower panel shows one-day magnetic-field data. The event is bracketed in vertical red dashed lines. Due to the magnetic depression at the boundaries, the enhancement in the magnetic-field strength seems to be very significant. However, based on our definitions, as shown in the zoomed-in magnetic-field profile in the upper panel, the ambient and the maximum magnetic-field strength (red horizontal dashed lines) are $1.15nT$ and $1.35nT$, respectively. Therefore the enhancement in magnetic-field strength is only 17%, which does not satisfy our selection criteria.

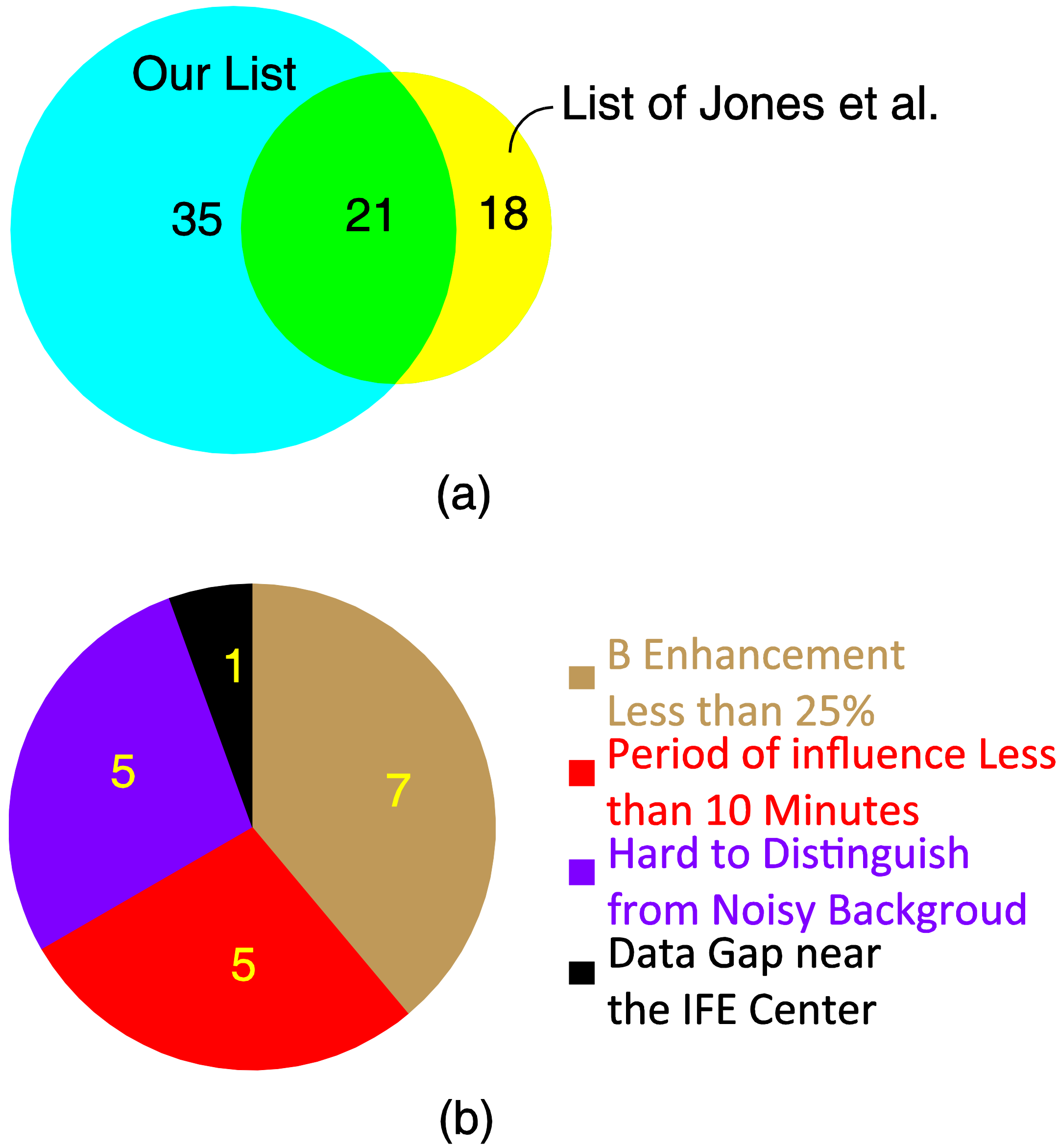

Figure 3.2 (a) A comparison between our IFE list and Jones' list. 18 events in Jones' list are excluded in our list and the reasons are shown in (b). The different IFE populations are due to the differences in IFE selection criteria and in definitions of ambient magnetic field.

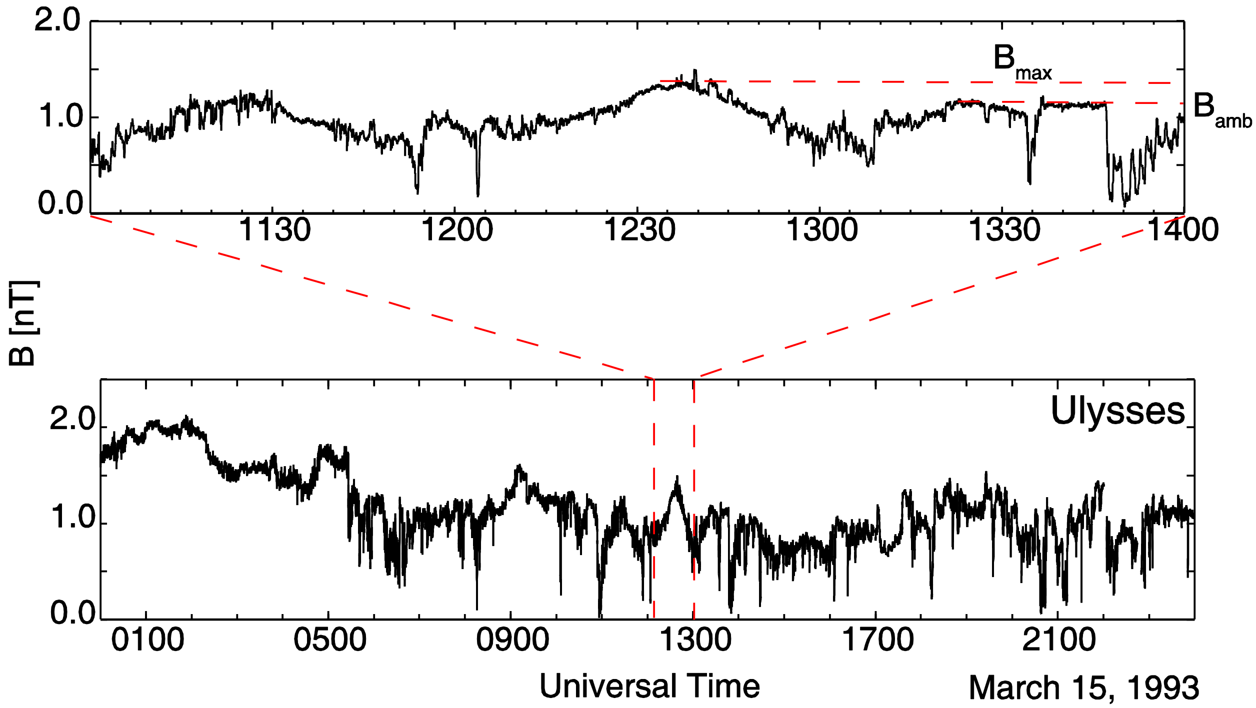

Figure 3.3 An event counted as an IFE in Jones' list but excluded in ours. This event stands out in the one-day magnetic-field profile (lower panel) due to the magnetic-field depressions at the boundaries. However, in our definition, the maximum and ambient magnetic-field strengths are selected as shown in the upper panel (red horizontal dashed lines). The magnetic-field enhancement is only 17%, which does not satisfy our selection criteria.

3.1.2 Latitudinal and Heliocentric Radial Variation of IFE Occurrence

Although we listed the IFE annual rate detected by *Ulysses* as a function of heliocentric distances in Table 3.1(b), we should notice that the orbit of *Ulysses* is highly inclined while all the other spacecraft orbit close to the ecliptic plane. To study the latitudinal effect on the IFE annual rate, we further group the *Ulysses* results shown in Table 3.1(b) every 20° in latitude. Observation times and IFE occurrences are recorded in each subgroup and the corresponding annual rate is obtained. To remove the heliocentric radial variation, we normalize each IFE annual rate by the annual rate in the same heliocentric distance range between latitude $0\,°$ and $20\,°$. Here the latitude is measured in heliocentric ecliptic (HE) coordinate system. In this coordinate, the Sun is at the origin, the longitude is measured in the ecliptic plane and the zero-degree longitude is pointing to the first point in Aries. In the later discussion, if not specified, all longitude and latitude are measured in this coordinate system. To reduce the statistical fluctuation, the original data have been smoothed by a moving three-point filter with weights $(1/4, 1/2, 1/4)$ for three successive rates. In this way, noise above the Nyquist frequency of the plot has been removed. The final results are shown in Figure 3.4. Here different symbols represent normalized IFE annual rate in different heliocentric distance ranges. The black solid line is the average. Figure 3.4 shows that generally the IFE annual rate increases as the latitude increases. In the northern hemisphere the data points are more spread. Therefore the latitudinal influence seems to be more significant.

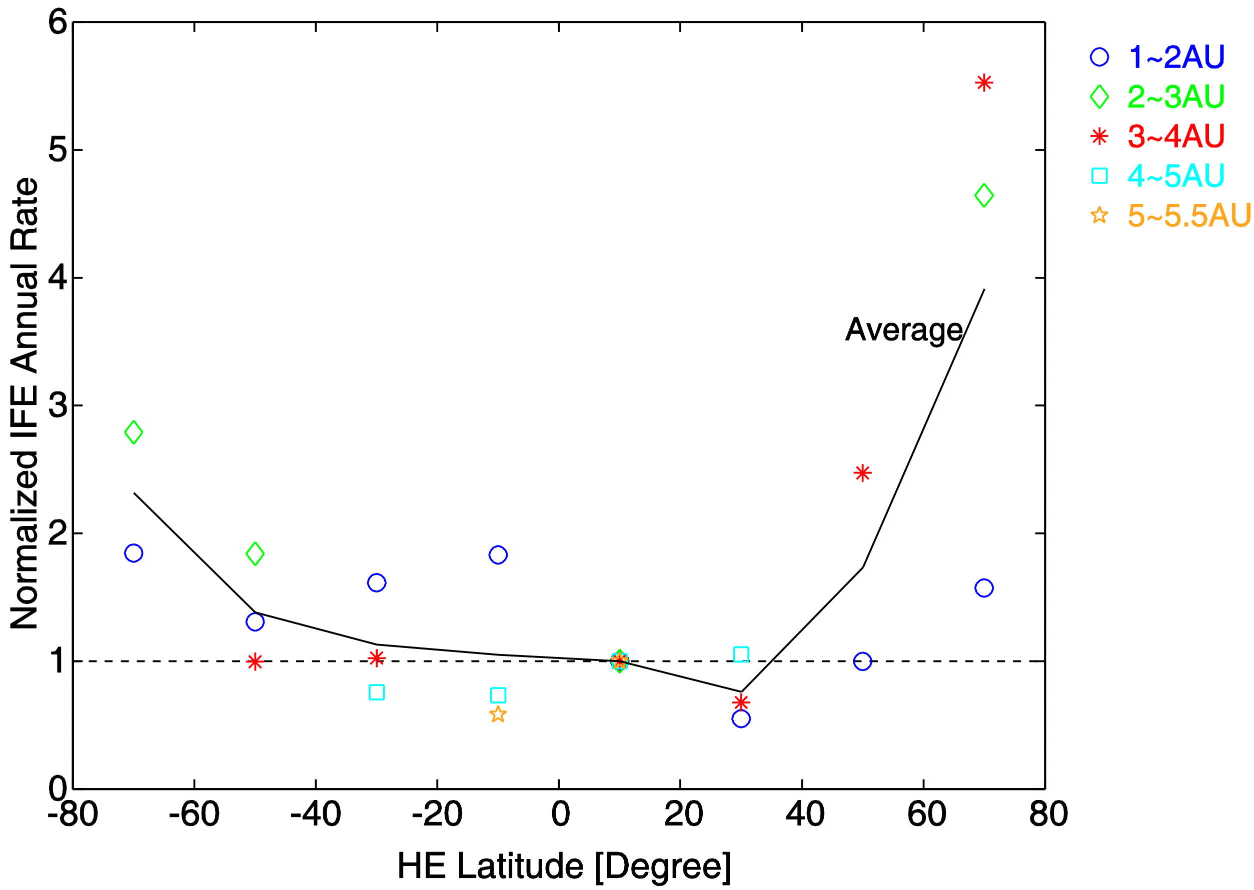

Figure 3.4 Normalized IFE annual rates observed by *Ulysses* as a function of latitude. Here different symbols represent IFEs detected at different heliocentric distance ranges indicated by the legends. All the IFE rates are normalized by the corresponding rate detected between 0° and 20° to reduce the heliocentric radial variation. The black solid line shows the average rate in each latitudinal range. Generally the IFE rate increases when the latitude increases. Since the data points in the northern hemisphere are more spread, this latitudinal effect seems to be more significant there.

Figure 3.5 summarizes the IFE annual rate as a function of heliocentric distance. In this figure, different colors represent observations from different spacecraft. Crossings are the average rate and bars indicate the probable errors. We use a second degree polynomial to fit the results as the red line shows. To estimate the probable errors, for each spacecraft, we use three months as an observation time unit and classify the total observations into three independent groups by the time unit successively. For each group, we calculate the annual rate. The mean and the standard error of the mean are then calculated based on the three rates belonging to the three groups. The *Ulysses* results shown here are the IFE annual rates in the latitudinal range between $-20°$ and $20°$. Since the IFE database is largely reduced by this latitudinal limitation, we group the *Ulysses* data every $2AU$. We need to point out that although we plot all the observations in one figure to show the heliocentric distance variation, there is temporal variation as well. For example, at $0.72AU$, the average IFE rates detected by PVO and VEX are close but their probable errors are quite different, which will be discussed in more details in Chapter 5. We should also notice that MESSENGER, *Helios* 1, *Helios* 2 and *Ulysses* have relatively short observation times, which may be responsible for the large probable errors. In Figure 3.5, when the heliocentric distance increases, the best-fitted results (red line) shows that the IFE rate increases slowly inside $1AU$ and decreases sharply outside $2AU$.

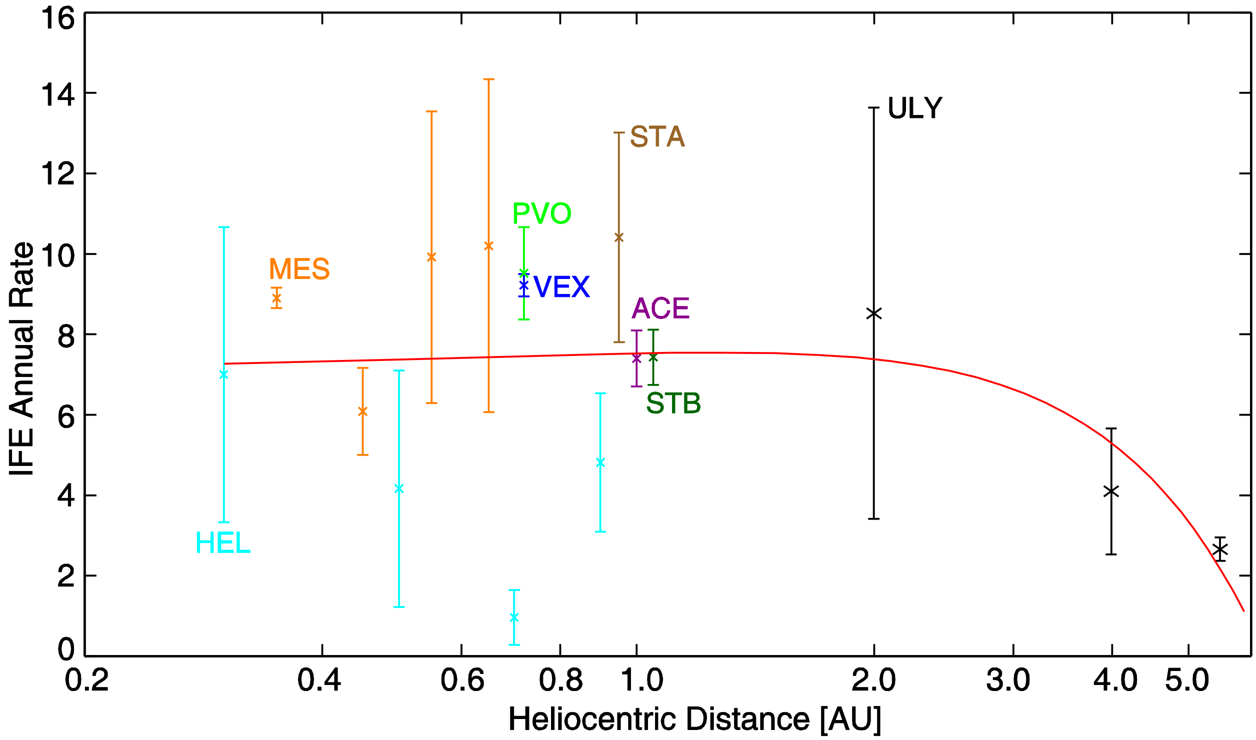

Figure 3.5 IFE annual rate as a function of heliocentric distance. Different colors represent observations from different spacecraft. The crossings are the averages and the bars are the probable errors. The red line is a second degree polynomial fit. We should bear in mind that any temporal variations will also appear in this plot. When the heliocentric distance increases, the fitted results show that the IFE rate increases slowly inside $1AU$ and decreases sharply outside $2AU$.

Based on our IFE formation hypothesis, the IFE occurrence is directly related to the interplanetary collision rate. Therefore the red line in Figure 3.5 indicates that the collision rate increases slowly inside $1AU$ and decreases significantly beyond $2AU$. This will be discussed in Chapter 4.

3.1.3 Clustering in Space

In the earlier PVO study, Russell *et al*. [1984a] revealed a spatial clustering feature in the IFE occurrence. Now with our more strict selection criteria, we re-examine the IFE longitudinal distribution and show the result in Figure 3.6. Here the longitude is measured in the HE coordinate system. Figure 3.6(a) shows the PVO results and Figure 3.6(b) shows the VEX results. Each sectors cover 30° in longitude and their radii represent the corresponding IFE annual rates. The red circle indicates the average annual rate over all longitudes while the green circles represent the standard deviations. We can see that the longitudinal distribution detected by PVO peaks between the longitude of 195° and 225°, which is consistent with the earlier studies [Russell *et al*. 1984a]. After 30 years, the longitudinal distribution of IFEs detected by VEX changed. Generally there are more IFEs between the longitude of 315° and 105°. Based on our hypothesis, the IFE occurrence rate is related to the interplanetary collision rate and thus the distribution of the interplanetary objects. We will discuss this temporal variation in longitudinal distribution in more detail in Chapter 5.

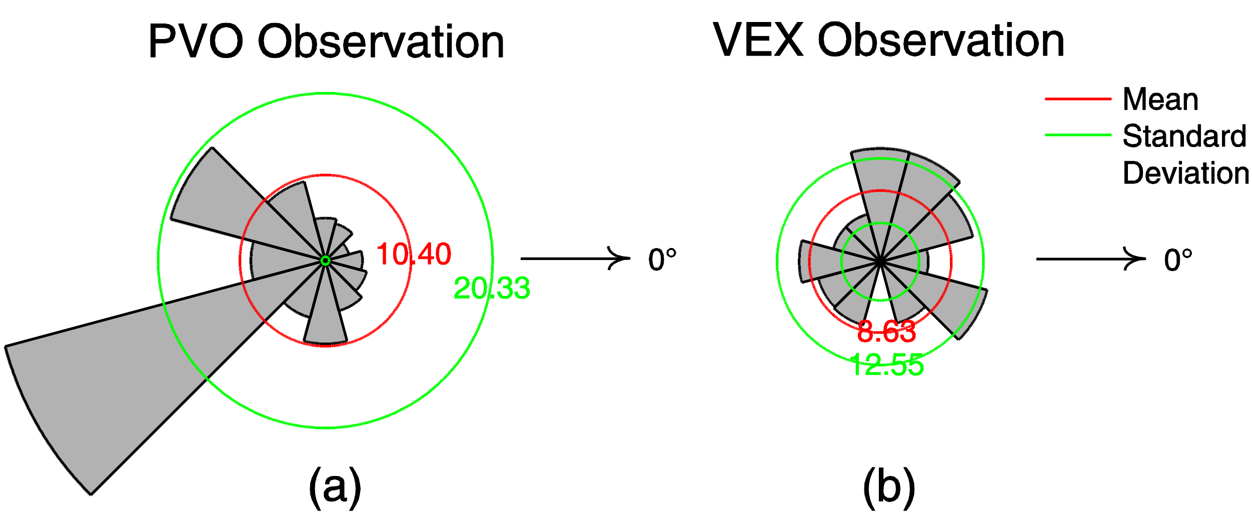

Figure 3.6 IFE longitudinal distribution at $0.72AU$ detected by PVO (a) and VEX (b). All the results are shown in the HE coordinate system and zero longitude is shown as the arrows. Each shaded sector covers 30° in longitude and its radius represents the corresponding IFE annual rate. The red line shows the average and the green lines show the standard deviations. The annual rate in PVO observation clearly peaks in the longitudinal range between 195° and 225°, which is consistent with the earlier studies [Russell *et al*. 1984a]. This longitudinal distribution changes after 30 years when VEX is in orbit.

Since ACE and *Wind* have completed more than 14 and 7 orbits around the Sun in ecliptic plane respectively, we can also use their observations to study the IFE longitudinal distributions at $1AU$. The results are shown in Figure 3.7 in the same format as the one in Figure 3.6. Although the distribution detected by *Wind* is not identical to the one detected by ACE, both annual rates are larger than average by more than one standard deviation between longitude of 195° and 225°. This cluster of events points to possible IFE sources near this longitudinal range. We will discuss this in more detail in Chapter 5.

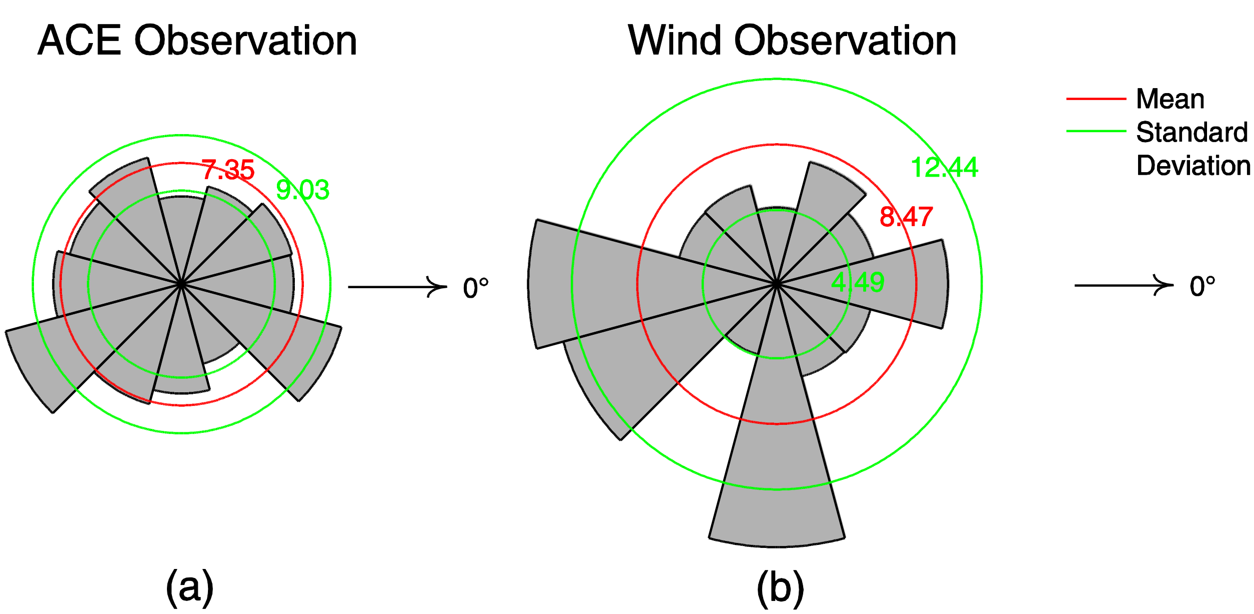

Figure 3.7 IFE longitudinal distributions at $1AU$ detected by ACE (a) and *Wind* (b). The format is the same as the one in Figure 3.6. In both distributions, the annual rates are more than one standard deviation larger between longitude of 195° and 225°.

Figure 3.8 shows the longitudinal distribution detected by STEREO A and B in the same format as the one in Figure 3.8 and Figure 3.9. Although their distribution patterns are different from the ones detected by ACE and *Wind*, the IFE annual rates are still large between longitude of 195° and 225°.

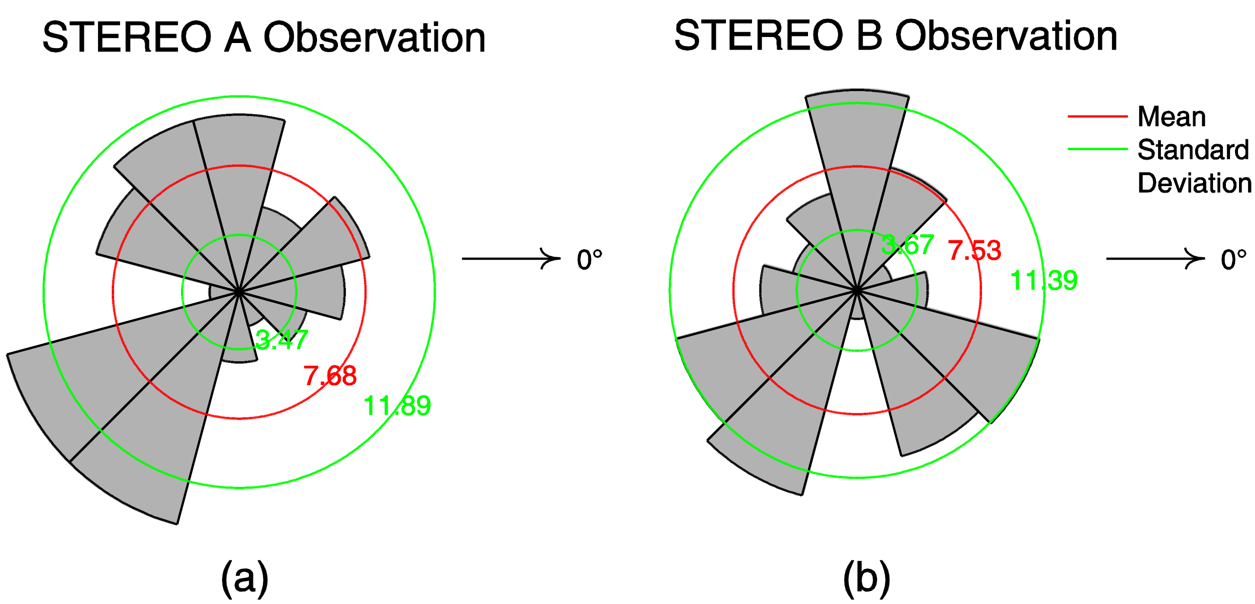

Figure 3.8 IFE longitudinal distribution near $1AU$ as detected by STEREO A (a) and STEREO B (b). The format is the same as the ones in Figure 3.6 and Figure 3.7. Although the detailed distributions are different from the ones in Figure 3.7, the annual rates are still large between longitude of 195° and 225°.

Since all spacecraft near $1AU$ detect high IFE rate near the longitudinal range of $195°$ and $225°$, we can combine their database. To ensure the databases from different spacecraft have the same weights, we only count the IFEs detected from 2007 to 2011, and their longitudinal distribution is shown in Figure 3.9. Again the radii of the sectors show the corresponding annual rate and this time the black\white solid bars indicate the standard errors. The IFE annual rate between longitudinal range of $195°$ and $225°$ clearly stands out in Figure 3.9, implying IFE sources in that longitudinal range.

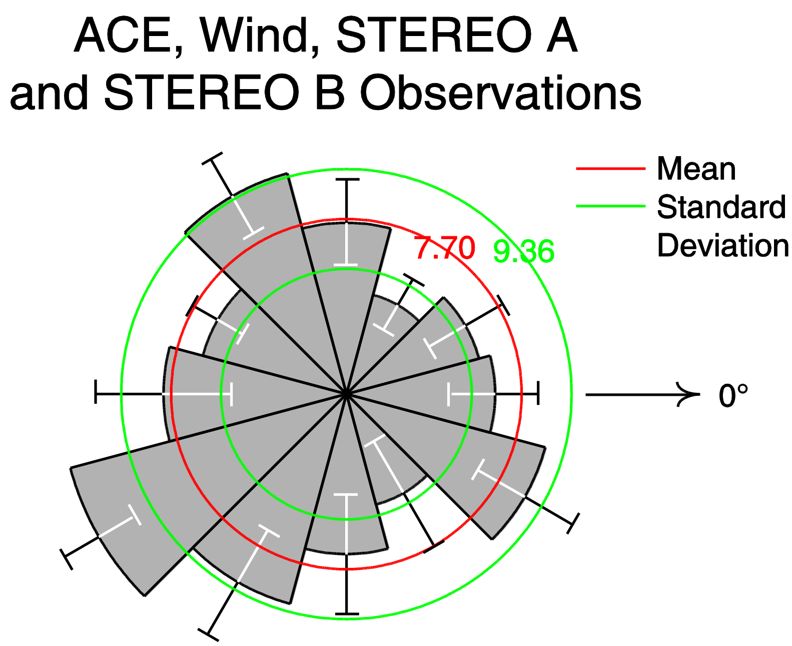

Figure 3.9 Longitudinal distribution of IFE annual rate based on observations from ACE, *Wind*, STEREO A and STEREO B from year 2007 to 2011. The format is the same as the one in Figure 3.8. Now we have standard errors in each sectors calculated from the four different databases. The IFE annual rate between longitudinal range of 195° and 215° is larger than the average by more than one standard deviation, implying the existence of IFE sources near this region.

3.1.4 Clustering in Time

The occurrence of IFEs not only clusters in space but also clusters in time. Figure 3.10 shows three examples when two IFEs were detected within 24 hours at $1AU$, at $0.72AU$ and at $5AU$, respectively. Table 3.2 lists all the dates when IFEs show such a clustering feature. This phenomenon is not a simple coincidence. Take the ACE observation as an example, the probability of having four two-on-one-day-IFE observations is only 0.0934 (Appendix II).

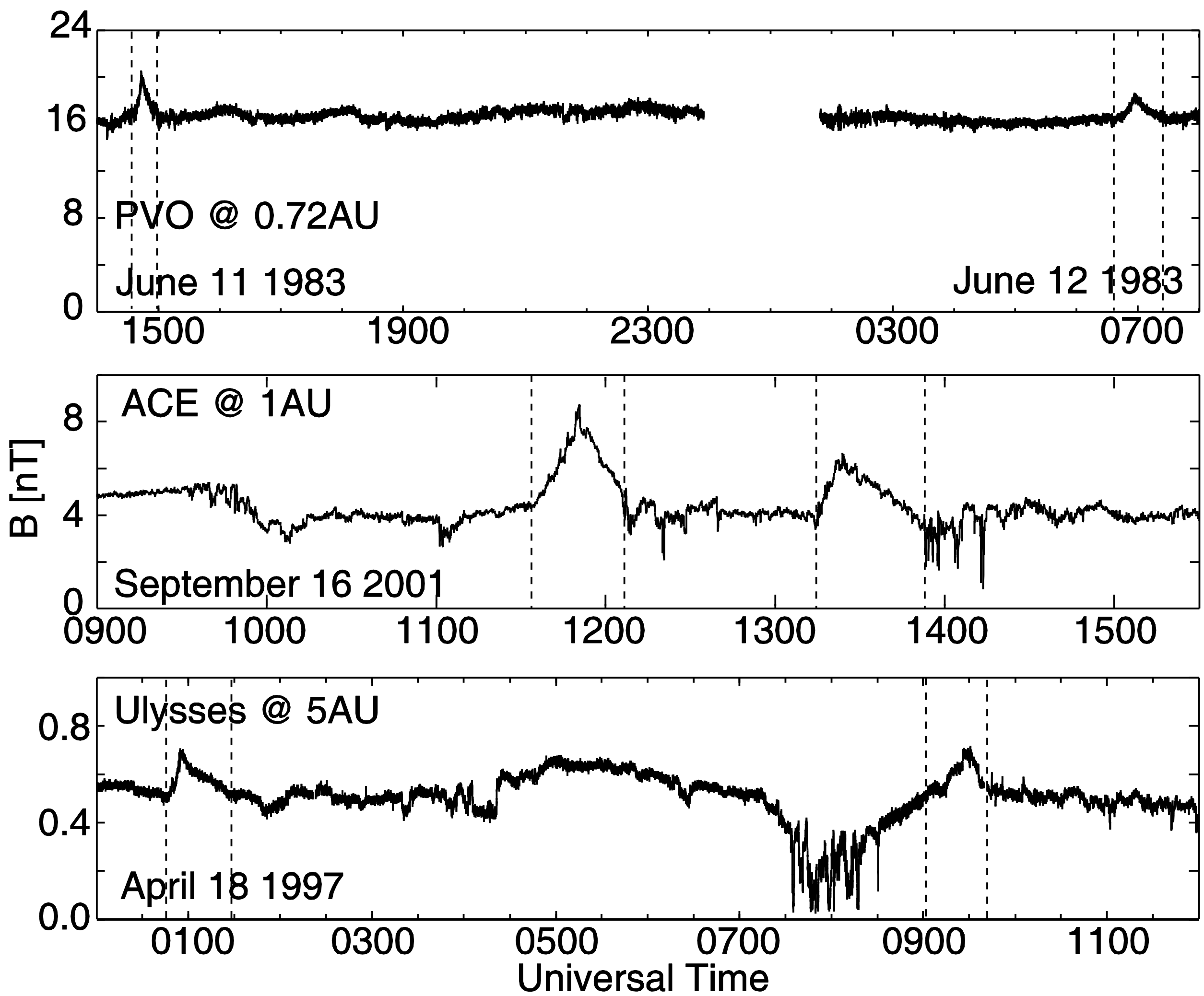

Figure 3.10 Magnetic-field profiles when two IFEs were detected within 24 hours. This is a non-random clustering feature shown in time.

S/C			**Date [YYYY/DOY]**		
ACE	2001/259	2001/318	2008/050	2010/231	\
Wind	2005/123	2006/321	2006/343	2009/096	2010/259
STEREO A	2007/150	2008/203	2012/337	\	\
STEREO B	2009/129	\	\	\	\
PVO	1980/098	1983/162	\	\	\
VEX	2006/205	2007/231	2009/023	2011/261	\
Ulysses	1997/108	\	\	\	\
MESSENGER	2008/253	\	\	\	\

Table 3.2 List of all the dates when two or more IFEs occurred within 24 hours.

Based on our hypothesis, a possible explanation for the "frequent" occurrence of this otherwise low probability phenomenon is that some of the interplanetary objects concentrate in streams, with a larger-than-normal density of impactors. When they come across another stream, many collisions take place and several dust clouds are released in a short period of time. Solar wind then interacts with those dust clouds and several IFEs could be produced in a short interval. Thus our multiple daily observations such as the ones shown in Figure 3.10 indicate that material orbiting the Sun has some concentration in streams possibly associated with an earlier collision.

3.1.5 Detections by Multi-Spacecraft

As we stated in Section 2.1, IFEs detected by multi-spacecraft are extremely important in understanding the geometry of the IFEs and $1AU$ is good place to obtain such observations. In Table 3.3, we list all the IFEs detected by two or more spacecraft. Most of them are bi-spacecraft observations. With four or more spacecraft simultaneous observations we can determine the IFE velocity; while with bi-or tri-spacecraft simultaneous observations, we have to assume that the IFE moves radially outward. Such a velocity estimation method has been applied to all the listed IFEs and their velocities are all found to be close to the in situ measured solar-wind velocity.

Date [YYYY/DOY]			**Spacecraft**		
2004/162	ACE	*Wind*	\	\	\
2005/088	ACE	*Wind*	\	\	\
2006/321	ACE	*Wind*	\	\	\
2007/016	ACE	STEREO B	\	\	\
2007/223	ACE	STEREO B	\	\	\
2007/280	ACE	*Wind*	\	\	\
2009/170	ACE	*Wind*	\	\	\
2006/358	ACE (*)	STEREO A	STEREO B	\	\
2011/008	ACE	ARTEMIS P1	ARTEMIS P2	\	\
2011/124	ACE	*Wind*	ARTEMIS P1	ARTEMIS P2	\
2011/062	ACE	*Wind*	ARTEMIS P1	ARTEMIS P2	*Geotail*

Table 3.3 List of IFEs detected by more than one spacecraft. On Day 358 of year 2006, there is an IFE detected by STEREO A and STEREO B. ACE (*) also detected some similar perturbations but the

magnetic-field profile does not satisfy our IFE selection criteria. For all the listed IFEs above, we checked their velocities and find that they all move radially outward at nearly the solar-wind speed.

We now show two examples of detailed case studies on the IFEs detected by multiple spacecraft simultaneously. In both cases, we will reconstruct the magnetic-field geometry based on the observations. This can test one of our predictions: the draping magnetic field in the upstream.

3.1.5.1 Five-spacecraft Simultaneous Observations

On March 3, 2011, an IFE (referred as "March 2011 IFE" later) was detected by ACE, *Wind*, ARTEMIS P1, ARTEMIS P2 and *Geotail*. The positions of the five spacecraft and the magnetic-field profile of this IFE are shown in Figure 3.11 and Figure 3.12, respectively. Both the positions and the magnetic-field components are shown in the Geocentric Solar Ecliptic (GSE) coordinate system. In this coordinate, X points from the Earth towards the Sun, Y is in the ecliptic plane pointing toward dusk, and Z completes the right-hand coordinate set.

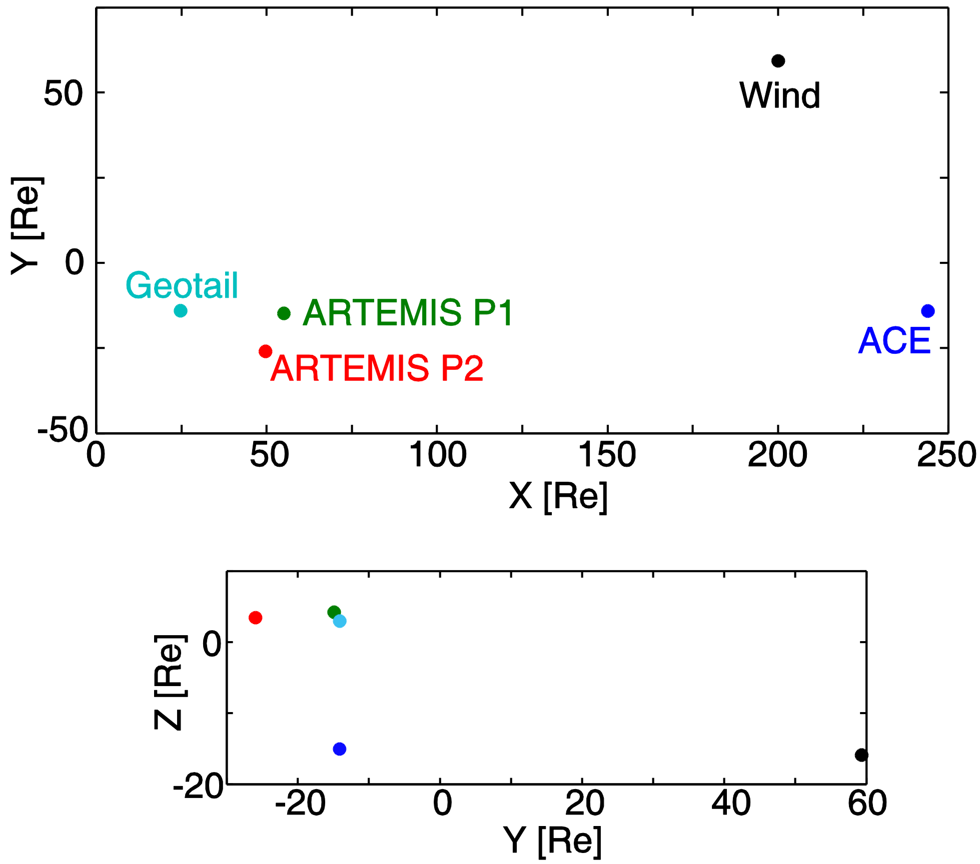

Figure 3.11 Projections of spacecraft (*Wind*, ACE, *Geotail*, ARTEMIS P1 and P2) locations in GSE coordinate system on March 3, 2011, when an IFE was detected by all the five spacecraft. *Wind* and ACE were upstream and *Wind* was far away from the other four spacecraft in Y direction.

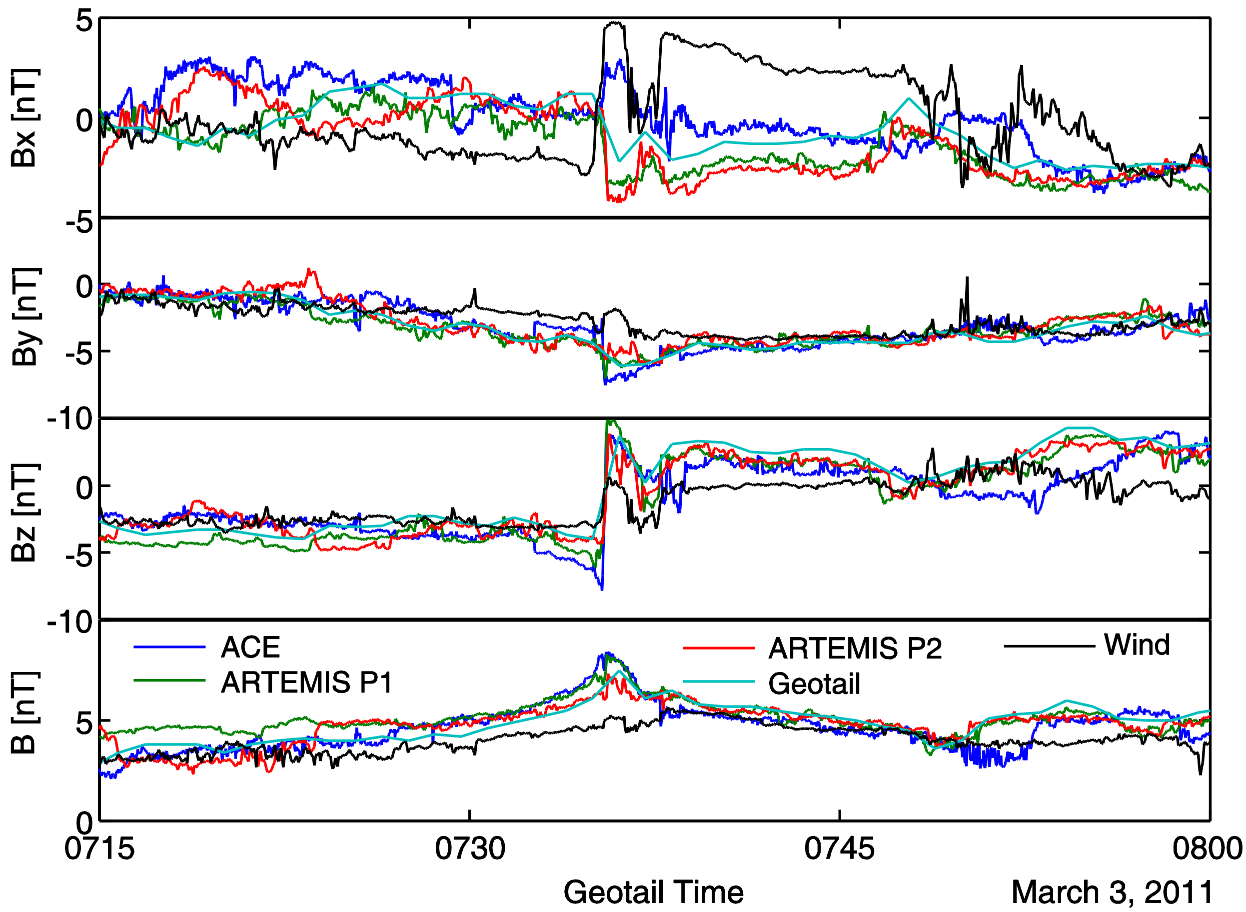

Figure 3.12 Magnetic-field profiles of the IFE detected by five spacecraft. The magnetic-field components are shown in the GSE coordinate system. The time delay has been adjusted so the sharp changes in the B_Z component are aligned. We use the *Geotail* time series as a reference.

In Figure 3.11, different colors indicate the position projections of different spacecraft as the legend describes. When this IFE was detected, ACE and *Wind* were upstream near the L-1 points while ARTEMIS P1, ARTEMIS P2 and *Geotail* were near the Earth. The position projections in the Y-Z plane shows that in Z direction *Wind* and ACE are below the other three spacecraft and *Wind* had the largest separation from the other four spacecraft in Y direction.

In Figure 3.12, we adjust the time delays of each spacecraft so that the sharp changes in the B_Z component were aligned and we use the *Geotail* time series as a reference. Although all the spacecraft captured the sharp change in B_Z component and the enhancement in the magnetic-field strength, the detailed magnetic-field profiles observed by individual spacecraft are different. This is due to both the spatial and temporal evolution of this IFE. We will discuss that later.

Table 3.4 shows the universal time when B_Z changes signs for each spacecraft. The locations of the spacecraft in the GSE coordinate system are also shown here. Based on the spacecraft locations and the time delay, we know that the IFE perturbation plane is moving outward from the Sun generally. The only exceptional case is the *Wind* observation. Comparing to ACE, *Wind* is over $40R_E$ downstream. However, it detected the sharp change in B_Z component four minutes earlier than ACE did. Considering that *Wind* has the largest separation from other spacecraft in Y direction, a possible explanation for this unusual time delay is that the IFE perturbation front is curved and *Wind* might locate near the IFE boundary.

S/C	Coordinate System	Position [R_E]	Time When B_Z Changes Sign [UT]
ACE	GSE	(243.92, -14.12, -15.05)	06:55:28
	VB	(-244.65, -4.79, -5.36)	
Wind	GSE	(200.01, 59.32, -15.90)	06:51:08
	VB	(-195.85, -69.98, 21.23)	
ARTEMIS_P1	GSE	(55.08, -14.88, 4.22)	07:29:21
	VB	(-55.82, 12.69, 0.97)	
ARTEMIS_P2	GSE	(49.64, -25.94, 3.45)	07:30:18
	VB	(-51,18, 22.71, -4.55)	

Geotail	GSE	(24.77, -14.08, 2.94)	07:34:58
	VB	(-25.58, 12.88, -1.59)	

Table 3.4 Spacecraft positions in GSE coordinate system and universal times when B_Z reversed sign. Based on the spacecraft locations and time delays in observations, we can see that the IFE is generally moving outward away from the Sun. In this table, we also show the spacecraft positions in the VB coordinate system. This coordinate system will be defined later.

In Russell *et al*. [1983b], a method to determine the normal of the perturbation plane and the velocity along that normal based on four or more-spacecraft simultaneous observations has been developed. In this method, there is a presumption that the curvature of the perturbation front is negligible. This assumption is not valid if we count the *Wind* observation. If we apply this method to the remaining spacecraft observations, we find that the normal of the perturbation plane points $(9 \mp 5)°$ away from the solar-wind flow and the IFE velocity along that normal is $(565 \mp 12) km/s$ (error estimation is based on [Vogt *et al*., 2011]). This velocity is very close to the projection of the solar-wind velocity in the same direction, which is $579\ km/s$ based on the observation from ACE.

The observed magnetic profile in Figure 3.12 involves both temporal and spatial evolutions, but which evolution dominates in this observation? In this case, ACE and *Wind* detected the IFE about half an hour before the other spacecraft did. If the temporal evolution dominates, the observations of ACE and *Wind* should be consistent but would be significantly different from the observations of other spacecraft. However, in Figure 3.12, the $B_{Y,}$ B_Z and magnetic-field magnitude patterns observed by ACE are quite different from the ones observed by *Wind* but similar to the ones observed by *Geotail*, ARTEMIS P1 and P2, which are closer to ACE in GSE Y-Z plane. This indicates that the time scale of the temporal evolution is much longer than our observation period. If the spatial evolution dominates, *Wind* observation would be the most different due to its largest separation in GSE Y direction. ACE observation can also be different from *Geotail*, ARTEMIS P1 and P2, because it is about $20R_E$ below the three spacecraft in GSE Z direction. This is what we show in Figure 3.12. Thus in the later discussion we only need to consider the spatial variation of the March 2011 IFE.

We can infer the characteristic magnetic features based on the observed magnetic-field profiles. But before that, we convert the magnetic profile from GSE coordinate system to a more natural one, where X points to the solar-wind flow direction, the ambient magnetic field lies in the X-Y plane and Z completes the right-hand coordinate system. This coordinate system will be referred as VB coordinate system in later discussion.

As this IFE was detected by multiple spacecraft, we use the average IMF direction and solar-wind flow direction to determine the convention matrix and the result is

$$\begin{pmatrix} -0.9972 & -0.0471 & 0.0578 \\ 0.0686 & -0.9110 & 0.4072 \\ 0.0291 & 0.4097 & 0.9115 \end{pmatrix}.$$

We can see that generally the solar-wind flow is antiparallel to the GSE X. The spacecraft positions in VB coordinate system is listed in Table 3.4, and the magnetic-field profile in this coordinate system is shown in Figure 3.13. Because the rotation matrix is determined by the average value, the ambient B_Z observed by individual spacecraft is not zero. However, we can see that after the coordinates convection, the B_Y and B_Z components observed by ACE almost lay on top of the ones observed by ARTEMIS P1, which is the closest spacecraft to ACE in the cross-flow direction.

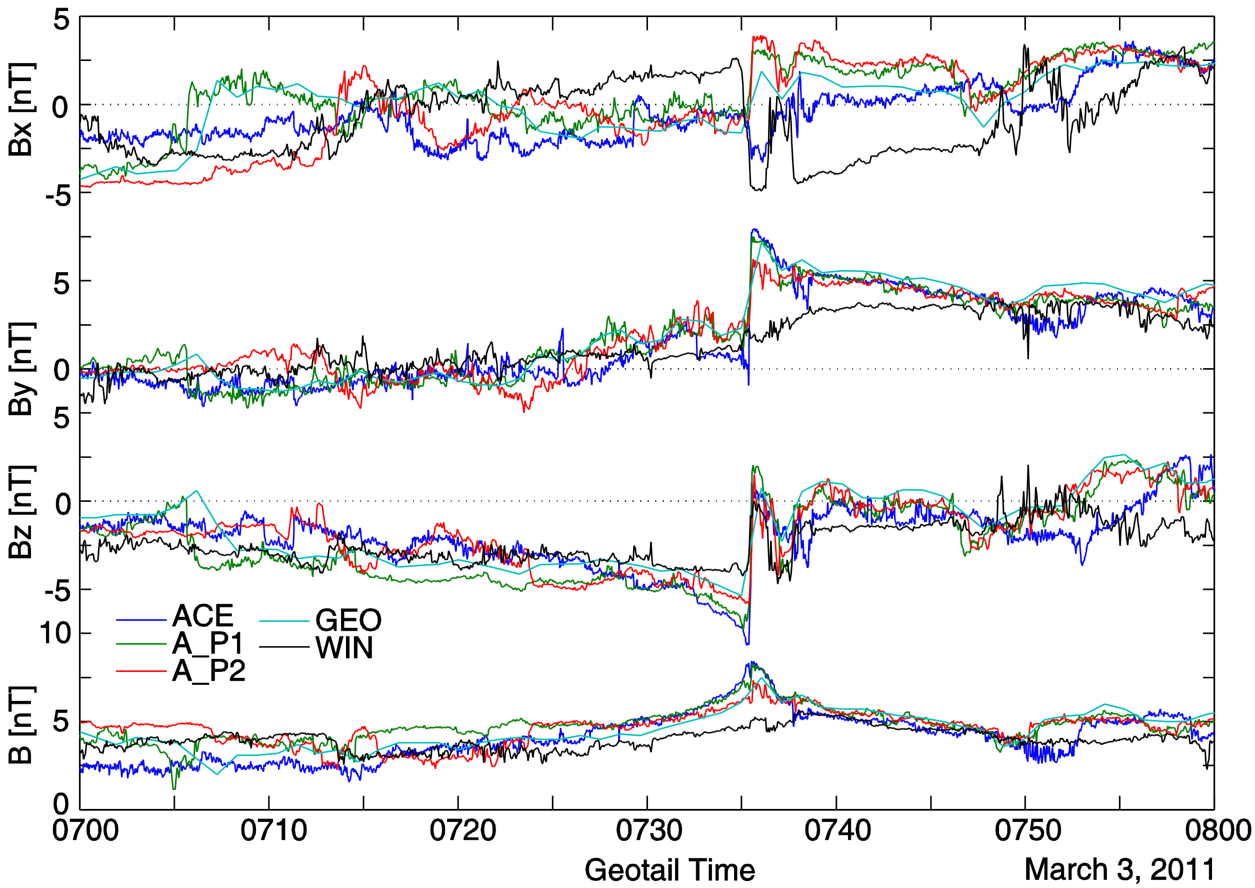

Figure 3.13 Magnetic-field profile of March 2011 IFE in VB coordinate system. Here X is the solar-wind flow direction, ambient IMF lies in the X-Y plane and Z completes the right-handed coordinate system.

To better understand the magnetic-field geometry, we choose nine points from Figure 3.13 (*Geotail* Time $0713UT$, $0718UT$, $0724UT$, $0730UT$, $0735UT$, $0736UT$, $0741UT$, $0747UT$ and $0752UT$) and plot their X-Y and X-Z components in Figure 3.14. Here the scale in X directions is determined by the time interval times the solar-wind speed. The solid circles show the spacecraft positions in VB coordinate system while the solid lines show the magnetic-field projections. Here the *Geotail* observation is not shown because it highly agrees with the ARTEMIS P1 observation but in a lower resolution. And in Y-Z plane in VB coordinate system, its position almost lays on top of the ARTEMIS P1 position. Based on Figure 3.14, this IFE can be separated into two parts. The magnetic field in the upstream part is dominated by B_X and B_Y components; while the magnetic field in the downstream part is dominated by the B_Z component. In the upstream part, the B_X component detected by *Wind* is always anti-parallel to the ones detected by ARTEMIS P1 and P2 (only at *Geotail* time $0736UT$ did ACE and *Wind* detected the B_X in the same direction). This is a clear draping geometry which is consistent with our first prediction. The magnetic-field feature in the IFE downstream part reminds us the AMPTE observation, where the magnetic field was observed to bend in the same direction. Such a bending feature may relate to the flow separation in that direction as the MHD results show [Jia *et al*, 2012].

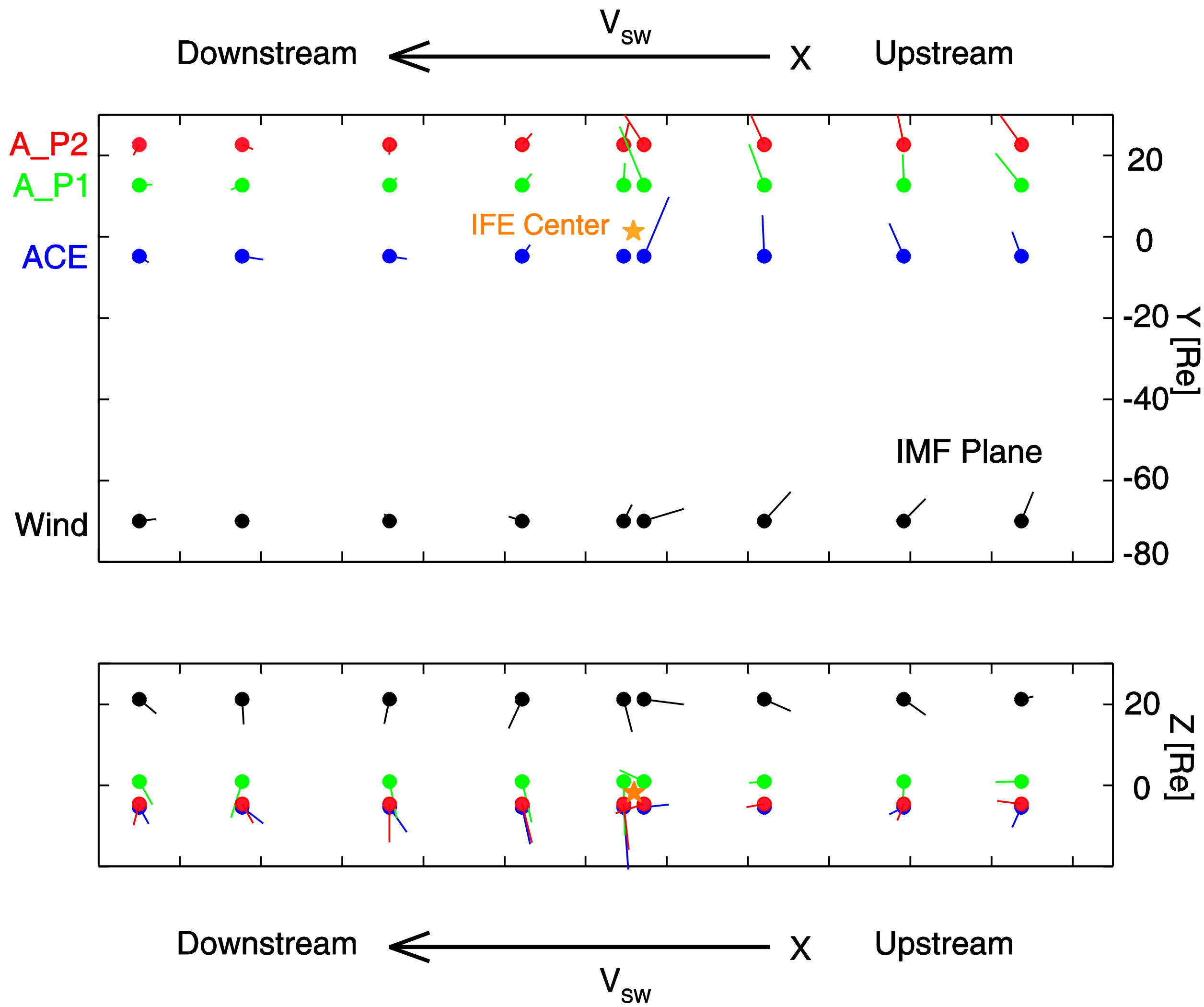

Figure 3.14 Magnetic-field projections in X-Y and X-Z plane in VB coordinate system. The solid cycles represent the spacecraft locations while the solid lines indicate the magnetic-field directions and strengths. The magnetic field in the upstream part of the IFE shows a clear draping feature in X-Y plane which is consistent with our first prediction. In the downstream part of the IFE, magnetic field is bent out of the plane in which the ambient IMF and flow lie. This is consistent with the AMPTE observation. The center of the IFE is determined in Section 3.3.

3.1.5.2 Four-spacecraft Simultaneous Observations

On December 24, 2006, an IFE was detected simultaneously by STEREO A and STEREO B. At that time the two STEREO spacecraft were in the solar wind close to the Sun-Earth line. Although the magnetic-field enhancements observed by ACE and *Wind* do not satisfy our selection criterion, they detected some similar perturbations. Figure 3.15 shows the locations of the four spacecraft in Geocentric Solar Magnetospheric (GSM) coordinate system. In this coordinate, X points from the Earth towards the Sun, Z is the projection of Earth's dipole axis on GSE YZ plane and Y completes this coordinates. From Figure 3.15 we can see that ACE and *Wind* were well separated from STEREO A and STEREO B in Y-Z plane. Therefore we can use their observations to reconstruct the IFE magnetic-field geometry.

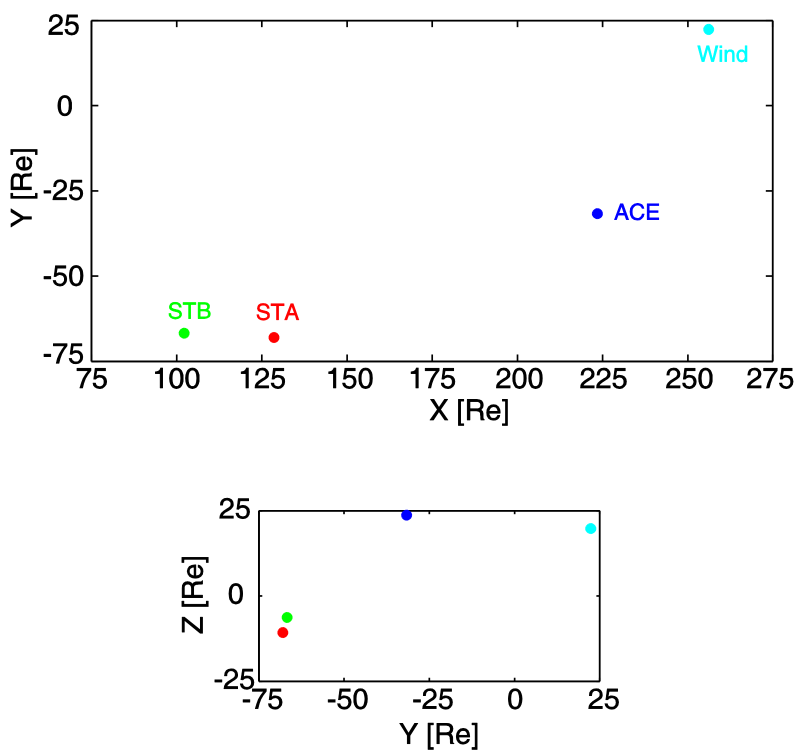

Figure 3.15 Spacecraft locations in GSM coordinate system on December 24, 2006 when STEREO A and STEREO B detected an IFE. ACE and *Wind* observed similar perturbations in the magnetic field.

Figure 3.16 shows the magnetic-field profiles observed by the four spacecraft. Here we use the time series of STEREO A as a reference. To adjust the time delays among ACE, STEREO A and STEREO B observations, we align the sharp change in B_y. The time delay of *Wind* observations has been determined by comparing it with ACE observation in B_x component. With the information of the spacecraft location and time delays, we find that this IFE also moves at nearly the solar-wind velocity. This is consistent with the earlier results [Russell *et al*., 2010].

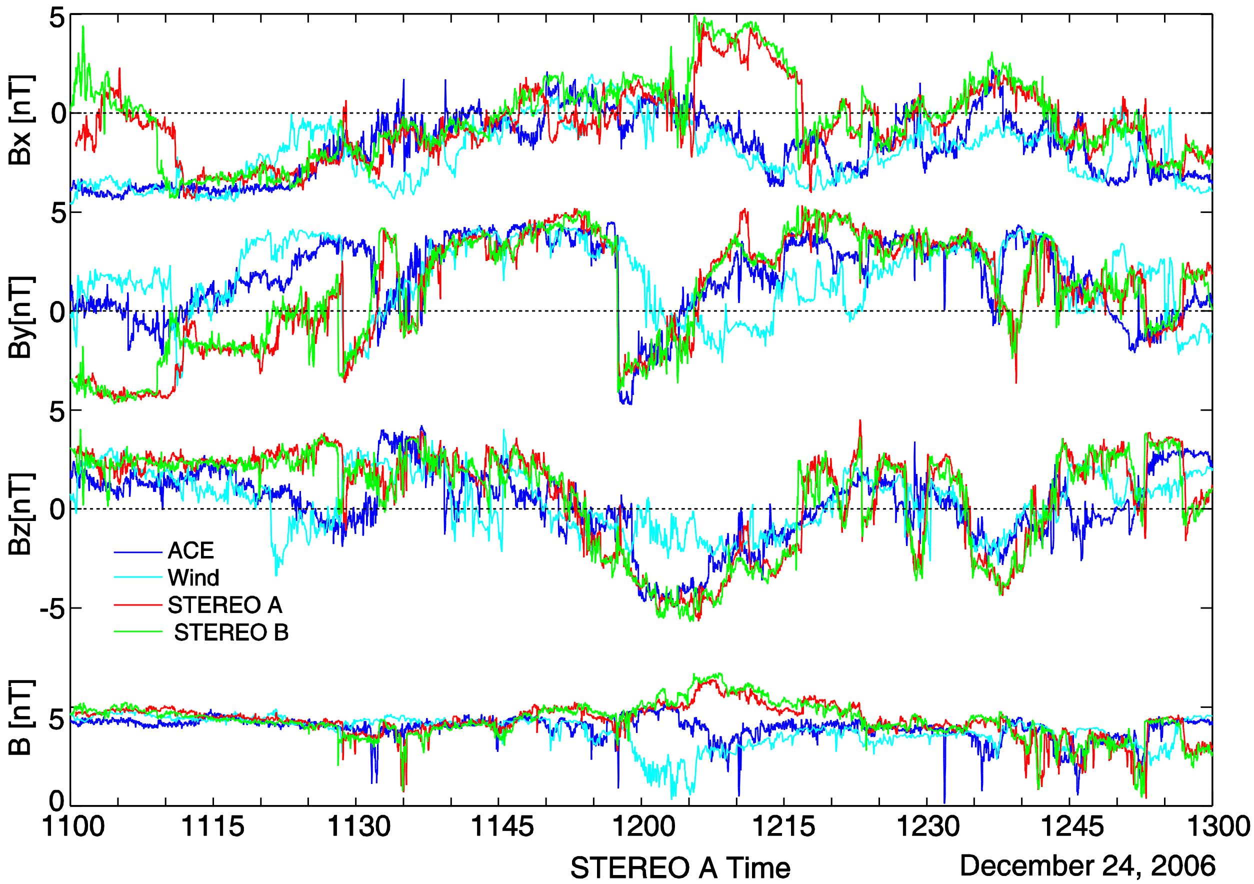

Figure 3.16 Magnetic-field profiles of the IFE detected on December 24, 2006. Here the time delays have been adjusted so that the sharp changes in B_y component detected by ACE, STEREO A and STEREO B are aligned and the B_x component detected by ACE and *Wind* are consistent.

We now rotate the spacecraft locations and the observations into the VB coordinate system to reconstruct the magnetic-field geometry as we performed in the previous case. The result is shown in Figure 3.17 with the same format as the one in Figure 3.14. Since the STEREO A and STEREO B observations are nearly identical and their locations in the Y-Z plane in VB coordinate system are very close, we only show STEREO A observations in Figure 3.17. We can see that the magnetic-field draping feature is again clear in the X-Y plane. In the X-Z plane, during the IFE, there is also a non-zero magnetic-field component in the direction perpendicular to both the ambient IMF and flow.

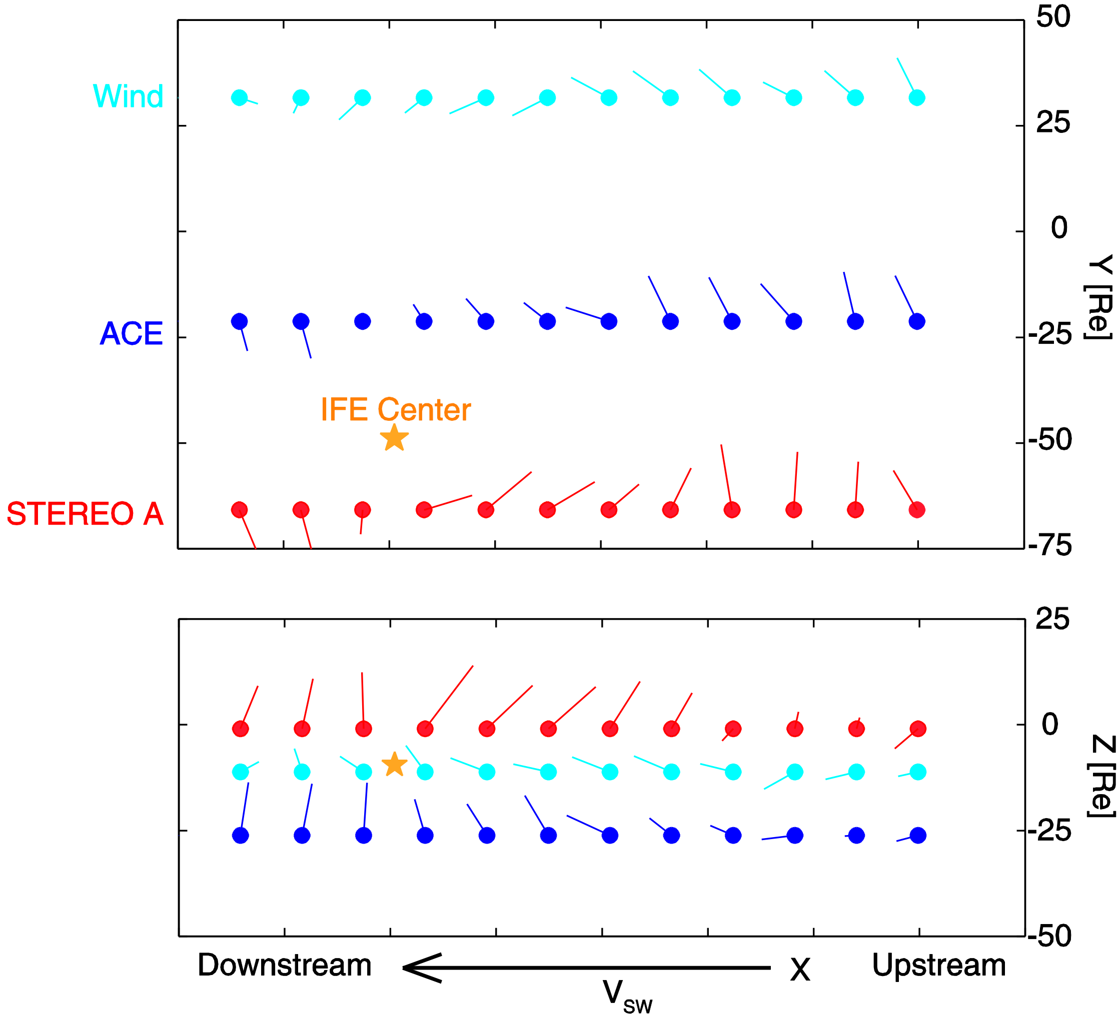

Figure 3.17 Magnetic-field projections in X-Y and X-Z plane in VB coordinate system. The format is the same as the one in Figure 3.14. Again, the magnetic field in the upstream part of the IFE shows a clear draping feature in X-Y plane. During the IFE, magnetic field is bent out of the plane in which the ambient IMF and flow lie.

3.2 Plasma Features

3.2.1 Plasma Profiles during IFEs: Event Study

With the available plasma data, we can study the plasma features of IFEs. Figure 3.18 shows the solar-wind bulk flow velocity, proton number density and proton temperature during the same IFE in Figure 2.12. From the plasma profile, we can see that perceptible changes in the solar-wind plasma properties can be detected only at the IFE boundaries where the magnetic field decreases. There the density and temperature increase slightly, which leads to the increase in plasma thermal pressure and compensates the decrease in the magnetic pressure. Thus the total pressure shows only an enhancement during the IFE (bottom panel in Figure 2.12). The pressure enhancement implies that the forces resulting from the pressure gradient initially push forward away from the Sun in the dust-cloud part and then push backward toward the Sun in the solar-wind part.

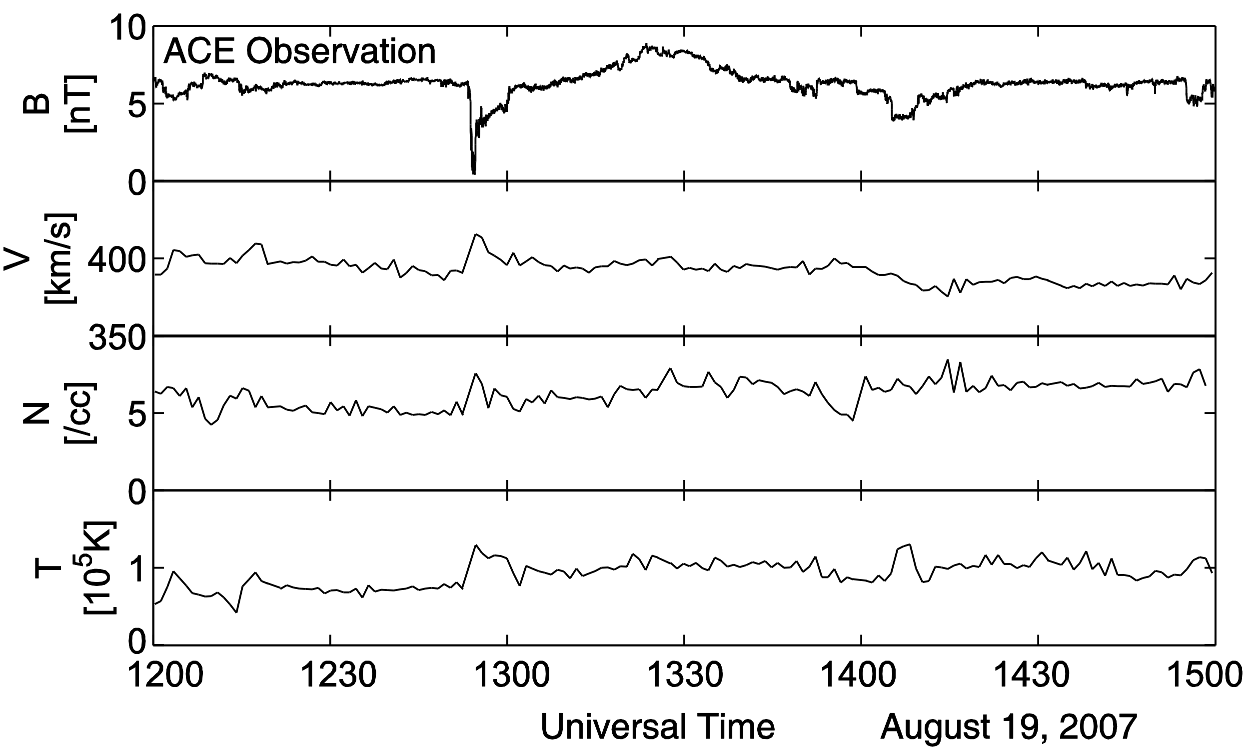

Figure 3.18 Magnetic-field and plasma profiles of the IFE shown in Figure 2.12. From top to bottom are the magnetic-field strength, the solar-wind bulk flow velocity, the solar-wind proton number density and

proton temperature. There are no significant changes in the solar-wind plasma parameters during an IFE. At the boundaries, the proton density and temperature increase. Thus in the total pressure profile, there is no depressions at the IFE boundaries as shown in Figure 2.12.

Some IFE events show velocity perturbations at the boundaries separating the solar wind and the dust clouds. The IFE in Figure 3.19 is such an example. Here from top to bottom we show the magnetic-field strength and the three components of solar-wind flow in RTN coordinate system. During this event, there is a sharp change in the V_t component near the IFE center. This can be a signature of the solar-wind flow deflection, depending on the geometry of the dust cloud and the trajectory of the spacecraft.

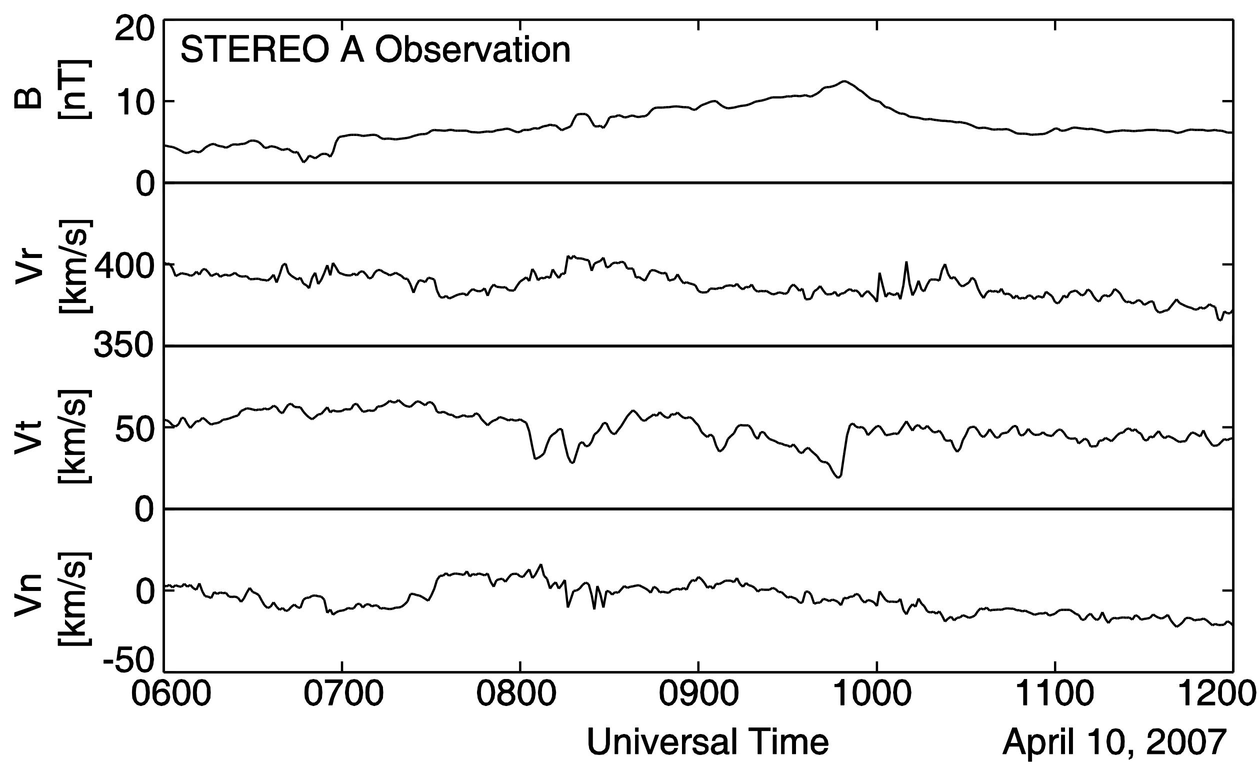

Figure 3.19 An IFE example with three components of the solar-wind velocity in RTN coordinate system. During this event, the V_t component changes sharply near the center of the IFE. This is possibly a flow-deflection signature.

3.2.2 IFE Radial Scale Length

With the knowledge of the in situ solar-wind speed, we can obtain the IFE radial scale length distribution. Figure 3.20 shows such a distribution of IFEs detected by ACE. We can see that the scale length ranges from $10^5 km$ to $10^7 km$. There is a peak in the distribution plot, which is probably not real, because our distribution is biased by the selection criteria. Since only IFEs lasting longer than 10 minutes are recorded, we might undercount the short-scale-length IFEs. If the average solar-wind speed at $1AU$ is $450km/s$, 10 minutes gives a radial scale of $2.7 \times 10^5 km$, corresponding to the vertical dashed line in Figure 3.20. Thus the first bin in the shaded region is strongly affected by the 10-minute-duration criterion. Based on our hypothesis, longer-radial-scale IFEs are possibly related to larger colliders. Since the number density of interplanetary objects decreases as their sizes increase, collisions involving larger objects should be rarer. Therefore we expect a monotonic decrease with increasing radial scale.

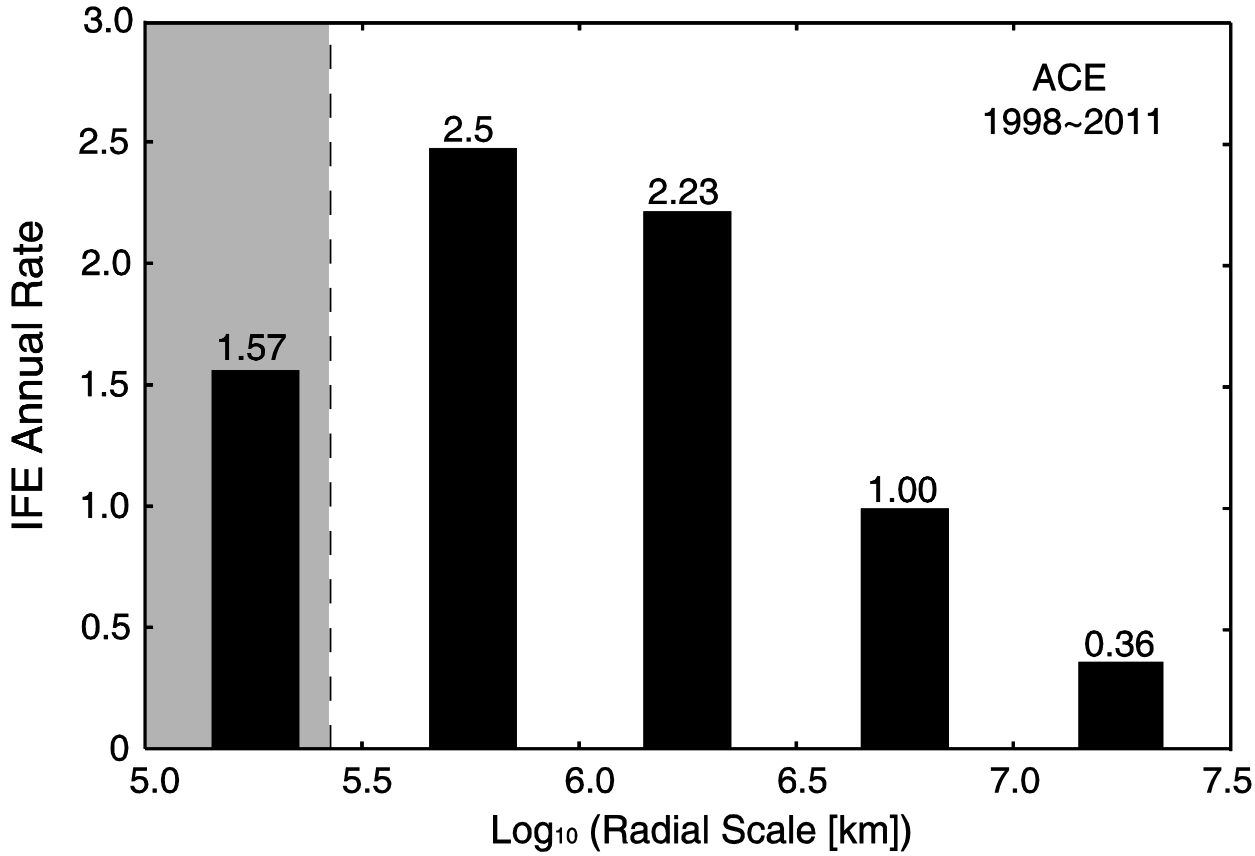

Figure 3.20 Annual rate of IFEs detected by ACE as a function of radial scale length. Most of the recorded IFEs are over millions of kilometers in radial scale. However, due to the 10-minute period of influence selection criterion, the bin inside the shaded area and even the bin next to it may be undercounted. The dashed line corresponds to $2.7 \times 10^5 km$.

3.2.3 Pressure Enhancement Index

The pressure enhancement index can also be calculated with the available solar-wind proton number density and proton temperature. Figure 3.21 shows the cumulative IFE rate as a function of the pressure enhancement index (ΔP) based on ACE observation. Here "cumulative" means that all the IFEs with ΔP exceeding the indicated number are counted. This pressure enhancement index distribution is also affected by the selection criteria. In average solar-wind condition at $1AU$ (Table 1.2), the 25% magnetic-field enhancement gives $\Delta P = 0.25$. This is indicated as the vertical dashed line in Figure 3.21. The bin in the shaded area is thus undercounted. If we extrapolate the bins outside the shaded area, we can get the first bin as shown in grey.

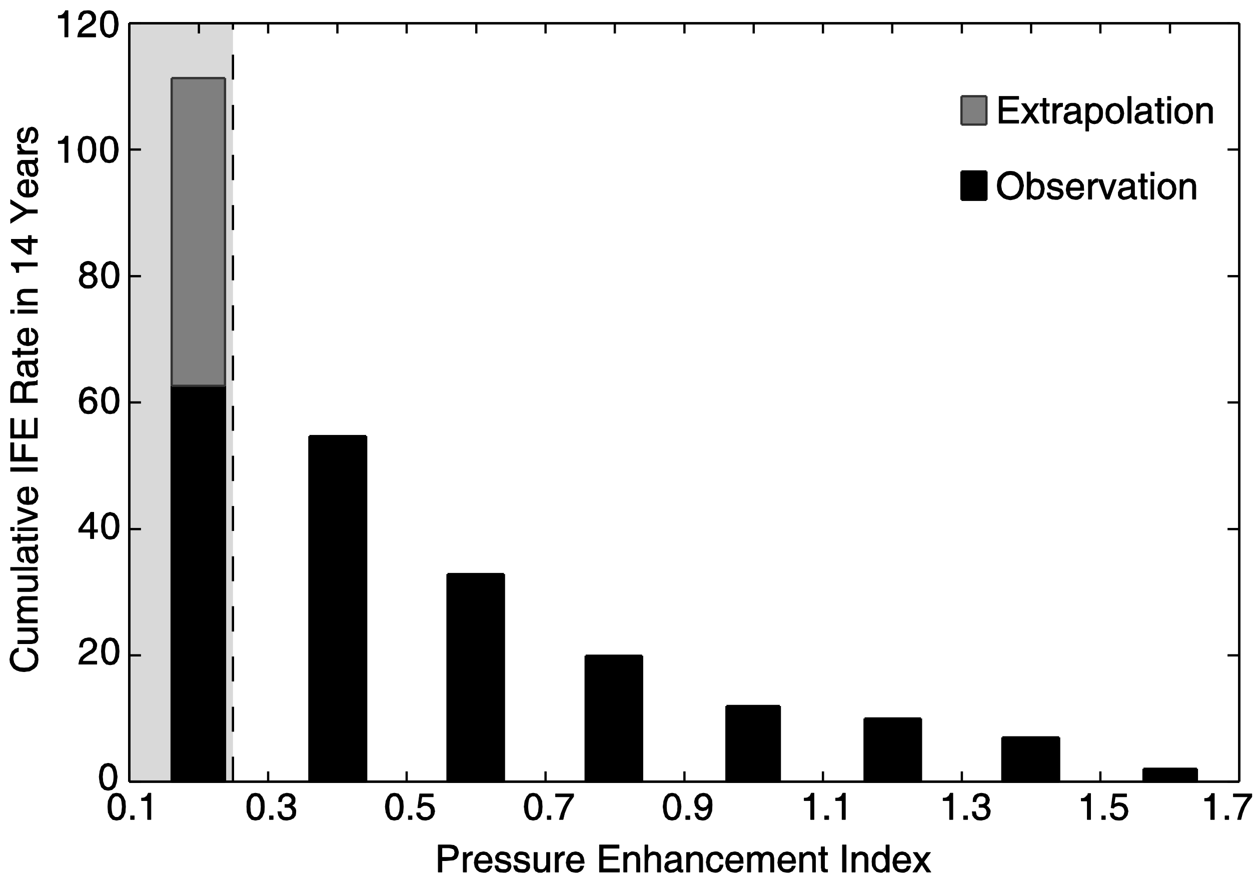

Figure 3.21 The cumulative IFE detection rate as a function of the pressure enhancement index. The dashed line corresponds to $\Delta P = 0.25$. The shaded area indicates the range of pressure enhancement index which is influenced by the selection criteria. If we extrapolate the bins outside the shaded area, we get the grey bin as shown.

Since both the scale and strength of IFEs vary a lot, are the two properties of IFEs associated with each other? To answer this question, we plot the normalized cumulative IFE rate as a function of the pressure enhancement index in different radial scale groups as shown in Figure 3.22. Here all the bins in the first index range are the extrapolated results as the one in Figure 3.21. The black bins are results of all IFEs regardless of sizes, the darker grey ones are results of the IFEs with radial scale lengths smaller than $10^6 km$ and the lighter grey ones are results of IFEs with radial scale lengths larger than $10^6 km$. To make a better comparison, each bin has been normalized so that the height of the first bin equals unity for each group. From the distributions, we can see that the scales of IFEs have no constrains on the strength of the IFEs. In another words, all the IFEs are self-similar.

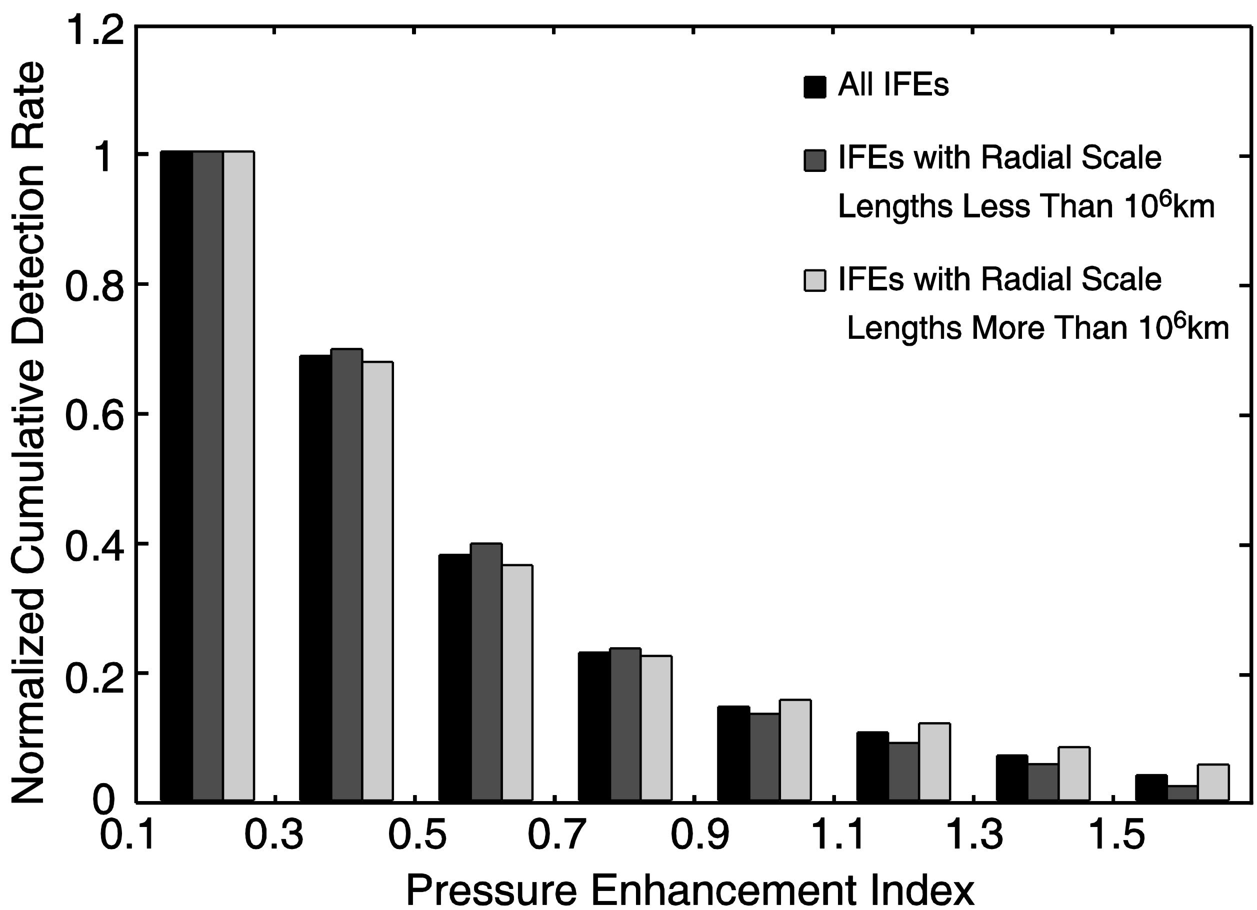

Figure 3.22 The normalized cumulative detection rates as a function of the pressure enhancement index in different radial scale groups. The black bins are for all the observed IFEs, the darker grey ones are for the IFEs with radial scale length less than $10^6 km$ and the lighter grey ones are for the IFEs with radial scale length larger than $10^6 km$. To make better comparison, all the bin heights have been normalized by the heights of the first bins, which contain all the observations of their groups. This figure shows that the pressure enhancement index distributions are independent of IFE sizes.

3.2.4 Plasma Profiles during IFEs: Superposed Epoch Study

Although no significant plasma signature is shown in most of the case studies, it is worth to check the statistical plasma properties. This time we will employ superposed epoch analysis as performed by Jones *et al*. [2003a]. To do that, we define time zero when the magnetic-field strength reaches its maximum. This time zero separates the IFE into the leading increase and trailing decrease parts. For each part, in order to superpose the data, we divide the time series into 150 points uniformly and interpolate the data. In performing this interpolation, the temporal interval between two successive points on the leading side may be different from the separation on the trailing side for the same IFE. The same interpolation is performed outside the IFEs, with 75 points downstream of the leading increase part (downstream for short) and 75 points upstream of the trailing decrease part (upstream for short). We first test our superposed analysis technique on the IFEs observed by *Ulysses*. Among the total 65 IFEs detected, we have plasma data available for 34 IFEs and their superposed results are shown in Figure 3.23. In Figure 3.23, from top to bottom we show the normalized profiles of magnetic-field strength, solar-wind proton number density, solar-wind velocity in radial direction, plasma beta, thermal pressure and total pressure, respectively. Here all the properties are normalized by their corresponding average values during the whole interval. The vertical lines mark the IFE boundaries. In all the panels, the light grey indicates the standard deviation and the solid black line is the average. Comparing to Figure 8 in Jones *et al.*, [2008], we can see that in our results the solar-wind proton number density does not increase during the IFEs. This difference is due to our different IFE database. To see more details in the plasma statistic properties, we use the higher resolution data from ACE and *Wind*.

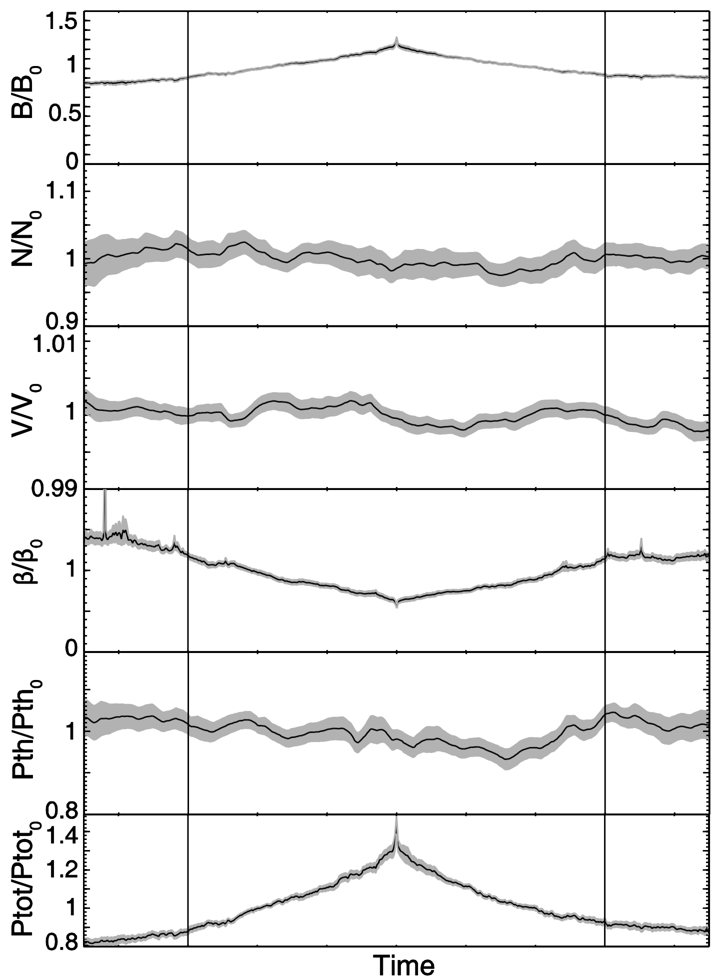

Figure 3.23 Superposed epoch analysis results of *Ulysses* observations. This plot is in the same format as the one in Figure 8 in Jones *et al*. [2003a]. All the observed results have been normalized to the

corresponding average value during the whole interval. In all panels, the solid black line is the average and the grey region indicates the standard deviation. Due to different IFE database, our results are different from Jones'. In our results, the proton number density does not increase during IFEs.

Figure 3.24 shows the ACE and *Wind* results. This time we show the magnetic-field strength, the proton number density, the proton temperature and the solar-wind velocity in radial direction from top to bottom. All the data have been normalized to the average ambient value. The vertical red lines indicate the centers of the IFEs. The horizontal red lines in the bottom panels show the average solar-wind velocity in the IFE downstream as references. From Figure 3.24, we can see that radial velocity decreases about 0.5% near the edges of the IFEs in the upstream region. This is the signature predicted by our IFE formation hypothesis. Another significant structure shown in both results is the density drop near the IFE centers, where the dust cloud might locate. The changes in the solar-wind proton temperature are complicated.

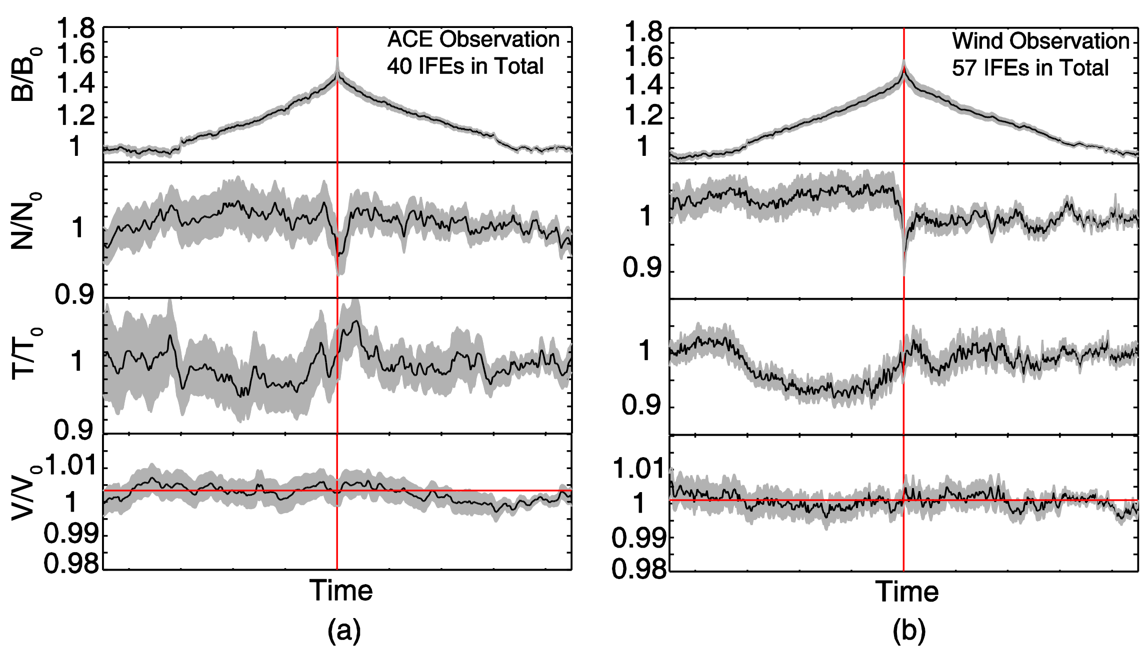

Figure 3.24 Superposed epoch analysis of IFEs detected by ACE (a) and *Wind* (b). From top to bottom we show the magnetic-field strength, the solar-wind proton number density, proton temperature and solar-wind velocity in radial direction. All the data have been normalized to the upstream value. The vertical lines indicate the centers of the IFEs. The horizontal red lines show the average velocity in the IFE downstream. In both observations, the radial velocity decreases a little near the edges of the IFEs in the upstream region and the proton density decreases near the centers of the IFEs.

If we separate the IFEs into small ones with radial scale lengths less than $10^6 km$ and large ones with radial scale lengths larger than $10^6 km$, as shown in Figure 3.25, we can see that the density and velocity decrease are more significant in large IFEs. These results are consistent with the second prediction based on our IFE formation hypothesis.

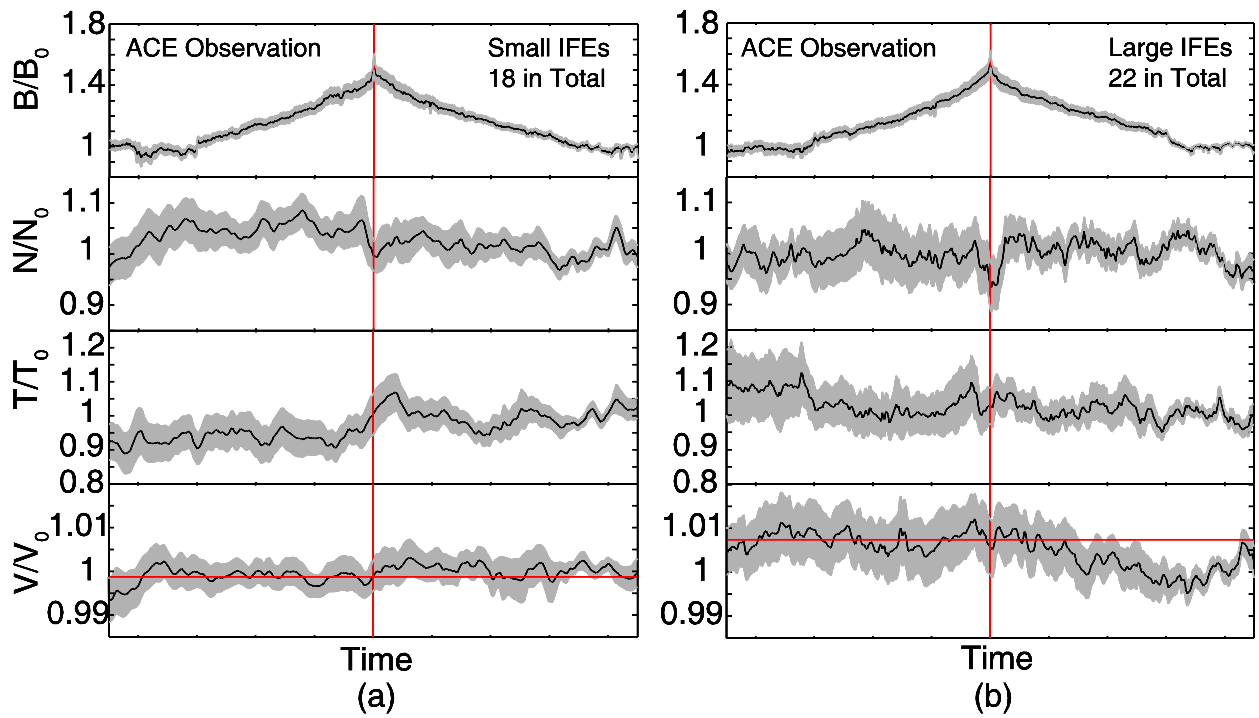

Figure 3.25 Superposed epoch analysis results of IFEs with radial scale length less than $10^6 km$ (a) and larger than $10^6 km$ (b). The format is the same as the one in Figure 3.24. The velocity decrease near the IFE upstream boundaries and the density decrease near the IFE centers are more significant in larger IFEs.

3.3 IFE Radius and Pressure Profile in the Cross-flow Direction

With single spacecraft measurements, the pressure profile and IFE scale can be obtained only in the radial direction. To reconstruct the IFE geometry, we need to turn to the multi-spacecraft simultaneous observations. But even five-spacecraft observations are not enough to completely reconstruct the IFE structure in the cross-flow direction. However, with several assumptions, the IFE cross-flow structure can be obtained statistically.

The first assumption is based on Figure 3.22, which implies that IFEs are self-similar disturbances just varying in scale-size but with the same pressure variations normalized to the ambient pressure. Thus the first assumption we employ is that the peak pressure enhancement is the same for all the IFEs. The observed variable pressure enhancements are due to the variable spacecraft impact parameters, *i.e.*, varying distances from the center of the structure. When the spacecraft passes close to the pressure enhancement peak, it will observe a large pressure enhancement and vice versa.

The second and the third assumptions are that the IFE cross section is a circle with its center at the location of the peak pressure and that the pressure profile decreases azimuthally symmetrically with the increasing spacecraft impact parameters. Thus the cumulative detection rate of a certain pressure index is proportional to the area enclosed by the index contour. For example, from the black bins in Figure 3.22, we know that the normalized cumulative detection rate of $\Delta P = 1.5$ is 0.04 while the rate of $\Delta P = 1.3$ is 0.07. Based on the assumptions outlined above, in the cross-flow plane, the pressure index contour of 1.3 encloses an area 1.75 times larger than the area enclosed by the contour of 1.5. Thus we can use the cumulative detection rates to calculate the cross-flow profile of ΔP. The results are shown in Figure 3.26, where the stars are based on the results in Figure 3.22 and the solid line is the best fit of a third-degree polynomial. We extrapolate the fitted results to zero pressure enhancements to get the boundaries of the IFE. The plot is symmetric because of our assumptions.

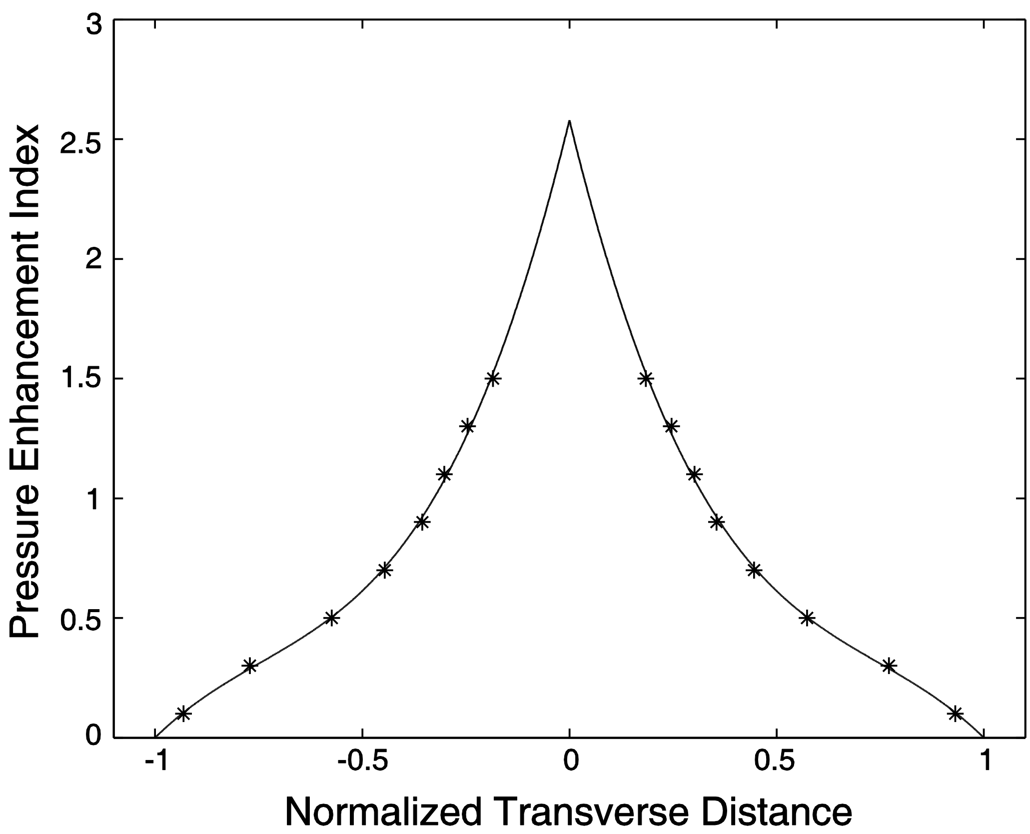

Figure 3.26 The cross-flow pressure profile of IFEs. The stars are based on the results in Figure 3.22. The black line is the fitted result with a third-degree polynomial. The edge of the IFE is obtained by extrapolation.

To determine the IFE center and estimate the IFE cross-flow radius, we need to solve three unknowns, two coordinates in transverse direction and one radius. Thus we can estimate the centers and cross-flow radii of all the IFEs detected by three or more spacecraft simultaneously. Here we show the March 2011 IFE as an example. For each spacecraft, with the knowledge of their observed pressure indexes ($\Delta P(ACE) = 1.65$; $\Delta P(ARTEMIS\_P1) = 1.05$; $\Delta P(ARTEMIS\_P2) = 0.75$; $\Delta P(Geotail) = 1.15$), the corresponding normalized transverse distances are obtained ($\rho(ACE) = 0.158R_{IFE}$; $\rho(ARTEMIS\_P1) = 0.311R_{IFE}$; $\rho(ARTEMIS\_P2) = 0.425R_{IFE}$; $\rho(Geotail) = 0.278R_{IFE}$). We assume that the IFE center was at (y, z) in the GSE Y-Z plane. Therefore we have three unknowns and four equations. In this case, the IFE center and radius are over-determined so we choose the best fitted results: IFE center is at $(-12.99, -8.58)R_E$ in GSE Y-Z plane and the IFE cross-flow radius is $41.57\ R_E$. *i.e.*, $2.65 \times 10^5\ km$. The spacecraft locations relative to the spacecraft is shown in Figure 3.27. The radial scale length of this IFE is $1.18 \times 10^6\ km$, which is 4.45 times the cross-flow radius.

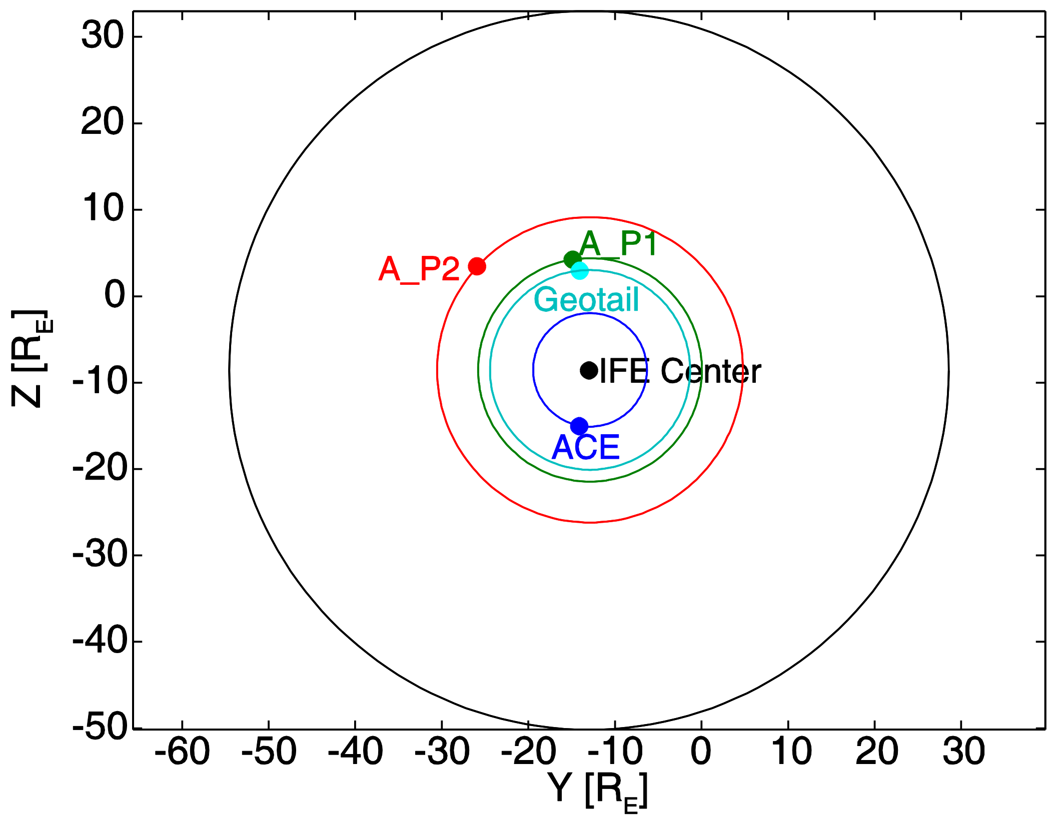

Figure 3.27 Map the normalized transverse distance to the actual distance based on the multi-spacecraft observations. For the March 2011 IFE, the cross-flow radius is found to be $2.65 \times 10^5 km$.

Such a technique is applied to this IFE but in the VB coordinate system. The same IFE radius is obtained and the location of the IFE center is shown in Figure 3.14, with the magnetic-field geometry. Another test is performed with the IFE detected on December 24, 2006 and the resultant center with the magnetic-field geometry is shown in Figure 3.17. In both cases, in the X-Y plane as shown in the upper panels, the estimated IFE centers are at the locations where the draped magnetic field reverses its direction in the flow direction. When estimating the IFE centers, the only information we used is the pressure enhancement index. The validity of such a technique is proven when the resultant IFE centers are in good agreements with the magnetic-field pattern.

Therefore a similar approach is applied to the other IFEs detected by three or more spacecraft, their cross-flow radius (ρ), radial scale (L) and ratio of the radial scale to the cross-flow scale (κ) are shown in Table 3.5. From the list we can see that the ratio of IFE radial scale to cross-flow scale is from 4.15 to 8.79 with an average of 5.60.

Date	$\rho\ [R_E]$	$L\ [R_E]$	κ	Mass [kg]
2006/358	37.58	155.96	4.15	$1.15 \times 10^8 kg$
2011/008	67.81	340.61	5.02	$8.80 \times 10^8 kg$
2011/124	30.52	268.40	8.79	$4.64 \times 10^7 kg$
2011/062	41.57	185.21	4.45	$1.5 \times 10^8 kg$

Table 3.5 Cross-flow radius (ρ) of IFEs detected by three and more spacecraft simultaneously. Also shown in this table are the IFE radial scale length (L), the radio of radial length to cross-flow radius (κ) and estimated mass (discussed in the next section).

3.4 Mass Contained in the IFEs

Since we have reconstructed the IFE geometry and pressure profile in the cross-flow direction, we can obtain the pressure gradient force $F = cr^2 P_{amb}$, where c is a constant determined by

$$c = \int_0^{2\pi} d\theta \int_0^1 \Delta P(r_N) r_N dr_N$$

and is 1.47. In the above integration ΔP is the pressure-enhancement index and r_N is the normalized distance from the center of the IFE.

For the actual case, take the March 2011 IFE as an example, we have determined that its cross-flow radius r is $2.65 \times 10^5\ km$ and the ambient total pressure P_{amb} is $8.59\ pPa$. So the pressure gradient force is

$$F_R = 1.47 r^2 P_{amb}.$$

The solar gravity exerted on the IFE is

$$F_g = \frac{G M_s M_{IFE}}{R^2}.$$

Here M_s is the mass of the Sun and R is the heliocentric distance, *i.e.*, $1AU$ in this case. For the nanoscale charged dust, the only force that can be comparable with the Lorentz force is the gravity. If we assume that there is no acceleration, solar gravity is balanced by the magnetic pressure gradient force. We equate the two forces here and find that the IFE mass is $1.5 \times 10^8\ kg$. A similar approach is applied to the IFEs listed in Table 3.5 and their corresponding masses are also listed there.

A mass of about $10^8\ kg$ is huge at first glance. However, considering the large volume occupied by the IFEs, the IFE mass density is reasonable. Take the IFE observed by five spacecraft as an example. Based on our hypothesis, the pileup of the magnetic field separates the IFEs into the solar-wind part and the dust cloud part. The dust cloud is $1.5 \times 10^8\ kg$ and we assume that it occupies one half of the IFE volume (a cylindrical volume with radius $2.65 \times 10^5\ km$ and length $1.18 \times 10^6\ km$). If the mass is distributed uniformly, the mass density would be $1.2 \times 10^{-18}\ kg/m^3$. If the mass is carried by dust particles with diameters of $10nm$ ($100nm$) and density of $3 \times 10^3 kg/m^3$, the number density would be $7.6 \times 10^2\ /m^3$ ($7.6 \times 10^{-1}\ /m^3$) and the inter-grain distance is $11cm$ ($1.1m$). Considering that they are immersed in the solar-wind plasma, the Debye length of the dust cloud and solar wind is about $10m$ at $1AU$. This is a $r_d \ll l < \lambda_D$ situation. Here r_d is the dust radius, l is the inter-grain distance of the dust particles and λ_D is the Debye length. Based on the definition given by Shukla *et al*, [2002], it is a dusty plasma, which is what we expect in the hypothesis.

To move $1.5 \times 10^8\ kg$ at $590km/s$ through the Sun's gravitational potential well at $1AU$, the solar-wind slowdown can be calculated by $\frac{GM_sM_{IFE}}{R^2} = m_i n_i V_{SW} \sigma_{IFE} \Delta V$. Here m_i is the proton mass, n_i is the solar-wind proton number density ($2/cc$), σ_{IFE} is the IFE cross section ($1.9 \times 10^{11} km^2$) and ΔV is the solar-wind slowdown. Solving for ΔV we find that the slowdown is $2.0km/s$, which is 0.3% of the ambient solar-wind speed. This slowdown is consistent with the result in our superposed epoch study in Section 3.2.4. Such an agreement proves the validity of our mass estimation method.

To the remaining IFEs which are observed by ACE only, the above mass calculation method cannot be applied directly since their cross-flow radii cannot be directly determined. However, for the four IFEs whose radii have been determined, their radial scales are 4.15 to 8.79 times the cross-flow scales. If we assume that this ratio can be applied to all the other IFEs, the masses contained in these IFEs can be estimated. We apply this method to the 63 IFEs with available plasma data detected by ACE and obtain their mass distribution. Then we assume that this mass distribution holds for all the IFEs and plot their annual rate (dark bins) as a function of mass as shown in Figure 3.25. Here the error bars come from the variation in the ratio of radial to cross-flow radius. We can see that the most frequently observed IFEs have mass of from 10^7 to $10^8 kg$. This distribution is also influenced by the selection criteria. The vertical dashed line shows the mass of the IFE ($2.4 \times 10^7\ kg$) with a 10-minute period of influence and average solar-wind parameters at $1AU$. The shaded region is the range in which we expect undercounting due to our selection criteria. If we fit the rates from $10^8\ kg$ to $10^{11}\ kg$, and extrapolate the results to estimate undercounting, we get the corrections as the hatched bins show. Also shown in this figure is the equivalent diameter of rock. Here we assume that the originals are spherical with density of $2.5 \times 10^3 kg/m^3$. Since even in catastrophic collisions, the released debris consists a significant amount of large fragments [Fujiwara *et al.*, 1977], the size of the rocks indicated in Figure 3.28 is the lower limit of the parent-body size. More details related to the collisions will be discussed in Chapter 4.

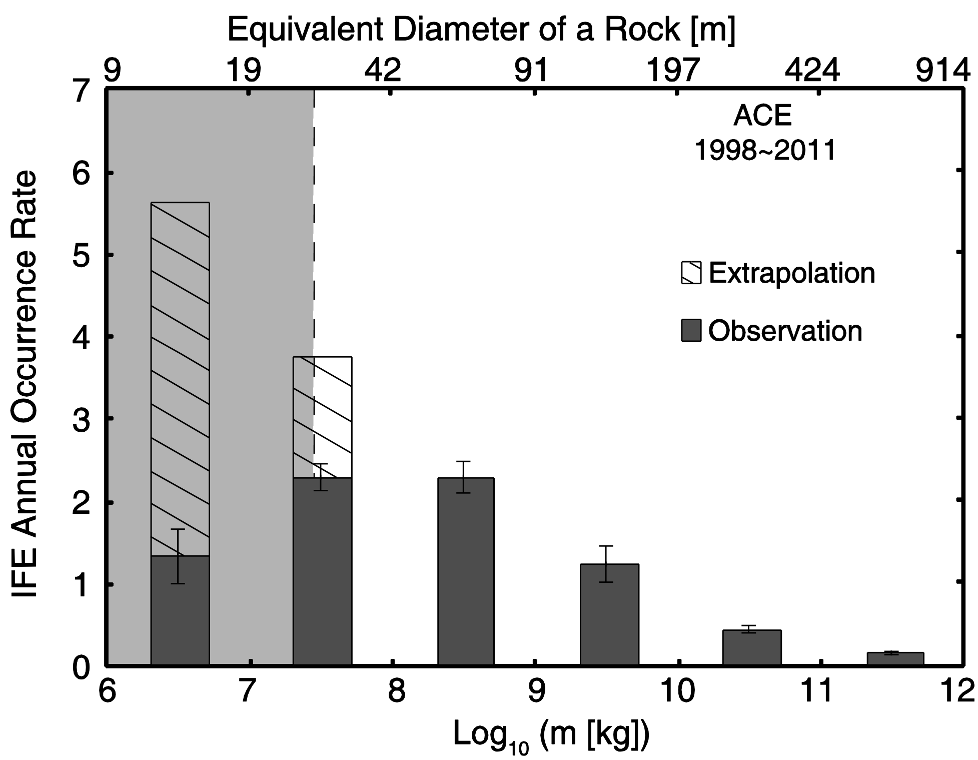

Figure 3.28 Mass distribution of IFEs detected by ACE, assuming the radial lengths of the IFEs are from 4.15 to 8.79 times the cross-flow radii. The most frequently observed IFE mass is from 10^7 to $10^8 kg$. However, the rates in the shaded area are influenced by the selection criteria. We expect the IFE rate to decrease monotonically with the increasing mass. Therefore we extrapolate the results of the last four bins to the first two as shown in hatched bins to estimate the undercounting at these sizes.

We apply the scale ratio to the other IFEs detected by *Wind*, STEREO A and STEREO B and obtain their mass distributions. Then we assign different weights, according to the observation time, to different database and combine their distributions in Figure 3.29. The standard deviations of the mean are also calculated and are shown in Figure 3.29 as the error bars. We can see that the IFEs detected by all the spacecraft near $1AU$ are located in the same mass range as the ones detected by ACE. And most frequently recorded IFEs located in the mass range between 10^7 and $10^8 kg$.

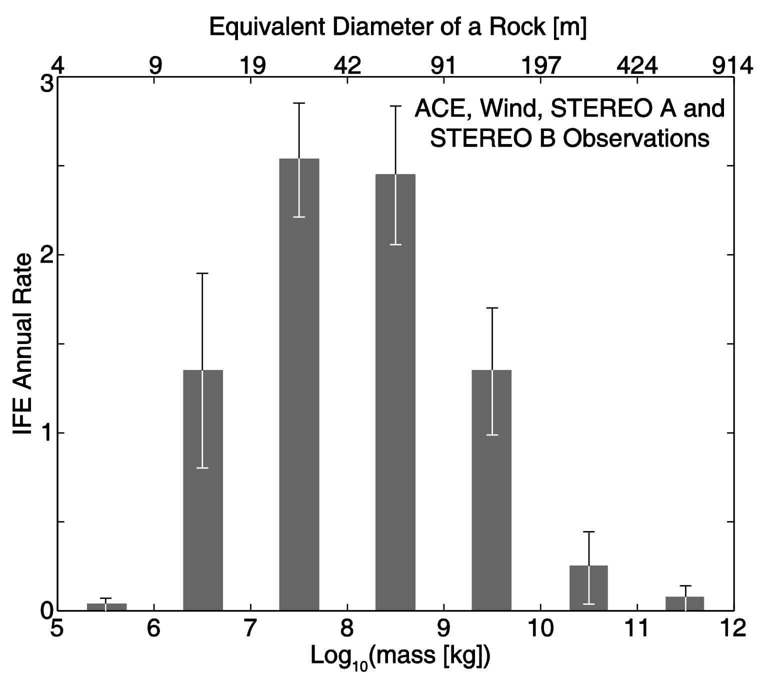

Figure 3.29 IFE mass distribution based on observations from ACE, *Wind*, STEREO A and STEREO B. We only show the recorded IFEs here without estimating the undercounted ones. We assume that the ratio of radial length to cross-flow radius is 5.60 times for all the IFEs and assign different weights to different databases according to the observation time of the spacecraft. From the distributions, most recorded IFEs near $1AU$ locate in the mass range between 10^7 and $10^8 kg$.

3.5 Summary

In this chapter, we study the IFE properties based on observations. We find that: (1) IFEs are generally rare phenomena; (2) the annual rate increases slowly with heliocentric distance inside $1AU$, decreases sharply with heliocentric distance outside $2AU$ and is lowest near ecliptic plane; (3) IFEs cluster in space as well as in time.

The magnetic-field draping feature in the upstream, which is the first prediction made in Chapter 1, is observed in multi-spacecraft simultaneous observations. With the available plasma data we are able to find that some IFEs show possible velocity deflection signatures at the boundaries separating the solar wind and the dust clouds. The superposed epoch study shows that the solar wind slows down in the upstream and there are plasma depletion regions near the solar-wind-dust-cloud boundaries. Both the solar-wind slowdown feature and density drop feature are more significant in larger IFEs. Such plasma features test our second prediction.

From ACE observations, we find that the pressure enhancement index distribution is independent of the IFE radial scale, implying that IFEs are self-similar structures. Based on the multi-spacecraft simultaneous observations, we reconstruct the IFE geometry and pressure profile in the cross-flow direction. We then balance the gravity with pressure gradient force and estimate the IFE masses. We find that the most frequently observed IFE mass is from 10^7 to $10^8\ kg$. This estimated mass gives a solar-wind slowdown which is consistent with the result in superposed epoch study.

Chapter 4

IFE Rate vs. Collision Rate

Our hypothesis is that IFEs result from interactions between solar wind and dust clouds released in interplanetary collisions. Thus a good test for this hypothesis would be comparing the expected collision rate with the IFE rate. Except for the flux model of interplanetary objects, our collision rate estimation method is based on the one developed by Grün *et al*. [1985].

4.1 Interplanetary Flux Model

As mentioned in Chapter 1, the impactors can disrupt targets much larger than themselves when the colliding velocity is tens of kilometers per second. Thus the mass range of the interplanetary objects in we are interested should be large. Here we modify the influx model given by Ceplecha [1992] to obtain our interplanetary flux model.

Figure 1 in Ceplecha [1992] shows the logarithm of the cumulative number of interplanetary bodies, with mass equal to or greater than the value indicated by the label, coming to the Earth. To produce such a single distribution curve, the author employed observations by different methods in different mass ranges. The resultant distribution is valid for a mass range covering 36 orders of magnitude. As this distribution gives the numbers of interplanetary bodies coming to the whole Earth surface, it has to be converted to a more general interplanetary flux model before it can be used in estimating the interplanetary collision rate. To perform such a conversion, we notice that from $10^{-20}kg$ to $10^{-9}kg$, Ceplecha adapted the lunar flux model discussed in Grün *et al*. [1985]. Thus we can compare the Earth influx model with the lunar flux model and get the ratio between the two. An interplanetary flux model covering a large mass range can be obtained by scaling the Earth influx model with that ratio. The resultant flux distribution is shown in Figure 4.1.

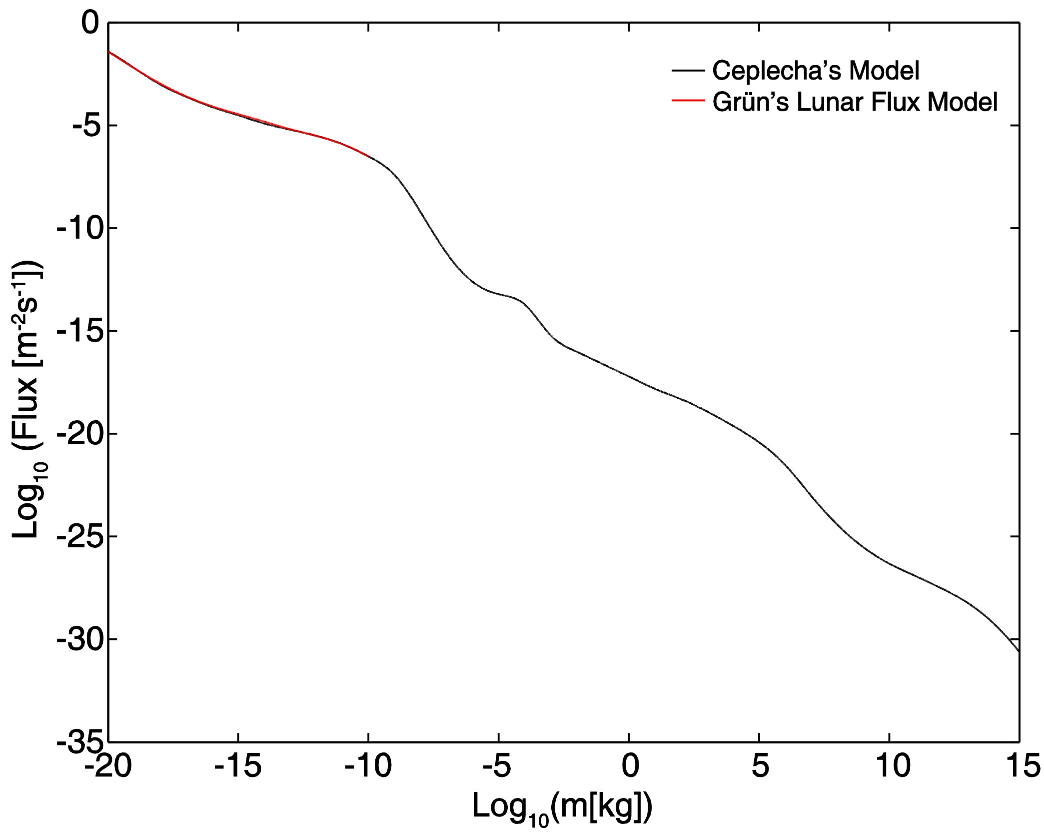

Figure 4.1 Scaling the Ceplecha's influx model (black line) to be comparable with Grün's lunar flux model (red line) in the small mass range. The scaled Ceplecha's model is used as the interplanetary flux model in our calculation.

The relation between the cumulative flux $F(m,r)$ and the cumulative spatial density $N(m,r)$ is given by

$$F(m,r) = \frac{v(r)}{k} N(m,r)$$

where r specifies the radial distance from the Sun, $v(r)$ is the average impact velocity and $k = 4$ in the case of an isotropic flux. For $v(r)$, the relationship is given by

$$v(r) = v_0 \left(\frac{r}{r_0}\right)^{0.5}$$

with $v_0 = 20 km/s$ and $r_0 = 1AU$. The differential spatial number density at $1AU$ is

$$\frac{dN(m,r_0)}{d(\log m)} = \frac{dF(m,r_0)}{d(\log m)} \frac{k}{v(r_0)}.$$

This distribution is shown in Figure 4.2. The number density generally decreases as the mass increases. Inside $1AU$, we assume that the number density of the interplanetary bodies goes as $\left(\frac{r}{r_0}\right)^{-1.5}$ [Leinert *et al*., 1978].

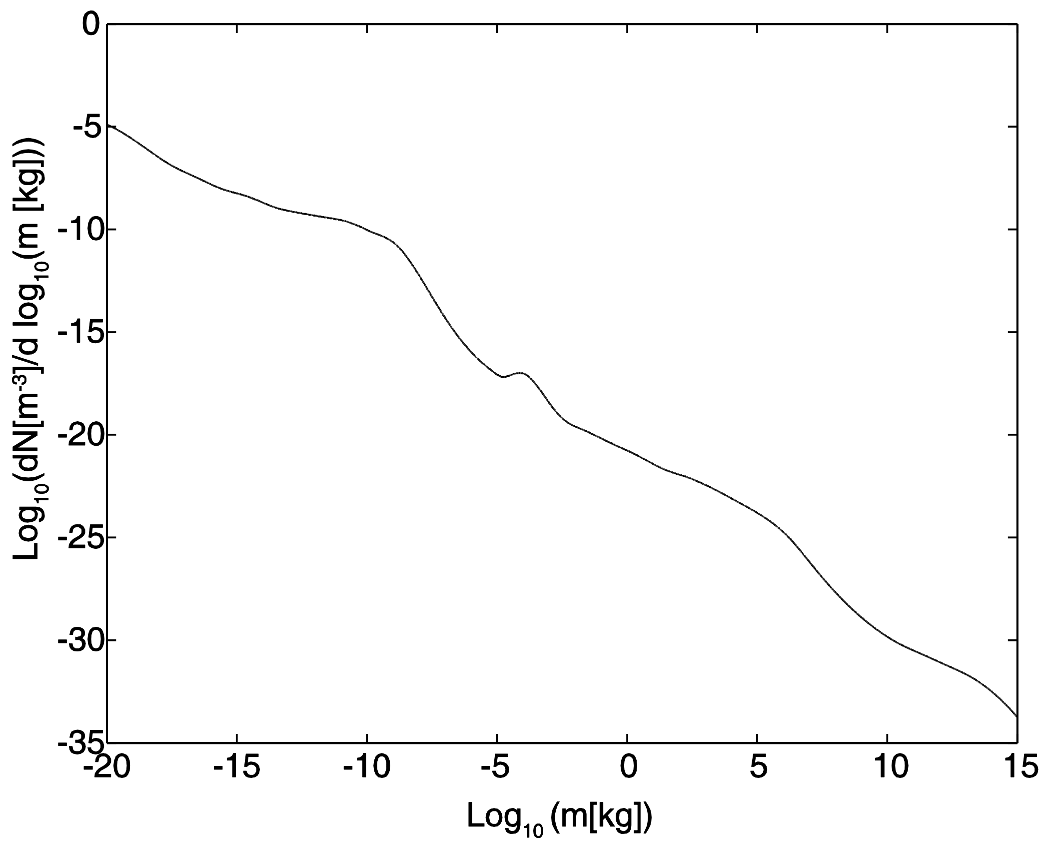

Figure 4.2 Differential spatial number density of interplanetary objects at $1AU$.

4.2 Collision Model

4.2.1 Catastrophic Collisions

A catastrophic collision is defined in the situation when a target (m_1) is completely destroyed into fine fragments. This requires that the impactor (m_2) satisfies

$$m_2 \geq \frac{m_1}{\mathrm{T}} \qquad (4.1)$$

where T is a function of the colliding speed and the material properties of the target and the impactor. As in Grün's collision model, we use

$$\mathrm{T}(r) = \mathrm{T}_0 \left(\frac{r}{r_0}\right)^{-1}$$

where

$$\mathrm{T}_0 = 9.76 \times 10^2 S_c^{-0.45} \left(\frac{m_1}{\rho_1}\right)^{0.075} {v_0}^2$$

For a crystalline rock target, $S_c = 3kbar$ and $\rho_1 = 2.5 \times 10^3 kg$. Figure 4.3 shows estimated T as a function of the target mass at $1AU$. We can see that when the collisional velocity is $20km/s$, T is generally larger than 10^4 and can reach 10^6 when the mass of the target is larger than $5.13 \times 10^5 kg$. Since the small interplanetary objects are quite numerous as shown in Figure 4.2, the collision rate is higher than one might expect.

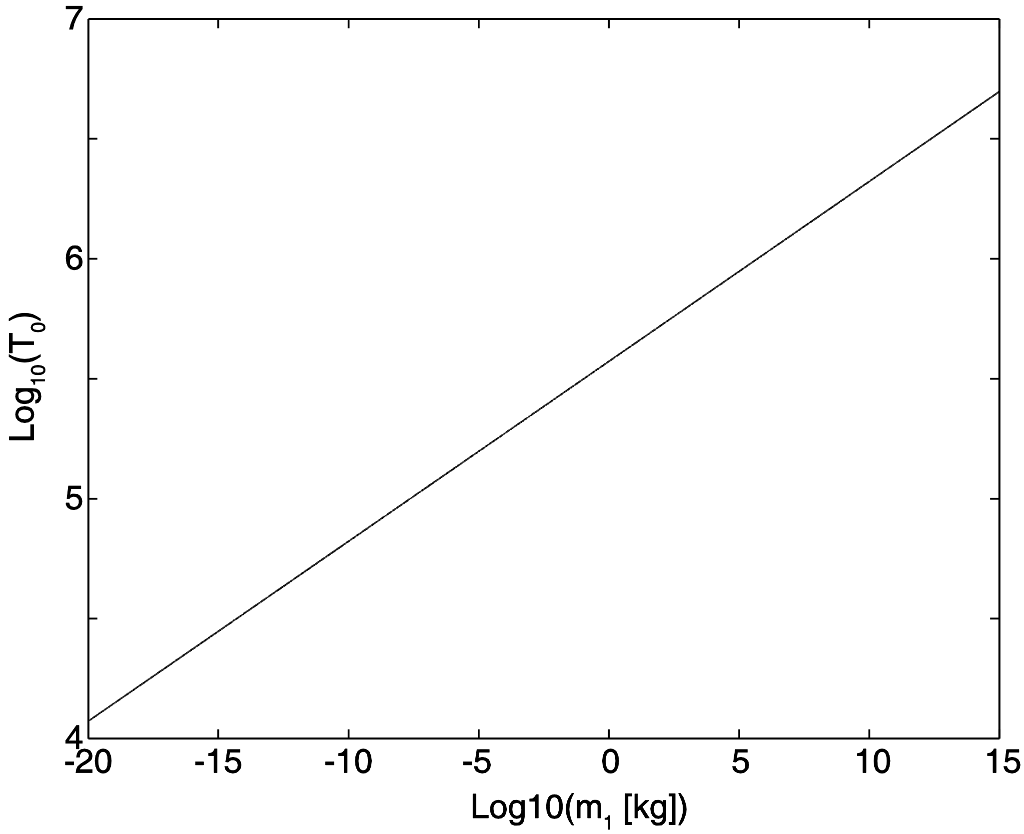

Figure 4.3 The mass ratio between the target and the smallest impactor which can destroy the target catastrophically. Here the colliding velocity is assumed to be $20km/s$, which is the average impact velocity at $1AU$. The ratio, as shown, is generally larger than 10^4 and can be larger than 10^6 when the target is massive enough.

4.2.2 Collision Rate Calculation Model

The collisional cross section can be expressed as

$$\sigma(m_1, m_2) = \pi \left(\frac{3}{4\pi\rho}\right)^{\frac{2}{3}} \left(m_1^{\frac{1}{3}} + m_2^{\frac{1}{3}}\right)^2$$

and the rate of catastrophic collisions of a target (m_1) by impactors with mass m_2 in the range $m_1/\mathrm{T} \le m_2 < M_\infty$ is given by

$$-\int_{m_1/\mathrm{T}}^{M_\infty} \sigma(m_1, m_2) k \frac{dF(m_2, r)}{d(\log m_2)} d(\log m_2) \qquad (4.2).$$

In a unit volume, the collision rate between targets (m_1) and impactors (m_2) is thus

$$\frac{dN(m_1, r)}{d(\log m_1)} \int_{m_1/\mathrm{T}}^{M_\infty} \sigma(m_1, m_2) k \frac{dF(m_2, r)}{d(\log m_2)} d(\log m_2).$$

Here M_∞ is set to be $10^{15} kg$ and the negative sign in (4.2) is due to the definition of cumulative flux.

4.2.3 Debris Distribution Model

The mass of the colliding objects is not lost from the system but reappears in the distribution of the fragments. Based on the experiments, the mass distribution of the fragments can be approximated by a power law [Fujiwara *et al*., 1977]

$$\frac{dG(m, m_1, m_2)}{d(\log m)} = c_1 m^{-\eta}.$$

Here $\eta = 0.83$ and c_1 can be calculated from the conservation of mass

$$\int_0^{m_L} m \frac{dG(m, m_1, m_2)}{d(\log m)} d(\log m) = m_1.$$

And the mass of the largest fragment m_L is found to be

$$\frac{m_L}{m_1} \approx 9.26 \times 10^{-8} \left(\frac{m_2}{m_1}\right)^{-1.24} \cdot \left(\frac{r}{r_0}\right)^{1.24}.$$

Based on our hypothesis, we are interested in the mass carried by nanoscale particles. If we assume that the maximum mass of the dust particle is m', the total mass of the dust cloud is

$$\int_0^{m'} m \frac{dG(m, m_1, m_2)}{d(\log m)} d(\log m).$$

We insert the numbers and get the expression of the mass of the dust cloud

$$m_d = 1.96 \times 10^3 m'^{0.17} m_1^{0.6192} m_2^{0.2108} \left(\frac{r}{r_0}\right)^{-0.2108}.$$

Figure 4.4 shows the ratio of debris mass (carried by dust with diameters of up to $500nm$) to the target mass at $1AU$. Here we only consider the collisions that can just destroy the targets disruptively, thus the impactors are the smallest ones that satisfy equation (4.1). From Figure 4.4 we can see that the debris released by smaller targets is generally in smaller sizes.

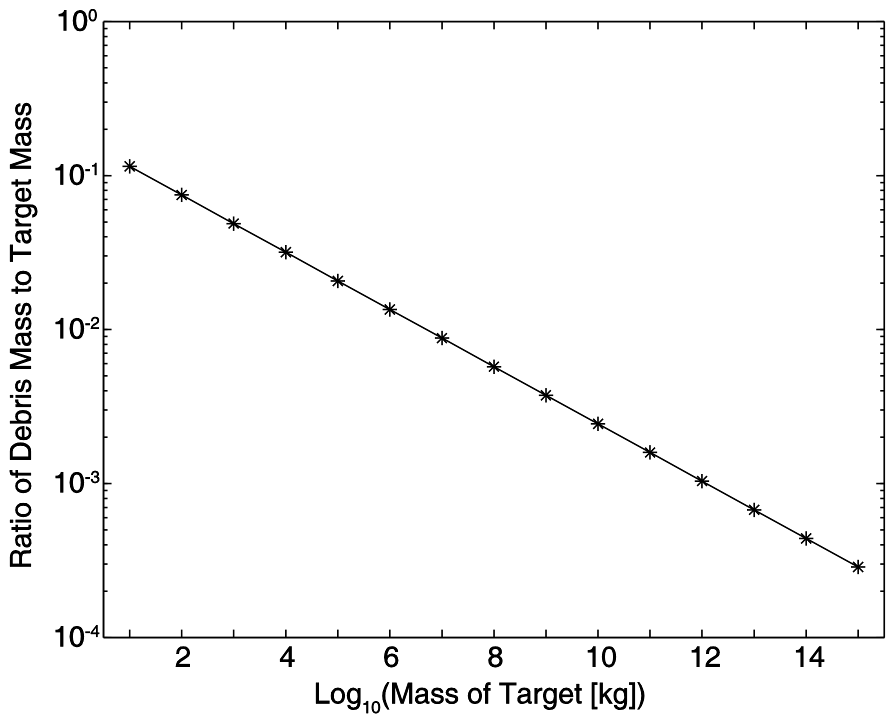

Figure 4.4 Ratio of debris mass (carried by dust with diameters of up to $500nm$) to the mass of target as a function of the target mass. In this calculation, we consider the collisions that can just destroy the targets disruptively at $1AU$. The debris released by smaller targets is generally in smaller size.

Now we know the mass of nanoscale debris released by the target m_1. In the collisions, the impactors m_2 can also be catastrophically destroyed when m_1 satisfies

$$m_1 \geq \frac{m_2}{\mathrm{T}}.$$

Therefore in our debris distribution model, we will consider the total mass of the nanoscale debris.

With the above knowledge we can estimate the collision rate as a function of the mass carried by nanoscale particles. Figure 4.5 shows the result at $1AU$. The maximum size of the debris is set to be $500nm$. Since we are interested in collisions that can produce huge mass, the horizontal axis starts from $10^3 kg$. Figure 4.5 shows that the collision rate decreases when the mass of the debris increases, which is expected.

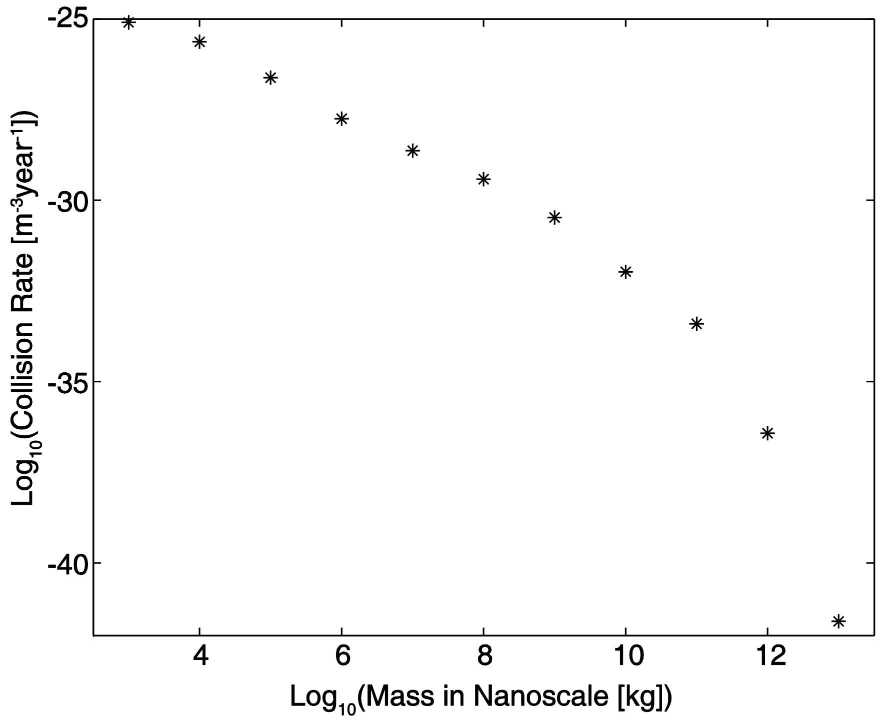

Figure 4.5 Collision rate as a function of mass carried by nanoscale particles at $1AU$. The collision rate decreases as the mass of debris increases. Here the maximum size of the debris is $500nm$.

4.3 Rate Comparison

4.3.1 Detectable Volume Model

Since the IFEs, after they are formed and before they dissipate, are carried outward by the solar wind and are expected to be detected by the spacecraft which they pass by, the counterpart of the IFE annual rate is the cumulative collision rate in a certain detectable volume. Now we know how to calculate the collision rate and the debris distribution, the remaining question is how large our detectable volume is.

We know that the IFEs can travel radially outward once they are formed and we can derive the cross-radius of IFEs with the knowledge of their mass and average solar-wind condition, but we do not have any firm observations showing the lifetime or the evolution of IFEs. Thus we make the simplest assumption that the detectable volume starts from $0.2AU$, inside which nanoscale dust particles will be lost due to evaporation [Czechowski and Mann, 2010, 2011].

The shape of the detectable volume is determined by the radial variation of the IFE cross section. If we assume the IFE mass does not change during its anti-sunward travel, the IFE cross section is given by

$$\frac{A}{A_0} = \frac{\left(\frac{B_0^2}{2\mu_0} + N_0 k T_0\right) r_0^2}{\left(\frac{B^2}{2\mu_0} + NkT\right) r^2}.$$

Here A is the cross section, r is the heliocentric distance, N is the solar-wind proton number density, T is the sum of proton and electron temperatures and the symbols with subscript zero (except μ_0) are the values at $1AU$. Using the radial variation model of the solar-wind parameter in Köhnlein [1996] (Appendix III), the radial variation of the normalized cross section is shown in Figure 4.6. We can see that as the IFEs expand slowly as they move radially outward. Thus the detectable volume is a truncated cone starting from $0.2AU$.

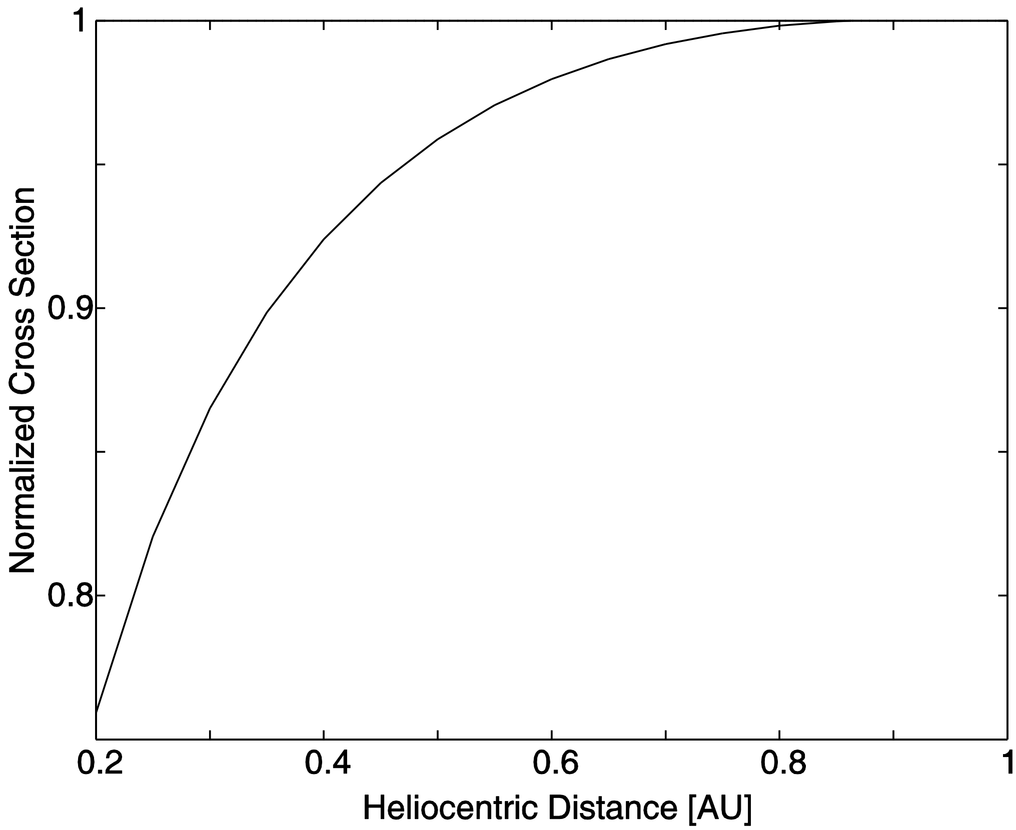

Figure 4.6 The heliocentric radial variation of the IFE cross-flow section normalized to the one at $1AU$. Here we assume that the mass of the IFEs does not change as they travel anti-sunward. Thus to balance the solar gravity exerting on the IFEs, the IFE cross-flow section will change due to the change in the solar-wind parameters. In our model, IFEs expand as they travel outward. Therefore the detectable volume is a truncated cone.

4.3.2 IFE Rate vs. Collision Rate at $1AU$

The detectable collision rate is the integrated collision rate obtained in Section 4.2.3 in the detectable volume. The results are shown in Figure 4.7. During the calculation, we find that the collision rate is very sensitive to the upper limit of the dust size: a little justification in the upper limit can change the collision rate in orders of magnitude. Therefore in Figure 4.7 we alter the upper limit and compare the resultant collision rate with the observed IFE rate. In this plot, we consider three upper limits of dust size, *i.e.*, $100nm$, $150nm$ and $200nm$ as the green, red and blue line shows, respectively. The IFE rate is the average in Figure 3.29. We compare the rates in the mass range where the IFE rate is most confident (the estimated errors are small in Figure 3.29). Being different from the results in Figure 4.6, the collision rates here do not decrease monotonically as the debris mass increases. This is because the detectable volume is mass dependent. From Figure 4.7, we can see that the differences between the IFE rate and the collision rates corresponding to an upper limit dust size of $150nm$ are always within one magnitude. Considering all the assumptions we made in estimating the collision rate as well as in estimating the IFE mass, this result is positive.

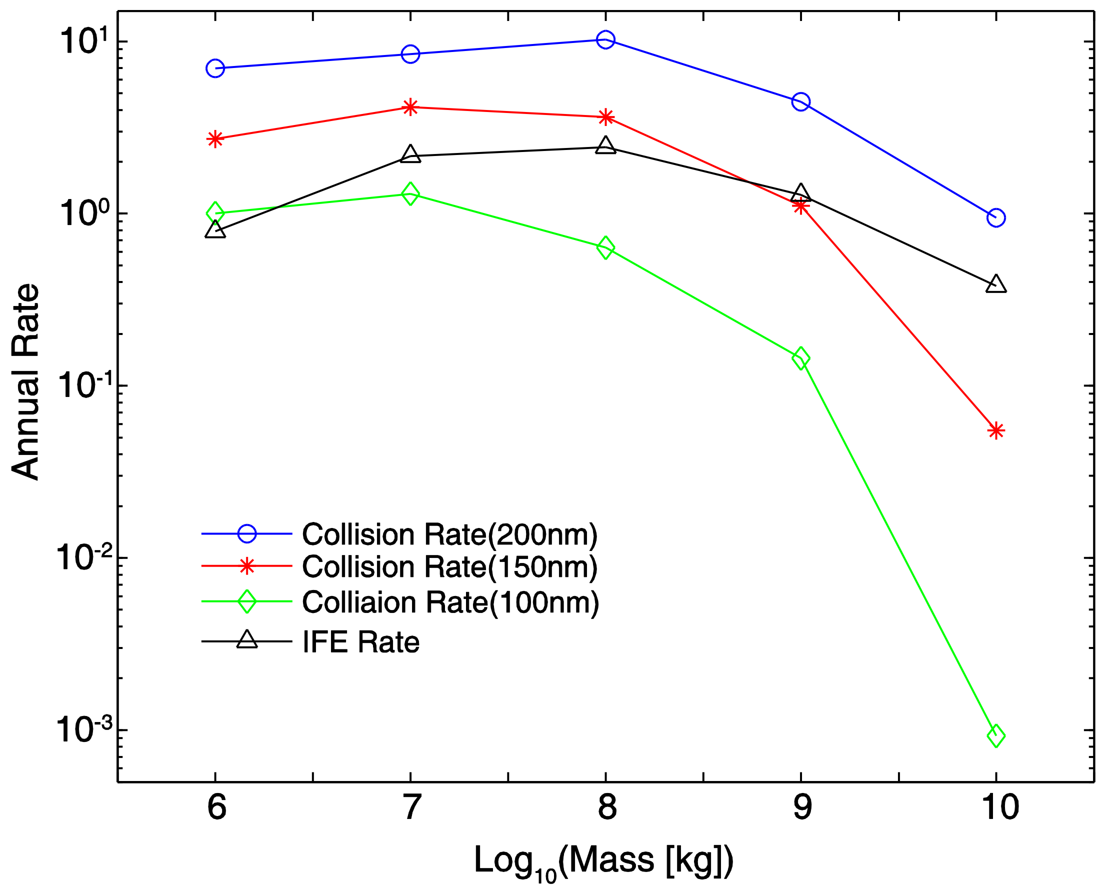

Figure 4.7 A comparison between the estimated collision rates and the observed IFE rates as a function of the debris mass at $1AU$. Here we alter the upper limits of the debris size and show the results in different colors. The differences between the IFE rate and the collision rates corresponding to an upper limit dust size of $150nm$ are always within one magnitude. This result is positive since we made many assumptions in both the collision model and the IFE mass calculation.

4.3.3 IFE Rate vs. Collision Rate from 0.3 to $1AU$

We can also compare the radial variation of the collision rate with the IFE rate. The result is shown in Figure 4.8. Here we only integrate the rate of collisions which can release $10^6 kg$ or more in nanoscale debris and the upper limit of the debris size is set to be $150nm$. Both rates are in the same magnitude and they increase slowly when the heliocentric distance increases from 0.4 to $1AU$. We do not compare the rates beyond $1AU$ because we know that the IFE rate decreases sharply beyond $2AU$ from *Ulysses* observation.

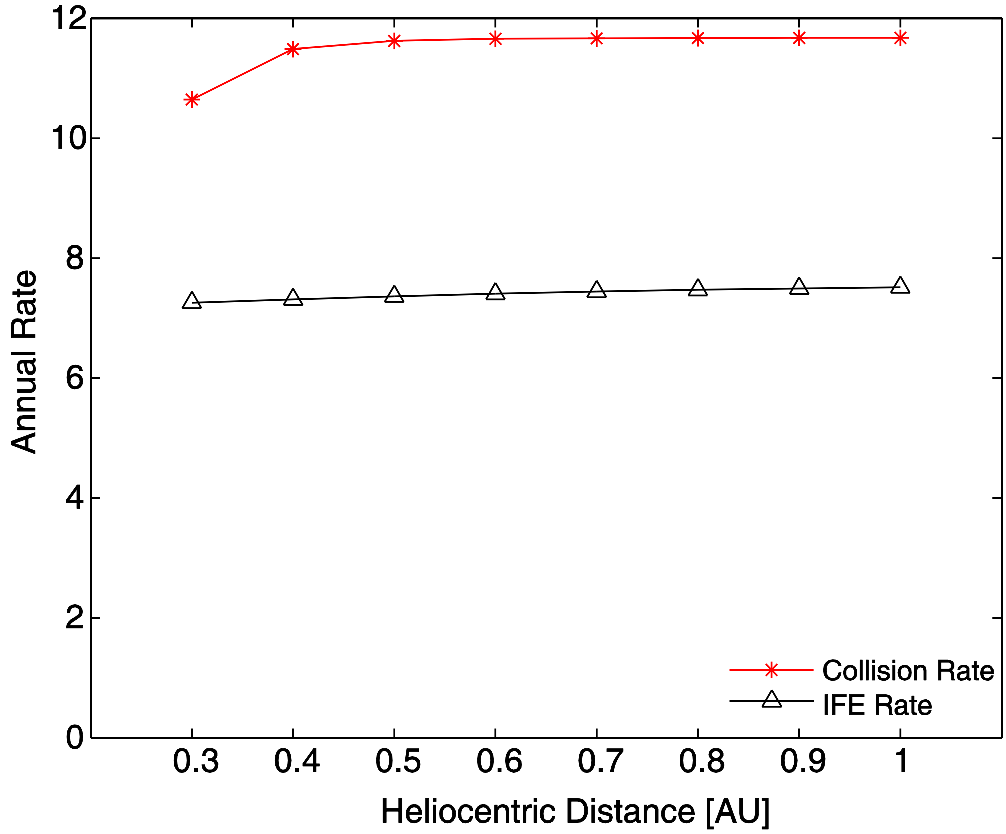

Figure 4.8 A comparison between estimated collision rate (red line) and best fit of observed IFE rate (black line) from 0.3 to $1AU$. We set the upper limit of the debris size to be $150nm$ when calculating the collision rate. Both rates are in the same magnitude and increase slowly as the heliocentric distance increases.

4.4 Summary

In this chapter, we modify the influx model of Ceplecha [1992] and use the collision model of Grün [*et al.*, 1985] to estimate the interplanetary collision rate. To compare with the IFE rate, we assume that the detectable volume of collisions is a truncated cone starting from $0.2AU$ and its cross section expands as the heliocentric distance increases. At $1AU$, we find that the collision rate is comparable with the observed IFE rate. This estimated collision rate also increases slowly as the heliocentric distance increases inside $1AU$, which is consistent with the IFE observations.

Our collision-rate-estimation model can be modified in many ways. One way is to include the lifetime of the IFEs, which will set a radial-distance-dependent inner boundary of the detectable volume. This effect can be very important outside $1AU$, since the *Ulysses* observation shows that IFE rate decreases as the heliocentric distance increases. To determine the lifetime of the IFEs, we need to have more multi-spacecraft simultaneous observations with large radial separations among spacecraft. Another modification can be made if we can have a non-isotropic interplanetary flux mode. This can help us to understand the latitudinal variation of the IFE occurrence. All these studies will leave in the future work.

Chapter 5

Responsible Interplanetary Objects

Since now all the three predictions made by our IFE formation hypothesis have been successfully tested, we now study the practical application of IFE observations: determining the spatial and temporal variation of small but potentially hazardous interplanetary objects. We will first reanalyze the association between Oljato and IFEs detected at $0.72AU$ and then look for similar IFE sources at $1AU$.

5.1 Association between $0.72AU$ IFEs and Co-orbiting Material of Oljato

5.1.1 Asteroid 2201 Oljato

In Figure 3.6, we show the IFE longitudinal distribution obtained by PVO. There the IFE occurrence clustered in the longitudinal ranges from $135°$ to $165°$ and from $195°$ to $225°$. This is consistent with the earlier study performed by Russell *et al.* [1984a]. And the co-orbiting material of asteroid 2201 Oljato was suggested to be responsible for many of the IFEs detected in those longitudinal ranges.

Oljato with a estimated diameter of 1.8 km, was originally discovered on December 12, 1947 by H.L. Giclas at the Lowell Observatory, Flagstaff. It is an unusual asteroid in the sense that its orbit parameters are associated with a meteor shower (Drummond 1982; Olsson-Steel 1988) and it occasionally has an unexpectedly high ultraviolet reflectance (McFadden *et al*., 1984). However, being different from a typical comet, Oljato has a higher radiometric albedo and an asteroid-like overall spectral reflectance (McFadden *et al*., 1993). It is now generally accepted that Oljato is a remnant of a comet. A later study in the motion of the asteroid reveals that the orbit of Oljato is perturbed by non-gravitational forces [Ziolkowski 1994], implying that there might be still residual outgassing processes. A spectroscopic search for gas produced by Oljato suggested an upper limit of production rate in water to be $1.5 kg/s$ [Chamberlin *et al*., 1996].

The orbital elements of Oljato are shown in Table 5.1. And the orbital projection in the ecliptic plane is shown in Figure 5.1. There we can see that Oljato crosses the Venus orbit and lies within it from HE longitude $126°$ to $220°$. This sector is shaded in grey in Figure 5.1 and is defined as the sensitive region. In this region, due to the Oljato's small inclination (0.88°) with respect to Venus' orbital plane, the transverse distance from Oljato's orbit to the Venus orbit plane is at most $1.45 \times 10^6 km$. This distance is shown in Figure 5.2. The sensitive region is again shaded in grey. Note the large difference in scales in the abscissa and ordinate. Here in Figure 5.2, we have converted the coordinate system so that the orbit of Venus lies in the X-Y plane with X pointing to the ascending node of Venus. The Sun is at the origin.

Orbital Element	Value
Eccentricity	0.7126
Semi-Major Axis [AU]	2.1721
Perihelion Distance [AU]	0.6243
Aphelion Distance [AU]	3.7198
Inclination [Deg]	2.5234

Period	1169.2435 Day (3.2 Earth Year or 5.2 Venus Year)

Table 5.1 Orbital Elements of asteroid 2201 Oljato at epoch 2014-05023 TDB (Barycentric Dynamical Time).

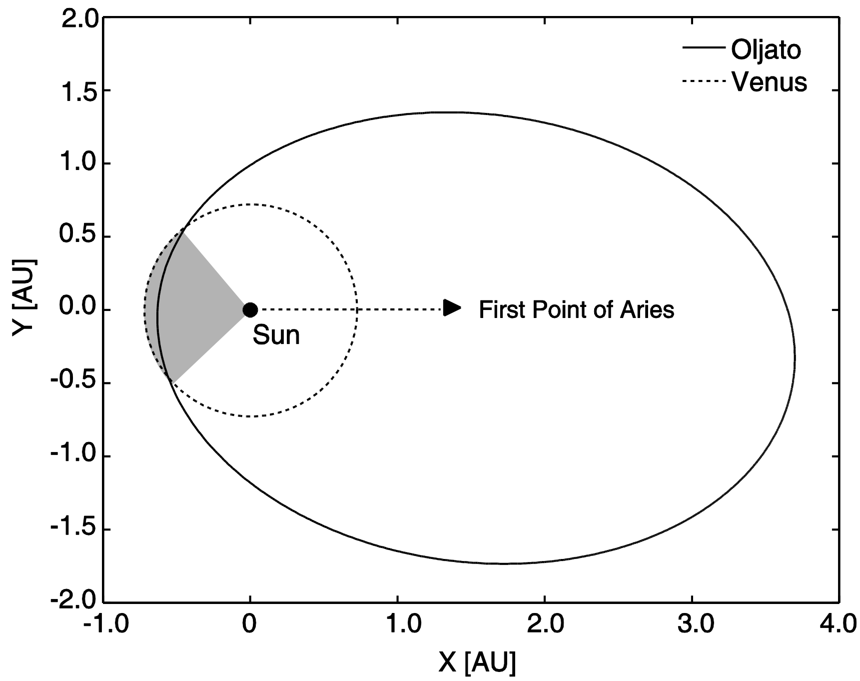

Figure 5.1 Orbital projections of Venus and Oljato in the ecliptic plane. Oljato's orbit lies inside the orbit of Venus from HE longitude 126° to 220° . This region is defined as the sensitive region and shaded in grey.

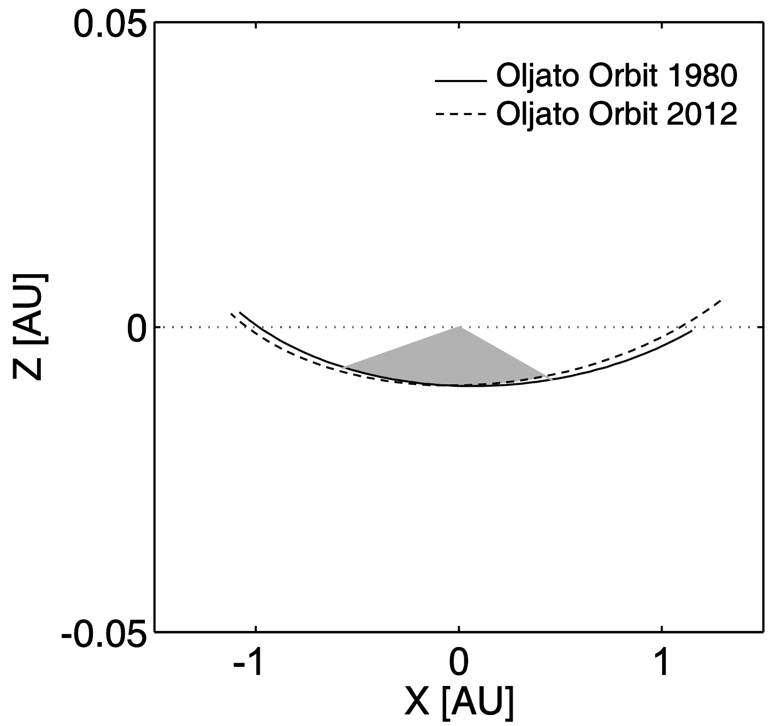

Figure 5.2 Orbits of Oljato in 1980 and 2012 in the plane perpendicular to the orbital plane of Venus (dotted line). The sensitive region is again shaded in grey. Although three decades passed, the orbital changes in this region are small. Note the large difference in scales in the abscissa and ordinate.

We define the phase difference between Oljato and Venus as their longitudinal difference at the same universal time and set the phase difference to be positive when Oljato leads Venus. Such a phase difference from 1976 to 2012 is shown in Figure 5.3. The solid circles show the phase difference when Oljato passes the longitude 173°, which is the center of the sensitive region. Also shown in this figure is the observation coverage of PVO and VEX. Based on this figure, we can see that after more than three decades, the orbit geometries of Oljato and Venus in 2012 are similar to the ones in the earlier encounter in 1980. Therefore us can compare the PVO and VEX observations directly.

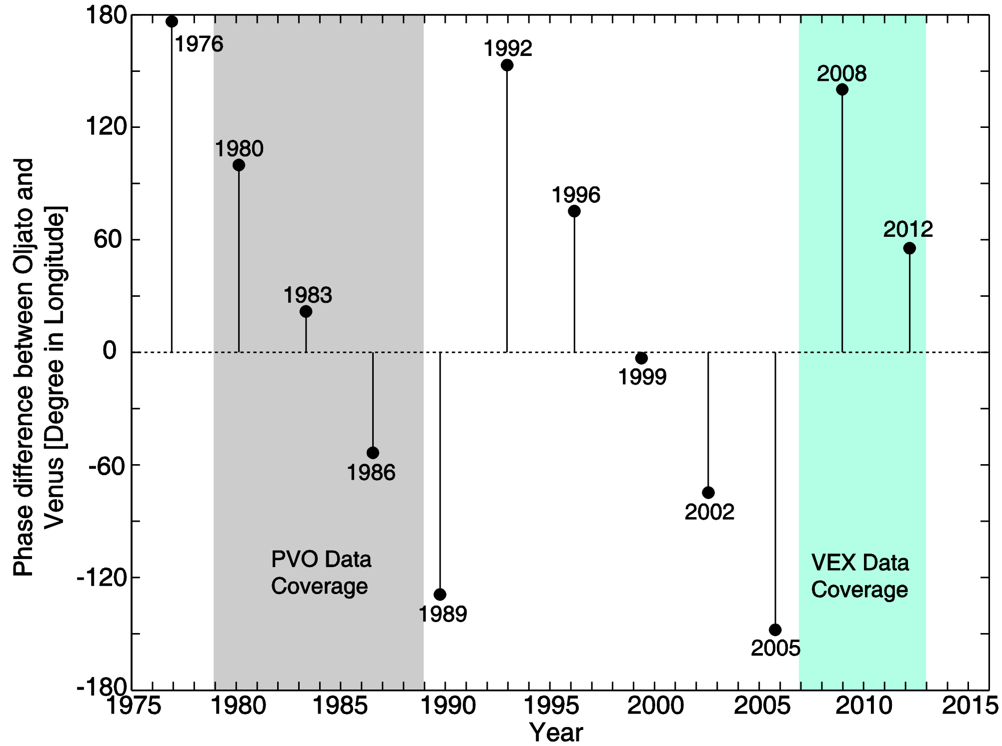

Figure 5.3 Phase difference between Oljato and Venus from 1976 to 2012 and the data coverage of PVO and VEX observations. The phase difference in 2012 is close to that in 1980.

5.1.2 Oljato Associated IFEs Detected by PVO

Since the orbit of Oljato shown in Figure 5.2 does not change significantly in the sensitive region from 1980 to 2012 and due to Oljato's small inclination with respect to Venusian orbital plane the transverse separation between Oljato's orbit and Venusian orbital plane is small comparing to the IFE scales, we consider all the IFEs detected inside the sensitive region to be potentially associated with Oljato. This is different from the earlier studies, in which only IFEs close to the "conjunction points" are considered to be Oljato associated [Russell *et al.*, 1984b; Russell 1987]. We also notice that in the earlier studies, IFEs were found to occur when Oljato was not close to the sun-spacecraft line [Russell 1987], indicating that the source of IFEs is co-orbiting material of Oljato and not Oljato itself. Thus in this study, we do not need to constrain the Oljato associated IFEs to be the ones detected in the years when Oljato itself entered the sensitive region (referred to as Oljato years). Therefore, all the IFEs detected in the sensitive region from 1978 to 1988 are considered to be potentially Oljato associated. This selection criterion is supported by Figure 5.4. Here on the left, we show one IFE detected in 1986, which is an Oljato year, and another IFE detected in 1982, which is a non-Oljato year. In the magnetic-field profiles, we use the maximum variance coordinate system and show the maximum variance component of the magnetic field as well as the strength of the magnetic field. We can see that despite the fact that the two IFEs differ in strength and duration, they have some similarities: a small current sheet leading the major central current sheet and a small “crater” close to the maximum in the magnetic-field strength. On the right we show the IFE and Oljato locations when the IFEs were detected. We can see that after four years, similar IFEs were detected at almost the same locations even though the phase difference between the IFEs and Oljato are different.

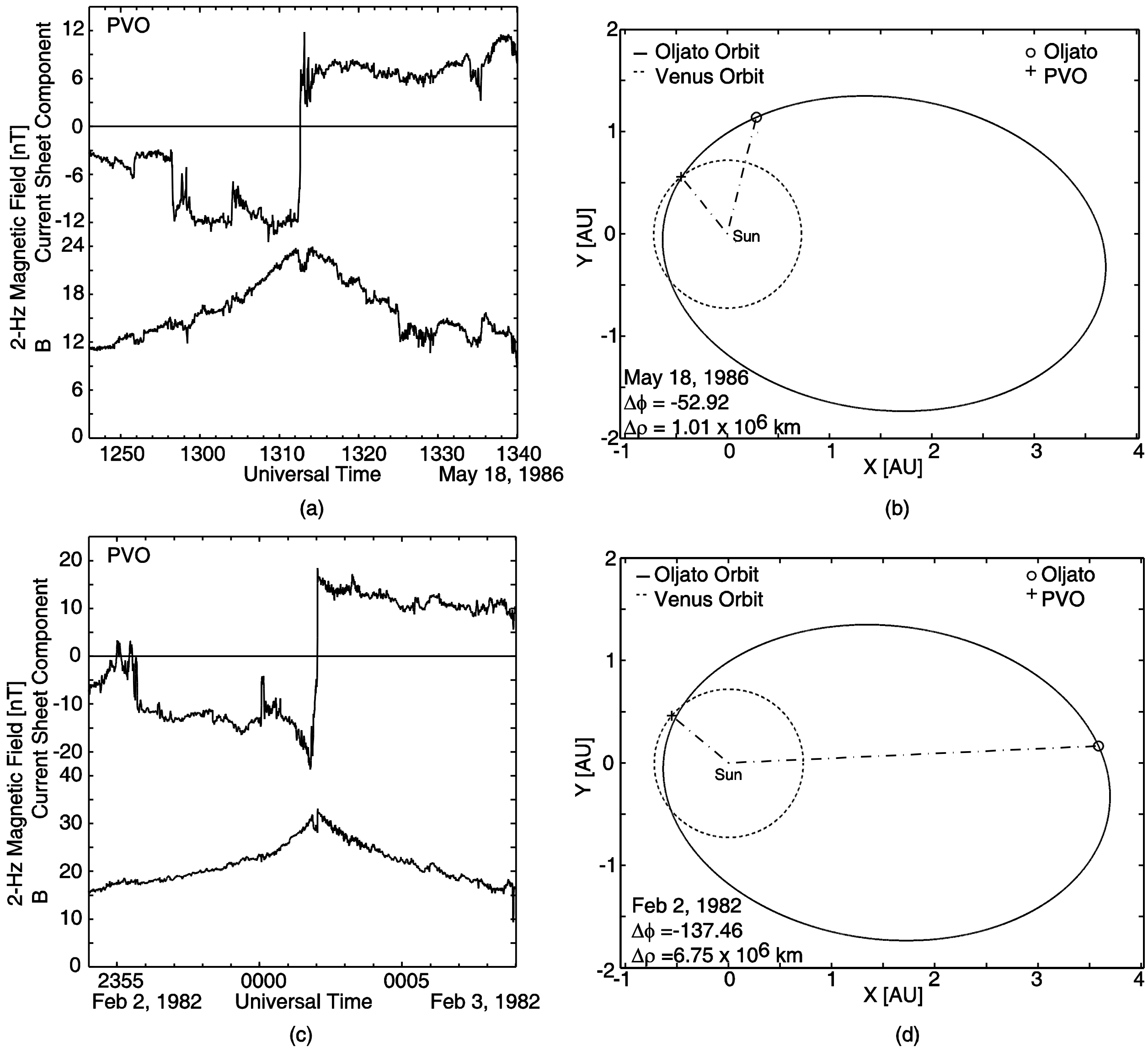

Figure 5.4 An IFE detected in an Oljato year (a) compared with another one detected in a non-Oljato year(c). Here we show the maximum variance component of the magnetic field and the strength of the magnetic field. Both IFEs have small current sheets leading the major central current sheets and have a "crater" near the maximum in the magnetic-field strength. (b) and (d) show the orbital geometries of Oljato and Venus when the two IFEs are detected. The IFE locations are close to each other although the Oljato locations are not. This implies that the co-orbiting material responsible for IFEs can be far away

from Oljato. In the orbital plots, Δϕ is the phase difference and Δρ is the radial distance between the two orbits at the longitude where the IFE was detected.

Among all the recorded 63 IFEs from PVO observation, 32 are detected in the sensitive region. Figure 5.5 shows the IFE daily rate as a function of the phase difference. Figure 5.5(a) shows the IFEs detected in the sensitive region while Figure 5.5(b) shows the IFEs detected outside the sensitive region. To calculate the probable error we classify the PVO data into three groups by the successive Venus years (224.7 days). Since the sensitive region is only about one quarter of the Venusian orbit, the observation time inside the sensitive region was relatively short especially during the period when the phase difference was small. As we classify the observation time into three groups, it happens that in one or all groups, there are no observations in some longitudinal ranges. Therefore we do not estimate the errors there.

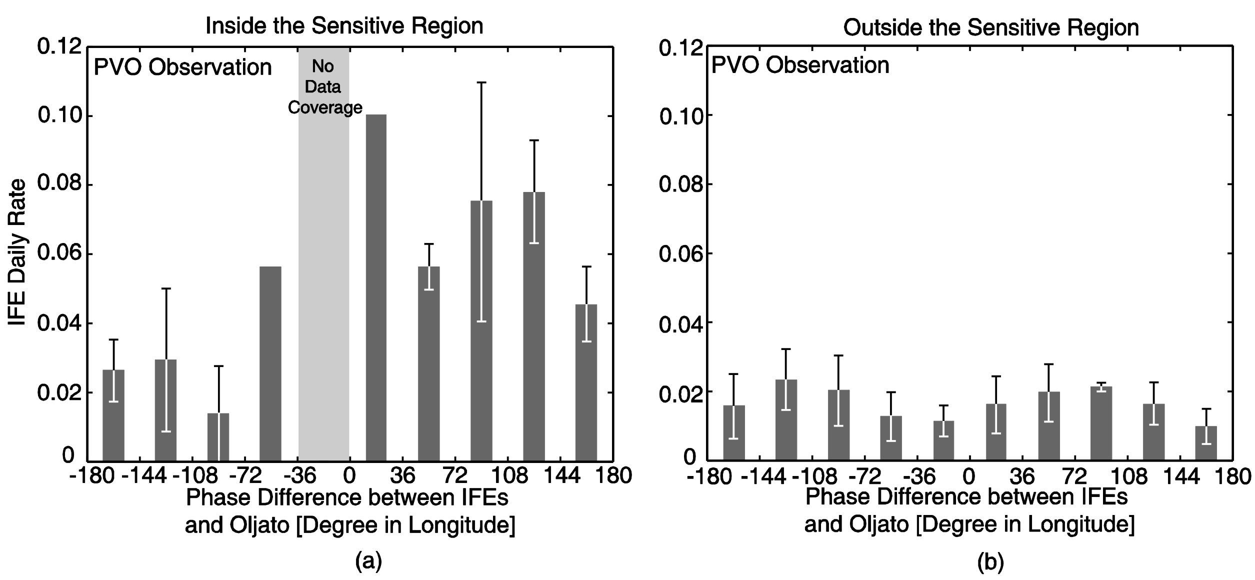

Figure 5.5 PVO observed IFE daily rate as a function of phase difference between Oljato and IFEs inside the sensitive region (a) and outside the sensitive region (b). Inside the sensitive region, the IFE rate

peaks when the phase difference is small while outside the sensitive region, the daily rate distribution is random.

The difference between Figure 5.5(a) and Figure 5.5(b) is obvious: the IFE daily rate inside the sensitive region is much higher than the rate outside the sensitive region. Inside the sensitive region, although the observation time is short when the phase difference between Oljato and Venus is small, the mean IFE daily rate has a trend to peak in the small phase difference region. This result is consistent with the earlier studies despite that we have more candidates IFEs here due to our more liberal definition of "Oljato-associated IFEs". Outside the sensitive region, the IFE daily rate distribution is random. This is again consistent with the results in the earlier studies. Although the results in Figure 5.5(a) suggest that more co-orbiting material was distributed close to Oljato, we cannot exclude the possibility that there is co-orbiting material far away from Oljato as suggested in Figure 5.4.

To estimate the mass of the Oljato-associated IFEs, we need to know the pressure enhancement index distribution and have at least one multi-spacecraft simultaneous observation as we do in Chapter 3. The pressure enhancement index distribution based on all the IFEs detected by PVO is shown as red stars in Figure 5.6. To make a comparison, we also show the ACE observations. To calculate the standard deviation, we classify the ACE data into three groups every three months. Based on Figure 5.6, only the last two points from PVO observation are outside one standard deviation of ACE observation. Thus the cross-flow pressure profiles at $0.72AU$ and at $1AU$ are generally the same. On February 11, 1982, an IFE was detected by PVO, Venera 13 and Venera 14 [Russell *et al*., 1985]. However, the plasma data from neither Venera

13 nor Venera 14 are available. Therefore we assume that the average ratio of IFE radial scale to cross-flow radius is also 5.6 at $0.72AU$. The resultant mass distribution of the Oljato-associated IFEs is shown in Figure 5.7. From this figure, most of the Oljato-associated IFEs are less than $10^{10} kg$, corresponding to minimum target diameters of less than $100m$. Material of such a small size in Oljato's orbit cannot be detected by traditional methods.

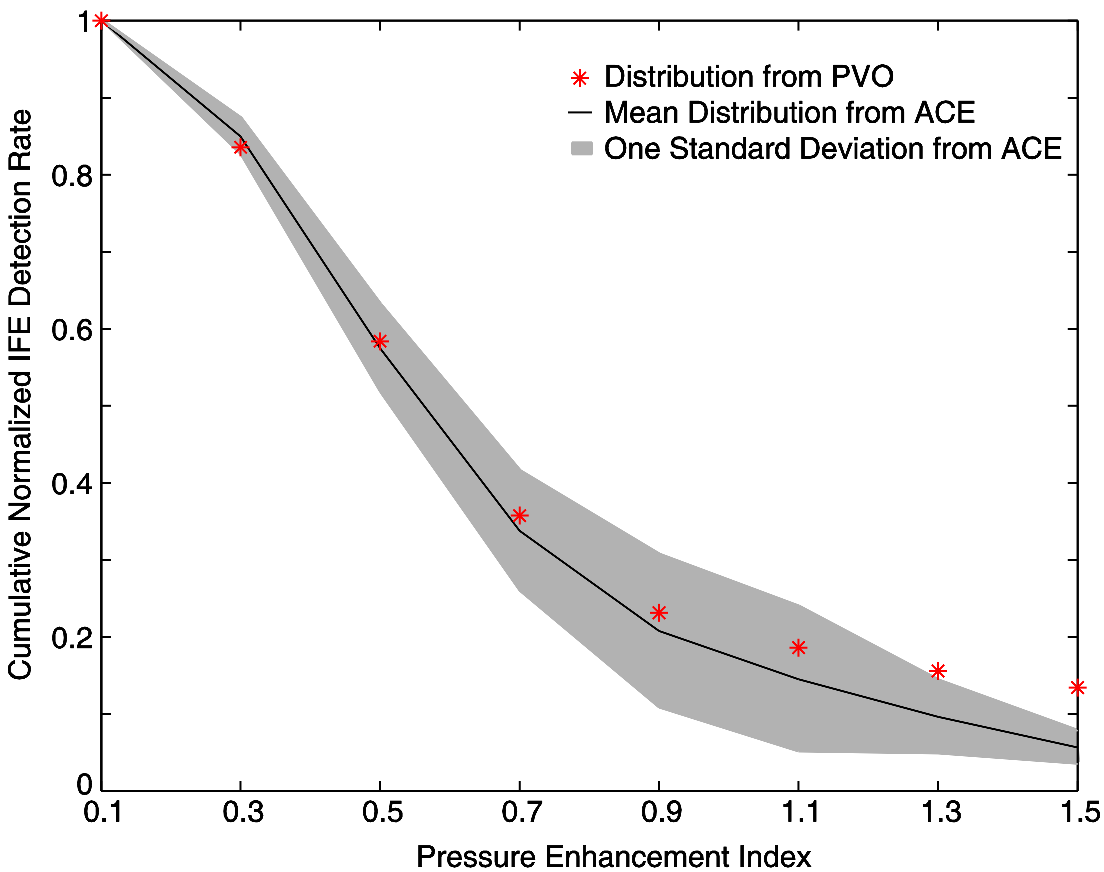

Figure 5.6 Pressure enhancement index distribution obtained by PVO (red stars). The distribution obtained by ACE is also shown. Only two out of eight PVO observed points are beyond one standard deviation of ACE observation. Thus the cross-flow pressure profile at $0.72AU$ is similar to the one at $1AU$.

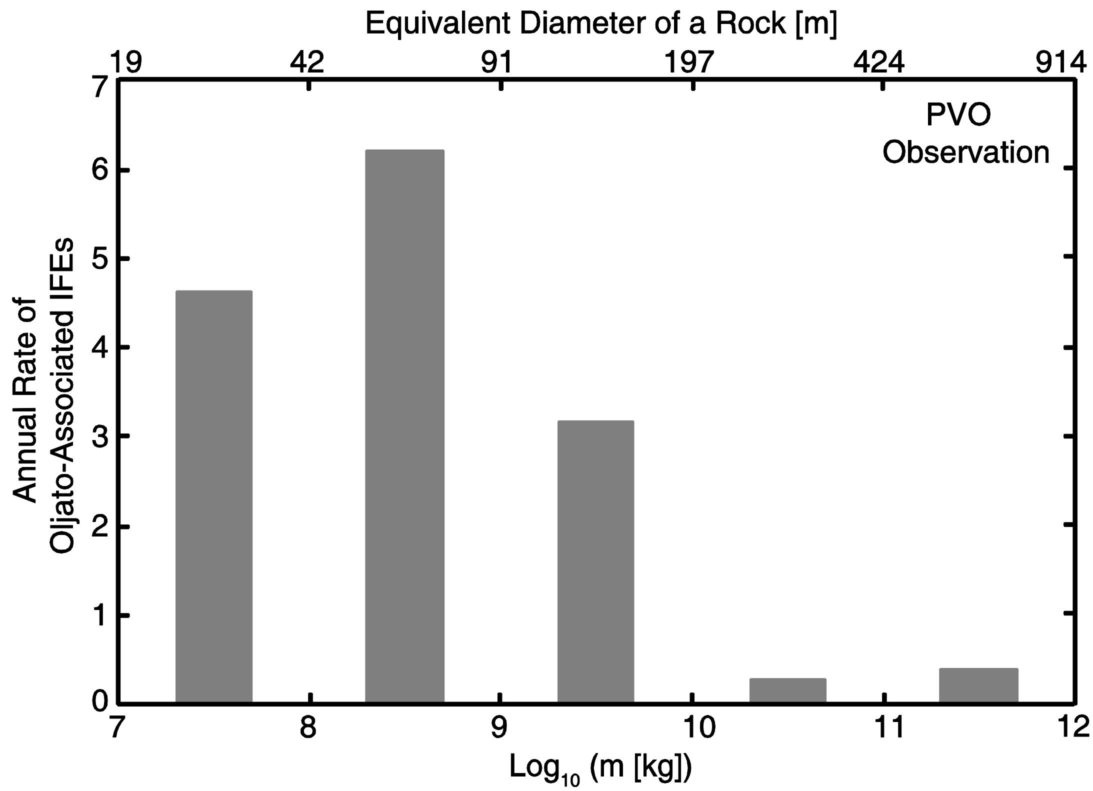

Figure 5.7 Mass distribution of Oljato-associated IFEs detected by PVO. Most of those IFEs are less than $10^{10}kg$. This indicates that the minimum co-orbiting material is less than $100m$ in diameter before it is destroyed in the collision. Such small objects are hard to detect by traditional method.

5.1.3 Oljato Associated IFEs Detected by VEX

We now apply a similar analysis procedure to the IFEs detected by VEX. Among the total 53 IFEs, 12 of them are detected in the sensitive region. The daily rates as a function of phase difference are shown in Figure 5.8, in the same format as the ones in Figure 5.5. To simplify the comparison, the scales in Figure 5.8 and in Figure 5.5 are the same. Unfortunately, the data coverage from VEX is even worse inside the sensitive region when the phase difference is small. But still we can see that VEX detected a lower IFE daily rate in the same phase difference ranges inside the sensitive region. This feature is also shown clearly in Figure 3.6. Outside the sensitive region, the distribution seems to be random with an average daily rate close to the one in Figure 5.5(b). To check whether there is any significant change in the daily rate outside the sensitive region from 1980s to present, we apply the student t-test where the null hypothesis is that there is no difference. The probability that the null hypothesis is false is 0.12 with $t = 1.59$ and the degrees of freedom being 58. Thus the IFE occurrence outside the sensitive region does not change in the three decades.

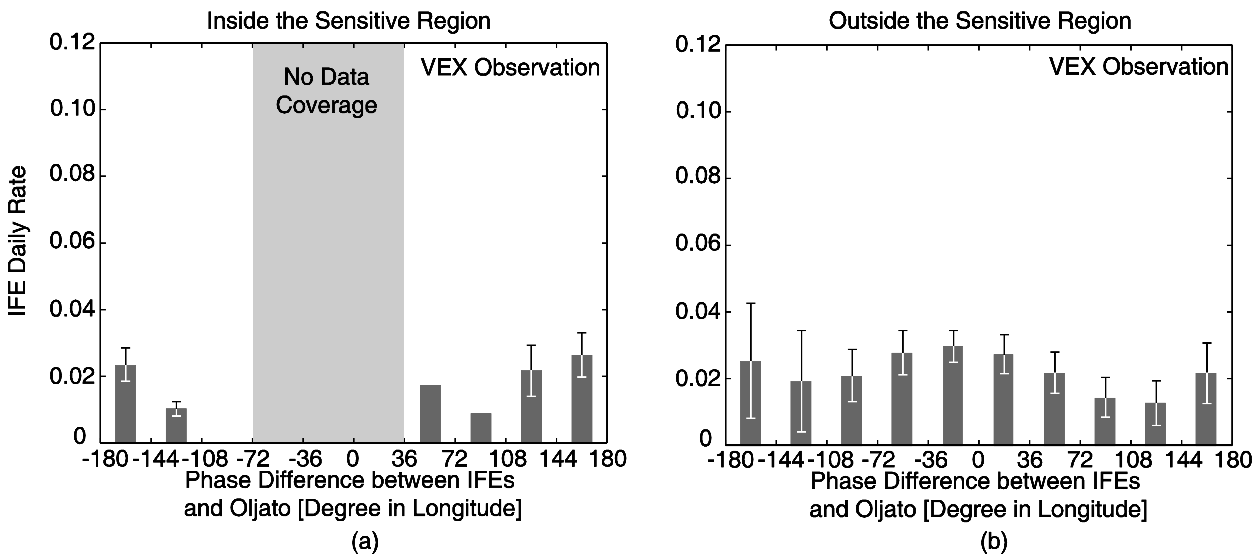

Figure 5.8 IFE daily rate distribution observed by VEX in the same format as shown in Figure 5.5. In the sensitive region, although the data coverage is not good, the daily rates are lower than the ones detected by PVO. Outside the sensitive region, the rate distribution is random and the average IFE daily rate is the same as the ones detected by PVO based on the student t-test results.

Since there are no solar-wind plasma data available from VEX. We cannot estimate the mass distribution of the VEX detected IFEs.

5.1.4 The Temporal Variation of IFEs Associated with Oljato

From Figure 5.5 and Figure 5.8 we know that there is no significant difference between the orbit geometries of Oljato and Venus in the past 30 years, and the comparison between Figure 5.5(b) and Figure 5.8(b) shows that the IFE occurrence outside the Oljato-sensitive region is the same, the only difference between the PVO and VEX observations is the IFE occurrence inside the Oljato-sensitive region: the IFE daily rate has dropped.

To see the temporal variation of the IFE occurrence better, we present the IFE daily rate as a function of time and show the results in Figure 5.9. In this plot, the IFE daily rates in the Oljato years are illustrated as stars. Also shown in this figure are the average IFE daily rates for all longitudes as solid lines and the average rates in the sensitive region in non-Oljato years as dotted lines. The decrease of the rates in the sensitive region in the Oljato years is significant. Over all longitudes, the average IFE daily rates observed from PVO and from VEX are close, *i.e.*, 0.027 and 0.024, respectively. However, in the sensitive region in non-Oljato years, the IFE rate detected by PVO is higher than the average background rate while the IFE rate detected by VEX is lower than the average background rate. This plot is consistent with the results shown in Figure 3.5: the average annual rates detected by PVO and VEX are close but the variations in the PVO epoch are larger.

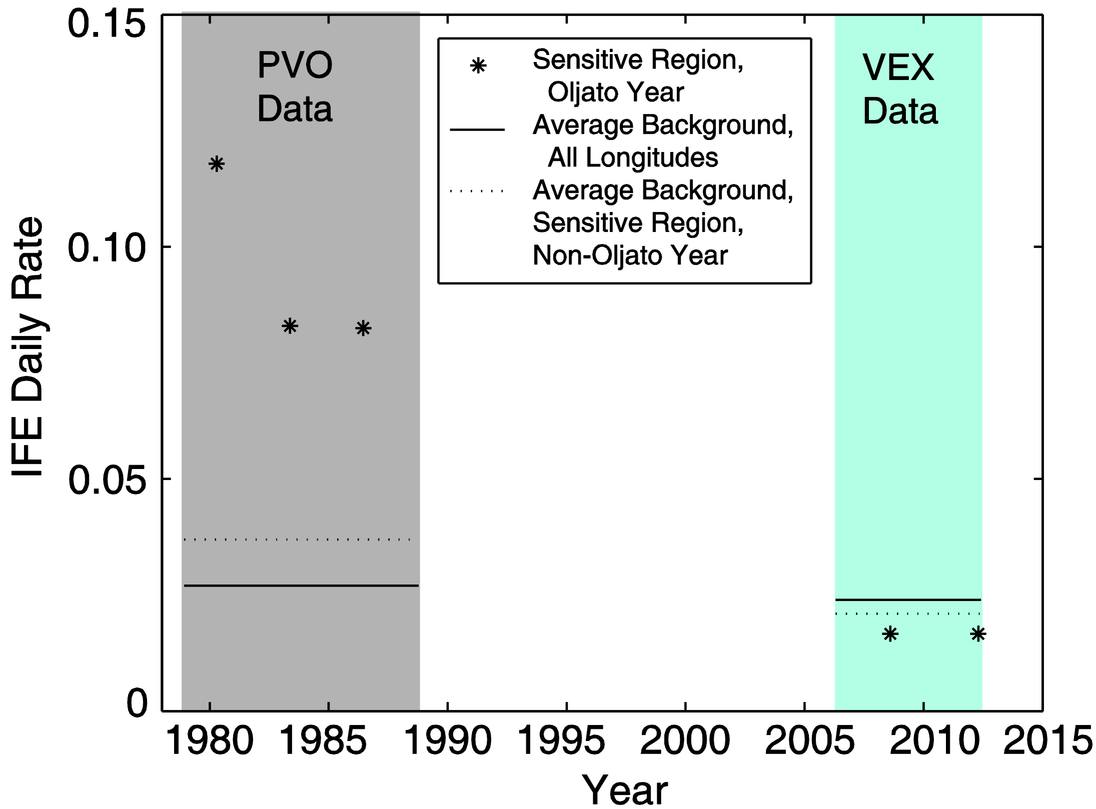

Figure 5.9 IFE daily rate as a function of time. Stars are for the rates in the sensitive region when Oljato passed by. Solid lines are average daily rate over all the longitude and in all the years. Dotted lines are average daily rate in the sensitive region in the years when there was no Oljato passage. The values of the two solid lines are very close. In the PVO epoch, the passage of Oljato significantly increased the daily rate, even in the non-Oljato years. However, in the VEX epoch, such an Oljato effect no longer existed.

Based on our IFE formation hypothesis, if the co-orbiting material of Oljato was responsible for many IFEs detected during the PVO epoch and gave the increased daily rate in the sensitive region, its IFE producing effect has diminished in the past three decades. This can be due to the loss of co-orbiting material from Oljato's orbit. One possible loss mechanism is the gravity perturbations from large planetary bodies. Since Oljato occasionally has very close approach to the Earth and Venus, similar to the situation of the material co-orbiting with asteroid 138175 as we reviewed in Chapter 1, gravity perturbations can change the spatial distribution of the co-orbiting material as Figure 5.10 shows.

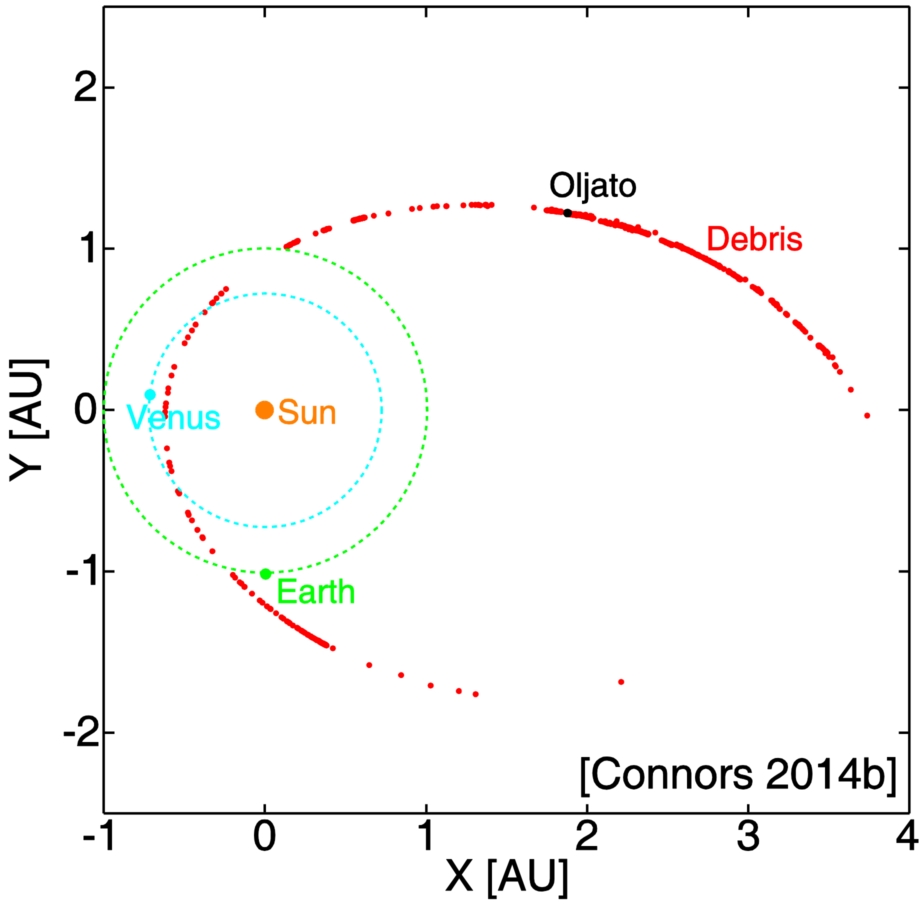

Figure 5.10 Debris distribution of Oljato in about 79 years. Similar to the situation of asteroid 138175 (Figure 1.1), Oljato can make close passes of the Earth and Venus occasionally. The debris in the trail is subject to the gravity perturbations from the Earth and Venus. Gaps are formed in the otherwise continuous debris trail. [Connors 2014b]

5.2 Association between *1AU* IFEs and Co-orbiting Material of Asteroid 138175

5.2.1 Asteroid 138175

To identify the IFE sources near $1AU$, we can perform a similar analysis as we have done at $0.72AU$. First we need to select the IFE database. We have observations from four modern spacecraft: ACE and *Wind* (from 2004) with period of one year, STEREO A with a period of slightly shorter than one year and STEREO B with a period of slightly longer than one year. Since we are most interested in the longitudinal regions where IFEs occur periodically and will use this period to search for candidate parent bodies, we combine ACE and *Wind* observations as one database and treat observations from STEREO A and STERO B as separate databases.

Now we reproduce the longitudinal distribution of IFE annual rate from ACE and *Wind* observations. Figure 5.11 shows the result. As this figure shows, the highest annual rate is between longitude $195°$ and $225°$. And in the longitudinal range $[165°, 195°]$, $[255°, 285°]$ and $[345°, 15°]$, the IFE annual rates are higher than the average over all longitudes. Based on our hypothesis and the study presented in Section 5.1, the most probably longitudinal range that we can find Oljato-like sources is $[195°, 225°]$.

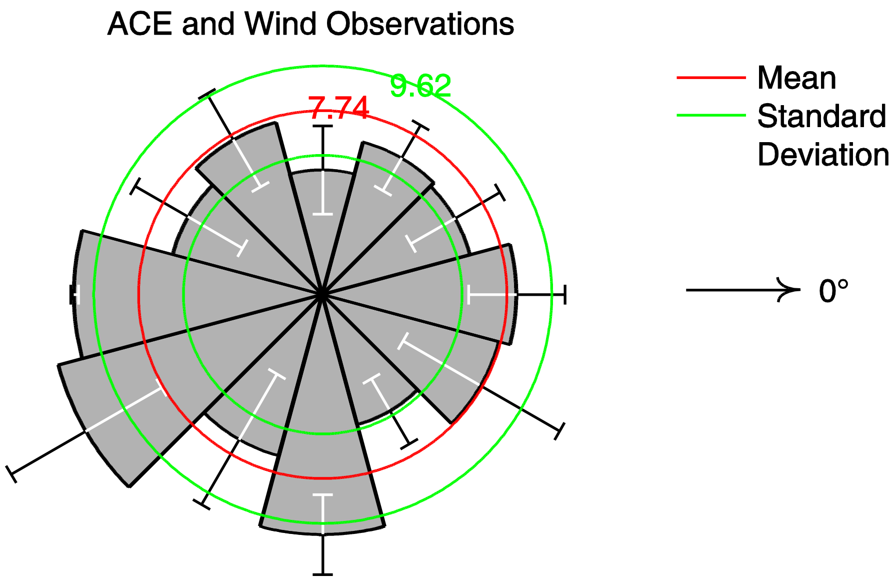

Figure 5.11 IFE longitudinal distribution from ACE and *Wind* observations. We combine the two databases because they have the same periods. It is clearly shown that the IFE annual rate peaks in the longitudinal range [195°, 225°]. Thus it is highly possible that we can find Oljato-like IFE sources in this region.

We will search for candidate asteroids using the JPL Small-Body Database Search Engine (http://ssd.jpl.nasa.gov/sbdb_query.cgi). Since all the IFEs detected at $1AU$ are in the ecliptic plane and must be formed upstream and then swept to $1AU$ by the solar wind, the selection criteria of the candidate asteroids are that parts of their orbits lie inside $1AU$ and are close to the ecliptic plane between longitude 195° and 225°. For asteroids with finite inclinations, the criterion is simply that the asteroids have ascending/descending nodes inside $1AU$ between longitude 195° and 225°. Since the $1AU$ observation covers at most 14 years, only asteroids with periods of less than five years might have significant statistical effect. Thus we will only focus on those short-period asteroids. Also during our candidate asteroid survey we notice that some documented asteroids have assigned designations while the others do not. As only asteroids with well determined orbits have designations, we will focus on them first.

By May 28, 2013, 5703 asteroids with perihelia less than $1AU$ and periods less than five years were recorded in the JPL database. Among them, 845 asteroids have been assigned designations. And 72 asteroids have descending/ascending node inside $1AU$ and between longitude 195° and 225°.

To further select our candidate asteroids, we go back to Figure 3.7(a). It shows the longitudinal distribution of IFE occurrence detected by ACE, which has the longest observation time. We notice that the cluster in our interested longitudinal range stands out significantly. As ACE orbits in the L-1 Lagrangian point, its period is exactly one year. This means that the candidate asteroid has a period (P_A) which can resonate with the one of the Earth (P_E). Thus we can further filter the candidate asteroids with the constraint that $P_A \pm 0.01 = N \cdot P_E$ or $P_A \pm 0.01 = \frac{P_E}{M}$, while $N = 1, 1.5, 2, 2.5,\ 3, 3.5, 4, 4.5, 5$ and M is an integer. There are only three asteroids satisfying the above criteria and we list their orbital properties below in Table 5.2. In this table we show the full name of the asteroid, the longitude of the node in HE coordinate system, the heliocentric distance of the node, the period, the inclination and the date when the asteroids passed their nodes from 1998 to 2012.

Asteroid Full Name	**85770 (1998 UP1)**
Node in HE [Deg]	198.372
$\boldsymbol{R_{Node}}$ **[AU]**	0.735

Period [Year]			0.997		
Inclination [Deg]			33.180		
Date When Passing	1998/06/15	1999/06/15	2000/06/14	2001/06/14	2002/06/13
the Node	2003/06/13	2004/06/12	2005/06/11	2006/06/11	2007/06/10
[YYYY/MM/DD]	2008/06/09	2009/06/08	2010/06/08	2011/06/07	2012/06/06

(a)

Asteroid Full Name			**255071 (2005 UH6)**		
Node in HE [Deg]			199.337		
R_{Node} **[AU]**			0.377		
Period [Year]			1.002		
Inclination [Deg]			2.641		
Date When Passing	1998/08/06	1999/08/07	2000/08/07	2001/08/08	2002/08/08
the Node	2003/08/09	2004/08/08	2005/08/09	2006/08/10	2007/08/10
[YYYY/MM/DD]	2008/08/10	2009/08/10	2010/08/11	2011/08/12	2012/08/12

(b)

Asteroid Full Name	**138175 (2000 EE104)**
Node in HE [Deg]	205.894

R_{Node} [AU]			0.975		
Period [Year]			1.007		
Inclination [Deg]			5.242		
Date When Passing	1998/04/15	1999/04/17	2000/04/18	2001/04/20	2002/04/23
the Node	2003/04/26	2004/04/28	2005/05/01	2006/05/04	2007/05/07
[YYYY/MM/DD]	2008/05/08	2009/05/11	2010/05/14	2011/05/17	2012/05/19

(c)

Table 5.2 Orbital properties of three candidate asteroids. For each asteroid, we list the full name, the HE longitude of the node, the heliocentric distance of the node, the period, the inclination and the dates when the asteroid passed the node from 1998 to 2012.

Another important criterion which we did not mention before is the phase difference. Although from the PVO observation we see that the co-orbiting material can be far leading or trailing the asteroid, it would be more convinced if we can find co-orbiting material close to the parent asteroid. Since we now have three asteroid candidates, we can use the phase difference criterion to select the most probable IFE source. We notice ACE always passes the longitudinal range of interest between April 5^{th} and May 6^{th}. This is the time interval when asteroid 138175 was close to its node from 1998 to 2006. Therefore asteroid 138175 satisfies all the selection criteria and is the most probable source of IFEs in the longitudinal range of interest.

Asteroid 138175 (2000 EE104) was discovered on March 11, 2000 by the *Catalina Sky Survey* with several pre-discovery observations and numerous subsequent ones over a period of nearly 15 years. Figure 5.12 shows the orbits of asteroid 138175 and the Earth in the HE coordinate system. As the orbital projections in the ecliptic plane (Figure 5.12(a)) shows, the orbit of asteroid 138175 lies upstream of $1AU$ between longitude of $200.8°$ and $52.7°$, with its descending node at $205.9°$. Although this sector covers a large longitudinal range, due to the finite inclination of the asteroid's orbit, the asteroid spends most of the time far away from the ecliptic plane as shown in Figure 5.12(b). Therefore we cannot use the whole sector from $200.8°$ to $52.7°$ as the sensitive region as we did in the Oljato study. If we go back to our IFE scale length distribution, we notice that among more than 230 IFEs with available scale length observed by ACE, *Wind*, STEREO A and STEREO B, only two IFEs have radial scale length larger than $10^7 km$, *i.e.*, $1.79 \times 10^6 km$ in cross-flow radius (assume 5.60 is the ratio of radial length to cross-flow radius). Therefore we define the sensitive regions as the ones where the orbit of asteroid 138175 lies upstream of the orbit of the spacecraft and the asteroid's orbit is within $1.79 \times 10^6 km$ from the ecliptic plane. The resultant sensitive region for ACE and *Wind*, which locate at L-1 Lagrangian point, is found to be from $200.8°$ to $214.6°$ and from $17.5°$ to $34.8°$. ACE and *Wind* pass the two regions from Apr 10th to Apr 24th and from Oct 10th to Oct 28th every year. We define the two regions as the sensitive region near the descending node and sensitive region near the ascending node, respectively, and shade them in grey in Figure 5.12.

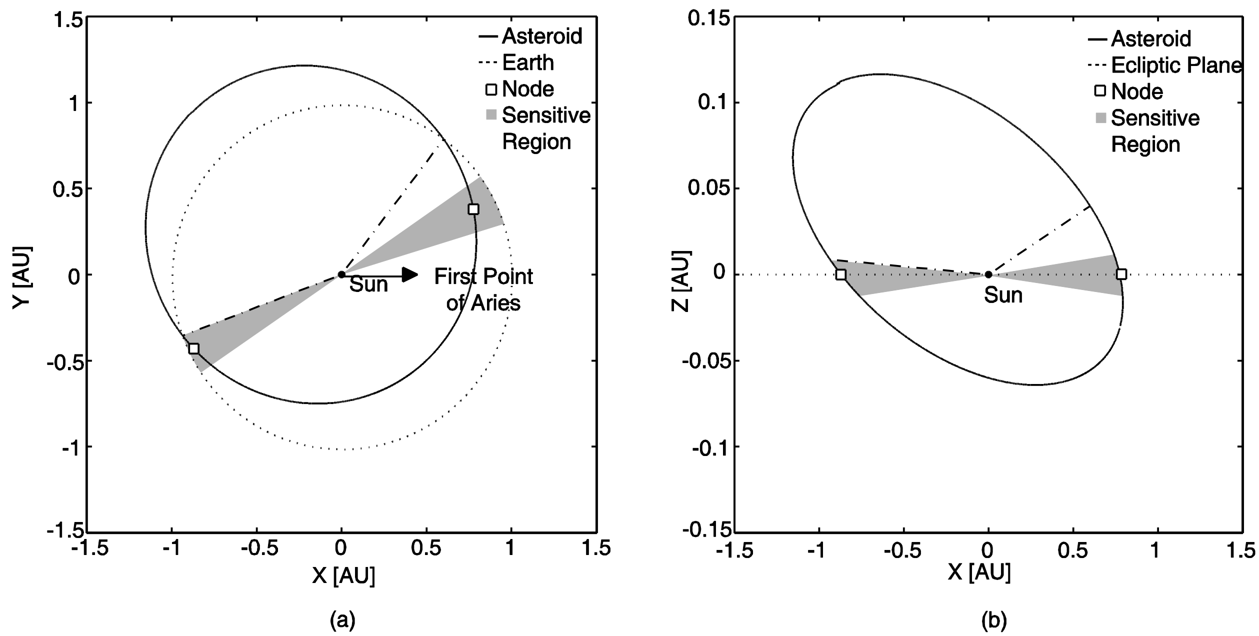

Figure 5.12 Orbital projections of asteroid 138175 in ecliptic plane (a) and in the plane perpendicular to ecliptic plane (b). The sensitive regions are defined as ones where the orbit of asteroid lies upstream of the one of the spacecraft and within $1.79 \times 10^6 km$ from the ecliptic plane. The sensitive region for ACE and *Wind* is shaded in grey.

In both Figure 3.9 and Figure 5.11, the sensitive region near the descending node locates inside the longitudinal sector where the IFE annual rate is highest. However the IFE annual rate in the longitudinal sector containing the sensitive region near the ascending node is lower than the rates in the adjacent longitudinal sectors in Figure 3.9. We notice that in both Figure 3.9 and Figure 5.11, each longitudinal sector covers 30°, almost twice of the longitudinal range covered by each of our defined sensitive region. Therefore in Figure 5.13 we re-plot the IFE annual rate longitudinal distribution with ACE, *Wind*, STEREO A and STEREO B observations. This time each longitudinal sector covers 15° in longitude and the sectors containing the sensitive region are shaded in blue. Based on this plot, the IFE annual rate in the sensitive region near the descending node is two standard deviations higher than the average and the rate in the sensitive region near the ascending node is one standard deviation higher than the rates in the adjacent sectors. This distribution pattern supports our hypothesis that co-orbiting material of asteroid 138175 produces many IFEs which can be detected by spacecraft near $1AU$. Such a distribution pattern also implies that our definition of the two sensitive regions is reasonable.

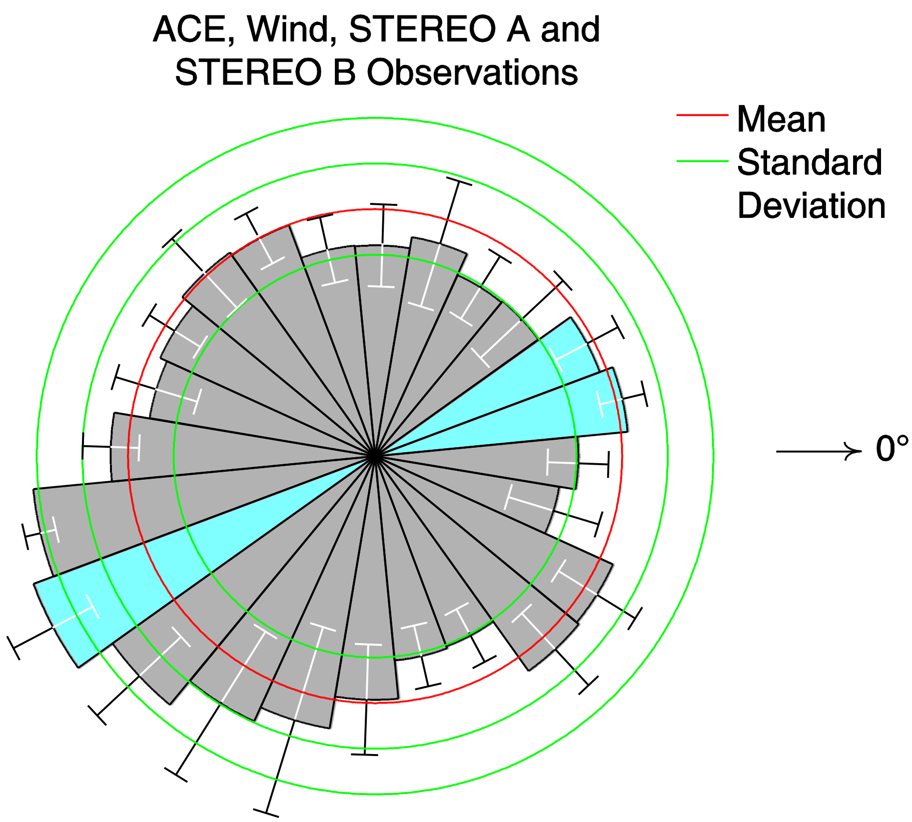

Figure 5.13 IFE longitudinal distribution near $1AU$. The format is similar as the one in Figure 3.9. This time each sector covers 15° in longitude. The blue shaded areas contain the defined sensitive regions. The IFE annual rate in the sector containing the sensitive region near the descending node is larger than the average IFE annual rate by more than two standard deviations. The IFE annual rates in the sectors

containing the sensitive region near the ascending node are also higher than the rates in the adjacent sectors.

Figure 5.14 shows two IFE examples detected in the sensitive region near the descending node and near the ascending node, respectively. Both IFEs have multiple current sheets and the magnetic-field strength enhancement patterns are similar. This implies that their production and evolution processes are similar. This figure also supports that our definition of the two sensitive regions is reasonable.

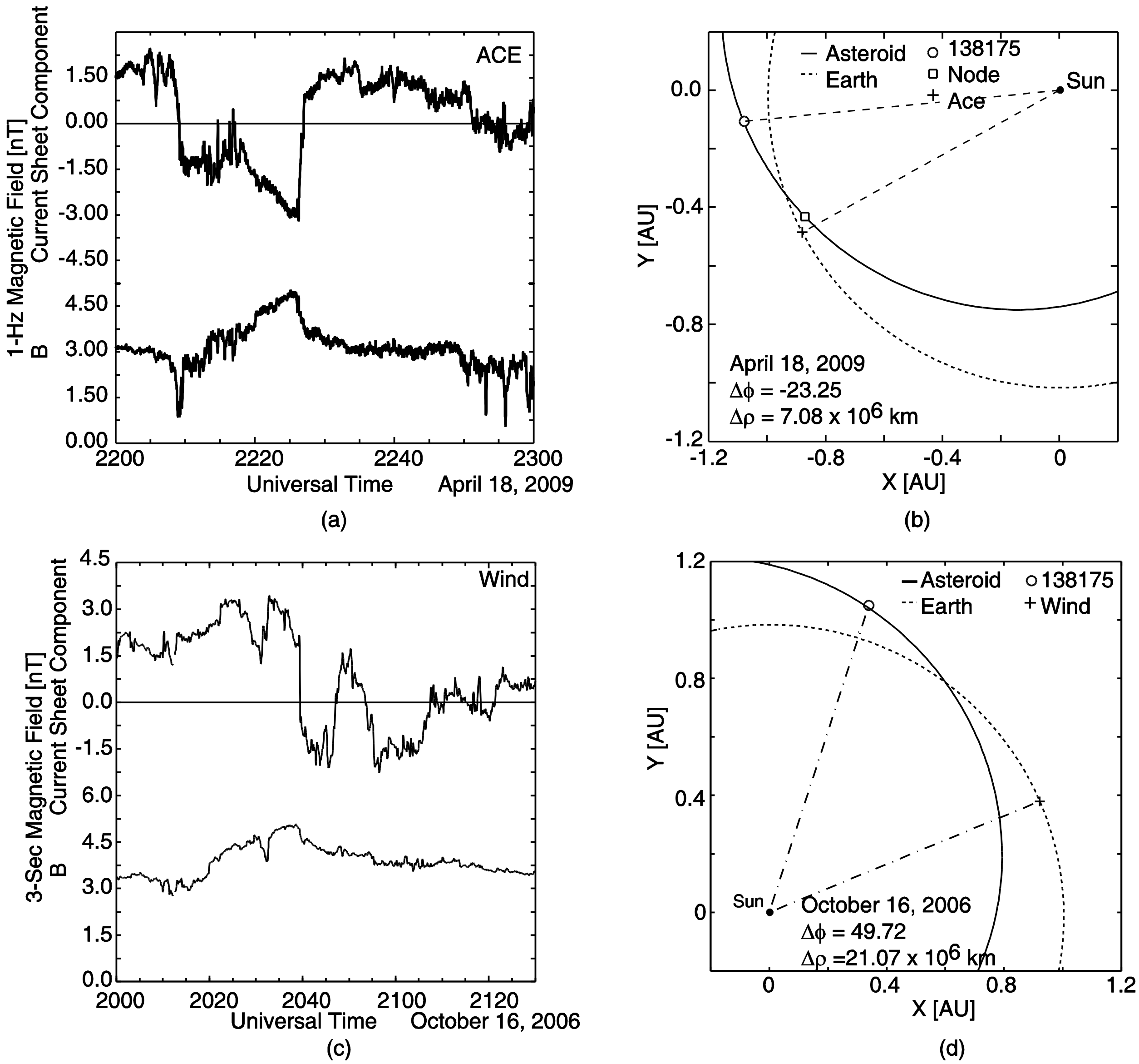

Figure 5.14 IFEs detected in the sensitive region near the descending node (a) and near the ascending node (c) have similar magnetic-field patterns. This indicates that their production and evolution processes are similar.

5.2.2 Asteroid 138175 Associated IFEs Detected by Modern Spacecraft

We first study the IFEs detected by ACE and *Wind*, as their orbits are very close to the one of the Earth. In total, there are 16 IFEs identified in the sensitive regions as listed in Table 5.3. In the table we also list the longitudes of the IFEs, the longitudes of the asteroid when the IFEs were detected and the phase differences. When calculating the phase difference, we set it to be positive when the asteroid leads IFEs. In the list, coincidently, eight IFEs are near the descending node while the remaining eight IFEs are near the ascending node. Due to the orbital geometries of the Earth and asteroid 138175 from 1998 to 2011, all the IFEs near the descending node are leading the asteroid while all the IFEs near the ascending node are trailing the asteroid.

Date [YYYY/MM/DD]	**S/C**	λ_{IFE} **[Deg]**	λ_a **[Deg]**	$\Delta\lambda$ **[Deg]**
2005/04/15	*Wind*	205.06	190.90	-14.16
2005/04/18	*Wind*	207.56	193.10	-14.51
2006/04/17	*Wind*	207.08	190.49	-16.53
2006/10/16	*Wind*	22.39	72.11	49.72
2011/10/16	*Wind*	22.11	61.23	39.12
2002/04/11	ACE	200.90	194.18	-6.72
2004/10/22	ACE	28.87	80.72	51.85
2006/04/11	ACE	200.88	185.31	-15.57
2006/10/25	ACE	31.34	78.84	47.50
2008/04/16	ACE	206.26	185.57	-20.69
2008/10/23	ACE	29.83	73.88	44.05
2009/04/13	ACE	203.07	180.98	-22.09
2009/04/18	ACE	207.96	184.88	-23.08
2009/10/14	ACE	20.64	64.45	43.81

2010/10/24	ACE	30.32	70.20	39.88
2010/10/26	ACE	32.31	71.76	39.45

Table 5.3 Asteroid associated IFEs detected by ACE and *Wind*. Here we list the longitudes of the IFEs, the longitudes of the asteroid at the mean time and the phase differences.

To overcome the orbital geometry limit, we can use the observations from spacecraft near $1AU$ but not near the L-1 point, such as STEREO A and STEREO B. We can also check the observations obtained in the earlier years, such as observations from IMP 8.

We first survey the modern data obtained. Since STEREO A orbits around the Sun slightly inside $1AU$ while STEREO B orbits around the Sun slightly outside $1AU$ and both of their orbits have small inclination angles, we need to re-define the sensitive regions. With the same criteria, *i.e.*, the orbit of the asteroid lies upstream in the solar wind and the transverse separation between the orbital planes of the spacecraft and the orbit of the asteroid is limited, we obtain the observation times when the spacecraft is inside the re-defined sensitive regions. Then we can compare the observation times with our IFE lists and find the candidates IFEs. In total, nine IFEs are suggested.

With all the ACE, *Wind*, STEREO A and STEREO B observations, similar to Figure 5.5 and Figure 5.8, we can plot the IFE daily rate inside and outside the sensitive region as a function of phase difference between the spacecraft and the asteroid. The results are shown as histograms in Figure 5.15. Again we classify the observations into three groups every three months and estimate the probable errors. Inside the sensitive regions there are many more IFEs detected within 72° leading the asteroid. Based on our hypothesis, this indicates that there is a source, maybe a cloud of co-orbiting material, in this longitudinal range. Outside the sensitive regions, the IFE daily rate distribution is generally random. There is a weak correlation with the phase differences, which may be related to the finite dispersion of the orbits of the co-orbiting material. When we define the sensitive region, we consider the orbital geometries of the asteroid and the Earth. But as the simulation shows, the material associated with asteroid 138175 can be spread in both azimuthal and radial directions [Connors *et al.*, 2014a]. Therefore we have undercounted some IFEs which are detected outside the defined sensitive region but produced by the co-orbiting material.

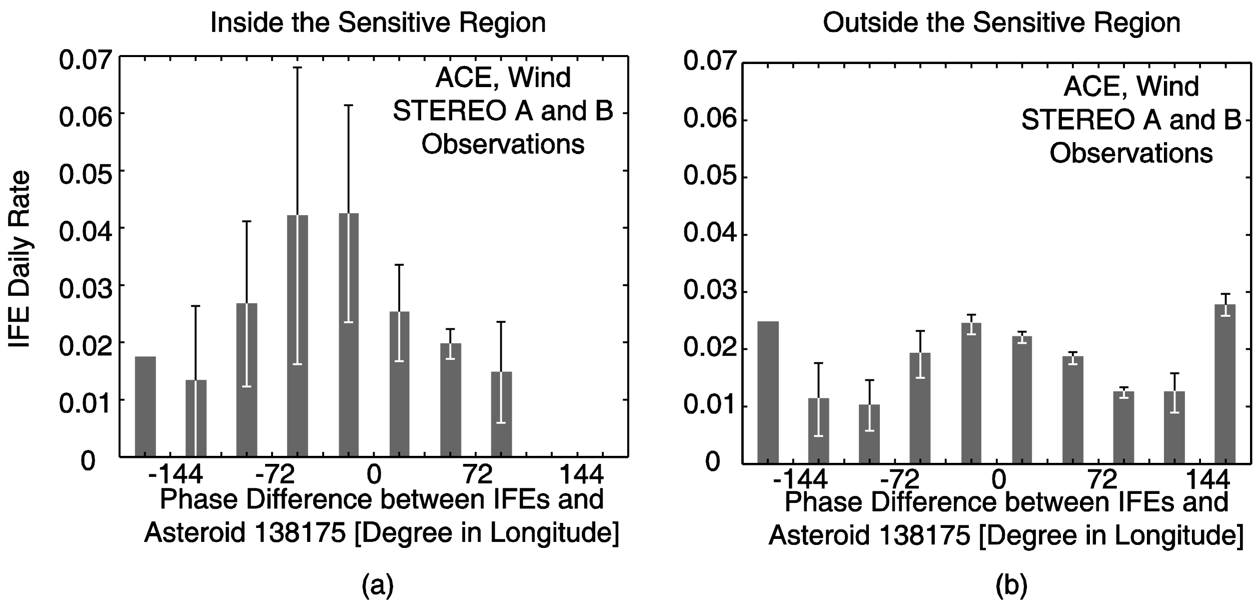

Figure 5.15 IFE daily rate as a function of phase difference inside the sensitive region (a) and outside the sensitive region (b). The daily rate distribution peaks within 72° leading the asteroid inside the sensitive region. Outside the sensitive region the rate is generally random except for a weak correlation. This is possiblely due to the finite spread of co-orbiting material.

The mass distribution of these asteroid-associated IFEs is shown in Figure 5.16. Compared to the mass distribution of IFEs associated with Oljato's co-orbiting material, the IFEs associated with asteroid 138175's co-orbiting material have a smaller mass range. This is consistent with the fact that asteroid 138175 is much smaller than Oljato, with an estimated diameter of at most $0.5km$. Thus we expect smaller material co-orbiting with asteroid 138175.

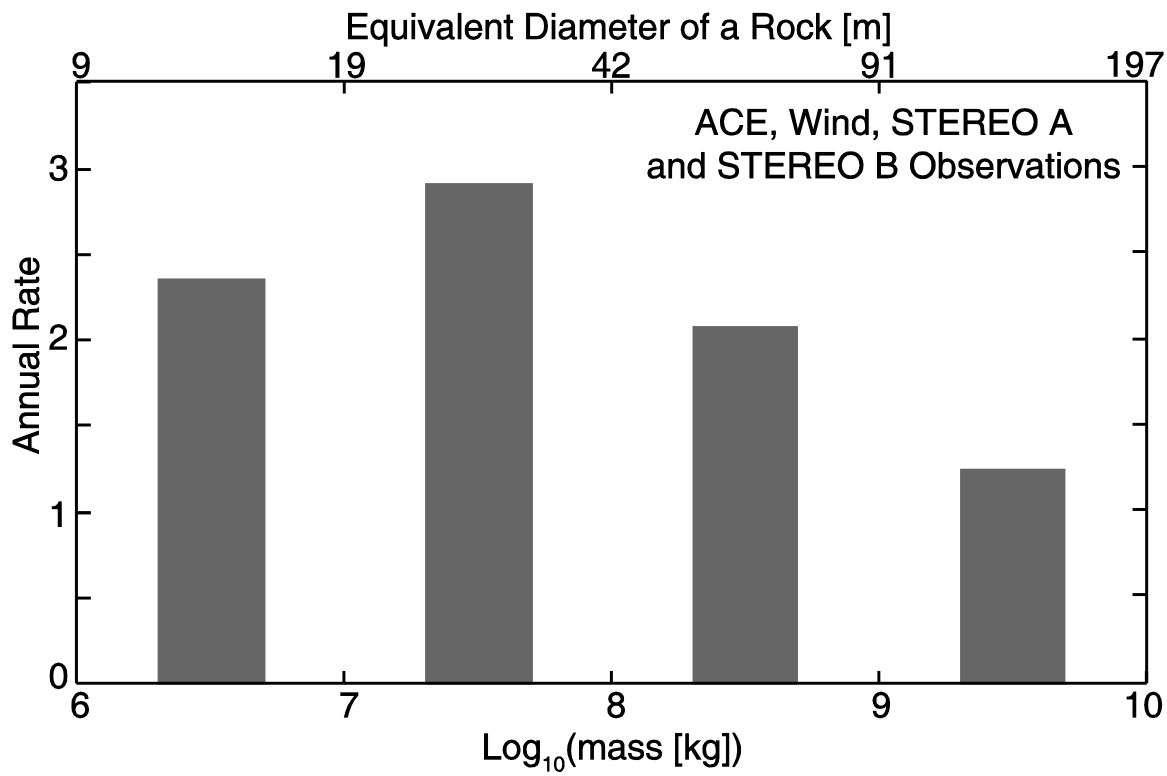

Figure 5.16 Mass distribution of IFEs associated with asteroid 138175. Generally the mass range is smaller than the one associated with Oljato. This is reasonable because asteroid 138175 is much smaller than Oljato. Therefore its co-orbiting material might be smaller than the co-orbiting material of Oljato.

5.2.3 Asteroid 138175 Associated IFEs Detected by IMP 8

If we go back to the earlier years, we can use observations from IMP 8 which operated from 1974 to 2000. Since the observations have lots of data gap, we only search IFEs in the intervals when the spacecraft was inside the sensitive region. In total, 22 IFEs satisfy our selection criteria. The resultant daily rate vs. phase difference is shown in Figure 5.17 as the grey bins. To make better comparison, we also include the ACE, *Wind*, STEREO A and STEREO B observations in Figure 5.17 as the blue bins. Based on this figure, the two distributions are similar but the average IFE rate in the earlier days is higher than its present value.

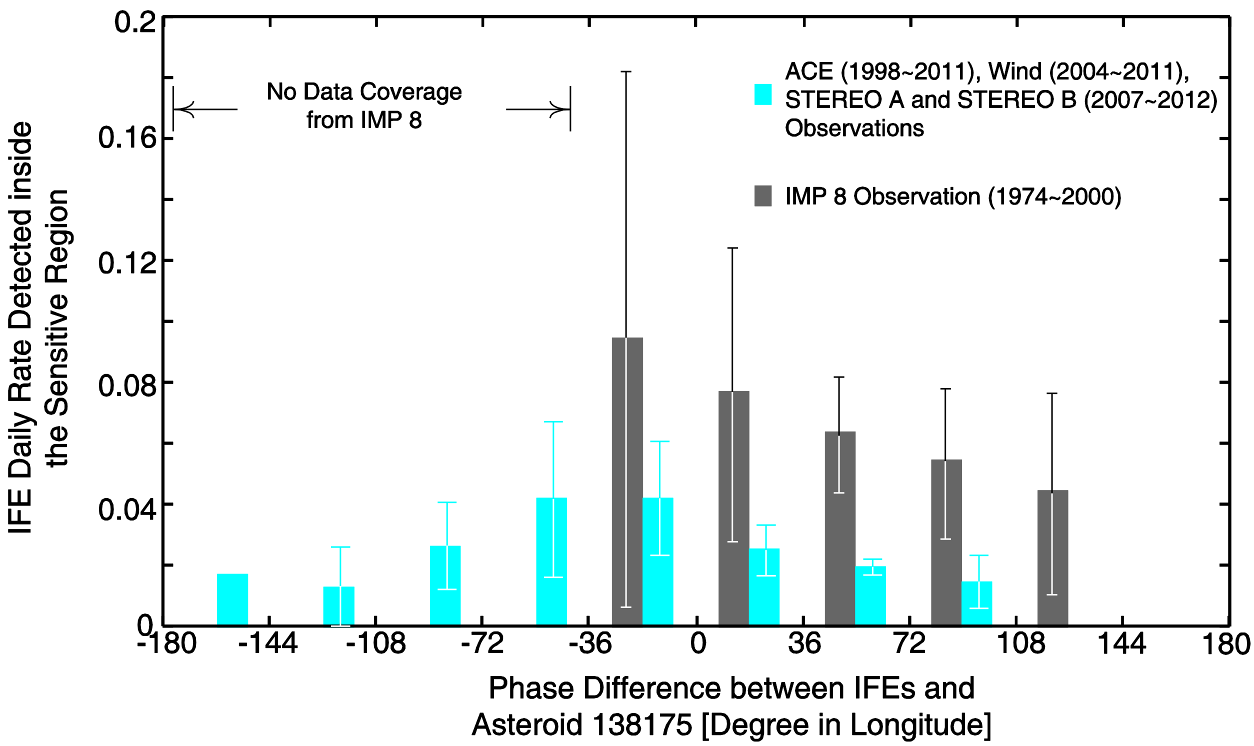

Figure 5.17 IFE daily rate inside the sensitive region detected by IMP 8 (grey) and detected by ACE, *Wind*, STEREO A and STEREO B (blue). We can see that the two distributions are similar but generally the daily rate detected by IMP 8 is higher.

5.2.4 Loss of Co-orbiting Material of Asteroid 138175

The temporal variation shown in Figure 5.17 suggests a loss in the co-orbiting material, which is consistent with the simulation results [Connors *et al*., 2014a]. If the responsible co-orbiting material for IFEs detected by IMP 8 located in the regions which were cleared by Earth or Venus in the later encounters, the decrease in the IFE daily rate detected by present spacecraft is expected.

5.3 The Undercounted IFEs

5.3.1 Effects of Orbital Geometry

As we state in Section 5.2.2, we might have undercounted some IFEs which are produce by the co-orbiting material but are detected outside the sensitive region. This is due to the orbital dispersion of the co-orbiting material. Perturbed by the initial impact which generates the debris or by the gravitational perturbations in the later large-objects encounters, the orbits of the co-orbiting material can be different from the orbit of the parent body. Therefore the sensitive region associated with the co-orbiting material is slightly different from the one associated with the parent asteroid. Such an orbital dispersion effect is more significant in the asteroid 138175 case, as shown in Figure 5.15(b). This can be due to its closer approach to Venus and its shorter period: material co-orbiting with asteroid 138175 encounters Earth and Venus more frequently thus the gravitational perturbation is more significant.

There is another orbital geometry effect that can result undercounting. Comparing the IFE longitudinal distribution obtained by PVO in Figure 3.6 with the orbital geometry in Figure 5.1, we notice that the IFE annual rate is highest in longitudinal range $[195°, 225°]$, is second highest in $[135°, 165°]$ and is lower than the average in between. Most of the three sectors are inside the sensitive region and it is highly possible that the abrupt IFE rate depression in the middle sector is due to the orbital geometry of Venus and Oljato other than sudden change in the IFE production rate.

Figure 5.18 shows the radial and transverse separations differences between Venusian and Oljato's orbits in longitudinal range $[135°, 220°]$ in 1983. Since we need to compare the difference in the orbital geometry in this longitudinal range, the difference of the separation is more important than the absolute value of the separation. Thus we set the minimum separation to be zero in both radial and transverse direction in Figure 5.18. It is obvious that both separation differences are largest in the middle sector. On average, the $[135°, 165°]$ sector is $3.39 \times 10^6 km$ and $5.10 \times 10^5 km$ farther away in radial and transverse direction, respectively; the $[165°, 195°]$ sector is $5.30 \times 10^6 km$ and $6.70 \times 10^5 km$ farther away in radial and transverse direction, respectively.

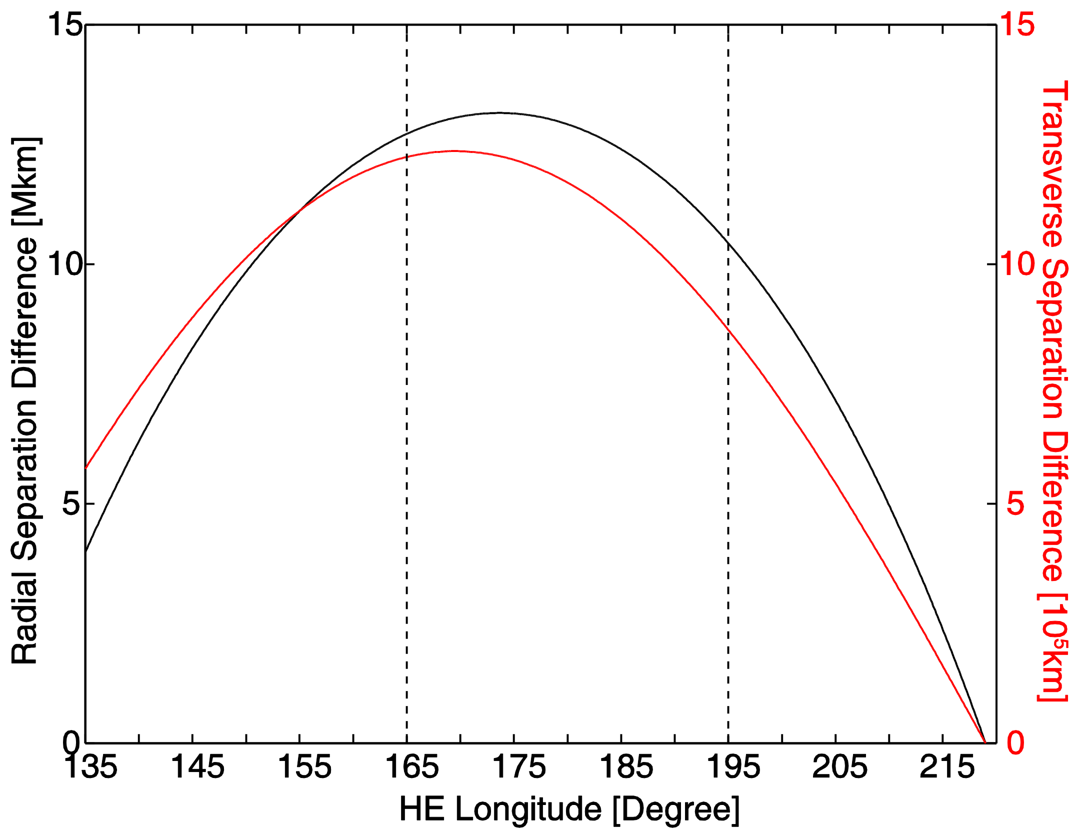

Figure 5.18 Radial (black) and transverse (red) separation differences between Venusian and Oljato's orbits in longitudinal range [135° 220°] in 1983. Here zero is set to be the minimum separation in both directions.

From the five-spacecraft simultaneous observations, we know that an IFE of $1.18 \times 10^6 km$ in radial scale can travel at least $1.40 \times 10^6 km$ (ACE to *Geotail*) in radial direction without significant changes in the magnetic-field structure. And the IFE detected by PVO on February 11, 1982 can be still identified in the observations of Venera 13 and 14, which were $5.85 \times 10^6 km$ and $6.59 \times 10^6 km$ downstream, respectively. Thus the radial separation difference does not dominate the longitudinal variation of IFE annual rate in the PVO observation.

We notice that the average radial scale of the IFEs detected inside the sensitive region is $2.75 \times 10^6 km$, corresponding to a cross-flow radius of $4.91 \times 10^5 km$. This is smaller than the transverse separation difference. Thus except the large IFEs, some moderate and many small IFEs produced near the center of the sensitive region would miss PVO when they travelled radially outward.

The same mechanism cannot be applied to the longitudinal variation of IFE annual rate at $1AU$. From Figure 5.13 we know that the IFE annual rate in the sensitive region near the descending node of asteroid 138175 is higher than the rate in the sensitive region near the ascending node. From the orbital geometry of the Earth and the asteroid shown in Figure 5.12 we know that on average the sensitive region near the ascending node is only $7.53 \times 10^4 km$ farther away in the transverse direction comparing to the sensitive region near the descending node. This is smaller than the average cross-flow radius of the IFEs detected in the sensitive regions, *i.e.*, $2.54 \times 10^5 km$. However, the sensitive region near the ascending node is $1.40 \times 10^7 km$ farther away in the radial direction comparing to the sensitive region near the descending node. This distance is almost ten times the average IFE radial scale, and we do not have any evidence that IFEs can survive after travelling for such a long distance. It is possible that for asteroid 138175, the radial separation difference dominates the longitudinal variation of IFE annual rate. Another possibility is that there are fewer impactors near the ascending node, which is supported by the generally lower rates in the adjacent regions.

5.3.2 Effects of Selection Criteria

From the IFE mass distribution in Figure 5.7 and Figure 5.16 we notice that the IFE annual rate seems to decrease in the small mass range, which is due to our selection criteria as we have discussed in Section 3.4. Since the IFEs associated with asteroid 138175 have generally smaller scale and contain less mass, we may have undercounted more IFEs there.

Figure 5.19 shows two examples. Both of the events have enhanced magnetic-field strength and strong central currents but neither of them is strong enough to satisfy our selection criteria. We are interested in these two events because they have similar magnetic-field patterns and are detected close to each other inside the asteroid sensitive region, even though they are detected one year apart and by different spacecraft. It is highly possible that both events are also associated with co-orbiting material of asteroid 138175 and are produced by the same mechanism as the one generates IFEs. Thus the co-orbiting material of asteroid 138175 is denser than we expect.

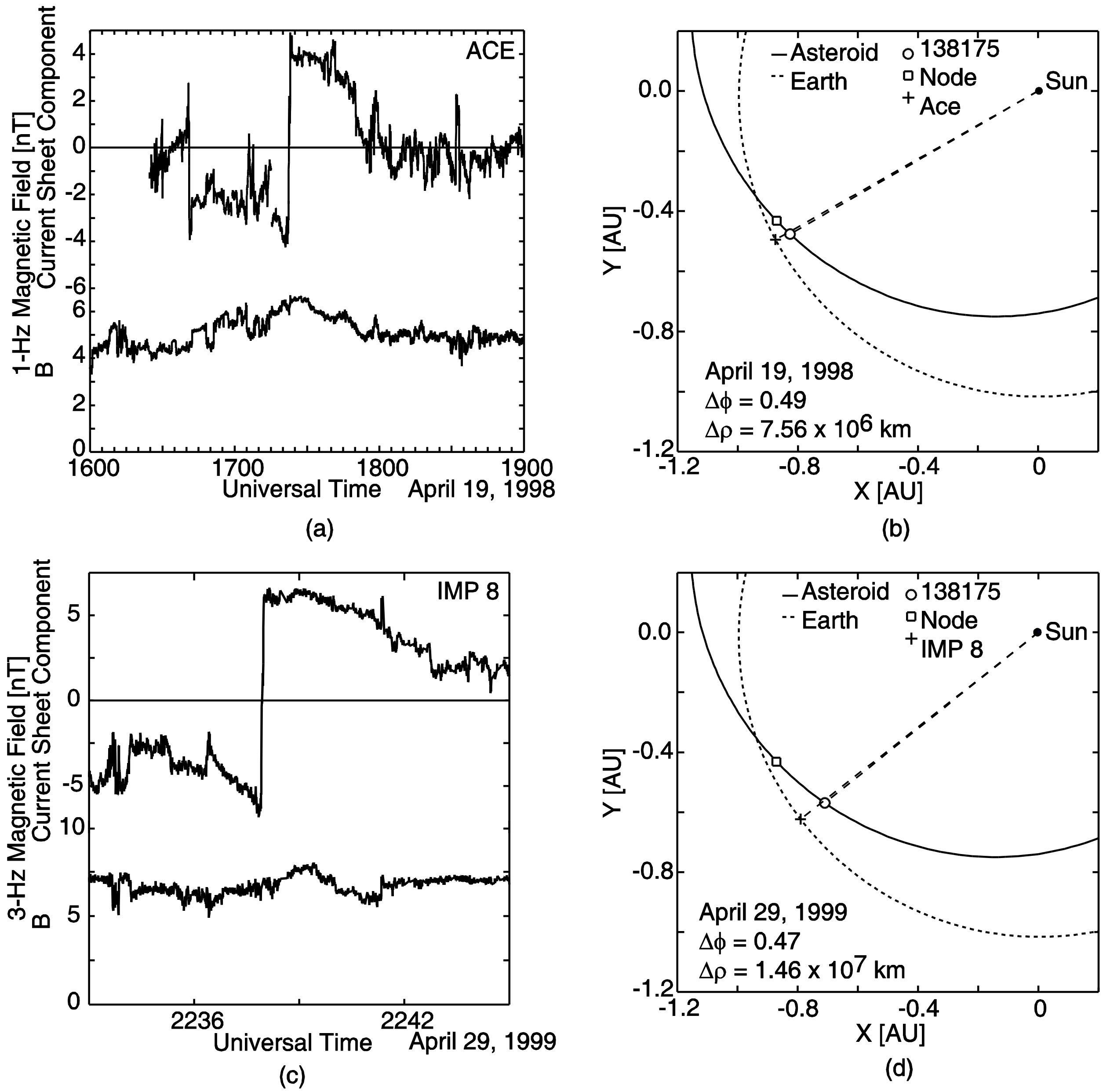

Figure 5.19 One year apart, near the same locations inside the sensitive regions, different spacecraft detected similar IFE-like perturbations. Neither of the perturbations is strong enough to be recorded as IFEs. But it is highly possible that they are generated by the same mechanism. We might have undercounted many of those structures.

5.4 Summary

In this chapter, we first reanalyze the PVO data using the new IFE database and obtain consistent results with the earlier studies: co-orbiting material of Oljato should be responsible for many of the IFEs detected inside the sensitive region. We then compare these results with the VEX observations and find that the IFE producing effect of the co-orbiting material has diminished in the past three decades. This can be caused by the loss of material co-orbiting with Oljato.

Using a similar technique, we suggest co-orbiting material of asteroid 138175 as a source of IFEs detected in the sensitive regions at $1AU$. This result supports that we can use IFE observations to find small interplanetary objects which are hard to detect by traditional methods. By comparing the present observations from ACE, *Wind*, STEREO A and STEREOB with the earlier observation from IMP 8, we also find a temporal variation in the IFE annual rate inside the sensitive region. This again indicates a loss of the co-orbiting material.

The loss of the material co-orbiting with both Oljato and asteroid 138175 can be caused by gravitational perturbations from the Earth and Venus.

We can use Figure 5.11 to identify more IFE associated asteroids whose nodes are in the longitudinal regions while the IFE annual rates are high. And even more candidate asteroids can be found based on the IFE annual rate longitudinal distribution obtained by STEREO A and STEREO B, considering their own periods. These identifications will be studied in future work.

Chapter 6

Summary and Future Work

6.1 Summary of This Study

6.1.1 IFE Formation Hypothesis and Its Application

In this thesis, we study a unique phenomenon in the solar wind, called an interplanetary field enhancement (IFE). Earlier studies show that the magnetic field enhanced during these events and meanwhile the solar-wind plasma is not compressed. These features are also observed in the magnetic barriers and plasma depletion layers which result from solar wind interacts with Venus- or Earth-like obstacles. Considering that IFEs are traveling at nearly the solar-wind velocity and the association between IFEs and co-orbiting material of Oljato, we develop our IFE formation hypothesis: IFEs result from interactions between solar wind and clouds of charged nanoscale dust particles which are released in interplanetary collisions.

This IFE formation hypothesis predicts some IFE features that have not been reported in earlier studies: (1) magnetic field drapes in the upstream region; (2) solar wind slows down in the upstream; (3) IFE occurrence rate is comparable with the rate of interplanetary collisions which release an appropriate amount of nanoscale dust particles.

Based on our hypothesis, one of the applications with the knowledge of IFE occurrence is to obtain the spatial distribution and temporal variation of material co-orbiting with known NEOs. This application is extremely important. Because co-orbiting material of tens of meters across can cause great civilian damage once it enters the Earth's atmosphere but it is hard to identify those objects by traditional survey techniques. In addition, the co-orbiting material can be in dispersed orbits around the orbit of the parent bodies, either due to the initial impact which produces the debris or due to the gravitational perturbations when the debris encounters large planetary bodies. Therefore, even though some known NEOs are considered to be safe for hundreds of years, they might have potentially hazardous material co-orbiting with them.

To test our hypothesis, we perform a systematic survey of IFEs from 1970s to present and from inner than $0.3AU$ to outer than $5AU$ using magnetic field as well as plasma data obtained by many spacecraft.

6.1.2 Case-Study Results

During our IFE survey, we find seven IFEs detected by two spacecraft, two IFE detected by three spacecraft, one IFE detected by four spacecraft and one IFE detected by five spacecraft simultaneously. When an IFE is observed by four or more than four spacecraft, we can determine the velocity of the IFE. When an IFE is observed by two or three spacecraft, we assume that the IFE is moving in the solar-wind direction and then estimate its velocity. Using this method, all the multi-spacecraft observed IFEs are found to move outward away from the Sun at nearly the solar-wind velocity, which is consistent with the earlier results.

An IFE detected by five spacecraft and another IFE detected by four spacecraft simultaneously are used to reconstruct the magnetic-field pattern. We find that in both cases, the magnetic field does drape in the upstream region, just as the hypothesis predicts. While the magnetic field during the IFEs has a significant component in the direction perpendicular to both the ambient magnetic field and flow directions. Such a feature was also detected in the AMPTE experiments.

In some IFE cases, the solar-wind velocity changes sharply in the cross-flow direction at the boundaries separating the solar wind and dust clouds. This feature can be explained by the flow deflection at the boundaries.

6.1.3 Statistical Study Results

In total, we find over 470 IFEs satisfying our selection criteria. They are detected at all heliocentric distance and in all solar and solar-wind conditions. The IFE annual rate increases slowly as the heliocentric distance increases inside $1AU$ and this rate decreases sharply beyond $2AU$. With *Ulysses* observations, we find that the IFE occurrence rate is low near the ecliptic plane and increases as the latitude increases. The longitudinal distribution of IFE occurrence at $0.72AU$ shows a clear cluster feature in the PVO epoch. However, when VEX took observations, such a cluster feature disappeared. At $1AU$, IFE occurrence rate is highest in the longitudinal range from $195°$ to $225°$ based on the observations of ACE, *Wind*, STEREO A and STEREO B. There is another non-random phenomenon: multiple IFEs can occur within a short time period.

Superposed epoch studies show that the solar-wind velocity drops 0.5% in the upstream. Meanwhile there is a solar-wind plasma depletion region near the center of the IFEs, where the magnetic field piles up. The solar-wind slowdown and plasma depletion are more significant in larger IFEs. These features are consistent with the second prediction made by our hypothesis.

Although IFEs vary in durations and strength, their total pressure enhancement distribution is independent of IFE sizes. Thus we make the assumption that IFEs are self-similar structures just varying in size but with the same pressure variation normalized to the ambient pressure. Therefore the observed variable strength results from variable spacecraft impact parameters. If we further assume that the IFE cross section is a circle with azimuthally symmetrical pressure distribution and with maximum pressure at the center, we can reconstruct the IFE pressure profile in the cross-flow direction. Therefore we can estimate the pressure gradient force for IFEs detected by three or more spacecraft. Mass contained in the IFEs can be estimated if we balance this pressure gradient force with solar gravity, assuming that the acceleration is negligible. The solar-wind slowdown results from that estimated mass is consistent with the result in superposed epoch study. From the multi-space observations, the IFE radial scale length is on average 5.6 times its cross-flow radius. If we use this ratio to all the IFEs detected by single spacecraft, we find that the mass of the most frequently observed IFEs is from 10^7 to $10^8 kg$ at $1AU$.

6.1.4 A Comparison between IFE Rate and Interplanetary Collision Rate

To estimate the interplanetary collision rate, we use the collision model of Grün [*et al*., 1985]. We modify the coming-to-Earth influx model [Ceplecha 1992] to get the interplanetary flux model at $1AU$, and assume the number density of the interplanetary objects goes as $\left(\frac{r}{r_0}\right)^{-1.5}$ inside $1AU$ [Leinert *et al*., 1978]. Here r is the heliocentric distance and r_0 is $1AU$. We also assume that the mass distribution of the fragments follows a power law [Fujiwara *et al*., 1977]. With the above assumptions, we find that an impactor with a colliding velocity of $20km/s$ can catastrophically destroy a target which is 10^4 to 10^6 times heavier. Smaller colliders tend to have smaller fragments and the mass carried by nanoscale dust particles can be less than 0.1% of the mass of the target in catastrophic collisions.

Since the IFEs can be carried out by the solar wind and detected by the spacecraft which they pass by, the counterpart of the IFE occurrence rate is the integrated collision rate in a detectable volume. If the IFE mass does not change when it travels radially outward, the cross section of the IFE expands slowly as the heliocentric distance increases. With the further assumption that all the collisions starting from $0.2AU$ can be detected, we can compare the detectable collision rate with the IFE occurrence rate. At $1AU$, the two rates are comparable in the same mass range. Inside $1AU$, the detectable collision rate increases slowly as the heliocentric distance increases, which is consistent with the IFE observations.

6.1.5 IFE Associated Co-orbiting Material

We first reanalyze the association between PVO observed IFEs and co-orbiting material of Oljato. This time we define the sensitive region as the sector where the orbit of Oljato lies upstream of the orbit of Venus. We find that the IFE rate is higher when PVO was inside the sensitive region and the phase difference between Oljato and Venus is small. Outside the sensitive region, the IFE dairy rate is low and random. These results are consistent with the earlier studies and suggest that co-orbiting material of Oljato produced many of the IFEs.

We then compare the modern VEX observation with the PVO observation in the 1980s. This time the IFE rate outside the sensitive region is the same as the one detected by PVO. But the IFE rate inside the sensitive region has decreased.

A similar technique has been applied to the IFEs detected near $1AU$. We search for candidate asteroids whose orbits lie inside $1AU$ and are close to the ecliptic plane in the region where IFE occurrence clusters. Asteroid 138175 satisfies our selection criteria and we suggest that its co-orbiting material produces many IFEs detected in the corresponding sensitive regions. Similar to the case of PVO observation, the IFE rate inside the sensitive region peaks when the phase difference between the asteroid and the Earth is small, and this rate appears to be random outside the sensitive region.

By comparing the modern observations from ACE, *Wind*, STEREO A and STEREO B with the earlier observation from IMP 8, we also find a temporal variation in the IFE daily rate inside the sensitive region: the daily rate was almost twice high in the IMP 8 observation period.

Both temporal variations of the IFE rate can be explained by the loss of the co-orbiting material. Simulation study shows that in decades, due to the gravitational perturbations, gaps will be formed in the otherwise continuous co-orbiting trails [Connors *et al*., 2014a; Connors 2014b]. Therefore if IFEs detected in the earlier days were produced by material which has been cleared out later, the IFE occurrence rate is expected to decrease.

6.2 Future Work

6.2.1 Observations

We note that in our study, multi-spacecraft observations are extremely important in reconstructing the IFE geometry and understanding the spatial and temporal evolution of IFEs. However, as IFEs are generally rare, the ones detected by multiple spacecraft are limited. To acquire more such observations, we can survey more recent data as well as data from other spacecraft which are not included in this study (*e.g.*, ISSE 3).

We have only searched for candidate asteroid in the region where the IFE annual rate is highest, and we notice that there are some other longitudinal ranges where the IFE rates are higher than the rates in the adjacent regions. We expect more IFE sources to be found. This can help us identify more potentially hazardous interplanetary objects and may also improve our understanding of the IFE evolution. Since if we know the IFE source location and we have observations in the downstream region at different distances, we can arrange these IFEs by “ages” and summarize their characteristics according to their ages. We may also be able to find the newborns of “IFEs” which is still in acceleration phase and have quite different magnetic-field geometries.

Once we know the lifetime of the IFEs, we can modify our collision model. Right now we assume that all the IFEs formed at $0.2AU$ can be detected up to $1AU$. The result is consistent with our observations inside $1AU$ but cannot explain the decrease in the IFEs rate beyond $2AU$. If we can set an inner boundary of the collision detectable volume according to the heliocentric distance where IFEs are detected, we can perform the comparison study between IFE rate and collision rate much better.

6.2.2 Simulations

Right now based on the available multi-spacecraft observations, we know that IFEs move at near the solar-wind speed. But we do not know how the IFEs are accelerated in detail. To have a better understanding of this process, we can use simulations. This can be done with the multi-fluid MHD code BATS-R-US, which can now simulate the interactions between magnetized plasma flow and clouds of charged dust in three dimensions in both supersonic and subsonic cases [Jia *et al*., 2012].

Since the simulations performed in Jia *et al*., [2012] are not aimed to reproduce the IFE structures, the initial and boundary conditions are different from what we need: there is a constant dust loading rate following an inverse-square law, which produces a spherical dust cloud in quite conditions; the dust particles have uniform charge to mass ratio; only Lorentz force is considered; the supersonic simulation stops before the dust is accelerated to the plasma flow speed. In a collision, the release of nanoscale dust cloud can be viewed as a transient phenomenon and we expect the dust has a variety charge to mass ratio. Only the ones with an appropriate amount of mass and charges can be accelerated to near the solar-wind speed in a reasonable time interval. We also expect the gravity plays an important role in the entire process, so that momentum still needs to be transferred via the enhanced magnetic field when the dust cloud has approached the solar-wind speed. The magnetic-field geometry and the plasma properties need to be traced during the entire acceleration process. Therefore we can compare the simulation results with the observations and further test our hypothesis.

Appendix I

Lists of IFEs

Table A.1 Parameters Used in the IFE Lists

Parameters	**Descriptions**
Date	In the format of MM/DD/YYYY
Time	Universal Time Corresponding to IFE Central Peak
R	Heliocentric Distance
HE_λ	Longitude in Heliocentric Ecliptic Coordinate System
HE_ϕ	Latitude in Heliocentric Ecliptic Coordinate System
L	IFE Radial Scale Length
T	IFE Duration
BEI	Magnetic-field Enhancement Index $\frac{B_{max}-B_{amb}}{B_{ave}}$
PEI	Total Pressure Enhancement Index $\frac{P_{max}-P_{amb}}{P_{amb}}$

*Depending on the different datasets, not all the parameters above are included in every lists.

*IFEs detected in sensitive regions are highlighted in red.

Table A.2 List of IFEs from ACE Data during 1998-2011

#	Date	Time[UT]	HE_λ [˚]	BEI	L [km]	PEI	M [kg]
1	04/20/1998	1541	199.95	0.39	5.28E+06	NaN	NaN
2	06/02/1998	0152	251.30	0.35	4.56E+05	0.34	4.36E+07
3	07/02/1998	2348	279.96	0.41	5.60E+05	0.29	1.62E+08
4	07/11/1998	0405	288.54	1.77	1.29E+07	1.80	7.02E+10
5	07/24/1998	1445	300.94	0.30	6.10E+05	0.62	6.89E+07
6	10/10/1998	0139	16.50	0.27	4.29E+05	0.47	3.43E+07
7	05/01/1999	1354	104.20	0.28	1.24E+06	0.29	4.95E+08
8	02/02/1999	2334	132.69	0.33	7.06E+05	NaN	NaN
9	05/04/1999	0214	223.11	0.64	6.04E+05	0.33	3.89E+07
10	10/01/1999	2349	7.38	1.08	3.65E+05	1.43	3.11E+07
11	01/20/2000	2257	119.22	0.45	8.69E+05	0.52	1.14E+08
12	05/15/2000	0512	234.47	0.73	8.64E+06	3.17	2.18E+10
13	06/01/2000	2045	250.81	0.68	1.41E+06	0.34	2.09E+08
14	08/25/2000	0318	332.09	0.31	2.91E+05	0.43	2.42E+07
15	09/08/2000	2230	345.64	0.42	2.04E+06	0.78	8.92E+08
16	02/12/2001	1259	143.32	0.31	8.32E+05	NaN	NaN
17	02/17/2001	2314	148.37	0.43	1.62E+06	NaN	NaN
18	03/15/2001	1557	174.45	0.51	1.25E+06	0.42	1.97E+08
19	04/06/2001	1855	196.24	0.56	7.37E+05	0.53	1.45E+08
20	09/16/2001	1150	353.18	0.80	9.97E+05	1.35	1.76E+08
21	09/16/2001	1323	353.18	0.36	9.97E+05	NaN	NaN
22	11/14/2001	0517	51.66	0.37	6.29E+05	NaN	NaN
23	11/14/2001	0735	51.66	0.28	6.10E+05	NaN	NaN
24	04/09/2002	1258	198.94	0.36	8.12E+05	NaN	NaN
25	04/11/2002	1001	200.90	0.42	2.27E+06	NaN	NaN
26	05/03/2002	2032	222.36	0.25	4.63E+05	0.37	3.68E+07
27	11/25/2002	0245	62.50	0.32	1.98E+06	0.37	9.75E+08
28	01/04/2003	2155	103.16	0.34	7.95E+05	0.34	1.23E+08
29	01/27/2003	0031	126.58	0.35	4.26E+06	0.59	6.65E+09
30	03/19/2003	1829	177.93	0.57	2.87E+06	1.12	3.50E+09
31	03/31/2003	0553	189.83	0.57	1.91E+07	0.66	1.51E+11
32	05/20/2003	1131	238.55	0.28	5.91E+05	0.35	9.23E+07
33	05/28/2003	0425	246.24	0.27	1.04E+06	0.34	7.04E+08
34	06/12/2003	0145	260.60	0.40	4.28E+05	0.61	2.10E+07
35	07/05/2003	2052	282.55	0.67	6.90E+05	1.03	5.05E+07
36	07/28/2003	1055	304.49	0.26	3.44E+06	1.50	3.43E+09
37	08/18/2003	0116	324.61	0.46	8.17E+05	0.89	1.02E+09

38	08/25/2003	1824	331.35	0.39	3.26E+05	0.66	1.33E+07
39	12/19/2003	0228	86.59	0.35	1.28E+06	NaN	NaN
40	02/06/2004	2303	136.47	0.35	2.56E+05	NaN	NaN
41	02/25/2004	2013	155.66	0.44	1.01E+06	NaN	NaN
42	03/05/2004	1035	164.70	0.41	7.42E+05	0.69	1.00E+08
43	06/10/2004	1747	259.40	0.28	3.75E+06	0.37	3.71E+09
44	07/09/2004	1847	287.06	0.27	3.17E+05	NaN	NaN
45	08/06/2004	2304	313.81	0.86	7.74E+05	NaN	NaN
46	08/09/2004	0441	316.68	0.99	7.47E+06	NaN	NaN
47	08/22/2004	1511	329.18	0.31	1.44E+06	0.36	3.69E+08
48	10/03/2004	2145	10.06	0.30	9.42E+05	0.23	3.69E+08
49	10/22/2004	1326	28.87	0.29	6.15E+05	0.20	7.18E+07
50	03/27/2005	0116	186.35	0.36	7.82E+05	0.89	1.56E+08
51	03/29/2005	1252	188.33	0.25	3.64E+06	0.29	2.98E+09
52	04/07/2005	0931	197.20	0.32	2.31E+06	0.41	5.30E+08
53	06/07/2005	1216	256.28	0.29	6.29E+05	0.16	1.03E+08
54	12/06/2005	0319	73.88	0.39	3.14E+05	0.43	1.12E+07
55	03/31/2006	2125	190.05	0.39	8.68E+05	0.25	2.05E+08
56	04/11/2006	0342	200.88	0.29	5.89E+05	0.28	2.92E+07
57	05/15/2006	0412	233.95	0.48	4.99E+05	NaN	NaN
58	05/27/2006	0736	245.50	0.30	1.53E+06	NaN	NaN
59	06/11/2006	0818	259.87	0.60	4.76E+06	0.31	2.73E+09
60	06/22/2006	1506	270.37	0.28	6.21E+05	NaN	NaN
61	07/24/2006	1356	300.89	0.25	2.26E+06	NaN	NaN
62	10/02/2006	0542	8.57	0.77	1.04E+06	NaN	NaN
63	10/25/2006	1539	31.34	0.62	5.36E+05	1.28	2.33E+07
64	11/17/2006	1253	54.39	0.49	6.49E+06	1.26	4.89E+09
65	01/16/2007	0429	115.36	0.34	6.61E+05	0.84	1.96E+08
66	05/19/2007	2356	237.56	0.29	2.28E+05	NaN	NaN
67	08/11/2007	1644	317.87	0.55	6.61E+05	0.96	5.55E+07
68	08/19/2007	1324	325.55	0.40	7.69E+05	0.40	1.57E+08
69	09/07/2007	0307	343.90	0.59	1.11E+06	NaN	NaN
70	10/07/2007	1147	13.24	0.52	4.50E+05	NaN	NaN
71	10/30/2007	1632	36.07	0.28	1.46E+06	0.37	2.24E+08
72	12/15/2007	0916	82.50	0.50	3.65E+05	0.78	1.02E+07
73	01/22/2008	1837	121.21	0.85	2.61E+06	0.77	7.63E+08
74	01/27/2008	1447	126.29	0.59	1.99E+05	0.65	7.30E+06
75	02/03/2008	1205	133.40	0.27	1.21E+06	0.47	2.42E+08
76	02/20/2008	0047	150.60	0.31	8.87E+05	NaN	NaN
77	02/20/2008	2116	150.60	0.27	1.16E+06	NaN	NaN

78	04/16/2008	1423	206.26	0.49	4.07E+05	1.35	6.11E+07
79	08/12/2008	1537	319.54	0.50	7.01E+05	0.70	5.46E+07
80	10/23/2008	1334	29.83	0.72	4.99E+05	0.87	3.05E+07
81	03/08/2009	0112	166.42	0.61	7.97E+05	0.67	1.28E+08
82	04/13/2009	1633	203.07	0.48	2.15E+05	0.77	1.92E+06
83	04/18/2009	2225	207.96	0.54	4.48E+05	0.52	1.56E+07
84	05/02/2009	1936	221.60	0.38	3.52E+05	NaN	NaN
85	05/21/2009	1703	239.95	0.44	1.91E+06	NaN	NaN
86	06/19/2009	2007	267.73	0.74	3.72E+06	NaN	NaN
87	10/14/2009	0805	20.64	0.28	1.91E+06	NaN	NaN
88	12/12/2009	1319	79.94	0.38	2.71E+05	NaN	NaN
89	12/30/2009	1853	98.27	0.57	1.52E+06	NaN	NaN
90	03/17/2010	0057	176.14	0.62	3.19E+05	0.38	3.91E+07
91	04/02/2010	1909	192.00	0.51	3.53E+05	0.36	3.73E+07
92	08/19/2010	1125	325.78	0.44	3.20E+06	NaN	NaN
93	08/20/2010	0719	326.74	0.33	1.44E+06	NaN	NaN
94	10/24/2010	0914	30.32	0.35	1.05E+06	NaN	NaN
95	10/26/2010	1610	32.31	0.41	1.29E+06	NaN	NaN
96	11/12/2010	0910	49.34	0.30	1.54E+06	NaN	NaN
97	01/08/2011	1506	107.18	0.38	2.17E+06	0.49	8.80E+08
98	01/24/2011	0221	123.47	0.84	1.07E+06	0.48	1.77E+08
99	03/03/2011	0656	161.89	0.65	1.18E+06	1.65	1.50E+08
100	05/04/2011	1343	223.04	0.52	1.71E+06	0.512	4.64E+07
101	08/08/2011	2050	314.97	0.46	7.82E+05	NaN	NaN
102	10/01/2011	1950	7.31	0.93	2.67E+06	NaN	NaN
103	11/30/2011	2154	67.25	0.35	2.51E+05	NaN	NaN

Table A.3 List of IFEs from *Wind* Data during 2004-2011

#	Date	Time[UT]	HE_λ [˚]	BEI	L [km]	PEI	M [kg]
1	06/10/2004	1800	259.40	0.32	4.27E+06	0.43	4.79E+09
2	02/12/2005	0050	143.30	0.63	6.71E+05	0.63	5.21E+07
3	03/09/2005	1840	168.44	0.42	6.66E+05	0.49	8.97E+07
4	03/29/2005	1300	188.33	0.68	3.34E+06	1.08	1.50E+09
5	04/15/2005	1335	205.06	0.27	3.84E+05	0.36	2.23E+07
6	04/18/2005	1320	207.99	0.29	2.14E+06	0.29	8.03E+08
7	05/03/2005	1435	222.59	0.27	8.30E+05	0.35	7.51E+07
8	05/03/2005	1530	222.59	0.30	3.83E+05	0.36	1.47E+07
9	06/20/2005	0210	268.70	0.31	9.90E+05	0.34	1.26E+08
10	07/04/2005	2055	282.05	0.74	3.42E+05	0.93	1.34E+07
11	08/29/2005	2100	335.68	0.34	7.66E+05	0.37	1.01E+08
12	11/03/2005	1145	40.59	0.66	7.98E+05	0.94	2.97E+08
13	11/27/2005	2120	64.75	0.29	8.47E+05	0.25	1.57E+08
14	04/17/2006	1300	206.76	0.38	2.45E+06	0.43	4.75E+08
15	06/16/2006	1255	264.64	0.26	9.32E+05	0.37	1.12E+08
16	07/30/2006	0050	306.63	0.84	5.87E+05	0.64	6.23E+07
17	09/17/2006	0930	353.88	0.55	3.44E+05	0.71	4.81E+07
18	10/16/2006	2040	22.39	0.42	6.90E+05	0.35	6.58E+07
19	11/17/2006	1300	54.39	0.70	2.42E+06	1.12	6.79E+08
20	11/17/2006	2230	54.39	0.43	2.34E+06	0.69	7.42E+08
21	12/09/2006	2130	76.66	0.30	6.08E+05	0.53	6.10E+07
22	12/10/2006	0135	76.66	0.36	1.72E+06	0.64	4.68E+08
23	01/02/2007	0655	121.47	0.44	9.17E+05	0.58	3.06E+08
24	01/28/2007	0110	126.55	0.29	1.13E+06	0.24	4.49E+08
25	02/22/2007	0840	152.88	0.25	1.16E+06	0.21	2.38E+08
26	05/20/2007	0035	238.52	0.25	9.24E+05	0.31	5.33E+07
27	06/18/2007	1240	266.31	0.47	5.83E+05	0.49	4.37E+07
28	08/27/2007	1825	333.26	0.47	5.66E+05	0.51	6.48E+07
29	09/25/2007	2135	1.45	0.35	1.34E+06	0.41	1.68E+08
30	09/27/2007	0030	3.40	0.65	2.93E+06	0.74	3.11E+09
31	10/07/2007	1205	13.24	0.40	4.45E+05	0.30	2.01E+07
32	10/30/2007	1635	36.07	0.60	1.11E+06	0.71	1.09E+08
33	01/24/2008	1813	123.24	0.49	3.03E+05	0.44	2.74E+07
34	03/02/2008	1330	161.67	0.32	8.94E+05	0.36	6.41E+07
35	03/09/2008	1538	168.68	0.31	7.36E+05	0.39	1.21E+08
36	03/12/2008	0630	171.68	0.37	2.95E+06	0.39	1.01E+09
37	03/31/2008	0710	190.54	0.55	3.31E+06	0.62	7.40E+08
38	05/20/2008	1440	239.24	0.60	1.71E+06	0.87	6.74E+08

39	07/02/2008	0730	280.37	0.45	6.70E+05	0.37	4.02E+07
40	07/18/2008	1555	295.63	0.43	2.99E+05	0.51	6.19E+06
41	08/06/2008	1945	313.79	0.62	1.42E+06	0.83	4.20E+08
42	08/13/2008	0420	320.50	0.54	5.64E+05	0.47	2.33E+07
43	11/12/2008	0130	49.85	0.52	1.02E+06	0.24	1.21E+08
44	02/18/2009	1340	149.33	0.42	9.11E+05	0.25	9.32E+07
45	03/07/2009	0135	166.42	0.37	8.44E+05	0.40	1.82E+08
46	03/14/2009	2155	173.41	0.41	1.32E+06	0.13	4.98E+08
47	03/27/2009	0220	186.33	0.33	3.57E+06	0.35	1.09E+09
48	04/06/2009	1720	196.20	0.38	4.51E+05	0.39	3.06E+07
49	04/06/2009	2255	196.20	0.93	4.74E+05	1.28	3.60E+07
50	04/25/2009	0425	214.79	0.41	7.54E+05	0.42	9.16E+07
51	05/02/2009	0245	221.60	0.44	3.03E+05	0.38	1.92E+07
52	05/11/2009	0320	230.31	0.56	3.23E+05	0.44	1.22E+07
53	06/19/2009	1930	267.73	0.47	3.70E+06	0.32	1.93E+09
54	07/06/2009	0825	283.94	0.42	3.28E+05	0.20	1.45E+07
55	07/25/2009	1825	302.07	0.30	4.85E+05	0.35	2.35E+07
56	12/24/2009	1940	92.16	0.56	4.59E+05	0.59	2.11E+07
57	01/12/2010	0148	111.52	0.42	3.40E+05	0.49	1.89E+07
58	03/07/2010	1548	166.16	0.59	3.30E+05	0.39	9.68E+06
59	03/20/2010	0135	179.13	0.38	4.54E+05	0.34	4.90E+07
60	06/13/2010	2345	261.75	0.33	5.80E+05	0.25	3.77E+07
61	07/1/2010	1700	278.93	0.60	3.78E+06	0.88	1.50E+09
62	09/16/2010	0720	352.88	0.65	5.41E+05	1.12	1.10E+08
63	09/16/2010	1730	352.88	0.37	7.06E+05	0.38	3.26E+08
64	10/02/2010	1000	8.54	0.25	1.97E+06	0.23	3.29E+08
65	11/11/2010	2140	48.33	0.35	6.95E+05	0.52	2.16E+08
66	03/03/2011	0651	161.89	0.34	1.18E+06	0.36	1.50E+08
67	05/04/2011	1326	223.04	0.30	1.71E+06	1.05	4.64E+07
68	06/09/2011	1945	257.69	0.69	7.07E+05	1.55	1.21E+08
69	08/11/2011	2105	317.85	0.54	4.08E+06	0.43	2.41E+09
70	10/16/2011	1200	22.11	0.27	8.85E+05	0.29	1.44E+08

Table A.4 List of IFEs from STEREO A Data during 2006-2012

#	Date	Time[UT]	R[AU]	HE_λ [˚]	HE_ϕ[˚]	BEI	L [km]	M [kg]
1	11/08/2006	2135	0.99	2.38	-0.01	0.87	NaN	NaN
2	12/01/2006	1320	0.99	6.89	-0.02	0.27	NaN	NaN
3	12/24/2006	1205	0.98	20.11	-0.05	0.33	9.94E+05	1.15E+08
4	12/28/2006	0305	0.98	23.26	-0.07	0.30	NaN	NaN
5	01/07/2007	1330	0.97	31.01	-0.10	0.34	NaN	NaN
6	01/26/2007	0400	0.97	43.13	-0.12	0.67	NaN	NaN
7	02/13/2007	1150	0.97	45.38	-0.12	0.82	NaN	NaN
8	04/04/2007	1850	0.96	67.62	-0.04	0.60	7.88E+05	5.75E+07
9	04/10/2007	0955	0.96	68.61	-0.03	1.19	4.96E+06	6.43E+09
10	04/12/2007	1422	0.96	82.10	-0.02	0.75	3.51E+05	7.73E+06
11	05/30/2007	0610	0.96	87.83	0.08	0.80	1.59E+06	2.49E+08
12	05/30/2007	1140	0.96	92.09	0.08	0.75	1.07E+06	9.38E+07
13	06/06/2007	1800	0.96	94.58	0.09	1.04	4.15E+06	1.98E+09
14	06/24/2007	1158	0.96	96.17	0.12	0.60	3.08E+05	3.42E+07
15	09/09/2007	0247	0.96	98.60	0.07	0.34	2.86E+05	1.46E+07
16	01/02/2008	0950	0.97	106.41	-0.13	0.38	5.90E+05	3.15E+07
17	03/14/2008	1445	0.96	110.54	-0.04	0.33	1.05E+06	1.07E+08
18	03/31/2008	0520	0.96	119.89	0.00	0.38	5.46E+06	2.17E+09
19	04/20/2008	2355	0.96	122.03	0.04	0.57	6.77E+05	7.37E+07
20	05/08/2008	2355	0.96	125.92	0.08	0.50	1.42E+06	1.77E+08
21	07/21/2008	0030	0.96	129.68	0.11	0.44	6.16E+05	3.92E+07
22	07/21/2008	0230	0.96	138.43	0.11	0.52	5.84E+05	2.96E+07
23	10/20/2008	1600	0.96	139.02	-0.07	0.55	3.57E+05	1.70E+07
24	11/15/2008	0605	0.97	144.46	-0.11	0.39	9.12E+05	4.10E+07
25	12/28/2008	1850	0.97	147.79	-0.12	0.28	3.00E+05	1.44E+07
26	02/03/2009	1435	0.97	148.77	-0.08	0.65	4.84E+05	2.68E+07
27	03/08/2009	0710	0.96	177.32	-0.01	0.36	8.56E+05	9.19E+07
28	07/19/2009	1750	0.96	196.21	0.08	1.61	7.85E+05	3.61E+07
29	08/15/2009	0155	0.96	196.58	0.03	0.85	3.39E+05	9.21E+06
30	08/18/2009	0908	0.96	197.96	0.02	0.69	1.86E+05	3.87E+06
31	09/06/2009	0730	0.96	202.46	-0.02	0.70	5.72E+05	2.64E+07
32	10/19/2009	0655	0.97	204.54	-0.10	0.74	4.33E+05	2.32E+07
33	11/19/2009	2135	0.97	211.66	-0.13	0.57	2.89E+05	8.25E+06
34	12/26/2009	1840	0.97	214.30	-0.11	0.37	3.17E+05	1.34E+07
35	09/23/2010	2120	0.97	218.82	-0.09	0.43	1.66E+05	3.36E+06
36	11/08/2010	1755	0.97	227.18	-0.13	0.67	3.95E+06	2.34E+09
37	05/01/2011	0445	0.96	235.23	0.12	0.30	4.95E+05	7.09E+07
38	09/30/2011	2100	0.97	239.30	-0.12	0.67	1.01E+07	1.07E+10

39	10/27/2011	2103	0.97	245.59	-0.12	0.45	5.31E+05	2.42E+07
40	11/06/2011	2108	0.97	254.14	-0.11	0.38	1.50E+06	3.48E+08
41	02/01/2012	1100	0.96	254.79	0.05	0.56	NaN	NaN
42	02/07/2012	1848	0.96	254.79	0.07	0.50	NaN	NaN
43	06/01/2012	2240	0.96	262.16	0.06	0.41	NaN	NaN
44	06/24/2012	0235	0.96	281.13	0.01	0.26	NaN	NaN
45	08/28/2012	2115	0.97	311.56	-0.11	0.46	NaN	NaN
46	12/02/2012	2205	0.96	332.25	-0.03	0.41	NaN	NaN
47	12/22/2012	0345	0.96	332.25	0.01	0.84	NaN	NaN
48	12/30/2012	1400	0.96	351.73	0.03	0.54	NaN	NaN

Table A.5 List of IFEs from STEREO B Data during 2006-2012

#	Date	Time[UT]	R[AU]	HE_λ [°]	HE_ϕ[°]	BEI	L [km]	M [kg]
1	12/24/2006	1210	0.98	9.30	-0.04	0.63	9.94E+05	1.15E+08
2	01/16/2007	0450	0.98	34.86	-0.04	0.52	NaN	NaN
3	01/25/2007	2210	0.98	63.31	0.08	1.46	NaN	NaN
4	02/16/2007	1815	1.00	66.16	0.06	1.58	NaN	NaN
5	04/07/2007	1930	1.03	69.13	-0.18	1.31	2.20E+06	4.72E+08
6	05/16/2007	0150	1.05	74.04	-0.28	0.44	2.81E+05	1.19E+07
7	05/20/2007	0925	1.06	77.80	-0.29	0.46	6.50E+05	2.47E+07
8	08/03/2007	0600	1.09	91.65	-0.17	0.53	8.45E+06	5.34E+09
9	08/11/2007	1615	1.09	92.09	-0.14	0.34	3.25E+05	5.40E+06
10	08/18/2007	1605	1.09	94.63	-0.11	0.31	9.70E+05	1.57E+08
11	08/19/2007	1315	1.09	94.66	-0.11	0.38	6.84E+05	1.13E+08
12	09/01/2007	0905	1.08	99.79	-0.06	0.40	3.09E+05	4.50E+07
13	09/05/2007	2140	1.08	115.36	-0.04	0.40	5.21E+05	4.21E+07
14	10/21/2007	0545	1.06	117.82	0.16	0.84	8.42E+05	5.13E+07
15	12/29/2007	1230	1.01	124.39	0.29	0.35	4.70E+05	2.38E+07
16	01/24/2008	1650	1.00	146.73	0.25	0.58	1.29E+06	2.49E+08
17	04/08/2008	1148	1.01	156.85	-0.09	0.64	3.35E+05	1.03E+07
18	05/05/2008	0510	1.03	174.68	-0.21	0.48	3.06E+06	1.07E+09
19	05/21/2008	2000	1.04	181.45	-0.25	1.01	6.58E+06	2.82E+09
20	08/10/2008	2020	1.08	181.45	-0.22	0.54	1.59E+06	1.12E+08
21	09/14/2008	0830	1.08	195.80	-0.10	0.69	1.08E+06	1.31E+08
22	12/11/2008	0830	1.04	200.63	0.25	0.41	4.29E+05	1.77E+07
23	01/10/2009	0200	1.02	209.98	0.29	0.30	1.59E+06	2.12E+08
24	01/16/2009	0305	1.02	210.81	0.29	0.32	8.08E+05	6.25E+07
25	03/06/2009	0225	1.00	215.58	0.18	0.87	1.04E+06	8.61E+07
26	05/09/2009	0900	1.02	223.82	-0.12	0.42	NaN	NaN
27	05/09/2009	1645	1.02	230.14	-0.12	0.77	NaN	NaN
28	06/08/2009	2103	1.04	231.98	-0.24	1.21	6.50E+05	3.95E+07
29	06/23/2009	1530	1.05	235.48	-0.27	0.58	7.52E+05	5.64E+07
30	07/09/2009	0305	1.06	235.58	-0.29	0.26	1.09E+06	1.24E+08
31	07/22/2009	1640	1.07	238.29	-0.29	0.38	2.47E+06	4.57E+08
32	11/18/2009	0940	1.07	249.85	0.08	0.55	1.55E+06	9.06E+07
33	02/06/2010	0932	1.02	251.49	0.29	0.48	4.73E+05	3.20E+07
34	05/08/2010	1705	1.01	274.13	0.00	0.31	5.54E+05	2.74E+07
35	07/24/2010	1905	1.05	287.15	-0.28	0.34	9.47E+05	1.13E+08
36	03/31/2011	0420	1.00	300.79	0.26	0.40	6.70E+05	3.88E+07
37	07/27/2011	0410	1.04	301.52	-0.24	0.83	3.08E+06	3.18E+09

38	12/11/2011	2252	1.08	307.61	-0.03	0.63	2.13E+05	8.87E+06
39	12/17/2011	1640	1.08	313.58	0.00	0.79	6.46E+05	2.63E+07
40	04/06/2012	0845	1.01	314.44	0.29	0.82	NaN	NaN
41	04/20/2012	0700	1.01	317.02	0.27	0.65	NaN	NaN
42	04/23/2012	1830	1.00	322.01	0.24	0.60	NaN	NaN
43	09/15/2012	0250	1.06	325.56	-0.29	0.96	NaN	NaN
44	10/03/2012	0018	1.07	329.00	-0.29	0.37	NaN	NaN
45	10/29/2012	1511	1.08	330.61	-0.26	0.77	NaN	NaN
46	11/30/2012	0625	1.09	335.79	-0.17	0.25	NaN	NaN
47	12/24/2012	1530	1.08	352.41	-0.07	0.33	NaN	NaN

Table A.6 List of IFEs from PVO Data during 1978-1988

#	Date	Time[UT]	R[AU]	HE_λ [˚]	HE_ϕ[˚]	BEI	L [km]	PEI
1	12/11/1978	0315	0.72	97.11	1.18	0.32	2.77E+05	0.14
2	01/04/1979	0510	0.72	137.68	2.97	0.62	2.37E+05	0.52
3	03/02/1979	0752	0.72	229.76	1.54	0.25	7.26E+05	0.21
4	03/16/1979	0040	0.73	252.06	0.28	0.25	1.18E+06	0.20
5	07/10/1979	1213	0.72	108.94	1.81	0.38	1.43E+06	0.76
6	10/04/1979	1435	0.72	215.84	2.22	0.60	1.27E+06	0.64
7	01/13/1980	2255	0.73	16.18	-2.96	0.85	2.43E+05	0.46
8	03/11/1980	2040	0.72	109.43	1.84	0.95	1.73E+06	NaN
9	03/27/1980	1607	0.72	135.40	2.90	0.25	7.40E+05	0.42
10	04/03/1980	1618	0.72	146.78	3.19	0.46	5.15E+05	0.65
11	04/07/1980	0213	0.72	153.28	3.30	0.34	3.91E+05	0.14
12	04/08/1980	0510	0.72	154.91	3.32	1.25	2.46E+06	2.23
13	05/07/1980	0053	0.72	201.86	2.78	0.41	9.24E+05	0.61
14	05/12/1980	1717	0.72	209.90	2.48	0.31	0.00E+00	NaN
15	06/13/1980	0610	0.73	260.95	-0.25	0.46	5.88E+06	0.54
16	07/08/1980	1050	0.73	300.51	-2.35	1.74	5.99E+06	1.36
17	07/30/1980	0732	0.73	335.32	-3.33	0.65	6.14E+05	0.98
18	12/11/1980	1455	0.72	191.05	3.09	0.36	5.18E+05	0.26
19	01/22/1981	1230	0.73	258.26	-0.09	0.52	1.11E+06	0.41
20	06/06/1981	0910	0.72	113.63	2.04	4.19	5.63E+06	0.54
21	06/09/1981	0720	0.72	118.50	2.26	0.80	1.14E+07	1.38
22	07/16/1981	0425	0.72	178.59	3.32	0.25	8.26E+05	0.63
23	10/04/1981	1045	0.72	135.24	2.90	0.32	2.79E+06	0.50
24	10/13/1981	1050	0.72	140.11	3.04	3.20	1.46E+07	11.44
25	11/03/1981	1600	0.72	153.12	3.30	1.13	7.63E+06	2.95
26	01/30/1982	1247	0.73	306.21	-2.58	0.38	1.20E+06	1.00
27	02/03/1982	0002	0.73	320.44	-3.04	0.87	6.92E+05	2.42
28	02/10/1982	0500	0.73	353.73	-3.37	1.37	3.36E+07	3.97
29	04/25/1982	1750	0.73	271.88	-0.89	0.29	3.90E+06	0.66
30	12/20/1982	1710	0.73	294.49	-2.08	0.54	1.09E+06	0.76
31	06/09/1983	0430	0.72	207.49	2.57	1.26	3.15E+06	NaN
32	06/11/1983	1445	0.72	212.31	2.38	0.25	7.07E+05	0.31
33	06/12/1983	1245	0.72	213.91	2.31	0.30	7.99E+05	0.13
34	06/13/1983	0825	0.72	215.52	2.24	0.50	0.00E+00	NaN
35	10/31/1983	1711	0.72	78.37	0.10	0.30	5.16E+05	0.52
36	11/22/1983	1126	0.72	113.95	2.06	0.83	3.78E+05	0.69
37	01/24/1984	0311	0.72	215.99	2.22	0.80	6.70E+05	0.20
38	01/26/1984	1145	0.72	219.20	2.07	3.16	1.58E+07	NaN

39	03/15/1984	1105	0.73	297.03	-2.20	0.25	1.54E+06	0.60
40	04/17/1984	0850	0.73	349.28	-3.39	0.28	1.43E+06	1.25
41	01/04/1985	0705	0.72	48.78	-1.59	1.31	8.74E+05	0.75
42	01/17/1985	1015	0.72	69.67	-0.42	0.50	9.94E+05	0.20
43	04/03/1985	1911	0.72	192.82	3.05	0.37	1.11E+06	0.20
44	05/10/1985	1109	0.73	252.06	0.28	0.64	4.49E+05	0.17
45	02/09/1986	0447	0.73	331.67	-3.28	0.74	1.59E+06	NaN
46	05/18/1986	1315	0.72	127.26	2.62	0.66	9.65E+05	1.50
47	05/29/1986	1545	0.72	146.77	3.19	0.36	1.80E+06	0.52
48	07/08/1986	2009	0.72	211.50	2.41	0.63	0.00E+00	NaN
49	07/11/1986	2040	0.72	216.32	2.20	0.59	7.09E+05	0.32
50	08/04/1986	0715	0.73	254.60	0.13	0.27	2.24E+06	0.08
51	08/27/1986	1653	0.73	291.02	-1.91	0.82	1.03E+06	0.47
52	12/31/1986	1450	0.72	132.62	2.81	0.38	4.16E+06	0.10
53	01/03/1987	0420	0.72	137.50	2.96	1.11	1.02E+06	0.54
54	01/30/1987	0447	0.72	181.33	3.29	0.69	1.66E+06	0.61
55	02/09/1987	0453	0.72	197.49	2.92	1.39	6.15E+05	0.37
56	03/22/1987	2001	0.73	263.00	-0.37	1.04	4.35E+05	0.52
57	09/25/1987	0525	0.72	202.80	2.74	1.13	NaN	NaN
58	09/27/1987	1700	0.72	206.02	2.63	0.37	6.13E+05	0.50
59	11/01/1987	1833	0.73	261.89	-0.31	0.44	1.03E+06	0.71
60	11/09/1987	1530	0.73	274.56	-1.04	0.49	7.71E+05	0.45
61	02/21/1988	0750	0.72	80.14	0.20	1.18	5.06E+05	0.34
62	04/30/1988	1041	0.72	192.00	3.07	0.32	7.55E+05	0.21
63	05/15/1988	1947	0.72	216.14	2.21	0.43	4.90E+05	0.27

Table A.7 List of IFEs from VEX Data during 2006-2012

#	Date	Time[UT]	R[AU]	HE_λ [˚]	HE_ϕ[˚]	BEI	T [min]
1	05/13/2006	1020	0.73	304.56	-2.52	0.50	177
2	06/01/2006	2005	0.73	334.64	-3.32	1.29	63
3	07/04/2006	1405	0.72	27.13	-2.58	0.38	94
4	07/24/2006	0515	0.72	59.17	-1.02	0.43	26
5	07/25/2006	1000	0.72	60.78	-0.93	0.33	84
6	11/18/2006	1630	0.73	248.04	0.51	0.54	148
7	05/12/2007	1510	0.72	168.17	3.39	2.00	54
8	07/27/2007	1840	0.73	289.71	-1.85	0.36	88
9	08/28/2007	1410	0.73	340.34	-3.37	0.32	46
10	08/19/2007	1235	0.73	341.93	-3.38	0.31	52
11	08/19/2007	1700	0.73	341.93	-3.38	0.36	64
12	11/19/2007	1209	0.72	113.42	2.03	0.51	16
13	02/07/2008	2106	0.73	242.63	0.82	0.68	18
14	03/06/2008	0855	0.73	287.02	-1.72	0.77	91
15	04/13/2008	1135	0.73	347.17	-3.39	0.42	75
16	05/11/2008	1955	0.72	31.77	-2.40	0.90	33
17	05/27/2008	1230	0.72	57.40	-1.12	0.66	33
18	06/21/2008	1042	0.72	97.70	1.22	0.87	48
19	08/20/2008	0351	0.72	195.03	2.99	1.31	24
20	09/17/2008	1706	0.72	239.92	0.98	0.28	27
21	10/17/2008	1708	0.73	287.49	-1.74	0.35	93
22	12/31/2008	1350	0.72	46.65	-1.70	0.49	126
23	01/23/2009	0033	0.72	83.64	0.41	0.57	59
24	01/23/2009	1027	0.72	83.64	0.41	0.57	67
25	01/29/2009	1403	0.72	93.34	0.98	0.39	50
26	03/19/2009	1928	0.72	172.87	3.37	0.35	38
27	06/30/2009	1055	0.73	337.01	-3.35	0.39	16
28	08/29/2009	1345	0.72	72.83	-0.23	0.49	32
29	09/24/2009	1237	0.72	114.88	2.10	0.54	25
30	11/10/2009	2348	0.72	191.16	3.09	0.53	32
31	12/06/2009	1206	0.72	232.90	1.37	0.30	12
32	03/18/2010	2143	0.72	34.79	-2.27	0.28	24
33	06/06/2010	0949	0.72	164.10	3.39	0.41	30
34	06/14/2010	1645	0.72	177.08	3.34	0.39	63
35	09/25/2010	2235	0.73	341.13	-3.38	0.91	98
36	10/24/2010	1120	0.72	27.28	-2.58	0.49	56
37	11/02/2010	0747	0.72	41.68	-1.95	0.38	21
38	01/08/2011	1000	0.72	149.96	3.25	0.33	40

39	02/01/2011	1905	0.72	188.88	3.14	1.28	17
40	02/13/2011	1845	0.72	208.22	2.54	0.40	96
41	05/01/2011	1650	0.73	330.51	-3.26	0.36	321
42	06/10/2011	0743	0.72	34.16	-2.29	0.69	11
43	06/26/2011	2105	0.72	59.80	-0.98	0.41	10
44	07/06/2011	1648	0.72	75.90	-0.04	0.49	32
45	07/27/2011	2125	0.72	109.84	1.86	0.45	50
46	09/18/2011	1625	0.72	195.82	2.96	0.52	102
47	09/18/2011	1805	0.72	195.82	2.96	0.49	81
48	01/05/2012	0300	0.73	9.10	-3.14	0.33	51
49	01/06/2012	1130	0.73	10.70	-3.10	0.52	65
50	02/15/2012	1320	0.72	74.77	-0.11	0.26	10
51	02/27/2012	2305	0.72	94.14	1.02	0.32	49
52	03/04/2012	0435	0.72	103.85	1.55	0.38	19
53	03/27/2012	2305	0.72	141.19	3.07	0.25	60

Table A.8 List of IFEs from *Helios* 1 Data during 1975-1981

#	Date	Time[UT]	R[AU]	HE_λ [˚]	BEI	T [min]
1	06/17/1975	0029	0.98	77.1	0.50	31
2	09/16/1975	2130	0.33	223.5	0.31	42
3	01/07/1976	2139	0.97	86.2	0.31	9
4	12/25/1976	0715	0.97	67.6	0.26	22
5	01/17/1977	1445	0.98	83.8	0.31	28
6	01/18/1977	1203	0.98	84.5	0.37	9
7	10/06/1977	2030	0.44	176.5	0.49	226
8	04/22/1979	0207	0.53	154.6	0.60	72
9	03/30/1980	0225	0.88	104.4	0.43	23
10	10/24/1980	1315	0.75	122.3	1.21	89
11	11/07/1980	1033	0.60	143.0	0.30	31
12	12/12/1981	1020	0.36	204.7	0.31	17

Table A.9 List of IFEs from *Helios* 2 Data during 1976-1979

#	Date	Time[UT]	R[AU]	HE_λ [˚]	BEI	T [min]
1	12/27/1976	0845	0.93	96.9	0.45	23
2	02/06/1977	0300	0.96	125.7	0.64	20
3	04/11/1977	1545	0.39	217.0	0.42	86
4	05/01/1977	1600	0.34	347.1	0.42	22
5	05/02/1977	0120	0.36	352.7	0.34	50
6	11/07/1977	0904	0.40	7.8	0.30	45
7	03/08/1979	1805	0.89	138.2	0.80	19
8	05/27/1979	0820	0.51	35.9	0.32	77

Table A.10 List of IFEs from MESSENGER Data during 2007-2010

#	Date	Time[UT]	R[AU]	HE_λ [˚]	HE_ϕ[˚]	BEI	T [min]
1	03/12/2007	1701	0.68	15.07	-4.28	0.45	15
2	04/23/2007	0035	0.55	113.15	7.50	0.65	41
3	06/15/2008	0835	0.38	122.00	6.59	0.32	9
4	08/17/2008	1014	0.69	246.86	-2.11	0.74	42
5	09/09/2008	0213	0.58	282.52	-5.54	0.57	11
6	09/10/2008	0920	0.57	284.44	-5.68	0.58	15
7	09/11/2008	0600	0.57	286.41	-5.81	0.45	16
8	02/08/2009	1125	0.31	58.00	1.18	0.34	19
9	02/25/2009	0242	0.41	152.89	6.77	0.25	16
10	03/08/2009	1850	0.50	187.67	4.57	1.07	310
11	03/30/2009	1425	0.62	231.34	-0.37	0.93	8
12	04/09/2009	1550	0.63	247.45	-2.30	0.95	39
13	04/13/2009	1635	0.63	253.82	-3.02	0.36	25
14	04/15/2009	1653	0.63	257.03	-3.37	0.34	19
15	06/13/2009	1655	0.33	104.97	5.85	0.49	42
16	07/04/2009	0105	0.50	188.47	4.49	0.25	97
17	08/14/2009	2320	0.62	262.43	-3.94	0.37	42
18	02/10/2010	0235	0.45	192.98	4.09	0.44	28
19	02/17/2010	0340	0.50	212.39	1.95	2.18	139
20	03/09/2010	1155	0.57	254.99	-3.16	0.64	24
21	05/27/2010	1530	0.45	193.87	4.00	0.82	18
22	08/04/2010	0140	0.37	4.00	-4.93	0.49	26
23	08/29/2010	1000	0.36	148.70	6.92	0.32	144
24	09/29/2010	2310	0.55	240.36	-1.46	0.34	10
25	11/12/2010	0920	0.42	341.31	-6.48	0.38	32
26	11/21/2010	0910	0.35	19.64	-3.40	0.44	10
27	12/14/2010	0850	0.37	154.81	6.75	0.65	14

Table A. 11 List of IFEs from *Ulysses* Data during 1990-2005

#	Date	Time[UT]	R[AU]	HE_λ [˚]	HE_ϕ[˚]	BEI	T [min]
1	11/30/1990	1305	1.26	77.36	1.80	0.82	31
2	05/14/1991	0617	3.02	136.43	1.67	0.81	18
3	12/22/1991	1750	5.01	155.88	1.21	0.32	50
4	03/15/1992	1440	5.40	158.40	-0.71	0.62	25
5	10/16/1992	2325	5.21	160.44	-11.50	0.30	9
6	11/28/1992	2320	5.13	160.89	-13.77	1.15	120
7	03/28/1993	1315	4.86	162.31	-20.56	0.33	39
8	04/01/1993	2127	4.85	162.37	-20.80	0.55	12
9	08/16/1993	1550	4.42	164.49	-29.78	0.28	22
10	09/27/1993	0320	4.25	165.32	-32.93	0.31	74
11	10/26/1993	0623	4.13	165.98	-35.25	0.42	31
12	10/30/1993	0335	4.12	166.07	-35.58	0.44	20
13	11/19/1993	1805	4.03	166.58	-37.27	0.42	33
14	02/22/1994	0535	3.56	169.84	-46.47	0.47	24
15	03/06/1994	0145	3.50	170.40	-47.81	0.36	26
16	04/10/1994	1315	3.30	172.39	-51.98	0.79	17
17	07/07/1994	2003	2.76	182.35	-64.88	0.43	17
18	08/26/1994	0300	2.42	199.74	-73.86	0.46	34
19	09/23/1994	2255	2.23	225.50	-78.25	0.48	49
20	10/20/1994	2050	2.03	269.03	-78.39	0.43	27
21	11/11/1994	1220	1.88	297.60	-73.56	0.44	41
22	12/04/1994	1000	1.73	313.87	-65.01	0.29	30
23	12/16/1994	1019	1.65	319.20	-59.45	0.42	5
24	02/09/1995	2315	1.39	332.95	-25.40	0.41	7
25	02/20/1995	0600	1.36	334.79	-17.14	0.58	15
26	03/10/1995	0610	1.34	337.59	-3.08	0.35	32
27	03/20/1995	1200	1.34	339.11	4.83	0.26	24
28	03/27/1995	2255	1.35	340.18	10.31	0.63	119
29	06/20/1995	2340	1.73	0.74	63.42	0.37	15
30	07/17/1995	1500	1.92	18.22	73.38	0.41	34
31	09/13/1995	0650	2.32	98.03	77.52	0.28	66
32	11/17/1995	1905	2.77	131.71	66.70	0.49	45
33	12/08/1995	0035	2.90	135.72	63.33	0.33	28
34	08/31/1996	2210	4.28	150.55	34.65	0.40	21
35	10/30/1996	0745	4.50	151.74	30.27	0.64	28
36	11/04/1996	2115	4.52	151.83	29.92	0.48	46
37	12/21/1996	0725	4.68	152.61	26.79	0.51	19
38	02/17/1997	2105	4.85	153.46	23.18	0.33	15

39	04/04/1997	0150	4.96	154.06	20.47	0.30	38
40	04/18/1997	0155	5.00	154.24	19.67	0.34	33
41	04/18/1997	0930	5.00	154.24	19.67	0.41	39
42	06/04/1997	0235	5.10	154.79	17.06	0.40	37
43	01/17/1998	0105	5.38	157.11	5.46	0.40	92
44	05/09/1998	1020	5.41	158.16	0.01	0.34	61
45	02/12/1999	1110	5.13	160.91	-14.04	0.58	114
46	12/23/1999	1410	4.20	165.62	-34.12	0.89	99
47	04/05/2000	0850	3.72	168.61	-43.40	0.80	261
48	07/28/2000	1900	3.09	175.36	-57.00	1.33	93
49	08/21/2000	1300	2.94	178.05	-60.56	0.63	102
50	09/08/2000	0730	2.82	180.74	-63.43	0.52	92
51	11/11/2000	1805	2.39	203.12	-74.79	0.40	57
52	12/11/2000	1020	2.18	235.79	-78.87	0.36	54
53	01/21/2001	2055	1.89	296.62	-73.83	0.37	36
54	03/11/2001	2130	1.58	323.55	-52.65	0.45	10
55	08/04/2001	0100	1.57	351.34	49.94	0.86	21
56	09/15/2001	0155	1.83	8.92	69.42	0.53	41
57	11/05/2001	1325	2.19	72.46	79.09	0.26	27
58	02/09/2002	0635	2.84	134.17	64.69	0.30	22
59	03/06/2002	1436	3.00	137.99	60.84	0.57	35
60	10/10/2002	1400	4.14	149.76	37.18	0.35	160
61	01/30/2003	1910	4.57	152.05	28.88	0.39	58
62	10/27/2003	0500	5.22	155.55	13.11	0.39	146
63	11/23/2004	0730	5.34	159.41	-6.55	0.43	87
64	12/09/2004	0900	5.33	159.58	-7.36	0.61	20
65	01/25/2005	2145	5.27	160.07	-9.76	0.40	24

Table A.12 List of IFEs from IMP 8 Data during 1974-2000 inside the Sensitive Region of Asteroid 138175

#	Date	Time[UT]	HE_λ [˚]	BEI	T[min]
1	04/11/1974	1345	201.65	0.30	26
2	10/11/1975	0434	17.39	0.28	28
3	10/24/1975	1716	30.29	0.31	8
4	10/25/1976	0229	32.03	0.81	16
5	10/15/1977	0942	21.84	0.31	19
6	10/14/1986	2333	20.54	0.64	32
7	10/17/1986	0148	23.51	0.46	31
8	04/13/1988	1208	203.94	0.43	28
9	04/15/1988	0018	205.42	0.30	9
10	04/15/1989	0137	205.21	0.33	30
11	04/24/1989	1230	213.94	0.38	73
12	10/14/1989	0748	20.77	0.27	26
13	10/22/1990	0710	28.46	0.31	10
14	10/27/1990	0428	33.44	0.30	22
15	10/24/1991	2205	30.19	0.28	106
16	10/16/1992	0515	22.98	0.34	5
17	10/25/1993	0240	31.68	0.27	11
18	10/15/1994	1230	21.48	0.36	17
19	10/14/1996	0028	20.97	0.45	33
20	04/18/1997	0345	208.20	0.37	41
21	04/18/1997	1735	208.75	0.52	29
22	04/17/2000	0426	207.47	0.30	10

Appendix II

IFE Clustering in Time Probability Calculation

From 14-year ACE observation, we detected 103 IFEs in total. Among them, there are four periods when two IFEs were detected within 24 hours. We perform the following steps to calculate the probability if the IFE occurrence is exactly random: (1) generate 103 random numbers between 0 and 5113 (the number of days in the 14 years); (2) sort the numbers; (3) calculate the difference between two successive numbers; (4) count the number of differences which are less than one. We repeat the above procedure 10^7 times and find that on average, the occurrence of having four cases in which the difference between two random numbers is less than one is 0.0934.

Appendix III

Solar-wind Parameters Radial Dependence Model

In order to estimate the radial variation of the IFE cross section, we need to know the values of background solar-wind parameters from 0.3 to $1AU$. Here we adapt the solar wind radial dependence model presented in Köhnlein [1996]. The empirical expressions for interplanetary magnetic-field (IMF) strength, solar-wind proton number density and temperature are derived using the data from *Helios* 1, *Helios* 2, *Pioneer* 10, *Pioneer* 11, *Voyager* 1 and *Voyager* 2. The values of all the solar-wind parameters have the form

$$Y = a_1 + a_2 X + a_3 \exp(a_4 X) \qquad (A.1)$$

where $Y = \log_{10} y$, $X = \log_{10} x$. y stands for IMF strength ([nT]), solar-wind proton number density ([/cc]) and temperature ([K]), and x stands for the heliocentric distance ([AU]). The coefficients $a_{1,2,3,4}$ are listed in Table (A.13). For the solar-wind electrons, we assume that they have the same number density as the protons do and have a constant temperature of $130000K$.

Coefficient	$\boldsymbol{B}$	$\boldsymbol{N_p}$	$\boldsymbol{T_P}$
$\boldsymbol{a_1}$	0.5	0.7766	4.858
$\boldsymbol{a_2}$	-1.1	-1.934	-0.668
$\boldsymbol{a_3}$	0.2815	0.01823	-4.69×10^{-42}
$\boldsymbol{a_4}$	0.875	-2.245	-40.91

Table A.13 Coefficient used in Equation (A.1) [Köhnlein 1996].

The resultant radial variation of solar-wind parameters are shown in Figure A.1. Here all the values have been normalized to the corresponding strength at $1AU$. In this figure we also include three dashed lines representing the dependences corresponding to r^{-2}, r^{-1} and $r^{-0.5}$, respectively. We can see that the density generally follows the inverse-square law. The pressure estimated based on this model is shown in Figure A.2. Here we show the magnetic pressure, the plasma thermal pressure and the total pressure profiles. All the pressures have been normalized to the total pressure at $1AU$. Also shown in this figure is the inverse-square law. We can see that at $1AU$, the magnetic pressure and the plasma thermal pressure are comparable; while inside $1AU$, the thermal pressure dominates. Therefore the total pressure decreases slightly faster than the inverse-square law. Thus to balance the gravity on the same amount of mass, the IFE cross section will slowly expands as the IFE moves outward.

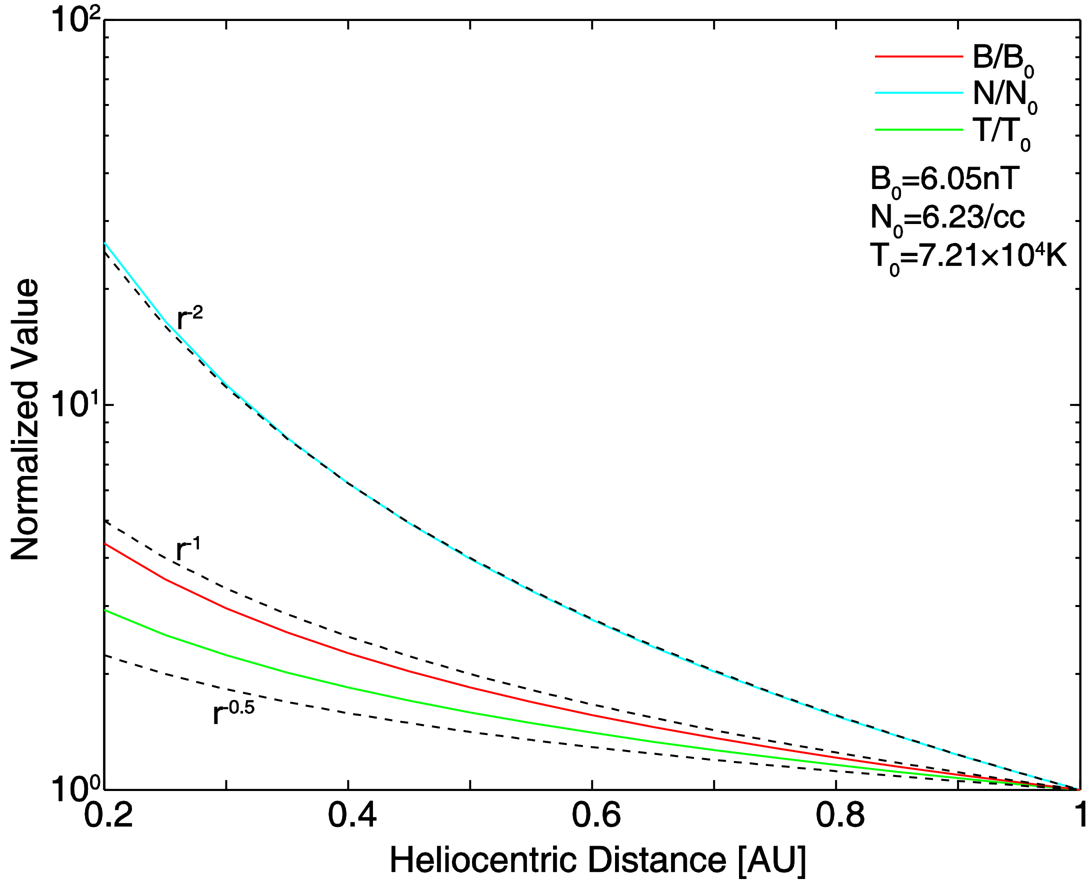

Figure A.1 Radial dependence of solar-wind parameters based on the model of Köhnlein [1996]. All the values have been normalized to the corresponding values at $1AU$.

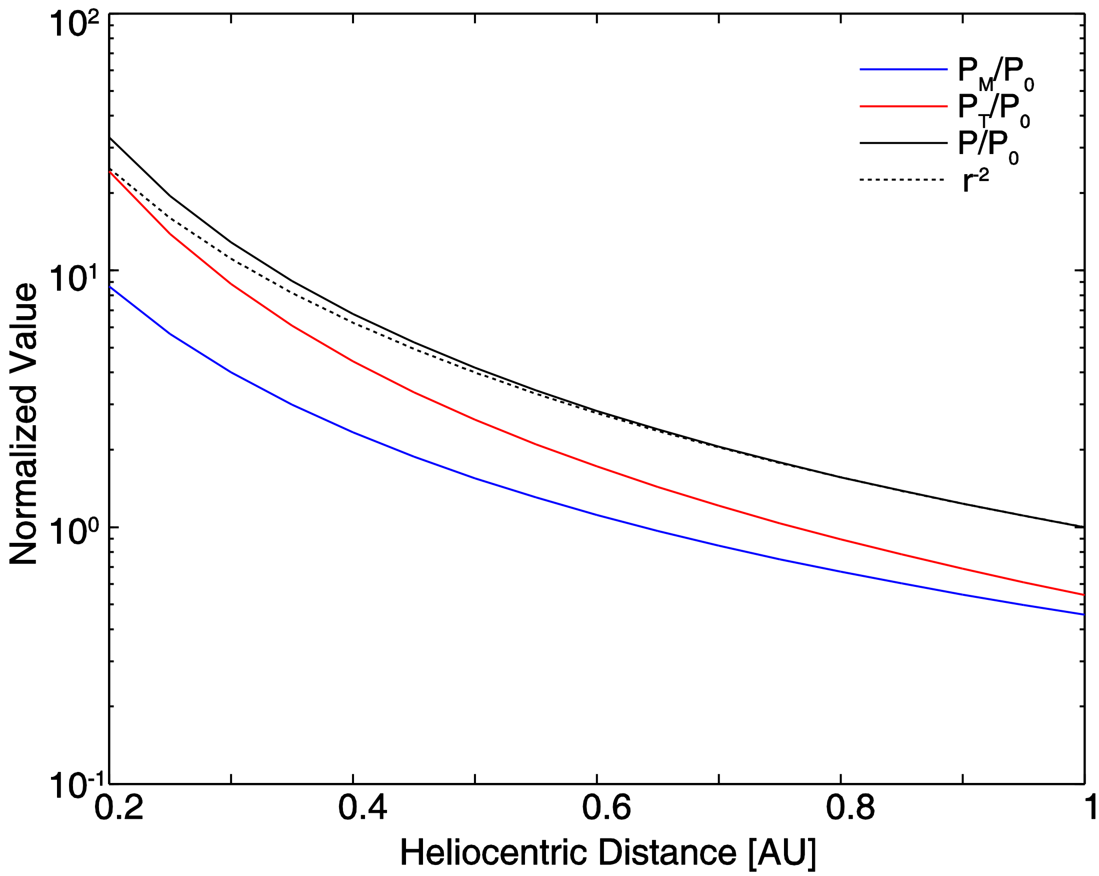

Figure A.2 Radial dependence of magnetic pressure (blue line), plasma thermal pressure (red line) and total pressure (black solid line). All the values have been normalized to the total pressure at $1AU$. The thermal pressure dominates the total pressure inside $1AU$. We can see that the total pressure decreases slightly faster than the inverse-square law (black dashed line).

References

Acuña, M.H., Curtis, D., Scheifele, J.L., Russell, C.T., Schroeder, P., Szabó, A., Luhmann, J.G., 2008. The STEREO/IMPACT magnetic field experiment. *Space Sci. Rev.* 136, 203-226

Anderson, B.J., Acuña, M.H., Lohr, D.A., Scheifele, J., Raval, A., Korth, H., Slavin, J.A., 2007. The magnetometer instrument on MESSENGER. *Space Sci. Rev. 131*, 417-450.

Angelopoulos, V, 2011. The ARTEMIS Mission, *Space Sci. Rev*. 165, 3-25.

Arghavani, M.R., Russell, C.T., Luhmann, J.G., Elphic, R.C., 1985. Interplanetary magnetic field enhancements in the solar wind: statistical properties at 1 AU. *Icarus* 62, 230-243.

Balogh, A., Beek, T.J., Forsyth, R.J., Hedgecock, P.C., Marquedant, R.J., Smith, E.J., Southwood, D.J., Tsurutani, B.T., 1992. The magnetic field investigation on the *Ulysses* mission-Instrumentation and preliminary scientific results, *Astron. Astrophys. Suppl. Ser*. 92, 221-236.

Bame, S.J., McComas, D.J., Barraclough, B.L., Phillips, J.L., Sofaly, K.J., Chavez, J.C., Goldstein, B.E., Sakurai, R.K., 1992. The *Ulysses* solar wind plasma experiment, *Astron. Astrophys. Suppl. Ser.* 92, 237-265.

Borrini, G., Gosling, J.T., Bame, S.J., Feldman, W.C., Wilcox, J.M., 1981. Solar wind helium and hydrogen structure near the heliospheric current sheet: a signal of coronal streamers at 1AU, *J. Geophys. Res*. 86, 4565-4573.

Bottke, W.F., Nolan, M.C., Greenberg, R., Kolvoord, R.A., 1994. Velocity distributions among colliding asteroids. *Icarus* 107, 255-268.

Ceplecha, Z., 1992. Influx of interplanetary bodies onto Earth. *Astron. Astrophys*. 263, 361-366.

Chamberlin, A.B., McFadden, L.-A., Schulz, R., Schleicher, D.G., Bus, S.J., 1996. 4015 Wilson-Harrington, 2201 Oljato, and 3200 Phaethon: Search for CN emission. *Icarus* 119, 173-181.

Connors, M., Russell, C.T., Lai, H.R., 2014a. A temporary Earth co-orbital linked to interplanetary field enhancements. *Mon. Not. R. Astron. Sco.*, submitted.

Connors, M., 2014b. Athabasca University, Canada. Personal communication.

Crooker, N.U., Eastman, T.E., Stiles, G.S., 1979. Observations of plasma depletion in the magnetosheath at the dayside magnetopause, *J. Geophys. Res.* 84, 869-874.

Czechowski, A., Mann, I., 2010. Formation and acceleration of nano dust in the inner heliosphere. *Astrophys. J*. 714, 89-99.

Czechowski, A., Mann, I., 2011. Erratum: ‘formation and acceleration of nano dust in the inner heliosphere”. *Astrophys. J*. 732, 127-127.

Drummond, J.D., 1982. Theoretical meteor radiants of Apollo, Amor, and Aten asteroids, *Icarus* 49, 143-153.

Fujiwara, A., Kamimoto, G., Tsukamoto, A., 1977. Destruction of basaltic bodies by high-velocity impact. *Icarus* 31, 277-288.

Galvin, A.B., Kistler, L.M., Popecki, M.A., *et al.*, 2008. The plasma and suprathermal ion composition investigation on the STEREO observatories. *Space Sci. Rev.* 136, 437-486.

Gosling, J.T., Pizzo, V.J., 1999. Formation and evolution of corotating interaction regions and their three dimensional structure. *Space Sci. Rev*. 89, 21-52.

Grün, E., Zook, H.A., Fechtig, H., Giese, R.H., 1985. Collisional balance of the meteoritic complex. *Icarus* 62, 244-272.

Harris, A., 2008. What spaceguard did, *Nature* 453, 1178-1179.

Hirshberg, J., Colburn, D.S., 1969. Interplanetary field and geomagnetic variations- a unifield view. *Planet. Space Sci.* 17, 1183-1206.

Jewitt, D., Weaver, H., Agarwal, J., Mutchler, M., Drahus, M., 2010. Newly disrupted main belt asteroid P/2010 A2, *Nature* 467, 817-819.

Jewitt, D., 2012. The active asteroids. *Astronomical J.* 143, 66.

Jia, Y.D., Ma, Y.J., Russell, C.T., Lai, H.R., Toth, G. and Gombosi, T.I, 2012. Perpendicular flow deviation in a magnetized counter-streaming plasma, *Icarus* 218, 895-905.

Jian, L.K., Russell, C.T., Luhmann, J.G., Skoug, R.M., 2006. Properties of stream interactions at 1AU during 1995-2004. *Sol. Phys*. 239, 337-392.

Jones, G.H., Balogh, A., McComas, D.J., MacDowall, R.J., 2003a. Strong interplanetary field enhancements at Ulysses-evidence of dust trails' interaction with the solar wind? *Icarus* 166, 297-310.

Jones, G.H., Balogh, A., Russell, C.T., Dougherty, M.K., 2003b. Possible distortion of the interplanetary magnetic field by the dust trail of comet 122P/De Vico. *Astrophys. J*. 597, 61-64.

Kivelson, M.G., Russell, C.T., 1995. Introduction to space physics. Cambridge University Press, Cambridge. Chapter 3.

Kimura, H. Mann, I, 1998. The electric charging of interstellar dust in the solar system and consequences for its dynamics, *Astrophys. J*.499, 454-462.

Kokubun, S., Yamamoto, T., Acuña, M.H., Hayashi, K., Shiokawa, K., Kawano, H., 1992. The *Geotail* magnetic field experiment. *J.Geomag. Geoelectr*. 46, 7-21.

Köhnlein, W., 1996. Radial dependence of solar wind parameters in the ecliptic (1.1R_S-61AU). *Sol. Phys*. 169, 209-213.

Leinert, C., Hanner, M., Pitz, E., 1978. On the spatial distribution of interplanetary dust near 1AU. *Astron. Astrophys*. 63, 183-187.

Lepping, R.P., Acuña, M.H., Burlaga, L.F., *et al*., 1995. The *Wind* magnetic field investigation, *Space Sci. Rev*. 71, 207-229.

Lin, R.P., Anderson, K.A., Ashford S., *et al*., 1995. A three-dimensional plasma and energetic particle investigation for the *Wind* spacecraft. *Space Sci. Rev*. 71, 125-153.

Lowell, J., Truscott, W.S., 1986. Triboelectrification of identical insulators: I. An experimental investigation. *J. Phys D: Appl. Phys*. 19, 1273-1280.

Lühr, H., Southwood, D.J., Klöcker, N., Dunlop, M.W., Mier-Jedrzejowicz, W.A.C., Rijnbeek, R.P., Six, M., Häusler, B., Acuña, M., 1986. In situ magnetic field observations of the AMPTE artificial comet. *Nature* 320, 708-711.

McComas, D.J., Gosling, J.T., Winterhalter, D., Smith, E.J., 1988. Interplanetary magnetic field draping about fast coronal mass ejecta in the outer heliosphere. *J. Geophys. Res*. 93, 2519-2526.

McComas, D.J., Bame, S.J., Barker, P., Feldman, W.C., Phillips, J.L., Riley, P., Griffee, J.W., 1998. Solar wind electron proton alpha monitor (SWEPAM) for the advanced composition explorer. *Space Sci. Rev*. 86, 563-612

McFadden, L.A., Gaffey, M.J. and McCord, T.B. 1984. Mineralogical-petrological characterization of near-Earth asteroids. *Icarus* 59, 25-40.

McFadden, L.A., Cochran, A.L., Barker, E.S., Cruikshank, D.P. and Hartmann, W.K. 1993. The enigmatic object 2201 Oljato: is it an asteroid or an evolved comet? *J. Geophys. Res.* 98, 3031-3041.

Meyer-Vernet, N., Maksimovic, M., Czechowski, A., Mann, I., Zouganelis, I., Goetz, K., Kaiser, M.L., St. Cyr, O.C., Bougeret J.L., Bale, S.D., 2009. Dust detection by the wave instrument on STEREO: nanoparticles picked up by the solar wind? *Sol. Phys*. 256, 463-474.

Neubauer, F.M., Beinroth, H.J., Barnstorf, H., Dehmel, G., 1977. Initial results from the *Helios* 1 search-coil experiment. *J. Geophys*. 42, 599-614.

Neugebauer, M., Goldstein, R., 1997. In: Crooker, N., Joselyn, J.A., Feynman, J. (*eds.*) Coronal mass ejections, *Geophys. Monogr. Ser.* 99, AGU, Washington, 245.

Olsson-Steel D. 1988. Identification of meteoroid streams from Apollo asteroids in the Adelaide radar orbit surveys. *Icarus* 75, 64-96.

Rodgers, D.J., Coates, A.J., Johnstone, A.D., Smith, M.F., Bryant, D.A., Hall, D.S., Chaloner, C.P., 1986. UKS plasma measurements near the AMPTE artificial comet. *Nature* 320, 712-716.

Rosenbauer , H., Schwenn, R., Marsch, E., Meyer, B., Miggenrieder, H., Montgomery, M.D., Muehlhaeuser, K.H., Philipp, W., Voges, W., Zink, S.M., 1977. A survey on initial results of the *Helios* plasma experiment. *J. Geophys*. 42, 561-580.

Russell, C.T., Snare, R.C., Means, J.D., Elphic, R.C., 1980. Pioneer Venus Orbiter fluxgate magnetometer. *IEEE Transactions on Geoscience and Remote Sensing* GE-18, 32-36.

Russell, C.T., Luhmann, J.G., Barnes, A., Mihalov, J.D., Elphic, R.C., 1983a. An unusual interplanetary event: encounter with a comet? *Nature* 305, 612-615.

Russell, C.T., Mellott, M.M., Smith, E.J., King, J.H., 1983b. Multiple spacecraft observations of interplanetary shocks: four spacecraft determination of shock normals. *J. Geophys. Res*. 88, 4739-4748.

Russell, C.T., Arghavani, M.R., Luhmann, J.G., 1984a. Interplanetary field enhancement in the solar wind: statistical properties at 0.72 AU, *Icarus* 60, 332-350.

Russell, C.T., Aroian, R., Arghavani, M., Nock, K., 1984b. Interplanetary magnetic field enhancements and their association with the asteroid 2201 Oljato. *Science* 226, 43-45.

Russell, C.T., Schwingenschuh, K., Phillips, J.L., Arghavani, M.R., 1985. Three spacecraft measurements of an unusual disturbance in the solar wind: further evidence for a cometary encounter. *Geophys. Res. Lett*. 12, 476-478.

Russell, C.T., 1987. Interplanetary magnetic field enhancements: further evidence for an association with asteroid 2201 Oljato. *Geophys. Res. Lett*. 14, 491-494.

Russell, C.T., Weimer, D.R., Omidi, N., Jian, L.K., Luhmann, J.G., Strangeway, R.J., 2010. Interplanetary field enhancements travel at the solar wind speed. *Geophys. Res. Lett*. 37, L07204, doi: 10.1029/2010GL042618.

Shukla, P.K., Mamun, A.A., 2002. Introduction to dusty plasma physics. London, UK: institute of Physics. Bristol. Chapter 1.2.

Smith, C.W., L'Heureux, J., Ness, N.F., Acuña, M.H., Burlaga, L.F., Scheifele, J., 1998. The ACE magnetic fields experiment. *Space Sci. Rev*. 86, 613-632

Smith, E.J., Wolfe, J.H., 1976. Observations of interaction regions and corotating shocks. *Geophys. Res. Lett*. 3, 137-140.

Spreiter, J.R., Summers, A.L. and Alksne A.Y., 1966. Hydromagnetic flow around the magnetosphere, *Planet, Space Sci*. 14, 223-250.

Valenzuela, A., Haerendel, G., Föppl, H., Melzner, F., Neuss, H., Rieger, E., Stöcker, J., Bauer, O., Höfner, H., Loidl, J., 1986. The AMPTE artificial comet experiments. *Nature* 320, 700-703.

Vogt, J., Haaland, S., Paschmann, G., 2011. Accuracy of multi-point boundary crossing time analysis. *Ann. Geophys*. 29, 2239-2252.

Woolfson, M., 2000. The origin and evolution of the solar system, *A&G*, 41, 1.12-1.19.

Zhang, T.L., Luhmann, J.G., Russell, C.T., 1991. The magnetic barrier at Venus, *J. Geophys. Res*. 96, 11145-11153.

Zhang, T.L., Baumjohann, W., Delva, M., *et al*., 2006. Magnetic field investigation of the Venus plasma environment: Expected new results from *Venus Express*. *Planetary & Space Sci*. 54, 1336-1343.

Ziolkowski, K., 1994. Orbit of the enigmatic object (2201) Oljato. *ACTA Astronomica*, 44, 213-221.

Zwan, B.J., Wolf, R.A., 1976. Depletion of solar wind plasma near a planetary boundary, *J. Geophys. Res*. 81, 1636-1648.